Dynamics of sand ridges in coastal seas: the effect of storms, tides and grain sorting

Dynamica van zandruggen in kustzeeën:
de invloed van stormen, getij en korrelgrootte sortering

(met een samenvatting in het Nederlands)

PROEFSCHRIFT

ter verkrijging van de graad van doctor aan de Universiteit Utrecht
op gezag van de Rector Magnificus, Prof. dr. W.H. Gispen,
ingevolge het besluit van het College voor Promoties
in het openbaar te verdedigen op

maandag 27 oktober 2003 des middags om 14:30 uur

door

Marianne Walgreen

geboren op 21 augustus 1976 te Amstelveen

Promotor: **Prof. dr. J. Dronkers**
Copromotor: **Dr. H.E. de Swart**
Instituut voor Marien en Atmosferisch onderzoek Utrecht (IMAU),
Faculteit Natuur- en Sterrenkunde, Universiteit Utrecht

Dit proefschrift werd mogelijk gemaakt door financiële steun van de Dr. Ir. Cornelis Lely Stichting (Delft) en is gedeeltelijk uitgevoerd in het kader van het EC-MAST 5 HUMOR project (contractnr. EVK3-CT-2000-00037).

ISBN 90-393-3469-2

Contents

1 Introduction **1**
- 1.1 The coastal system: physical and geographical aspects . . . 1
- 1.2 Central focus of this thesis . . . 3
- 1.3 Observations and classification of sand ridges . . . 5
- 1.4 Theories concerning the presence of shoreface-connected and tidal sand ridges . . . 8
- 1.5 Process-based morphodynamic models: concepts . . . 8
- 1.6 Free and forced morphodynamic behaviour . . . 9
- 1.7 Modelling shoreface-connected and tidal sand ridges: state of the art . . . 10
- 1.8 Objectives of this thesis . . . 14
- 1.9 Overview of subsequent chapters . . . 14

2 Growth of large-scale bedforms due to storm-driven and tidal currents **17**
- 2.1 Introduction . . . 18
- 2.2 Model formulation . . . 19
  - 2.2.1 Sediment transport and bed shear stress during storms . . . 21
  - 2.2.2 Sediment transport and bed shear stress during fair weather . . . 22
- 2.3 Solution method . . . 23
  - 2.3.1 Basic state . . . 23
  - 2.3.2 Linear stability analysis . . . 24
- 2.4 Results . . . 25
  - 2.4.1 Storms . . . 25
  - 2.4.2 Fair weather . . . 27
  - 2.4.3 Storms and fair weather combined . . . 31
- 2.5 Conclusions . . . 35

Appendix . . . 35
- 2.A Sediment flux . . . 35
- 2.B Basic state velocity profile . . . 36
- 2.C Flow over topography problem . . . 37

3 Effect of grain size sorting on the formation of shoreface-connected sand ridges **39**
- 3.1 Introduction . . . 40
- 3.2 Model formulation . . . 41

3.2.1 Hydrodynamics . . . 41
3.2.2 Sediment characteristics . . . 43
3.2.3 Sediment continuity . . . 43
3.2.4 Sediment transport . . . 45
3.3 Basic state, stability analysis and solution procedure . . . 49
3.3.1 Basic state . . . 49
3.3.2 Stability analysis . . . 50
3.3.3 Solution procedure . . . 52
3.4 Results . . . 53
3.4.1 Parameter values . . . 53
3.4.2 Standard deviation . . . 53
3.4.3 Hiding functions: bed load . . . 56
3.4.4 Hiding functions: suspended load . . . 57
3.5 Physical interpretation . . . 59
3.5.1 Hiding in bed load . . . 59
3.5.2 Hiding in suspended load . . . 61
3.6 Discussion . . . 63
3.7 Conclusions . . . 63
Appendix . . . 65
3.A Suspended load concentration . . . 65
3.B Bottom friction coefficient . . . 66
3.C Sediment flux . . . 66
3.D List of frequently used variables . . . 67

4 A model for grain size sorting over tidal sand ridges 69
4.1 Introduction . . . 70
4.2 Model formulation and solution methods . . . 70
4.2.1 Hydrodynamics . . . 71
4.2.2 Sediment dynamics . . . 71
4.2.3 Basic state . . . 73
4.2.4 Stability analysis . . . 74
4.3 Results . . . 75
4.3.1 Shelf characteristics . . . 75
4.3.2 Sensitivity to standard deviation . . . 76
4.3.3 Sensitivity to hiding coefficient . . . 79
4.4 Discussion . . . 80
4.4.1 Symmetrical tidal forcing . . . 80
4.4.2 Asymmetrical tidal forcing . . . 81
4.4.3 Comparison with field observations . . . 82
4.5 Conclusions . . . 84
Appendix . . . 85
4.A Sediment flux . . . 85

5 Nonlinear evolution of shoreface-connected ridges and grain sorting 87
5.1 Introduction . . . 88
5.2 Model formulation and methods . . . 91
5.2.1 Morphodynamic model: equations of motion . . . 91
5.2.2 Stability analysis . . . 94
5.2.3 Summary of previous model results . . . 96
5.3 Results . . . 97
5.3.1 Parameter values: default case . . . 97
5.3.2 Linear analysis: default case . . . 98
5.3.3 Linear analysis: sensitivity to parameter values . . . 99
5.3.4 Nonlinear analysis: default case . . . 101
5.3.5 Process analysis . . . 104
5.3.6 Nonlinear analysis: sensitivity to parameter values . . . 111
5.4 Discussion and conclusions . . . 114
Appendix . . . 116
5.A Sediment flux . . . 116
5.B Matrix elements . . . 118

6 Discussion and conclusions 121

Bibliography 129

Samenvatting 135

Dankwoord 139

Curriculum Vitae 141

Chapter 1

Introduction

The general topic of interest of this thesis concerns the dynamics of bedforms that are observed in coastal seas in water depths between 5 and 30 m and which have horizontal length scales of a few kilometres. Both field observations and model studies indicate that the dynamics of these features is due to the interaction of the hydrodynamic processes and the sandy bottom through the motion of sediment.

In this introductory chapter the existence of these large-scale bedforms as part of the coastal system is discussed (section 1.1 + 1.2). An overview of what the observations reveal about these ridges is given in section 1.3, followed by a discussion on the existing theories with regard to their formation (section 1.4). Sections 1.5 and 1.6 present a brief overview of the basic concepts of morphodynamic models, used to verify the theories, and their applications. These concepts are applied in most modelling efforts for large-scale ridges done so far (section 1.7). It will become clear that there are still many open questions, of which only a few are discussed in this thesis (section 1.8). An outline of the thesis is given in section 1.9.

1.1 The coastal system: physical and geographical aspects

Coastal seas form the transition from land to sea; they extend from the shoreline to the seaward end of the continental shelf, usually at depths of about 100-200 m. The offshore limit is marked by a steep slope in the sea floor, which separates the shelf from the deep ocean. Examples of coastal seas are the North Sea, the East Chinese Sea and the shallow waters of the Mid-Atlantic Bight of North America.

The water motion in coastal seas is influenced in a number of different ways. The wind blowing over the water surface induces surface waves, wind-driven currents and a set-up (or set-down) of water towards the shoreline. Tidal forcing results in changes in the water level and current direction between the ebb and flood period of the tide. In most coastal seas the dominant tidal constituent is the semi-diurnal lunar (M_2) tide. At the landward boundary of the coastal sea, the outflow of fresh river water in the more saline sea water induces density gradients which force an estuarine type of circulation.

The water motion occurs on a wide range of timescales, from seconds for short waves to

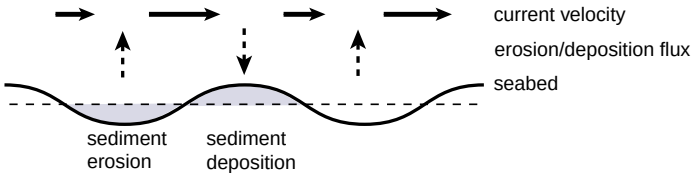

Figure 1.1: Changing current velocity resulting in convergence (deposition, vertical downward arrow) and divergence (erosion, vertical upward arrow) of the sediment flux in case of growing perturbations in the seabed (no migration).

hundreds of years related to the changes in the sea level. An essential aspect of the coastal system is that these currents and waves are capable of transporting water and sediment, and redistribute heat and salt. In case of sediment, the currents must exceed a certain threshold value before the sediment is eroded from the seabed (Dyer, 1986). Stronger currents are capable of eroding and transporting more sediment, so that changes in the current velocity can lead to a spatial convergence or divergence in the sediment transport (Figure 1.1). A morphological change in the seabed, e.g. the development of a sand bank, is the result. If the location of the maximum erosion (deposition) is shifted with respect to the location of the maximum (minimum) perturbation in the seabed the morphological pattern is migrating. In turn, these changes in the bottom can affect the currents due to changing water depths. The result is the generation of different types of bedforms, on many different length and timescales.

The dense population in coastal lowlands and the use of the shallow coastal seas for transport, recreation, sand mining, etc., make the need for a good understanding of the coastal system inevitable. Nevertheless, the understanding and the prediction of coastal morphodynamics is still limited. The problem is the lack of fundamental knowledge about the underlying physical processes like sediment transport, wave-current interaction and turbulent mixing, mainly due to the overall complexity of these processes. The wide range of length and timescales involved in coastal seas make it difficult, if not impossible, to deal with all hydro- and morphodynamic processes at once. Often this is solved by focusing only on a specific zone, characterised by specific dominant physical processes (see, e.g., Wright, 1995).

The different zones within the coastal region are indicated in Figure 1.2, which shows a sketch of a shore-normal section of the coastal shelf, starting at the landward limit of the beach. In the nearshore zone (typical cross-shore slope of 1:100) the water motion is dominated by shoaling, refraction and breaking of surface waves. Besides, tides play a role: they cause relatively large changes in the water level during the tidal period. The shoreface is roughly defined as the part of the nearshore zone that is permanently covered by water, i.e. seaward from the low tide shoreline. The nearshore zone is a highly variable system, where bedforms grow and disappear on timescales of hours to several years. The smallest bedforms, such as ripples (length scale $\sim$ cm) that are often observed on the beach, change on the shortest timescales, while larger banks in the zone where waves start to break (horizontal lengthscale of $\sim$ 100 m) evolve on longer timescales (Short, 1999). Between these two extremes, field observations show a large variety of morphodynamic features, including beach

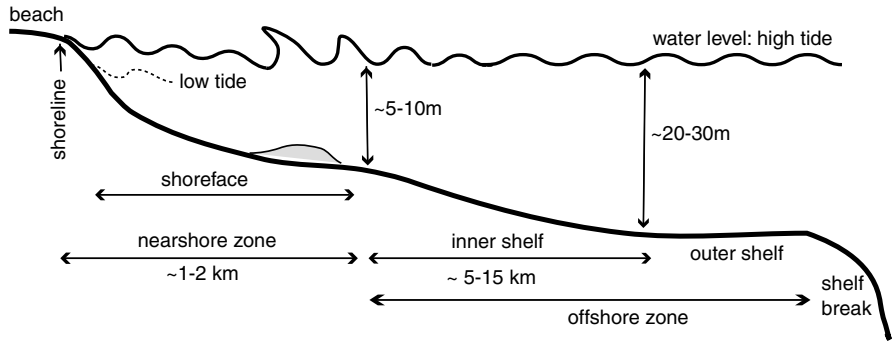

Figure 1.2: Sketch of the coastal region; the different subareas are indicated.

cusps and swash bars. The spatial extent of the bedforms is strongly related to the temporal scale of the dominant hydrodynamical forcing.

The influence of waves is less dominant in the more offshore located areas; here other forcing mechanisms (wind, tides) become more important. Besides the dominant constituents of the water motion, also the depth range and the cross-shore slopes of the sea bed discern the regions. The water depth in the offshore zone gradually increases from the seaward limit of the shoreface (~ 10 m) over the inner shelf, with slopes of the seabed being small (1:1000) compared to those in the nearshore. A further decrease in bedslope to almost constant depths marks the transition to the outer shelf. The shear stresses exerted by the water motion on the bottom are sufficiently large to mobilise the sandy sediment until depths of about 30 m.

The different hydrodynamic forcing conditions, with respect to those in the nearshore zone, do not only result in slower response timescales, but also in a large variety of bottom patterns. This can be seen in Figure 1.3, which shows the depth variations along the Belgian coast in the southern North Sea, a coastal sea which has a maximum depth of ~ 50 m. This is a meso-tidal shelf, a terminology that is often used to indicate the maximum tidal range. The classification is from micro-tidal (range < 2 m) to meso-tidal and macro-tidal (> 4 m). Large sand ridges are present at several locations, from a distance of 1-2 km offshore up to depths of about 30 m, with heights ranging from 1-8 m and a length of 10-20 km. Other types of bedforms can also be seen on this map.

1.2 Central focus of this thesis

In this thesis the focus will be on the large-scale sand ridges that are present on the inner and outer shelves of many coastal seas. Their horizontal extent is of the order of several kilometres and they evolve on long morphodynamical timescales (decades to centuries). It should be realised that these bedforms only form a small part of the entire spectrum of possible bedforms that are observed within the complex coastal system. Besides pure scientific interest in the question of why these ridges are there, their social and economical impact is equally important. Focusing again on the southern North Sea, these large-scale bedforms are

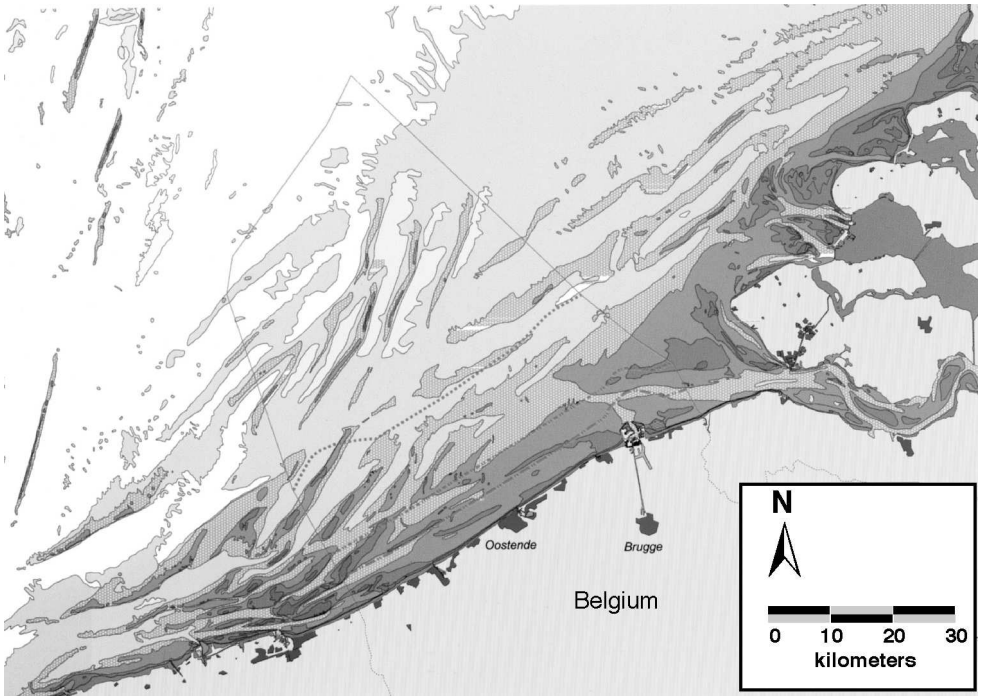

Figure 1.3: Sand ridges in the southern part of the North Sea, along part of the Dutch and Belgian coast. The different shades of grey indicate the water depth, where shallower areas are darker. The offshore ridges off the coast of Belgium are tidal sand ridges, the ones closer to the coast are shoreface-connected ridges. Note the difference in orientation of the crests. Based on Maes et al. (1997).

also present along the central part of the Holland coast, which is thought to be less subject to erosion than the regions further north and south (Van de Meene, 1994). The presence of these ridges (see Figure 2.1 in chapter 2) might be one of the causes, although there is no hard evidence to support this hypothesis. The intersection of the ridges with major shipping lanes and offshore located oil rigs is one of the obvious reasons to develop a good understanding of the dynamical behaviour of the ridges. The large volumes of sand stored in the crests is of interest to the construction industry, but clearly knowledge is required about the type of sediment and how the ridges respond to large-scale sand extraction. Furthermore, the coastal waters in which the ridges are present are of interest to ecologists. The morphology interacts with the benthos that are present in the seabed by their mutual preference for grain size, bottom slope and wave influence. Also, the troughs between the ridges provide feeding grounds for fish, relevant to the fishing industry. In general, owing to their size and proximity to the coast, these ridges are important features to study in detail.

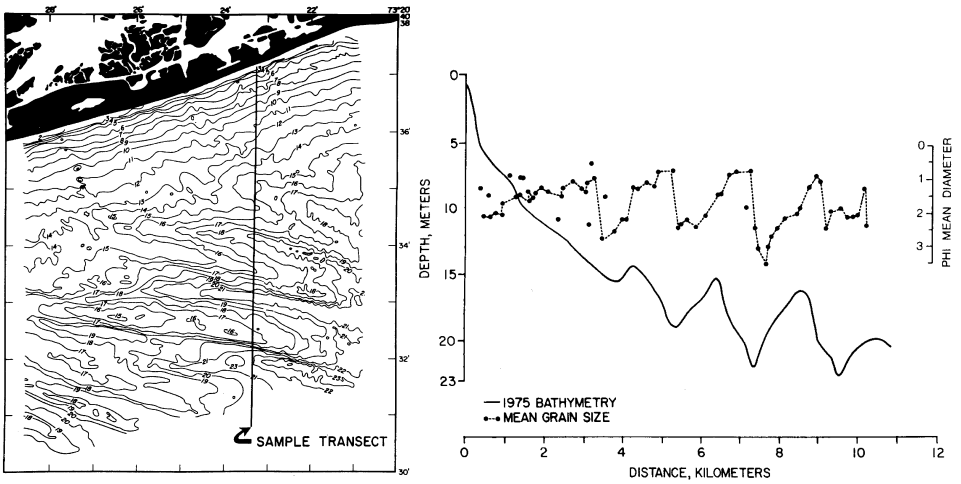

Figure 1.4: (Left) Bathymetry (in metres) of the shoreface and inner shelf showing the topography of shoreface-connected ridges on the Long Island inner shelf (Atlantic coast of North America). The mean longshore current is directed from northeast to southwest. (Right) Measured profi le of water depth (in metres) and mean grain size (in phi units) for the offshore directed sample transect. Larger phi values imply smaller grain sizes. Reprinted from Niedoroda et al. (1985), Copyright, with permission from Elsevier.

1.3 Observations and classification of sand ridges

In an overview paper of Dyer and Huntley (1999) it becomes clear that different types of sand ridges can be identified in coastal seas (see Figure 1.3). Besides ridges on the open shelf, ridges are also present in the proximity of headlands and estuaries. The descriptive classification used by these authors is based on the long-term development of the bedforms in connection with their present-day hydrodynamic setting. It follows that the ridges which are considered in this thesis are the Type 1 and Type 2B(ii) ridges. Type 1 are open shelf ridges, located on the outer shelf in a meso-tidal environment and comprise the tidal sand ridges. The second type (Type 2B(ii)) includes the shoreface-connected sand ridges. These are located somewhat closer to the coast on the inner shelf. The length scale of these two types of bedforms is the same order of magnitude and both evolve on timescales of decades to centuries. The different characteristics of shoreface-connected ridges and tidal sand ridge are discussed hereafter.

Observations of shoreface-connected ridges are reported on different coastal shelves, most prominently present along the Atlantic shelf of North America (Swift et al., 1978; Swift and Field, 1981), see Figure 1.4, along the Dutch coastline (Van de Meene and Van Rijn, 2000a), in the German Bight (Antia, 1996), on the Canadian Scotian shelf (Hoogendoorn, 1986; Amos and Nadeau, 1988), and in the southern hemisphere along the coast of Argentina and Brazil (Figueiredo et al., 1982; Parker et al., 1982). Generally, patches of 4-8 ridges are observed in water depths between 5-20 m, located several kilometres offshore. As the name

already suggests, the landward end of the ridges often extends up to the transition from inner shelf to the shoreface. Overall characteristics of these bedforms are: a shore-oblique orientation of their crests with respect to the coastline (average angle of 29°) (McBride and Mosow, 1991), a height of 1-6 m, a width of 2-3 km, and a spacing between successive crests of 2-6 km, while crestlines can extend for several kilometres. Side slopes of the ridge flanks are normally less than 1^o and the ridges have an asymmetrical profile, i.e. they have a steeper slope on the seaward flank. The shoreface-connected ridges are present on shelves where storms contribute significantly to the mean longshore current, whereas the strength of the tidal currents strongly varies over the regions of occurrence. The orientation of the crests is such that their seaward ends are shifted upstream with respect to their attachments to the shoreface. Also, the ridges migrate in the direction of this storm-driven current, with a velocity of 1-10 myr^{-1}. The sediment at the surface is coarsest in the troughs and finest on the seaward flanks. This means that, viewed in the cross-shelf direction, there is a phase difference of approximately 90^o between the mean grain size and the topography, as illustrated in Figure 1.4. The mean grain size ranges between 0.5-3.0 on the phi scale, which correponds to 0.7 - 0.1 mm.

Tidal sand ridges on the other hand are only present on meso-tidal shelves (Off, 1963). In these areas the tidal current velocities range from $0.5 - 1.0$ ms^{-1} and net longshore currents induced by, for example, the wind are substantially weaker. The size of these ridges can be larger than that of shoreface-connected ridges, amplitudes can be much higher (up to tens of metres), and the general orientation of their crests is oblique (cyclonic, i.e. anticlockwise in the Northern Hemisphere) with the main tidal current axis. Sometimes they rise close up to the water surface, as on the Belgian shelf in average depths of 10 m (Lanckneus et al., 1994), see Figure 1.5, but they are also present in deeper waters ($\sim$ 20-30 m), for example on the Dutch shelf (Van de Meene, 1994). It is not clear whether they migrate or not. Other examples of tidal sand ridges are found in the Bristol channel (Pattiaratchi and Collins, 1987), the Florida inner shelf (Davis et al., 1993) and the South Chinese Sea (Liu et al., 1998). Like the shoreface-connected ridges, the tidal sand ridges also exhibit a striking and intriguing variation of sediment over their topography. The sedimentological data on the Belgian shelf ridges is quite extensive and show the coarsest sediment for the tidal sand ridges near the crestline, whereas the mean grain size is finest on the landward flank or in the troughs, see Figure 1.5. The differences in the sediment size over the topography of the ridges often dominates over any large-scale trend within the region. Nevertheless, the variation in the mean grain size of the sediment at the surface layer always remains within the sand range; only very small amounts of gravel and mud are present.

Superimposed on both types of bedforms, smaller-scale bedforms can be present, such as megaripples and sandwaves (wavelengths of order 10 m and 100 m, respectively). The orientation and shape of these bedforms can be used to deduce the direction of the net sediment transport. For the shoreface-connected ridges on the Dutch shelf both indicate a northward directed net sediment transport (Van de Meene et al., 1996), i.e. in the direction of the mean storm-driven current. Gao et al. (1994) state that for one of the tidal sand ridges on the Belgian shelf (Kwintebank) these small scale bedforms indicate a net circulation around the bank, with opposing dominant transport directions on either side of the ridge. Furthermore, they demonstrate that the net sediment transport direction can also be deduced by investigating the grain size trends over the area (a combination of the mean, sorting and skewness). Williams

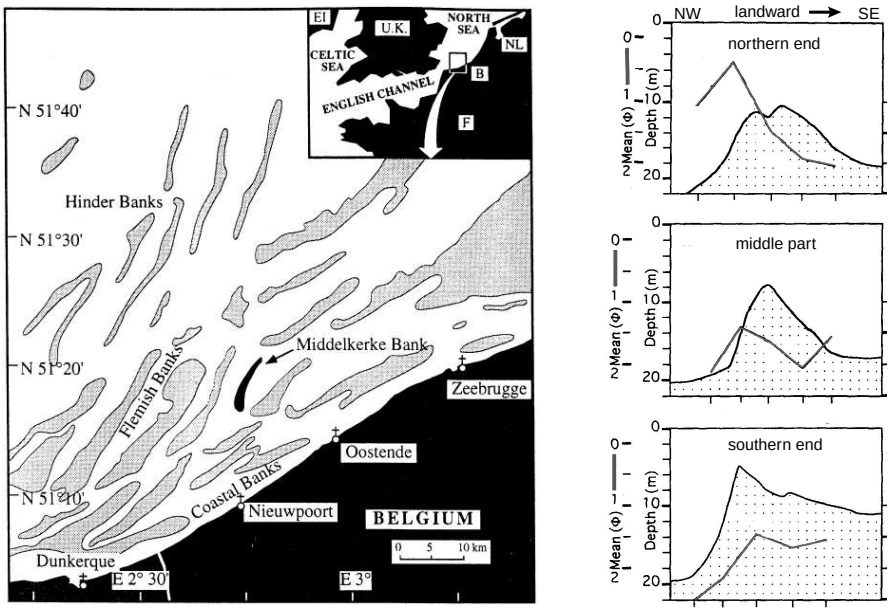

Figure 1.5: (Left) Sketch of the ridges on the Belgian shelf. The location of the Middelkerke Bank is indicated, which is one of the tidal sand ridges in the group of ridges referred to as the Flemish Banks. Reprinted from Trentesaux et al. (1999), Copyright, with permission from Elsevier. (Right) Measured profi le of water depth (in metres) and mean grain size (in phi units) perpendicular to crestline for three different positions along the Middelkerke Bank. Based on Trentesaux et al. (1994).

et al. (2000) report a similar net clockwise movement of sediment around the Middelkerke Bank.

Observations reveal that the most common situation is that on a certain shelf only one of the ridge types is present. This is related to the local dominant hydrodynamic conditions that favour the formation of either shoreface-connected ridges or tidal sand ridges. Two prototype regions will be defined, which will reappear throughout this thesis. For shoreface-connected ridges the Atlantic shelf of North America is considered. This micro-tidal shelf is strongly influenced by storms and waves, causing a strong steady alongshore current of the order $0.4 - 0.7$ ms^{-1} (Niedoroda and Swift, 1981; Niedoroda et al., 1984; Lentz et al., 1999). Shoreface-connected ridges are present on this shelf (see Figure 1.4), but no tidal sand ridges occur here. The Dutch-Belgian shelf is considered as a prototype meso-tidal shelf to study the formation of tidal sand ridges. The hydrodynamics are dominated by tidal currents and fair weather conditions (as opposed to storm conditions) (Lanckneus et al., 1994; Vincent et al., 1998; Van de Meene and Van Rijn, 2000a). It is important to realise that on the more onshore part of these shelves also shoreface-connected ridges are observed. Therefore, the Dutch-Belgian shelf will also be used to study the simultaneous presence of both types of ridges.

1.4 Theories concerning the presence of shoreface-connected and tidal sand ridges

Because of the long time periods involved in the development of large-scale ridges, it is difficult to understand the dynamics with the use of only observations. Also the lack of data including combined information on the bottom topography, sediment transport and the hydrodynamics, especially during the (potentially) important periods of storms, is a problem. Pattiaratchi and Collins (1987) give an overview of the proposed mechanisms, theories and models for sand bank formation and maintenance up to that time. In Dyer and Huntley (1999) an updated state of development is summarised. For shoreface-connected ridges and tidal sand ridges the most relevant hypotheses can be split into two categories, based on basically different concepts.

The first category finds it origin in the geology of the sea floor. It states that the shoreface-connected ridges are relict features and that they developed during an earlier retreat of the shoreline (Swift et al., 1972; Schwab et al., 2000). Sand ridges which became detached from the coastline due to sealevel rise are now maintained at their present location on the shelf floor. The slow or apparently absent changes in morphology support this hypothesis, which also assumes that the ridges are not active under the present-day hydrodynamic conditions. Also the existence of tidal sand ridges is sometimes related to the presence of a core of eroded fluvial or estuarine sediments. This hypothesis of the first category assumes that the sediment was deposited during a time period in which the hydrodynamic setting of the ridges was different from to the present-day forcing (Berné et al., 1994; Trentesaux et al., 1994; Liu et al., 1998).

The hypothesis of the second category provides the basis for the work presented in this thesis and assumes that the ridges are active under the local hydrodynamical forcing. Although only a limited amount of field measurements over long time periods are available to verify this hypothesis, data by Swift et al. (1985) and Van de Meene et al. (1996) support the idea of a dynamically active system. One way to investigate the validity is with the use of process-based morphodynamical models.

1.5 Process-based morphodynamic models: concepts

The coupling between the water motion and the seabed is the essential part in a morphodynamic model. The usual structure of such a model is that it first solves the hydrodynamic equations for a fixed bottom topography. Next, it uses the bed shear stresses exerted by the flow on the bed to compute the sediment flux, for which a suitable formulation has to be selected. Finally, the bottom changes are calculated as the result of the convergence and divergence in the net sediment flux. If this loop is repeated with the newly determined bottom the feedback between the bottom, changes and the velocity field is included.

In this thesis only the transport of fine to coarse sand (grain sizes of $100 - 1000\mu$m) is considered. This sediment is noncohesive. The dynamics of sediment erosion and the subsequent transport of the bottom sediment only occurs above a critical value of the shear stress (see, e.g., Dyer, 1986; Fredsøe and Deigaard, 1992; Soulsby, 1997). Above this critical value the movement of the grains will be dominated successively by rolling (continuous contact

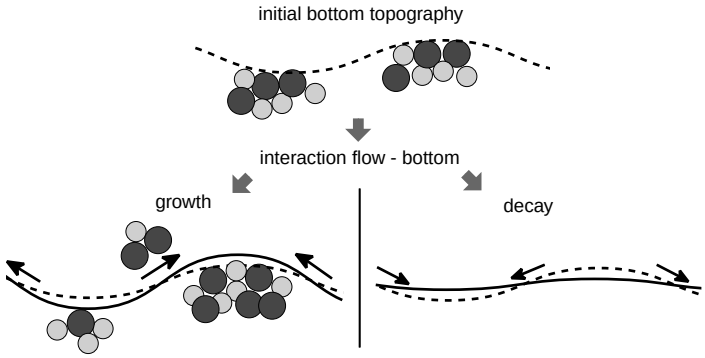

Figure 1.6: Schematic view of the growth or decay of bottom perturbations through the transport of sediment. Hiding effects result in a reduced bed load transport of the fi ner grain sizes and cause perturbations in the initially uniform probability distribution of the sediment.

with bed), saltation (jumping of a particle into the water column keeping regular contact with the bed) and suspension (no regular contact with bed) as the stress on the bed increases. These different ways of the movement of sediment are described with different formulations, where the distinction is normally made between two modes of transport: bed load (rolling) and suspended load (grains suspended into the water column). The latter depends on the sediment concentration, which can be solved by incorporating a concentration equation. The preferred downslope movement of the sediment is represented by a flux which is proportional the slope of the bed (see, e.g. in Dyer, 1986; Fredsøe and Deigaard, 1992).

Furthermore, it is important to remark that many formulations for the sediment flux are based on the mean grain size of the sediment, i.e. a single size approach. This suffices for many applications, but in order to understand phenomena like variations in the mean grain size over the bedforms it is necessary to deal with grains that have different sizes, i.e. using multiple grain sizes. In the latter case, the behaviour of the sediment mixture is influenced by the effect of dynamic hiding: smaller grains feel the fluid drag less intensely than larger grains. If the reduced exposure of the finer grains changes the critical shear stress for erosion it is called static hiding (see, e.g., Ludwick, 1989; Seminara, 1995). To model these changes, additional equations which describe the evolution of the probability of occurrence of grains from a specific size class in the bottom layer are required.

1.6 Free and forced morphodynamic behaviour

The interaction between the water motion and bottom topography through the transport of sediment can result, in some cases, in a positive feedback due to which small perturbations in the bottom start to grow, as indicated in Figure 1.6. A bottom topography that does not change in time under a certain forcing is in equilibrium with this forcing. If small perturbations are superimposed on this equilibrium state and they start to grow, this is called free behaviour of the system. If the changes and patterns in the system are fixed by external factors, it results in forced behaviour. The specific conditions under which this feedback mechanism results in,

e.g., ridges with the general characteristics of either shoreface-connected ridges or tidal sand ridges, provides information on the potentially relevant processes for their formation.

The formation of bedforms and the analysis of the dominant physical processes requires studies with models having different degrees of complexity. The more complex the model, the more processes are represented and the more realistic (and therefore more complicated) are their parameterisations. Examples that distinguish idealised from complex models are the way in which exchange processes between different subareas in the coastal region, (shelf/basin) geometry and boundary conditions are incorporated. The formation of large-scale sand ridges so far have been mainly studied with idealised models. The advantage of the latter is that they allow for a systematic analysis with mathematical methods, whereas complex models have to be solved numerically. Analysing idealised models thus provides insight in the actual mechanisms that are crucial for the existence of a certain type of bed feature.

Within this idealised model context, the mathematical technique of performing a stability analysis is applied in a variety of subjects. Besides the models for large-scale sand ridges, that will be discussed in the next section, stability models for uniform sediment have also been successfully used to explain the formation of other types of bedforms, such as sea ripples (Vittori and Blondeaux, 1992), sand waves (Gerkema, 2000; Neméth et al., 2002), nearshore bars (Falqués et al., 2000; Ribas et al., 2003) and channel-shoal formation in tidal embayments (Schuttelaars and De Swart, 1999), to mention only a few. Morphodynamic pattern formation in tidal basins has been investigated by Van Ledden et al. (2002b) for a sediment mixture consisting of a sand and a mud fraction.

There is no existing literature which describes the modelling of shoreface-connected ridges or tidal sand ridges on a bed consisting of nonuniform sediment. An overview of the influence of grain sorting on other types of bedforms is given by Seminara (1995). In Foti and Blondeaux (1995) a stability model for the formation of sea ripples includes the dynamics of sediment consisting of two grain sizes. Their theoretical findings (coarse sand on the crests, fine sand in the troughs) turn out to be in agreement with field and laboratory data. Lanzoni and Tubino (1999) have applied the concepts of linear stability to study the development of alternate bars and the grain size distribution over them. Their model results are in qualitative agreement with experimental findings which show a reduced height, wavelength and migration of the bars with respect to the uniform sediment case. Also the sorting pattern with coarse sediment prevailing on upstream flank of the bar crest is reproduced in their model.

1.7 Modelling shoreface-connected and tidal sand ridges: state of the art

In Van de Meene (1994) (see also Van de Meene and Van Rijn, 2000b) a study of the potential stability of a single ridge along the central Dutch coast was presented. A 1D current model and 2DV morphodynamics were used, in which it is assumed that the interaction water-morphology is local. A stationary forcing for the flow was applied, and the sediment transport along a cross-section was calculated for a given ridge topography, assuming the crests have an infinite length. By comparing the calculated values for the sediment fluxes with the vol-

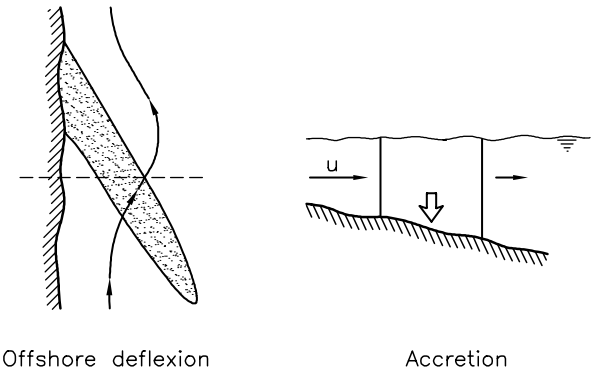

Figure 1.7: Schematic view of the transverse bottom slope mechanism. An upcurrent-oriented ridge produces an offshore deflection of the flow. This is a consequence of mass-conservation that causes the cross-bank flow component to increase over the ridge, while the along-bank component remains unchanged in the limit of an irrotational flow. The movement of a column into deeper water will cause a mass deficit which must be compensated by a convergence of the flow. If the sediment flux is proportional to the velocity of the current, there will be a convergence of sediment above the crest and thus the ridge will grow. The convergence of the sediment flux is more effective on the downstream side of the ridge, because the longshore movement of the control volume causes an additional mass deficit in this area. This causes the downstream migration of the bedforms. From Calvete et al. (2001b), based on concepts discussed by Trowbridge (1995).

ume of the ridge, they concluded that the ridges can be considered active on the timescale of thousands of years and they are no geological relicts.

A different approach was used by Trowbridge (1995), who was the first to present a process-based model for the generation of shoreface-connected ridges. He used an irrotational flow, steady forcing (no tides) and a simple sediment flux which is linear in the velocity. The model domain has a sloping bottom and includes a coastline on one boundary. He demonstrated that an essential condition for the growth of ridges is the cross-shore bottom slope of the inner shelf. The latter results in an offshore decrease in the carrying capacity of sediment. In combination with a deflection of the alongshore current over the crest of the ridges, this model reproduced the correct orientation of the ridges (seaward ends of the crest shifted upstream with respect to their shoreface attachment). The mechanism is explained in Figure 1.7, from which it becomes clear that the shoreface-connected ridges are trapped to the inner shelf, because in this area the slope of the bottom in much larger that in the outer shelf. However, his model was unable to predict a preferred length scale for these ridges and timescales for the growth were too long.

The former problem was solved by Falqués et al. (1998), who introduced a contribution to the sediment flux that accounts for the preferred downslope movement of grains. Calvete et al. (2001b) demonstrated that the transport of sediment as suspended load, in addition to bed load, as well as the stirring of the sediment due to waves was needed to obtain more realistic timescales for the growth of the ridges. Restrepo (2001) tested the influence of non-steady flows on the evolution of shoreface-connected ridges with a model that is based on wave-current interaction. It appears that wave-induced Stokes drift on the relevant long

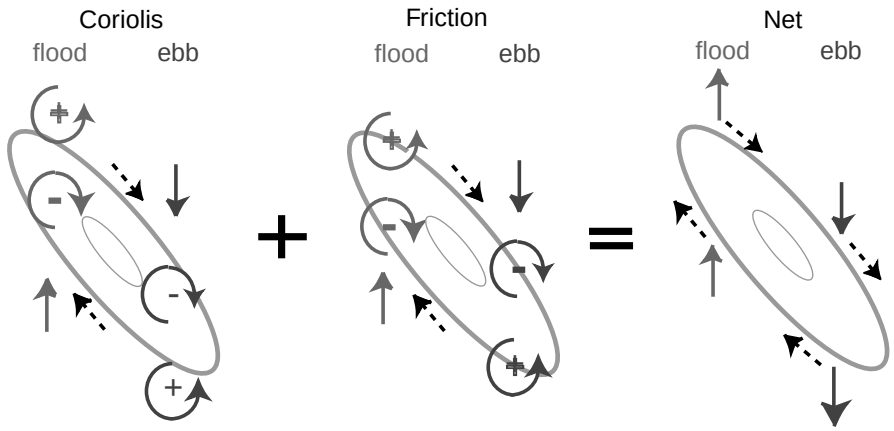

Figure 1.8: Sketch (top view) of vorticity production resulting from a tidal current flowing over a ridge, rotated cyclonically with the tidal axis and on a flat bottom. The vorticity during the flood phase (left side of ridge) and ebb phase (right side of ridge) of the tide, as well as the resulting (averaged over tidal period) current direction (dashed arrow) are indicated. The production of anticyclonic vorticity is indicated by $-$, cyclonic vorticity by $+$. The contributions due to Coriolis (left) and friction (middle) both result in a anticyclonic residual circulation (right) around the ridge.

timescales can influence the shoreface-connected ridges if its magnitude is comparable to that of the steady background current. A steady state condition for the hydrodynamics appeared essential for the existence of shoreface-connected ridges, which confirms earlier findings by Trowbridge (1995) and Calvete et al. (2001b).

The second type of large-scale bedforms, i.e., tidal sand ridges, have been the subject of several studies. Zimmerman (1981) proposed a mechanism for the development of residual circulations around tidal sand ridges. Observational evidence indicates that the length scales and orientation of these ridges are such that they cause the largest possible residual flow velocities around them. Zimmerman (1981) considers a (depth-averaged) tidal current over a ridge, and argues that residual eddies develop due to tide-topography interaction. If a tidal current moves over a ridge, continuity effects cause an acceleration of the flow over the shallower area. The Coriolis force experienced by a water parcel on the crest is higher than in the deeper water and it produces a torque. Conservation of potential vorticity results in the production of anticyclonic (clockwise on the Northern Hemisphere) vorticity over the ridge crest, during both the ebb and flood phase of the tide, as indicated in Figure 1.8. A net anticyclonic circulation around bar, following the topographic contours, and irrespective of the orientation of the ridge is the result. In addition, the bottom friction causes a stronger deceleration of the flow over the shallower areas, which produces frictional torques over the flanks of the ridge. This vorticity is advected by the tide. For a ridge oriented cyclonically with respect to the tidal flow, anticyclonic residual vorticity is generated over the crest during the tidal period. In that case both torques enhance each other and the strongest residual circulation around the ridge is found. For a ridge of which the crest is rotated anticyclonically with respect to the main tidal axis, the Coriolis and frictional torques have opposite signs

above the crest and a weak residual circulation is induced.

The first model that deals with the free behaviour resulting from the feedback between a tidal current and sandy sea bottom was presented by Huthnance (1982a). This model differs from that of shoreface-connected ridges in several respects. First, only tidal forcing was used and transport of sediment is assumed to be faster than linear in the instantaneous flow velocity. Furthermore, the domain has a flat bottom and is not bounded by a coastline. This model captures the dominant wavelength, initial growth and migration of tidal sand ridges. In addition, it was shown by Huthnance (1982a) that the residual circulation around the ridge, as was explained by Zimmerman (1981), indeed plays an important role in the positive feedback mechanism between the water motion and the bottom such that the amplitude of the ridge will grow. The instantaneous velocity over the upcurrent flank is enhanced due to the residual circulation, while it is reduced over the downcurrent flank (see Figure 1.8). The net effect over a tidal period results, in case of a 'faster than linear' sediment transport, in a convergence of sediment over the crest.

Hulscher et al. (1993) extended the model by Huthnance (1982a) by including circular tides, which allowed for the determination of critical parameters below which the growth of bedforms is suppressed. Only one tidal component is included in the external forcing of the water motion. The influence of 3D effects appeared not to be important for tidal sand ridges, although they did generate smaller-scale bedforms such as sand waves (Hulscher, 1996). These model results sustain the hypothesis that these ridges form due to inherent feedbacks between tidal currents and the sandy bottom. The forcing has been restricted to an M_2 tide and overtides (e.g. M_4) have been neglected, albeit Davies et al. (1997) show that M_4 is important.

The simultaneous existence or absence of shoreface-connected ridges and tidal sand ridges was investigated by Calvete et al. (2001a). Motivated by observations from the central Dutch coast, which show the presence of both types in close proximity of each other, they used a model domain representing the coastal shelf, extending seaward from the shoreface. Over the inner shelf the water depth increases offshore, and the outer shelf is horizontally flat and infinitely wide. With the combination of a forcing partly by the M_2 tide and partly by steady currents, connected to a sediment transport formulation that has terms which are cubic and linear in the instantaneous velocity, respectively, the simultaneous presence of both types of ridges was found. However, the timescales for the growth of the shoreface-connected ridges were unrealistically long due to the neglect of suspended load sediment transport.

All these models are able to reproduce at least qualitatively the main characteristics of the large-scale sand ridges. One drawback is that the models discussed above all use sediment transport parameterisations based on one single (representative) mean grain size. So, no insight in the dynamics of variations in mean grain size over the ridges was found. The relation between mean grain size or sorting patterns and the topography of these ridges is often mentioned in literature, along with some hypotheses on its origin. However, they lack a structural (model) investigation to support them. Another shortcoming of these models is that (owing to the methods used) only the initial development of low-amplitude ridges is modelled. No conclusions can be drawn on the long-term evolution and the final state of maintenance of the ridges. Although the results of the linear stability models already compare well with the field observations, the final state of the modelled ridges could be very different from their initial shape and behaviour. Because the ridges in the field have well-

developed amplitudes, they are probably more representative for the final 'equilibrium state', rather than for an 'initial state'. Calvete et al. (2002) studied the finite amplitude behaviour of shoreface-connected ridges in case of a uniform grain size. The work done by these authors is a nonlinear extension of that presented in Calvete et al. (2001b), which is based on a linear stability analysis. The nonlinear model results show the development of ridges with an asymmetrical profile. Moreover, the final state represents migrating ridges with a constant amplitude.

With regard to the finite-amplitude behaviour of tidal sand ridges, Huthnance (1982b) looked at the evolution of a small isolated bump into equilibrium bank forms under tidal forcing. A nonlinear analysis for tidal sand ridges, using a numerical model, was performed by Idier and Astruc (2003). This model provides a reasonable estimate for the temporal evolution, although saturation heights are overestimated. At present, this work is being continued by Roos (2003, pers.comm.), using a more analytical approach.

1.8 Objectives of this thesis

The considerations presented in the previous sections have clearly identified gaps in the knowledge on large-scale sand ridges that form the basis of the work that will be described in this thesis. The general objectives can be formulated as four main questions that will reappear in this thesis:

(i) Which processes determine whether shoreface-connected ridges, tidal sand ridges, or both types of ridges can exist on a coastal shelf? It is aimed at improving the understanding of the initial formation and characteristics of large-scale bedforms on storm-dominated and tide-dominated shelves.

(ii) What is the quantitative role of residual currents and the M_4 tide on the growth and migration of tidal sand ridges?

(iii) What is the influence of sediment sorting on the initial temporal (i.e. growth and migration) and spatial characteristics of large-scale sand ridges, and which physical mechanisms are responsible for the observed grain size distribution over these sand ridges?

(iv) What is the finite-amplitude behaviour of shoreface-connected ridges in combination with the long-term development of the grain size pattern in case of nonuniform sediment?

1.9 Overview of subsequent chapters

Following the questions raised above, which are applied to the prototype shelves as discussed in section 1.3, the subsequent chapters in this thesis exhibit the following structure.

Chapter 2 addresses the first two questions for the Dutch shelf. Here tides, as well as storms that are capable of transporting sediment, are considered in relation to their potential capacity to generate shoreface-connected ridges and tidal sand ridges. Taking into

account the conclusions of previous studies, this hydrodynamical setting is optimal for the presence of both types of ridges. The model is an extension of the model by Calvete et al. (2001a) (see section 1.7) with an idealised geometry. It takes into account the forcing by the combined effect of storms, i.e., wind-driven currents and stirring of sediment by waves, and tidal currents. A second tidal constituent, M_4, is added to the M_2 tidal forcing to study the role of tidal asymmetry in exciting tidal sand ridges.

Chapter 3 addresses the third question for shoreface-connected ridges on the Atlantic shelf of North America. The most important consideration for this location is the presence of only shoreface-connected ridges (no interference of other large-scale bedforms such as tidal sand ridges), no significant tidal currents and the availability of sufficient data on the sediment properties.

Chapter 4 also addresses the third question, but now for the tidal sand ridges on Belgian shelf. Here the water motion is dominated by tides and tidal sand ridges are present of which a large amount of sedimentary and hydrodynamical data are available.

Chapter 5 addresses the last question for shoreface-connected ridges on the Atlantic shelf of North America, as a nonlinear extension to the work discussed in chapter 3.

In all the chapters the objective is to find an answer to (one of) the questions, within the context of a morphodynamical model. Idealised models are used, which allow for a systematic analysis by using mathematical methods, so that the focus is on analysing the basic mechanisms. A schematised geometry represents the coastal shelf of a semi-infinite width. The depth-averaged shallow water equations are used, which involves the implicit assumption that 3D processes are not essential for the formation and maintenance of the ridges. In chapter 2 the model equations are introduced and used for the case of uniform sediment (single representative grain size). A modified model, suitable to describe the morphodynamics in case of two sediment classes is used in chapter 3. A stability analysis is performed, where the linearised equations only apply to the initial stage of development (chapters 2-4), and the full nonlinear equations are solved to study the evolution in the time and the final 'saturated' state of shoreface-connected ridges (chapter 5). Time constraints prevented the study of the nonlinear evolution of grain sorting patterns over tidal sand ridges, which would make a logical topic of a next chapter. With this method of stability analysis, information on growth rate, migration velocity, wavelength, bottom patterns, sediment patterns and final height of the bedforms is retrieved. Finally, in chapter 6 the main conclusions of the work presented in this thesis are summarised, along with a discussion on the parameterisations used in the models and some suggestions for further research.

Chapter 2

Growth of large-scale bedforms due to storm-driven and tidal currents

Abstract

An idealised morphodynamic model is used to gain further understanding about the formation and characteristics of shoreface-connected sand ridges and tidal sand ridges on the continental shelf. The model consists of the 2D shallow water equations, supplemented with a sediment transport formulation and describes the initial feedback between currents and small amplitude bedforms. The behaviour of bed forms during both storm and fair weather conditions is analysed. This is relevant in case of coastal seas characterised by tidal motion, where the latter causes continuous transport of sediment as bed load.

The new aspects of this work are the incorporation of both steady and tidal currents (represented by an M_2 and M_4 component) in the external forcing, in combination with dominant suspended sediment transport during storms. The results indicate that the dynamics during storms and fair weather strongly differ, causing different types of bedforms to develop. Shoreface-connected sand ridges mainly form during storm conditions, whereas if fair weather conditions prevail the more offshore located tidal sand ridges develop. Including the M_4 tide changes the properties of the tidal sand ridges, such as growth rates and migration speeds, due to tidal asymmetry. Finally a probabilistic formulation of the storm and fair weather realisation of the model is used to find conditions for which both types of large-scale bedforms occur simultaneously. These conditions turn out to be a low storm fraction and the presence both tidal and steady currents, with a strong steady component during storms. *

*This chapter is based on the paper entitled *Growth of large-scale bedforms due to storm-driven and tidal currents: a model approach*, by M. Walgreen, D. Calvete and H.E. De Swart, published in Cont. Shelf Res., 22, 2777-2793, 2002.

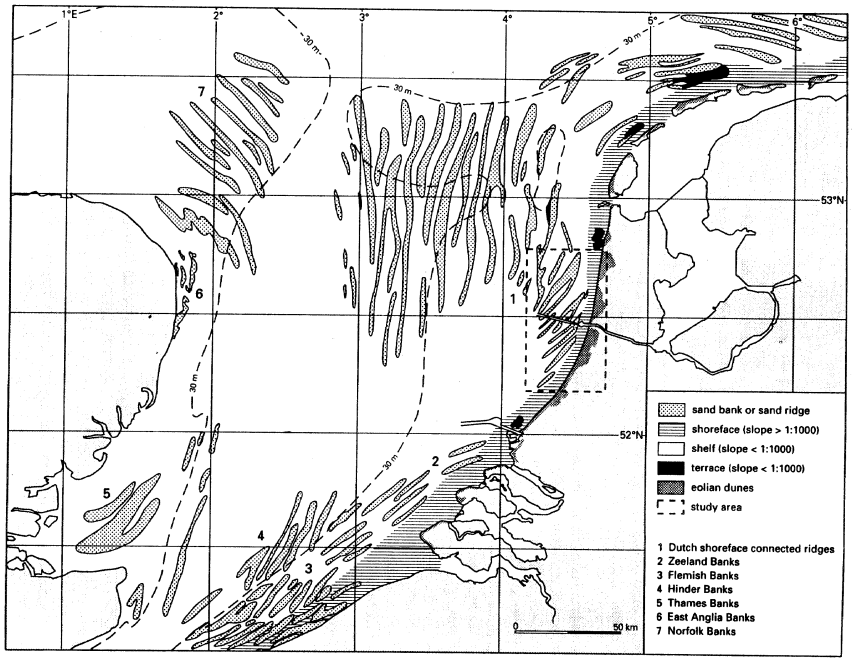

Figure 2.1: Large-scale sand banks in the North Sea, contours of the Netherlands are shown on the right, part of England on the left. The dashed box (1) indicates the location of the shoreface-connected ridges along central Dutch coast, these ridges are also found east of 5°E, along the Dutch and German Wadden Islands. Examples of tidal sand ridges are found in regions 4 and 7, where the ridges are cyclonically rotated with respect to the dominant tidal current. The large patch of ridges in the middle of the figure are possibly also tidal sand ridges. (Van de Meene, 1994).

2.1 Introduction

On the inner and outer part of many coastal continental shelves the hydrodynamics and transport processes are strongly affected by the presence of large-scale bedforms. In this chapter two types of bedforms are considered: the first are shoreface-connected sand ridges (Swift et al., 1978; Parker et al., 1982; Van de Meene and Van Rijn, 2000a), which occur on storm-dominated inner shelves of coastal seas, where intense steady currents (of the order of 0.5 ms^{-1}) prevail. The second class of bedforms are the tidal sand ridges, which can be found on the outer part of meso-tidal shelves, characterised by strong tidal currents (Dyer and Huntley, 1999). The alongshore spacing of both types of bedforms ranges from $2 - 10$ km and an oblique orientation of the ridges with respect to the mean current is observed (Figure 2.1). An important difference between the bedforms is the orientation of the crests with respect to the dominant current. The crests of the shoreface-connected ridges are upcurrent oriented, i.e. their seaward ends are shifted in the upstream direction of the storm-driven current with respect to their shoreface attachment. Those of tidal sand ridges are cyclonically

rotated with respect to the dominant tidal current. This indicates that these types of bedforms are generated by different mechanisms.

In this chapter an idealised morphodynamic model is used to gain further understanding about the initial formation and characteristics of these large-scale bedforms. Most modelling studies investigate either storm-driven shelves (Trowbridge, 1995; Calvete et al., 2001b; Restrepo, 2001), resulting in bed forms resembling the shoreface-connected ridges, or tidally dominated shelves with a basic M_2 tidal component (Zimmerman, 1981; Huthnance, 1982a; Hulscher et al., 1993). The two latter studies explicitly deal with the onset of tidal sand ridges. However, in the North Sea the simultaneous presence of these two bottom modes is observed, in an area where the quarter-diurnal overtide (M_4) significantly contributes to the tidal current structure (Davies et al., 1997). A first attempt to combine these two bottom modes in one model is discussed by Calvete et al. (2001a). In their model a steady current is driven by the background pressure gradient, only one tidal constituent is used and suspended sediment fluxes are neglected. The simultaneous presence of both bottom modes is found, but timescales for the growth of the shoreface-connected ridges appear to be too long with respect to those characterizing the migration of the ridges. This aspect was further investigated by Calvete et al. (2001b), in which they focused on the storm-dominated inner shelf of the Atlantic coast of North America and neglected tidal motion. They found that suspended sediment fluxes during storms control the growth of the shoreface-connected ridges, resulting in more realistic growth times.

In this chapter the situation of a shelf, where both storm-driven currents and tidal currents are important, will be investigated. As a prototype example we will consider the central Dutch shelf in the southern part of the North Sea (see Figure 2.1). A new aspect of this work is the incorporation of both steady and tidal currents, represented by the semi-diurnal M_2 component and the quarter-diurnal M_4 tide in the external forcing. Furthermore, in addition to bed load transport, a formulation of suspended load transport during storm conditions will be used. Another new aspect included in the hydrodynamics is the strong density gradient in the vicinity of the Dutch coast as a result of the outflow of fresh water from the river Rhine (De Ruijter et al., 1997). The motivation for the present study is therefore twofold. The first is to investigate the influence of the M_4 tide and the more realistic hydrodynamic conditions on the formation of tidal sand ridges. The second objective is to understand under which conditions shoreface-connected ridges and tidal sand ridges occur simultaneously, as is the case in the southern North Sea.

In section 2.2 the set-up of the model is given and in section 2.3 the method of analysis is discussed. Model results are presented in section 2.4; first the storm mode is discussed (section 2.4.1), next the results for the fair weather realisation are presented (section 2.4.2) and in section 2.4.3 these two realisations of the model are combined. In the final section the conclusions are given.

2.2 Model formulation

Following earlier studies by Huthnance (1982a), Hulscher et al. (1993), Trowbridge (1995) and Calvete et al. (2001a), we hypothesize that tidal sand ridges and shoreface-connected sand ridges form as an inherent instability of a morphodynamic system. A local model is

used to investigate the flow-topography interaction on coastal shelves under different hydrodynamic conditions. The shelf geometry is schematised as a semi-infinite domain, bounded on the landward side by the transition from the shoreface to the inner shelf, see Figure 2.2. The reference bathymetry is uniform in the longshore direction (y). In the cross-shore direction (x) it consists of an inner shelf (linearly sloping bottom) and an outer shelf represented by a horizontal bottom. The water depth at the landward side of the inner shelf ($x = 0$) is H_0, L_s the inner shelf width and the depth of the outer shelf is indicated by H_s. Representative values for the central Dutch coast are $H_0 \sim 15$ m, $H_s \sim 20$ m and $L_s \sim 12$ km. In the model the 2DH shallow water equations are used to describe the water motion. Consequently, no vertical circulation is represented. This depth-averaged approach is supported by field data on the shoreface-connected ridges along the Dutch coast, which show no indication for such a circulation (Van de Meene and Van Rijn, 2000a). This follows the same approach as was used in the sudies metioned above.

The dimensional momentum equations and the mass conservation read:

$$\frac{\partial \vec{v}}{\partial t} + (\vec{v} \cdot \vec{\nabla})\vec{v} + f\vec{e_z} \times \vec{v} = -g\vec{\nabla} z_s - \frac{gD}{2\rho}\vec{\nabla}\rho + \frac{\vec{\tau}_s - \vec{\tau}_b}{\rho D} \tag{2.1}$$

$$\frac{\partial D}{\partial t} + \vec{\nabla} \cdot (D\vec{v}) = 0 \tag{2.2}$$

Here $\vec{v}$ is the depth-averaged velocity, f is the Coriolis parameter, $\vec{e_z}$ a unit vector in the vertical direction, g the acceleration due to gravity, $\vec{\nabla}\rho$ is a constant horizontal density gradient, $\vec{\tau}_s$ the wind-stress and $\vec{\tau}_b$ the bed shear stress. Furthermore, D is the local water depth, given by $D = z_s - z_b$, z_s is the free surface elevation, z_b the bottom depth, t the time and $\vec{\nabla}$ the horizontal nabla operator. Typical values for the Dutch shelf will be discussed in section 2.3.1. The bottom depth is given by an undisturbed water depth H and perturbations h on this undisturbed depth due to the presence of undulations on the bottom: $z_b = -H + h$. The forcing due to radiation stresses is not included, and we assume the breaking of waves does not occur in the water depths under consideration. Furthermore, small Froude numbers are assumed, so that the free surface elevation is much smaller than the undisturbed water depth. This implies that the free surface effects can be neglected in the equations of motion, except in the pressure gradient force.

The evolution of the bottom is a result of convergences and divergences in the sediment flux and reads

$$(1-p)\frac{\partial h}{\partial t} + \overline{\vec{\nabla} \cdot \vec{q}} = 0 \qquad\qquad \vec{q} = \vec{q}_b + \vec{q}_s \tag{2.3}$$

Here $\vec{q}_b$ represents the volumetric transport per unit width of sediment as bed load and $\vec{q}_s$ the suspended transport of sediment, and $p \sim 0.4$ is the porosity of the bed. Our interest lies in the long-term evolution of the bottom and therefore tidally and wave-averaged equations are used, indicated by the overbar. Here we use a sediment transport formulation, which is based on expressions derived by Bailard (1981) by using physical concepts, see also references herein. In fact he applies the idea that part of work done by shear stresses acting on the sediment is used for transport, the rest is lost by frictional collisions. For more background information we refer to Dyer (1986) and Fredsøe and Deigaard (1992). These considerations

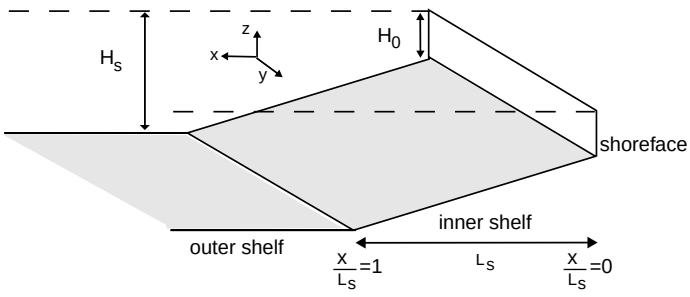

Figure 2.2: Sketch of the geometry of the model, representing the inner shelf (width L_s) and part of the outer shelf of a coastal sea.

result in the expressions for $\langle \vec{q}_b \rangle$ and $\langle \vec{q}_s \rangle$, given in appendix 2.A. Here the brackets indicate an average over the wave period. Note that both the bed load part and suspended load part are influenced by local bed slopes, as denoted by the terms proportional to $\vec{\nabla} h$. This is because gravitational effects influence both the sediment in the bed load layer, but also the immersed weight of the suspended load sediment (Bailard, 1981). Support for the latter assumption also comes from laboratory experiments (Talmon et al., 1995). We further assume that the bed slope terms will only involve $\vec{\nabla} h$ instead of $\vec{\nabla} z_b$, i.e., the slope effects of the reference bathymetry are not explicitly taken into account. We will return to this in section 2.3.1. In the present model two different realisations of the model are analysed, which are representative for conditions during storms and fair weather, and are characterised by different hydrodynamic and sediment transport conditions.

2.2.1 Sediment transport and bed shear stress during storms

In the storm mode transport of sediment mainly takes place as suspended load, which is supported by field measurements (Green et al., 1995). It is assumed that the amplitude u_w of the wave-orbital velocity $\vec{u}_w$ is much larger than that of the wave-averaged (steady plus tidal) velocity $\vec{v}$. To compute the wave-average it has been assumed that the waves are symmetrical and monochromatic. If this is applied to the expressions given in eq. (2.A-1) and (2.A-2) it then follows that the advective sediment flux, averaged over the wave period, is linear in the wave-averaged velocity, $\vec{v}$. The physical interpretation is that sediment is stirred by waves and subsequently transported by the steady and tidal currents.

A modification on the original formulation of Bailard (eq. (2.A-2)) is made for the advective contribution of the suspended load flux, similar to the approach used in Calvete et al. (2001b). We have computed the advective part of the suspended load sediment flux by using the fact that it is defined as the product of velocity vector times the depth-integrated volume concentration C. An expression for C is then found from the concentration equation and using a parameterisation for the sediment pick-up function given by Van Rijn (1993). The result is that the advective term should be replaced by $\nu_s \langle |\vec{v}_t|^3 \vec{v}_t \rangle D/H_0$, where $D \simeq H - h$ is the local water depth and the brackets indicate an average over the wave period. The numerical value of coefficient ν_s is larger than that given by Bailard (1981), for details we refer

to Calvete et al. (2001b). The contributions of bed load and suspended load are given by:

$$\langle \vec{q}_b \rangle = \nu_b \left(\quad 3\langle |\vec{\hat{u}}_w|^2 \rangle \vec{v} - \lambda_b \langle |\vec{\hat{u}}_w|^3 \rangle \vec{\nabla} h \right) \tag{2.4}$$

$$\langle \vec{q}_s \rangle = \nu_s \left(4\frac{D}{H_0} \langle |\vec{\hat{u}}_w|^3 \rangle \vec{v} - \lambda_s \langle |\vec{\hat{u}}_w|^5 \rangle \vec{\nabla} h \right) \tag{2.5}$$

To derive these expressions the waves are almost parallel to the storm-driven current. Here h is the elevation of the bed with respect to its reference level and the bed slope coefficients describe the preferred downslope movement of the sediment due to gravitational forces. The bed slope coefficient for bed load transport λ_b is related to the dynamic angle of friction, while for suspended load this coefficient λ_s depends on the fall velocity of the suspended sediment. The parameter values for the Dutch shelf (bottom consists of medium sand) are:

$$\nu_b \sim 4.5 \times 10^{-5}\ \mathrm{s^2 m^{-1}} \quad \lambda_b \sim 1.7 \quad \nu_s \sim 5.6 \times 10^{-4}\ \mathrm{s^3 m^{-2}} \quad \lambda_s \sim 0.3\ \mathrm{s m^{-1}}$$

Calvete et al. (2001b) showed that it is essential for the growth of shoreface-connected ridges to parameterise the effect that the wave-orbital velocity increases towards shallower water, thereby changing the amount of sediment which is stirred into the water column. This effect is included by writing the wave-orbital velocity amplitude as $u_w = U_w \left(H_0/H\right)^{m/2}$, where $U_w \sim 1\ \mathrm{ms^{-1}}$ is the amplitude at $x = 0$ (water depth H_0) and $m \sim 1.6$ is a coefficient. This explicitly models the depth dependence of the wave stirring process and has been derived from a simple wave shoaling model.

A linearised bed shear stress is used in equation (2.1) following earlier studies: $\vec{\tau}_b = \rho r \vec{v}$, with r the friction parameter. During storms this results in a bottom friction parameter r which is related to the wave-orbital velocity: $r(x) = c_d \langle |\vec{\hat{u}}_w| \rangle$. Here c_d is a constant drag coefficient. This gives an onshore increasing bottom friction, due to the increase in the wave-orbital velocity amplitude onshore (Calvete et al., 2001b). A characteristic value is $r(x = 0) \sim 1 \times 10^{-3}\ \mathrm{ms^{-1}}$.

2.2.2 Sediment transport and bed shear stress during fair weather

The second realisation of the model represents the fair weather case and is characterised by negligible wave stirring. This implies that the sediment transport is controlled by bed load processes and it is cubic in the instantaneous velocity, see eq. (2.A-1). In this case the suspended sediment flux is negligible and the bed load flux, averaged over the wave period, is given by

$$\langle \vec{q}_b \rangle = \nu_b (\vec{v}^3 - \lambda_b |\vec{v}|^3 \vec{\nabla} h) \tag{2.6}$$

The linearised bed shear stress during fair weather ($\vec{\tau}_b = \rho r \vec{v}$) results in an expression for the friction parameter r which is different than for storms. The wave stirring is not important during fair weather conditions, and the linearisation is based on the characteristic wave-averaged velocity U: $r = c_d U$. In this case the friction parameter is constant.

Boundary conditions are such that the cross-shore velocity field and bottom perturbations h are zero at the $x = 0$ (the landward boundary) and very far offshore, thus no water exchange and no advective sediment fluxes are allowed from the shoreface to the inner shelf. There is

only a (very small) cross-shelf flux due to the gravitational downslope effects. The motivation for these boundary conditions is that field data indicate that shoreface-connected ridges are trapped in the inner shelf and that there is hardly any sediment exchange between shoreface and inner shelf.

2.3 Solution method

2.3.1 Basic state

We will now investigate the possible onset of bedforms as free morphodynamic instabilities which evolve on a basic state of the water-bottom system. In this case the model allows for a basic state which is uniform in the longshore (y) direction: it describes a longshore current $V(x,t)$ over a reference bottom profile $z_b = -H(x)$. A linearly sloping reference bottom profile is used in the inner shelf, based on the characteristic length scales of the Dutch inner shelf, resulting in a bed slope of $(H_s - H_0)/L_s \sim 4 \times 10^{-4}$. A horizontal flat bottom is used to represent the outer shelf further offshore and the Coriolis parameter for this latitude (52.5° N) is $f \sim 10^{-4}$ s^{-1}. The basic state has no cross-shore component of the current ($\vec{v} = (0 + u', V + v')$, where u' and v' are the perturbations in the cross-shore and longshore direction, respectively), from which it follows that the basic state satisfies $\overline{\vec{\nabla} \cdot \vec{q}} = 0$. This is a steady state solution of the bottom evolution equation (2.3) and hence the basic state is a morphodynamic equilibrium. It should be remarked that this is a consequence of the fact that in the present model the transverse slope of the reference bathymetry does not cause a net seaward sediment flux. It is assumed that this flux is compensated by the net landward fluxes which are caused by physical processes not explicitly accounted for in the model (such as wave asymmetry).

The basic state velocity consists of a steady component V_0 and a tidal component, due to the M_2 and M_4 tidal wave, with amplitudes V_{M_2} and V_{M_4} respectively:

$$V(x,t) = V_0(x) + V_{M_2}(x)\sin(\omega t + \varphi_{M_2}(x)) + V_{M_4}(x)\sin(2\omega t + \varphi_{M_4}(x) + \theta) \tag{2.7}$$

Here ω is the frequency of the M_2 tide, further details and the expressions for the cross-shore profiles of these velocity components are given in appendix 2.B. Characteristic values on decadal timescales (i.e. averages over many storm periods), which determine the basic longshore velocity profile for the central Dutch coast during storm conditions are:

$$s_0 \sim 2 \times 10^{-7} \text{ m m}^{-1} \qquad \tau_{sy} \sim -0.4 \text{ Nm}^{-2} \qquad \frac{\partial \rho}{\partial y} \sim -1 \times 10^{-5} \text{ kg m}^{-4}$$

Here s_0 is the longshore gradient in the steady part of the sea surface elevation. From these numbers a characteristic magnitude and direction of the steady current along the Dutch coast is obtained (see eq. (2.B-4)): $V_0(x = 0) \sim -0.4$ ms^{-1}, where the negative sign indicates a northward directed current. During fair weather s_0 and $\partial\rho/\partial y$ are the same, but the wind forcing is weaker. Here we use a value of $\tau_{sy} \sim -0.08$ Nm^{-2}, such that the steady current amplitude is smaller and of magnitude -0.1 ms^{-1}. The characteristic value for the steady current is defined as $U_0 = |V_0\ (x = 0)|$. Tidal current amplitudes, which are the same

during both realisations, are chosen as $V_{M_2}(x = 0) \sim 0.45$ ms^{-1} for the M_2 component and $V_{M_4}(x = 0) \sim 0.05$ ms^{-1} for the M_4 tide, resulting in a maximum tidal current amplitude of $U_{tide} = V_{M_2}(x = 0) + V_{M_4}(x = 0) \sim 0.5$ ms^{-1}. The choice of these values determines the magnitude of the sea surface elevations s_1 and s_2 of the M_2 and M_4 tidal wave, as defined in the appendix 2.B. These characteristic current amplitudes will be used in the next sections, where the maximum total current amplitude for storm conditions is $U = U_0 + U_{tide} \sim 0.9$ ms^{-1}, whilst during fair weather $U \sim 0.6$ ms^{-1}. For the phase θ between M_2 and M_4 sea surface gradient (see eq. (2.B-3)) we use the default value $\theta = 0°$. The motivation for this is as follows: θ can be related to the actual Greenwich phase of the vertical M_2 tide, g_{M_2}, and M_4 tide, g_{M_4}, by the relation: $\theta = 2g_{M_2} - g_{M_4}$. This quantity is highly variable in the southern North Sea due to the presence of an amphidromic point in both the vertical M_2 tide and M_4 tide (see Prandle, 1980). However, along the central part of the Dutch coast the maximum flood velocities exceed the maximum ebb velocities (Van der Molen, 2000), giving an indication that θ has a value between $-140°$ and $40°$. We will return to this in section 2.4.2. Our first assumption of $\theta \sim 0°$ is thus a reasonable approximation.

2.3.2 Linear stability analysis

Next, the stability properties of the basic state are considered by studying the dynamics of small perturbations evolving on this basic state. Thus solutions are of the form

$$\vec{v} = (u', V(x,t) + v')\,, \qquad z_s = s(t)y + z_{s0}(x,t) + \eta'\,, \qquad z_b = -H(x) + h\,.$$

In case of a positive feedback between flow and bottom topography, rhythmic bottom features will develop. The linearised momentum and mass conservation equations are solved at the tidal timescale to find the perturbed velocity field as a function of the bottom topography. The flow variables are substituted in the bottom evolution equation. Therefore, the perturbations u', v' and η' in the water motion are functions of x, y and t, and the same applies to h. The solutions are of the form

$$h = Re\left\{\hat{h}(x)e^{iky+\Omega t}\right\} \qquad (u', v', \eta') = Re\left\{(\hat{u}(x,t), \hat{v}(x,t), \hat{\eta}(x,t))e^{iky+\Omega t}\right\}$$

with k the longshore wavenumber and Ω the complex frequency. The longshore wavelength of the perturbations is given by $\lambda = 2\pi/k$. The stability analysis then yields the growth rate (Ω_r, i.e. the real part of Ω) of the topographic features as a function of the longshore wavelength. Here the timescale related to the growth of the bottom perturbations is much longer than the timescale of the hydrodynamics (related to the tidal frequency ω), i.e. $\Omega^{-1} \gg \omega$. For each k modes with a different cross-shore structure exist. The mode with the largest growth rate for perturbations with wavenumber k is the dominant cross-shore mode for that specific value of k. The preferred mode is defined as the mode having the largest possible growth rate and is attained for a specific wavenumber $k = k_0$. We are specifically interested in instabilities and thus for solutions which satisfy $\Omega_r > 0$ and assume that the perturbation corresponding to the wavenumber for which a maximum in the growth rate curve is found is the preferred mode. The migration velocity is obtained from $-\Omega_{Im}/k$, where Ω_{Im} denotes the imaginary part of Ω. This problem is then governed by an eigenvalue problem, for which the equations are given in appendix 2.C. Further details of this procedure are given in

Trowbridge (1995) and Calvete et al. (2001a). This flow over topography problem is solved numerically by using spectral methods in the space domain and Fourier methods in the time domain. The perturbations are expanded in Chebyshev polynomials and evaluated at the collocation nodes (see, for example in Falqués et al., 1996). The expansions are truncated in both the number of Fourier modes and the number of collocation points that are included. Solutions are tested for convergence if these numbers are increased.

2.4 Results

2.4.1 Storms

In this section results are presented for the model realisation representing storm conditions. The important parameter values are given in the previous sections. In the computations of the characteristic timescale for the growth of the bedforms it is assumed that storms prevail during a time fraction of 5%, whereas no growth of perturbations occurs during the remaining time fraction. The e-folding timescale for the growth of the ridges ($1/\max(\Omega_r)$) is corrected for this storm fraction. Figure 2.3 shows the growth rate and migration velocity of the dominant cross-shore mode as a function of the longshore wavenumber. In the figures the individual contributions of the suspended- and bed load fluxes are also indicated. Discontinuities in the curves denote values of wavenumbers where a different cross-shore mode becomes the preferred mode. Suspended transport of sediment is dominant for the growth of bed forms, while bed load transport dominates the migration of the bed forms. The preferred bottom mode has a wavenumber of $k_0 = 14.0/L_s$ m^{-1}, where $L_s \sim 12$ km is the characteristic horizontal length scale. This corresponds to a longshore wavelength of the bedforms of $\lambda_0 \sim 5.4$ km, with an e-folding time of the growth process $1/\Omega_{r0} \sim 380$ yr (where $\Omega_{r0} = \max(\Omega_r)$) and a migration of $c_0 \sim 3$ m yr^{-1} in the downcurrent direction. A second maximum with almost the same growth rate is found for a wavelength of 10.5 km ($k \sim 0.5k_0$) and a downcurrent migration of 2 m yr^{-1}. This second maximum dissapears if the tidal current during storms is zero and is only present if the tidal and steady current have similar amplitudes. Also, the migration velocity for the bedforms corresponding to this second maximum is similar, while the crestlines open at an angle of approximately 40° with the coastline. The spatial structure of the preferred bedforms with wavelengths of 10.5 km and 5.4 km are shown at the right-hand side of Figure 2.3. They resemble shoreface-connected ridges trapped to the inner shelf, represented by the cross-shore area between $x = 0$ and $x = 1$. Their crests are rotated in the direction of the mean longshore current, indicated by the thick arrow (compare with ridges in dashed box of Figure 2.1). The thin arrows denote the flow perturbation and show that there is an offshore current deflection over the crests of the bars. The outcome of the model (spatial pattern, e-folding time, migration speed) are in good agreement with the available field data on shoreface-connected ridges (see Swift et al., 1978; Van de Meene and Van Rijn, 2000a).

The difference between the present model and that of Calvete et al. (2001b) is that here a different steady current profile is used and two tidal components are added. From comparing the results of these two models we conclude that the steady forcing is dominating the formation of shoreface-connected ridges. Furthermore, from a sensitivity study of the model results we conclude that a transverse sloping bottom is essential for the growth of shoreface

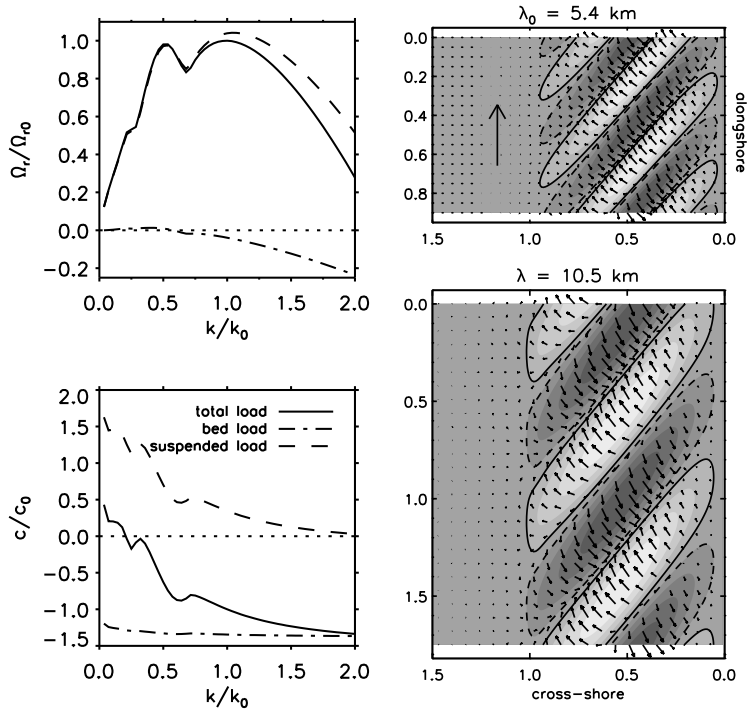

Figure 2.3: (LEFT) Growth rates (Ω_r/Ω_{r0}) and migration rates (c/c_0) of the dominant cross-shore mode as a function of the longshore wavenumber k/k_0, values are scaled by their values for the preferred mode. Results are shown for storm conditions and current amplitudes representative for the Dutch shelf. The contribution of the suspended load flux and bed load flux to the growth and migration rates for all wavenumbers is also indicated. Here $k_0 = 14.0/L_s$, corresponding to a wavelength $\lambda_0 \sim 5.4$ km, $\lambda_0 = 2\pi/k_0$, the growth time $1/\Omega_{r0} \sim 380$ yr and $c_0 \sim 3$ m yr^{-1}. (RIGHT) Bottom perturbations (shaded) corresponding to the maxima ($k = k_0$ and $k \sim 0.5\ k_0$) in the growth rate curve for storm conditions, dark colours are troughs, light colours bars. The coast and shoreface are on the right. Distances are in units of the inner shelf width L_s (12 km). Also indicated are the perturbations (small arrows) in basic longshore velocity field (in direction of thick arrow).

connected ridges, as was already found by Trowbridge (1995). For a discussion on the physical mechanism for the growth of the shoreface-connected ridges the reader is referred to the introductory chapter (section 1.7). The wave-orbital velocity and the steady current amplitude should be large enough ($U_w > 0.8$ ms^{-1} and $U_0 > 0.2$ ms^{-1}), otherwise the timescale for the growth of the bedforms increases very rapidly to unrealistically high values of several thousands of years. Changing the tidal current amplitude, for a fixed steady current, has little influence on the growth and migration, while the wavelength of the bed forms varies between 5 and 11 km. The presence of the M_4 tide has an even smaller effect and does not influence the results presented above, due to the linear relationship between the sediment flux and the current velocity. Furthermore, the bedslope coefficients in the sediment transport for-

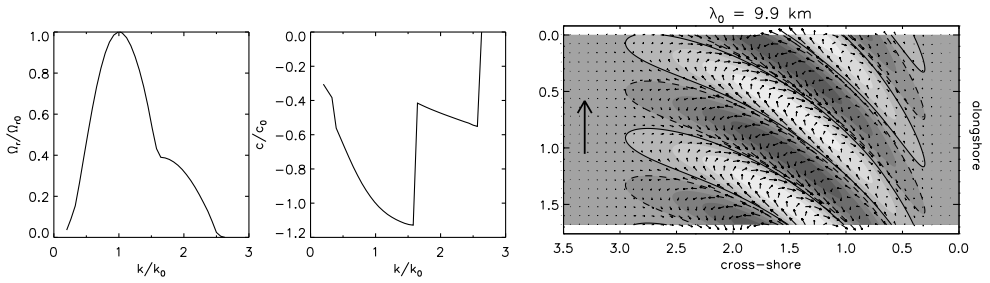

Figure 2.4: As Figure 2.3, but for fair weather conditions. Here $k_0 = 7.6/L_s$, corresponding to a wavelength $\lambda_0 \sim 9.9$ km, $1/\Omega_{r0} \sim 980$ yr and $c_0 \sim 6.6$ m yr^{-1}.

mulations mainly cause a reduction of the growth of perturbations with small wavelengths. An increase in λ_b or λ_s therefore increases the preferred wavelength and reduces the growth rates. The sensitivity of the growth and migration of shoreface-connected ridges on the steady current forcing (wind vs. pressure), the value of the exponent m in the wave-stirring and the Coriolis parameter is small, for which the results are presented in Calvete et al. (2001a).

2.4.2 Fair weather

Effect of changing current amplitude

In this section we apply the fair weather conditions for different combinations of steady and tidal currents. Here we extend the work of Calvete et al. (2001a) by including a second tidal component and add the influence of density gradients and wind stress in the steady part of the longshore current. Results for the fair weather case, with parameter values representative for the Dutch shelf (section 2.3.1), are shown in Figure 2.4. The preferred mode has a maximum for a longshore wavelength of $\lambda_0 \sim 9.9$ km ($k_0 = 7.6/L_s$), with a characteristic e-folding time of $1/\Omega_{r0} \sim 980$ yr and a downcurrent migration of 6.6 m yr^{-1}. The bedforms extend over the inner- and part of the outer shelf $(x > 1)$. They also have the anticlockwise rotation in the Northern Hemisphere with respect to the tidal current axis, which is shore-parallel. The bedforms resemble the tidal sand ridges found further offshore of the shoreface-connected ridges in the North Sea. A sensitivity analysis was done by changing the current amplitude. Experiments were carried out by fixing the steady current and increasing the tidal current. The same was done for a constant tidal current and changing steady contributions. Results are shown in Figure 2.5 for tidal currents which are varying between 0 and 1 ms^{-1} ($U_0 \sim 0.1$ ms^{-1}) and steady currents between 0 and 0.6 ms^{-1} ($U_{tide} \sim 0.5$ ms^{-1}). The ratio of the amplitude of the M_2 tidal current over the maximum M_2 plus M_4 tidal current is kept constant. The results indicate that e-folding times change rapidly if the tidal current amplitude is increased: larger tides result in a faster growth of the bedforms. Migration velocities and wavelengths increase if current amplitudes increase, although the steady current is the most effective.

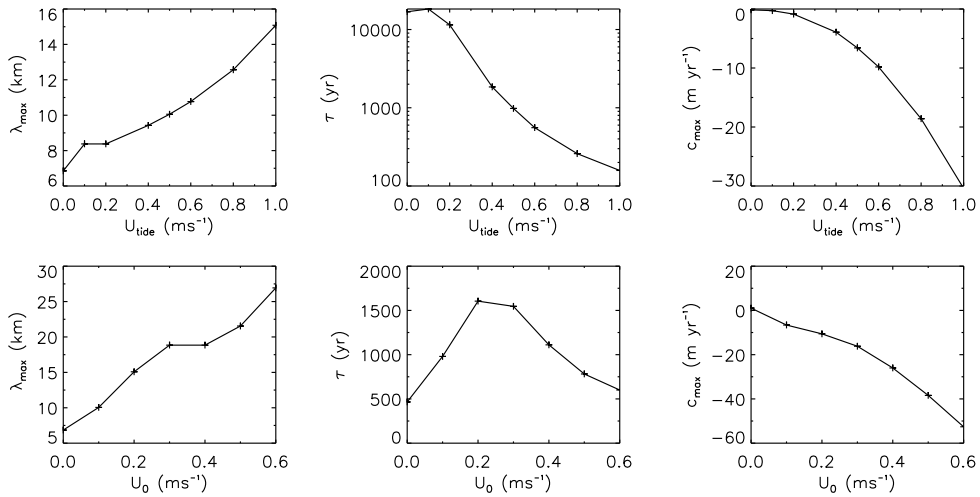

Figure 2.5: Fair weather case: wavelength of preferred mode, characteristic growth time and migration velocities for a steady current velocity of 0.10 ms^{-1} and increasing tidal current (TOP). Also shown a tidal current velocity of 0.50 ms^{-1} and increasing steady current (BOTTOM). Default values are $U_{tide} \sim 0.5$ ms^{-1} and $U_0 \sim 0.10$ ms^{-1}.

Influence of tidal asymmetry

In this subsection we will investigate the influence of tidal asymmetry on the growth and migration of bedforms in the fair weather mode of the model, which is characteristic for tidally dominated coastal shelves. The results in the previous sections are shown for a tide consisting of two tidal components, where the sea surface elevations of both components are in phase ($\theta = 0°$). In the southern part of the North Sea, where the quarter-diurnal component (M_4) of the tide is relatively important over the main semi-diurnal tide (M_2), a difference between the maximum ebb- and maximum flood velocities occurs. This asymmetry in the tidal curve is due to a phase difference between these two tidal components and might be important for the transport of sediment in the coastal seas (see e.g. Van de Kreeke and Robaczewska, 1993; Van der Molen, 2000).

The influence of the M_4 tide is investigated by changing a parameter α_1, which measures the contribution of the maximum M_2 tidal current amplitude to the maximum possible total tidal current amplitude at $x = 0$:

$$\alpha_1 = \left. \frac{V_{M_2}}{V_{M_2} + V_{M_4}} \right|_{x=0}$$

The value of this parameter ranges between zero and one, $\alpha_1 = 1$ corresponds to only an M_2 component, $\alpha_1 = 0$ represents the (unrealistic) situation without semi-diurnal tide, and only a quarter-diurnal tide is used. The maximum possible tidal current, U_{tide}, is kept constant. From the parameter values discussed in section 2.3.1 it follows that the default value is $\alpha_1 = 0.9$. Also the effects of changing the external phase θ between M_2 and M_4 tidal current on

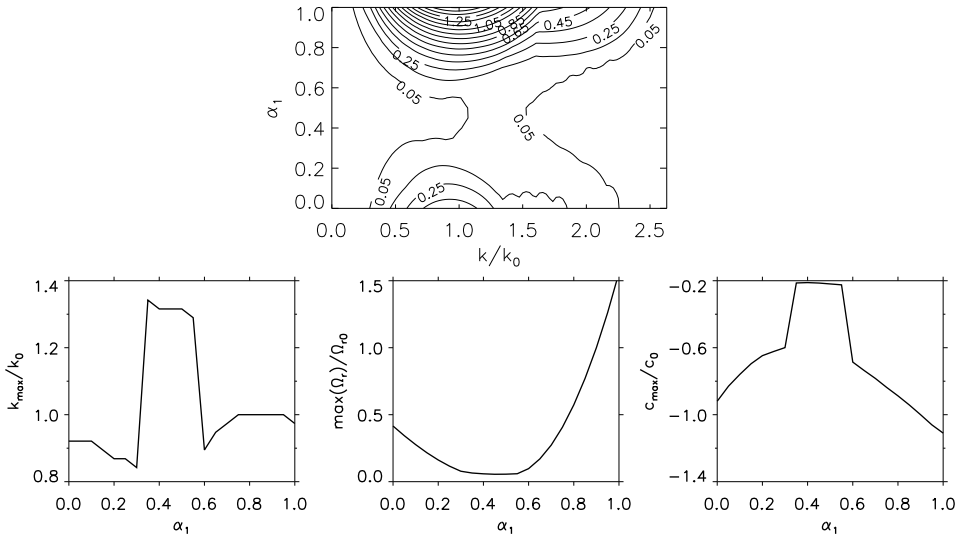

Figure 2.6: (TOP) Contour plot of equal growth rates Ω_r/Ω_{r0} of the dominant cross-shore mode in the $k/k_0 - \alpha_1$ plane for fair weather case and $U_{tide} \sim 0.5$ ms^{-1}. Here α_1 is the ratio of the maximum M_2 tidal current amplitude over the maximum total tidal current amplitude ($V_{M_2} + V_{M_4}$). (BOTTOM) Wavenumber corresponding to the maximum growth rate, maximum growth rate and migration velocity for the preferred mode as a function of parameter α_1. Values are scaled by their default values for fair weather. The default case is for which $k_{\max} = k_0$ is defined at $\alpha_1 = 0.9$, for which the parameter values are defined in Figure 2.4.

the instability mechanism will be investigated. In this way the asymmetry in the tidal current is controlled. Results are summarised in Figure 2.6. In the top figure a contour plot of the growth rates as a function of the scaled wavenumber k/k_0, in the range $0 \leq \alpha_1 \leq 1$ is shown. All other parameters have their default values. By adding a second tidal component to the single M_2 tide, both the growth and the migration of the bedforms becomes slower for $\alpha_1 > 0.4$. This can be seen from the other plots in Figure 2.6. For lower values of α_1 the tidal regime is dominated by M_4, instead of M_2. The default velocity amplitudes ($\alpha_1 = 0.9$) are used to vary the phase θ. In Figure 2.7 results are shown for the case that the phase θ is varied and all other parameters have their default values. It appears that the effect of tidal asymmetry can increase or decrease the migration, while at the same time the growth rates change. The changes in the growth rates are $\sim$ 40% over the complete range of phases θ, and in migration rates a variability of $\sim$ 30% is found. Maximum asymmetry, with maximum flood velocities (negative y direction) larger than maximum ebb velocities, is found for $\theta \sim -50°$, while ebb-dominance is found for $\theta \sim 130°$. Tidal velocity profiles at maximum asymmetry at the landward side of the inner shelf ($x = 0$) are shown in Figure 2.8 for one tidal cycle.

An explanation for the variation in the growth rate in Figure 2.6 and of the migration speed Figure 2.7 can be found by examining the equation for the bottom perturbations. The latter can be derived from eq. (2.3) and the linearised and tidally-averaged version of equation (2.6)

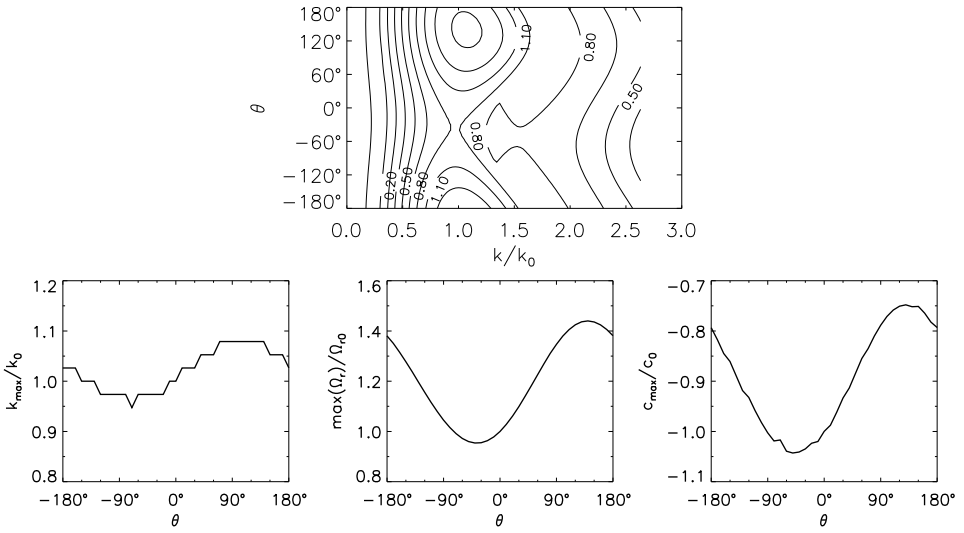

Figure 2.7: Influence of asymmetry in the tidal current on the growth rate, migration speed and preferred wavenumber for fair weather conditions. As in Figure 2.6 but the variables along the axes of the contour plot are here k/k_0 and θ; $\alpha_1 = 0.9$. The default case is for which $k_{\max} = k_0$ and is defined at $\theta = 0°$, see Figure 2.4.

(fair weather conditions, hence $\vec{q}_s$ can be neglected) and it reads:

$$(1-p)\frac{\partial h}{\partial t} + \overline{\vec{\nabla}\cdot\vec{q}_b'} = 0$$

where

$$\overline{\vec{\nabla}\cdot\vec{q}_b'} = \nu_b \left\{ 3\frac{\overline{V^3}}{H}\frac{\partial h}{\partial y} - \lambda_b \left(3\overline{V|V|\frac{\partial V}{\partial x}}\frac{\partial h}{\partial x} + \overline{|V|^3}\,\nabla^2 h \right) \right.$$
$$\left. -2\overline{V^2\frac{\partial u'}{\partial x}} - \overline{V^2\left(\frac{3}{H}\frac{\partial H}{\partial x} - \frac{2}{V}\frac{\partial V}{\partial x}\right)u'} \right\} \qquad (2.8)$$

The contribution proportional to $\partial h/\partial y$ describes the alongshore migration of the bottom perturbations, the part proportional to λ_b is mainly diffusive. The different sources of instability are given by the last two terms in (2.8), of which the largest contribution to the growth of bedforms is related to the divergence of the offshore flow component. Here u' is the perturbed cross-shore velocity, the perturbed longshore velocity v' is elimated using the perturbed version of the mass conservation (eq. (2.2)), and the overbar means an average over a tidal and wave period. Therefore, the migration is proportional to $\overline{V^3}$, and the growth is proportional to $\overline{V^2}$. For a velocity profile consisting of a steady component and M_2 and

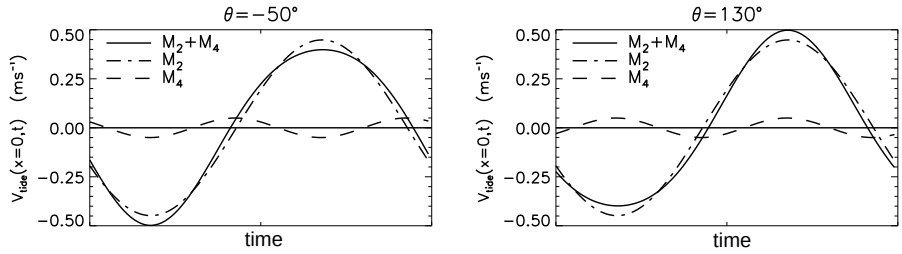

Figure 2.8: M_2 and M_4 tidal velocity components at the landward side of the inner shelf ($x = 0$) during one M_2 tidal period. This results in an asymmetrical (fbod-dominant) tidal current for $\theta = -50$ ° and ebb-dominated for $\theta = 130°$. Here $\alpha_1 = 0.9$, $U_{tide} \sim 0.5$ ms^{-1}.

M_4 overtides, as defined in appendix 2.B. and eq. (2.7), these averages are given by

$$\overline{V^3} = V_0^3 + \frac{3}{2}V_0(V_{M_4}^2 + V_{M_2}^2) + \frac{3}{4}V_{M_2}^2 V_{M_4}\sin(2\varphi_{M_2} - \varphi_{M_4} - \theta)$$
$$\overline{V^2} = V_0^2 + \frac{1}{2}(V_{M_4}^2 + V_{M_2}^2)$$

The tidal velocity is derived from the deformation of the sea surface due to a tidal wave. The vertical tide and the horizontal tide have different phases, due to the presence of bottom friction, as expressed by the phases φ_{M_2} and φ_{M_4}. At the landward boundary of the domain the last term in $\overline{V^3}$, which is the only term that depends on θ, is zero for $\theta \sim -140°$ and $\theta \sim 40°$ and in that case the tidal current is symmetrical, i.e. the maximum ebb-currents are equal to the maximum flood currents. The bottom perturbations for these situations strongly resemble those shown in Figure 2.4 ($\theta = 0°$: flood dominated). The main difference is a shift in the location of maximum crest height, which is more onshore in the ebb-dominated case compared to the flood-dominated case. The M_2 and M_4 tidal velocity components during one tidal period, as well as their resultant velocity profile, are shown in Figure 2.8 for a typical flood-dominated and a typical ebb-dominated case. We conclude that the phase lag between the M_2 and M_4 tidal constituents is not essential for the instabilities causing the growth of tidal sand ridges, but merely causes a change in the characteristic growth time and migration velocities. Fast migration of these bedforms is only found for bedforms with long growth times, while faster growing banks migrate more slowly.

2.4.3 Storms and fair weather combined

The conclusion from the previous sections is that storm conditions are favourable for the growth of shoreface-connected ridges, whereas during fair weather conditions bedforms are excited which resemble the more offshore located tidal sand ridges. Motivated by these results, experiments have been carried out in which the variation in weather conditions is taken into account. This is done by assigning a probability distribution to the two realisations of the model. The parameter μ is used to change the fraction of time during which storms prevail such that $\mu = 0$ indicates only fair weather conditions and $\mu = 1$ means continuous storms.

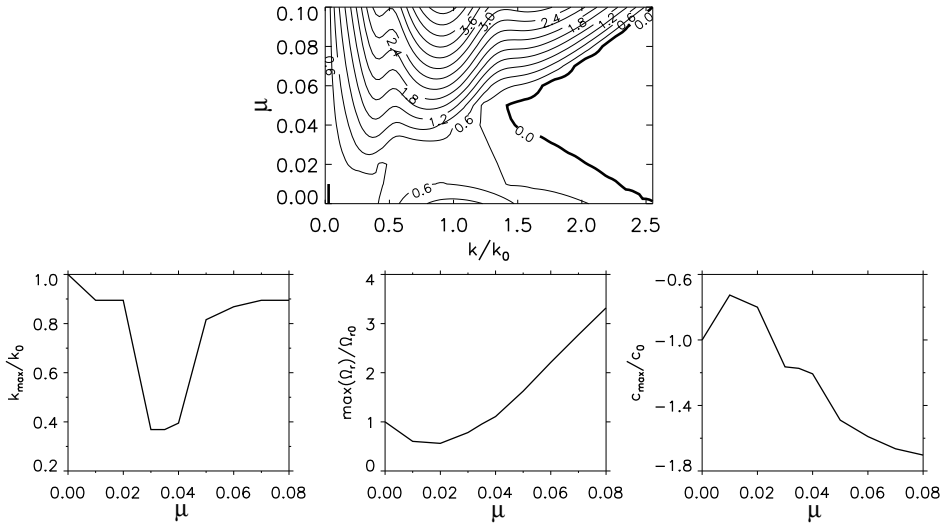

Figure 2.9: Contour plot of equal growth rates of the dominant cross-shore mode for a storm fraction $0 \leq \mu \leq 0.1$ as a function of the wavenumber. Also shown are the wavenumber corresponding to the maximum growth rates, maximum growth rates and migration velocities for the preferred mode. The default case is for which $k_{\max} = k_0$ and is defined at $\mu = 0$ (fair weather), parameter values as in Figure 2.4.

Then the evolution of the bottom is found from eq. (2.3), with the sediment flux given by

$$\vec{q} = \mu\, \vec{q}_{\text{storm}} + (1-\mu)\, \vec{q}_{\text{fair}} \tag{2.9}$$

where for the storm contribution expressions (2.4) and (2.5) are used ($\vec{q}_{\text{storm}} = \langle \vec{q}_b \rangle + \langle \vec{q}_s \rangle$) and for fair weather expression (2.6), with ($\vec{q}_{\text{fair}} = \langle \vec{q}_b \rangle$). In section 2.4.1 the growth times were already corrected for a storm fraction of 5% ($\mu = 0.05$), but the sediment transport during the remaining time of fair weather was neglected: $\vec{q}_{\text{fair}} = 0$. In this section a transport during this remaining time of fair weather will be included. In the model the amount of sediment transported during storms is about 200 times larger than during fair weather. The default parameter values for these situations have already been discussed in section 2.3.1.

In Figure 2.9 the dependence of the model results on variations in the storm fraction μ are shown. For $0 < \mu < 0.08$ the maximum growth rates shift between different modes with different wavelengths, as shown in Figure 2.10, where the behaviour of these different modes is indicated. For $\mu = 0$ the only unstable modes are those related to the tidal sand ridges. However, if μ is increased other modes with characteristics of the shoreface-connected ridges start to dominate. In this range of μ both modes have similar growth rates. Also shown is the appearance of a second maximum in the shoreface-connected ridge mode (C) which exceeds maximum B for storm fractions lower than 4%. The bottom perturbations for the tidal sand ridge mode A and the shoreface-connected ridges mode B are also shown in Figure 2.10 for a storm fraction of 5%. The shoreface-connected ridge mode will cause instabilities in the sloping part of the shelf, whilst the mode for the tidal banks grows offshore on a horizontal

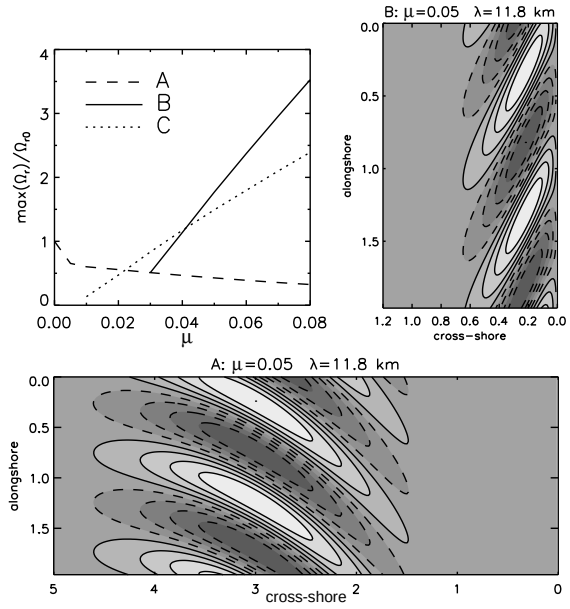

Figure 2.10: Maximum growth rates corresponding to three different modes for a storm fraction in the range $0 - 8\%$. A is the tidal sand ridge mode, with $\lambda_{\max}$ in the range $\sim 10 - 12$ km, B is the shoreface-connected ridge mode, with $\lambda_{\max}$ in the range $\sim 11 - 14$ km and C is a second maximum in the shoreface-connected ridge mode for $\lambda_{\max} \gtrsim 23$ km ($k_{\max} \sim 0.4\, k_0$). Also shown are the different bottom perturbations for a storm fraction of 5%: mode A and B ($\lambda_{\max} = 11.8$ km).

bottom. Both modes will be able to grow independently. For larger storm fractions the modes resembling the shoreface-connected ridges are dominating the tidal sand ridges, but for the parameters that are currently considered, this situation corresponds to unrealistically large values of μ.

Comparing the spatial patterns of the tidal sand ridge mode in Figure 2.10 and Figure 2.4 shows that perturbations in the bottom are found further offshore if $\mu = 0.05$ (nonzero storm fraction) than for $\mu = 0$. Experiments for which the steady component of the current is neglected during fair weather demonstrate this effect more clearly. The bedforms in this situation and for $\mu = 0$ are found on the inner shelf and have the orientation of tidal sand ridges. Including a storm-related contribution to the sediment flux will result in a growth rate curve of the dominant cross-shore mode (Figure 2.11) which is characterised by two maxima, one related to tidal sand ridges (A) dominating for storm fractions $\leq$ 3% and another for the shoreface-connected ridge mode (B). The latter mode grows faster for larger values of μ. The second maximum in the shoreface-connected ridges mode (C curve in Figure 2.10) corresponding to a very long wavelength is less pronounced in this case. The wavelength of this second mode does not agree with realistic spacings between the ridges along the Dutch coast, which can be up to 10 kilometers. The bedforms for the no storms and 4% storms case are shown in Figure 2.12. Clearly the inner shelf structure found for only fair weather ($\mu = 0$)

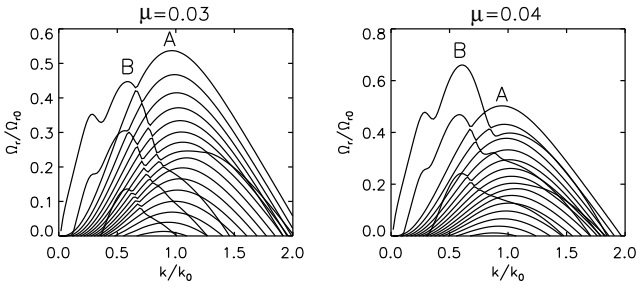

Figure 2.11: Growth rates corresponding to all unstable modes for $U_0 = 0$ ms^{-1} during fair weather conditions and a storm fractions of 3% (LEFT) and 4% (RIGHT). A indicates the maximum of the tidal sand bank mode ($k_{\max} \sim k_0$), B the maximum of the shoreface-connected ridge mode ($k_{\max} \sim 0.6\ k_0$). The growth rates are scaled by the values found for $\mu = 0$: $\lambda_0 \sim 6.9$ km, Ω_{r0} corresponds to a growth time of $\Omega_{r0}^{-1} \sim 470$ jr.

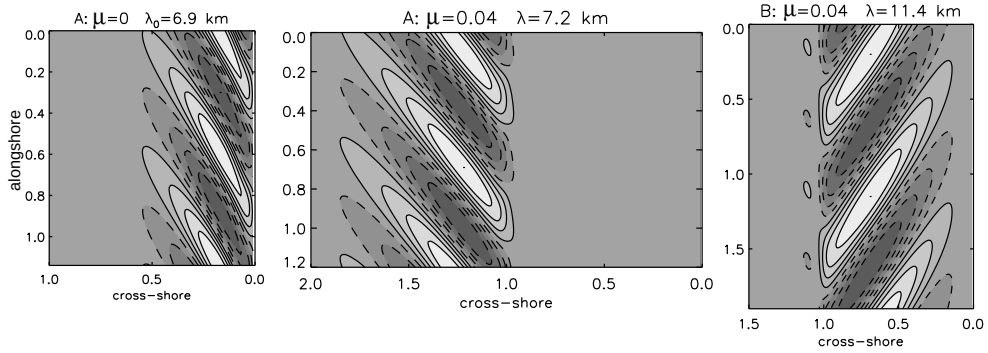

Figure 2.12: Bottom perturbations for mode A (LEFT) related to tidal sand ridges by using only fair weather conditions, i.e. $\mu = 0$ and $\lambda_0 \sim 6.9$ km. Also shown are the bedforms corresponding to a storm fraction of 4% (for growth rates see fi g. 2.11): mode A (MIDDLE), $\lambda_{\max} \sim 7.2$ km and mode B (RIGHT), $\lambda_{\max} \sim 11.4$ km. In these experiments $U_0 = 0$ ms^{-1} is used.

is destroyed in case of small storm fractions. This behaviour might explain the absence of tidal sand ridges closer to the coast. This is also seen in Figure 2.1, where along the central Dutch coast the tidal ridges are found seaward of about 20 m, while the shoreface-connected ridges are found in the more landward part of the shelf, where bottom slopes are higher. It therefore seems that the simultaneous formation of these two types of bedforms in the North Sea can be understood from this model, as two different modes with similar growth rates for low storm fractions.

2.5 Conclusions

The present model is able to explain the formation of both shoreface-connected ridges and tidal sand ridges due to inherent instabilities of the coupled water-bottom system. Necessary conditions for growth of shoreface-connected ridges appear to be a transversely sloping bottom, a storm fraction of a few percent and dominant suspended load transport. Then, the combined action of strong steady currents and large wave-orbital velocities cause realistic growth times of bedforms resembling shoreface-connected sand riges. Tidal currents turn out to be of minor importance for the formation of these ridges. Offshore tidal sand banks on the other hand require strong tides and they form during fair weather conditions.

One of the objectives of this study was to examine the influence of the M_4 tide, on the growth of large-scale bedforms. It was found that including the M_4 tide and a phase lag between M_2 and M_4 has only significant effects during fair weather conditions. It then changes the properties of the bedforms, which are tidal sand ridges for this case, due to tidal asymmetry. Migration velocities can be enhanced by tidal asymmetry, while at the same time growth rates decrease. Density gradients, driving a depth-averaged and shore-parallel flow in our model, only result in small changes in the characteristics of the bedforms. The second objective was to gain understanding about the simultaneous presence of shoreface-connected ridges and tidal sand ridges in the North Sea. In this chapter it is shown that both bedforms can form at the same time on a coastal shelf as a result of two different modes which have positive growth rates and which appear in different regions of the shelf: one on the inner shelf and the other on the outer shelf. To have a situation where both modes are unstable and have growth rates within realistic estimates, essential conditions (for parameter values representing North Sea conditions) are: storms conditions during $\sim 2-8\%$ of the time and the presence of both tidal- and steady currents (with a strong steady component during storms). The simultaneous growth of both modes prevents the formation of tidal sand ridges closer to the coast. In the North Sea these conditions prevail: the probability of storms coming from a south-western direction is indeed in this range.

One of the limitations of the present model is that uniform sediment is considered, while sediment with different grain sizes results in selective transport and grain size sorting, which is observed for most ridge fields. Also it describes only the initial growth of the bed forms, and therefore gives no information about the amplitudes and the time evolution of the bedforms. These aspects will be the topic of forthcoming chapters.

Appendix

2.A Sediment flux

The formulation of Bailard (1981) for the total load transport on a sloping bed can be written as follows:

$$\langle \vec{q_b} \rangle = \nu_b \left[\langle |\vec{v_t}|^2 \vec{v_t} \rangle - \lambda_b \langle |\vec{v_t}|^3 \rangle \vec{\nabla} h \right] \tag{2.A-1}$$

$$\langle \vec{q_s} \rangle = \nu_s \left[\langle |\vec{v_t}|^3 \vec{v_t} \rangle - \lambda_s \langle |\vec{v_t}|^5 \rangle \vec{\nabla} h \right] \tag{2.A-2}$$

Here h is the bottom perturbation, λ_b and λ_s are coefficients which measure the influence of a bed slope on bed load and suspended load transport and ν_b, ν_s are coefficients which depend on the sediment properties. Furthermore $\vec{v_t}$ is the depth-averaged velocity which consists of a wave-averaged part $\vec{v}$, due to steady and tidal currents, and a wave part $\vec{u}_w$. The brackets $\langle..\rangle$ indicates an average over a wave period. By assuming one of these (wave or wave-averaged) velocity components is larger than the other, we can distinguish between two situations: storms and fair weather.

2.B Basic state velocity profile

The equations for the basic state of the momentum equations (2.1) are given by:

$$-fV = -g\frac{\partial z_{s0}}{\partial x} - \frac{gH}{2\rho}\frac{\partial \rho}{\partial x} + \frac{\tau_{sx}}{\rho H} \tag{2.B-1}$$

$$\frac{\partial V}{\partial t} = -gs - \frac{gH}{2\rho}\frac{\partial \rho}{\partial y} + \frac{\tau_{sy}}{\rho H} - \frac{rV}{H} \tag{2.B-2}$$

The basic state velocity profile is a solution of the momentum equation in the y direction (2.B-2), where the longshore gradient in the free surface s is defined by a steady component s_0 and two oscillating components with the frequency of the M_2 and M_4 tide:

$$s \equiv s_0 - s_1\cos(\omega t) - s_2\cos(2\omega t + \theta) \tag{2.B-3}$$

Here s_0, s_1 and s_2 are the amplitudes of the sea surface elevations for the steady and the oscillatory contributions, respectively, and ω is the frequency of the M_2 tide. Note that the water motion is forced by two tidal harmonics, with θ being a (constant) phase. This phase can be determined from observations along the Dutch coast. The basic state velocity consists of a steady component (V_0) and a tidal component, due to the M_2 and M_4 tidal wave:

$$V(x,t) = V_0(x) + V_{tide}(x,t)$$

The steady component is driven by a prescribed longshore wind stress, longshore free surface pressure gradient s_0 and a prescribed density gradient:

$$V_0(x) = \frac{1}{r}\left(\frac{\tau_{sy}}{\rho} - gs_0H - \frac{g}{2\rho}\frac{\partial \rho}{\partial y}H^2\right) \tag{2.B-4}$$

The tidal velocity profile is found from the time-dependent part of the momentum eq. (2.B-2):

$$\frac{\partial V_{tide}}{\partial t} + \frac{r}{H}V_{tide} = g(s_1\cos(\omega t) + s_2\cos(2\omega t + \theta)) \tag{2.B-5}$$

The solution of this equation reads:

$$V_{tide}(x,t) = V_{M_2}\sin(\omega t + \varphi_{M_2}) + V_{M_4}\sin(2\omega t + \varphi_{M_4} + \theta) \tag{2.B-6}$$

where the tidal current amplitudes and phases are given by:

$$V_{M_2}(x) = \frac{gs_1H}{\sqrt{(\omega H)^2 + r^2}} \qquad \varphi_{M_2}(x) = \arctan\left(\frac{r}{\omega H}\right)$$

$$V_{M_4}(x) = \frac{gs_2H}{\sqrt{(2\omega H)^2 + r^2}} \qquad \varphi_{M_4}(x) = \arctan\left(\frac{r}{2\omega H}\right)$$

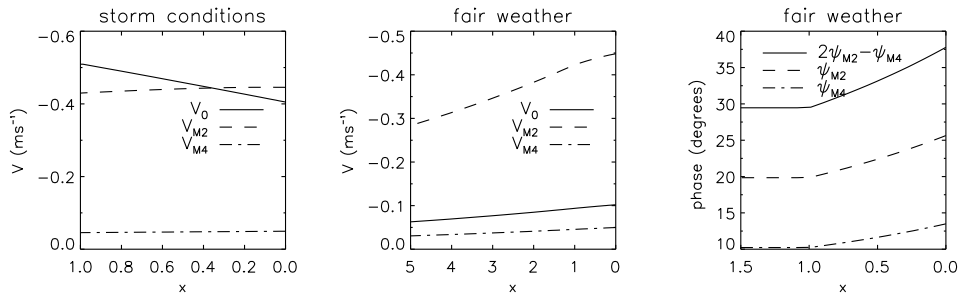

Figure 2.13: Cross-shore velocity profi les for storm and fair weather conditions. Also shown are the phases of the M_2 and M_4 tidal current during fair weather. Parameter values are given in section 2.3.1.

The cross-shore profile of the tidal current amplitudes V_{M_2} and V_{M_4} and the phases φ are functions of the bottom friction r and the undisturbed water depth. In addition to the expressions in (2.B-4) and (2.B-6), an the current amplitudes decrease exponentially offshore during fair weather. This is motivated by a reduced forcing further offshore and allows for solutions which are confined to that part of the outer shelf which is closest to the inner shelf (in the model the outer shelf extends to $x \to \infty$). An e-folding length of 120 km is used. The cross-shore velocity profiles during storm conditions and fair weather are plotted in Figure 2.13, where also tidal phases are indicated.

2.C Flow over topography problem

First the dynamics on the short, tidal timescale are analysed. From cross-differentiation of the linearised momentum equations and substituting the solutions for u', v', η' and h (section 2.3.2), we obtain the Fourier-transformed vorticity equation. An expression for the amplitude of the alongshore velocity perturbation as a function of $\hat{h}$ and $\hat{u}$ follows from the perturbed mass continuity equation (2.2):

$$\hat{v} = \frac{V}{H}\hat{h} + \frac{i}{k}\hat{u}_x + \frac{i}{k}\frac{H_x}{H}\hat{u} \tag{2.C-1}$$

The subscripts x and t are used to denote differentiation with respect to that variable, except for the subscripts in τ_{sx}, which denotes the cross-shore component of the wind stress. Substitution of this expression in the Fourier-transformed vorticity equation yields a single equation for the cross-shore velocity amplitude, $\hat{u}$, as a function of the bottom perturbation, $\hat{h}$:

$$\mathcal{U}_{12}\hat{u}_{txx} + \mathcal{U}_{11}\hat{u}_{tx} + \mathcal{U}_{10}\hat{u}_t + \mathcal{U}_{02}\hat{u}_{xx} + \mathcal{U}_{01}\hat{u}_x + \mathcal{U}_{00}\hat{u} = \mathcal{H}_1\hat{h}_x + \mathcal{H}_0\hat{h} \tag{2.C-2}$$

The coefficients of the flow over topography problem are given by

$$
\begin{aligned}
\mathcal{U}_{12} &= 1 \\
\mathcal{U}_{11} &= \frac{H_x}{H} \\
\mathcal{U}_{10} &= -k^2 + \frac{H_{xx}}{H} - \frac{H_x^2}{H^2} \\
\mathcal{U}_{02} &= \frac{r}{H} + ikV \\
\mathcal{U}_{01} &= ikV\frac{H_x}{H} + \frac{r_x}{H} \\
\mathcal{U}_{00} &= r\left(-\frac{k^2}{H} + \frac{H_{xx}}{H^2} - 2\frac{H_x^2}{H^3}\right) + r_x\frac{H_x}{H^2} \\
&\quad + ik\left(-k^2V - V_{xx} + \frac{V_xH_x + VH_{xx} + fH_x}{H} - \frac{VH_x^2}{H^2}\right) \\
\mathcal{H}_1 &= -\frac{k^2V^2}{H} + ik\left[\frac{V_t}{H} + r\left(\frac{2V - V_0}{H^2}\right) - \left(\frac{s_0}{H} + \frac{gH}{\rho}\rho_y\right)\right] \\
\mathcal{H}_0 &= k^2\left(\frac{-2VV_x - fV}{H} + \frac{V^2H_x}{H^2}\right) + ik\left(\frac{V_{tx}}{H} - \frac{V_tH_x}{H^2}\right) \\
&\quad + ik\left[r\left(\frac{2V_x - V_{0x}}{H^2} - \frac{2\left[2V - V_0\right]H_x}{H^3}\right) + r_x\left(\frac{2V - V_0}{H^2}\right)\right] \\
&\quad + ik\left[\frac{s_0}{H^2}H_x + ik\left(\frac{\tau_{sx}}{\rho H^2} + \frac{gH}{2\rho}\rho_x\right)\right]
\end{aligned}
$$

Here r_x is the cross-shore gradient in the bottom friction, which is only nonzero in case of storms. This covers the so-called flow over topography problem: for a given bottom perturbation the flow components u' and v' can be computed. From this the tidally- and wave-averaged sediment transport can be computed which in turn determines the evolution of the bottom. The linearised bottom evolution equation (2.3) becomes, after substitution of equation (2.9) and the solutions for the perturbations:

$$
\Omega(1-p)\hat{h} = -\mu\,\overline{\vec{\nabla}\cdot\vec{q}_{\text{storm}}} - (1-\mu)\,\overline{\vec{\nabla}\cdot\vec{q}_{\text{fair}}} \tag{2.C-3}
$$

where the parameter μ is used to change the fraction of time during which storms prevail. It should be remarked that the hydrodynamic problem for a specific reference bottom $H(x)$ and bottom perturbation h, as defined by equations (2.C-1) and (2.C-2), is solved separately for the two different flow regimes occurring in the model, i.e. storms and fair weather with frequencies μ and $1-\mu$, respectively. Ultimately, these results are combined in a statistical sense in the bottom evolution equation (2.C-3) to solve for the bottom perturbations. The expression for the divergence of the sediment flux during fair weather conditions is given in (2.8).

Chapter 3

Effect of grain size sorting on the formation of shoreface-connected sand ridges

Abstract

Field data of shoreface-connected ridges show persistent spatial variations of mean grain size over the bedforms. In the shore-normal direction, the profiles of bottom topography and mean grain size are approximately 90° out of phase. To investigate the mechanisms responsible for the observed grain size distribution and the influence of sediment sorting on the temporal and spatial characteristics of shoreface-connected ridges a model is developed and analysed. A linear stability analysis of an alongshore uniform basic state (describing a storm-driven flow on a micro-tidal inner shelf) with respect to small bottom perturbations is carried out. The transport of non-uniform sediment is described by formulations for both bed load and suspended load, both of which account for dynamic hiding effects. A one-layer model for the bed evolution and a bottom friction term which depends on the grain size are used. The initial formation of the ridges is studied for a bimodal sediment mixture. The results of the model indicate that the phase shift between bed topography and mean grain size for shoreface-connected ridges is due to the selective transport via suspended load of grains with different sizes. A net stabilising effect on the growth of bedforms and enhanced migration are predicted, caused by the bimodal character of the sediment. The wavelengths of the bedforms are only slightly affected. A physical explanation for the model results is also given. *

*This chapter is based on the paper entitled *Effect of grain size sorting on the formation of shoreface-connected sand ridges*, by M. Walgreen, H.E. De Swart and D. Calvete, published in J. Geophys. Res., 108 (C3), 3063, doi:10.1029/2002JC001435, 2003.

3.1 Introduction

Shoreface-connected ridges are rhythmic bedforms that are observed on storm-dominated inner shelves of coastal seas, in water depths of 4-20 m. Analysis of field observations (Swift et al., 1978; Antia, 1996; Van de Meene and Van Rijn, 2000a) has revealed that the spacing between the crests is in the order of 5-10 km, with heights varying between 1 and 6 m. Migration occurs in the direction of the mean alongshore storm-driven flow and characteristic phase speeds are 1-4 m yr^{-1}. Previous model studies have demonstrated that the formation of these large-scale bedforms is due to inherent positive feedbacks between the water motion and the eroding bed (Trowbridge, 1995; Calvete et al., 2001a,b). The combined action of stirring of sediment by waves and transport by storm-driven currents on a shelf with a transverse bottom slope is necessary to generate shoreface-connected ridges. Furthermore, these studies have found that the seaward end of the ridges is always shifted upcurrent with respect to their attachments to the shoreface and explanations for this morphological characteristic have been put forward. For the Long Island inner shelf (North America) the most frequently observed orientation of the ridges in relation to the shoreline is between 45-49° (McBride and Mosow, 1991). The model developed by Calvete et al. (2001b) provides information on the spatial pattern, evolution timescale and migration speed of the bedforms. These results are in good agreement with available field data of many different shelves.

A basic limitation of these models is that they assume a uniform grain size distribution of the sediment. This is not consistent with field data, which show persistent spatial variations of the mean grain size over the bedforms. Especially the ridges on the Mid Atlantic shelf are documented extensively and detailed information on the grain size characteristics has been given in the literature (see, for example, Swift et al., 1972; Hoogendoorn, 1986; Schwab et al., 2000). The ridges located in the Mid Atlantic Bight on the North American inner shelf (Swift et al., 1978; Swift and Field, 1981; Figueiredo et al., 1982) reveal, in the direction normal to the shore, grain size and topography variations that are approximately $90°$ out of phase: the coarsest material occurs on the landward (upcurrent) flank. This out-of-phase relationship extends over the entire ridge area (see Figure 1.4 in chapter 1). The phi parameter plotted here measures the mean size and is defined in section 3.2.2. Similar trends in mean grain size are observed for shoreface-connected ridges on the inner shelf of Brazil (Figueiredo et al., 1982) and Argentina (Parker et al., 1982), and for similar ridges located in the German Bight of the southern North Sea (Antia, 1996).

In the present study, the effect of sediment sorting on the formation of shoreface-connected ridges is investigated by extending the model by Calvete et al. (2001b) for sediment mixtures. New dynamics related to the presence of different grain sizes are incorporated in the sediment transport formulation, the sediment continuity equation, and in the formulation of the bottom friction in the hydrodynamic equations. Previous model studies on sediment sorting have mainly focused on river bars and sea ripples (Ribberink, 1987; Seminara, 1995; Foti and Blondeaux, 1995; Lanzoni and Tubino, 1999), i.e. on spatial scales much smaller than those for sand ridges. These studies indicate that the non-uniform character of sediment has a stabilising effect on the growth of bedforms.

The work presented in this chapter contains several new aspects. First, it focuses on sediment sorting in the sand regime in combination with ridge formation, while previous work has largely concentrated on gravel and sand-gravel mixtures (representative of river sediments).

Second, the influence of grain size on the entrainment and deposition of suspended sediment is included. Third, it incorporates nonuniform sediment in a model for large-scale bedforms in coastal seas. The first objective of this work was to investigate the influence of sediment sorting on the temporal and spatial characteristics of shoreface-connected ridges. The second goal was to gain insight into the physical mechanisms responsible for the observed grain size distribution over shoreface-connected ridges. This chapter focuses on the initial formation of shoreface-connected ridges, i.e. small bottom perturbations are assumed. For this purpose, a one-layer model for the bottom evolution, based on the concept of an active transport layer overlaying an inactive substrate, is used. The model uses a two-size sediment mixture. The motivation for using a simple model is that it allows for a systematic analysis of the underlying processes.

In section 3.2 the formulation of the model is given, followed by an outline of the solution procedure in section 3.3. Results are presented in section 3.4 and a physical interpretation is given in section 3.5. A discussion of the model results, including a comparison with field observations, is presented in section 3.6, followed by conclusions in the last section.

3.2 Model formulation

3.2.1 Hydrodynamics

Following earlier studies by Trowbridge (1995) and Calvete et al. (2001b), we hypothesize that shoreface-connected sand ridges form as an inherent instability of a morphodynamic system, in which there is a feedback between the storm-driven flow and the eroding bed. A highly idealised model is used to investigate the flow-topography interaction on coastal shelves during storm conditions. The shelf geometry is schematised as a semi-infinite domain, bounded on the landward side by the transition from the shoreface to the inner shelf, see Figure 3.1. The undisturbed bathymetry (no ridges present) is uniform in the alongshore (y) direction. In the cross-shore (x) direction it consists of an inner shelf (with a linearly sloping bottom) and an outer shelf represented by a horizontal bottom. The water depth at the beginning of the inner shelf ($x = 0$) is H_0, L_s is the inner shelf width and H_s is the depth of the outer shelf. Representative values for the Long Island inner shelf (Mid Atlantic Bight, US), which is considered as a prototype storm-driven shelf in this study, are $H_0 \sim 14$ m, $H_s \sim 20$ m and $L_s \sim 5.5$ km. Note that in this chapter the figures are such that the coastline is on the left (eastcoast of America), as opposed to the figures in chapter 2 that have the coastline on the right (westcoast of The Netherlands).

In the model the water motion is described by the depth-averaged (2DH) shallow water equations. They read

$$\frac{\partial \vec{v}}{\partial t} + (\vec{v} \cdot \vec{\nabla})\vec{v} + f\vec{e_z} \times \vec{v} = -g\vec{\nabla} z_s + \frac{\vec{\tau}_s - \vec{\tau}_b}{\rho D} \tag{3.1}$$

$$\frac{\partial D}{\partial t} + \vec{\nabla} \cdot (D\vec{v}) = 0 \tag{3.2}$$

Here $\vec{v}$ is the depth-averaged and wave-averaged velocity, with components u and v in the x and y direction, respectively, $f \sim 10^{-4}$ s^{-1} is the Coriolis parameter, $\vec{e_z}$ a unit vector

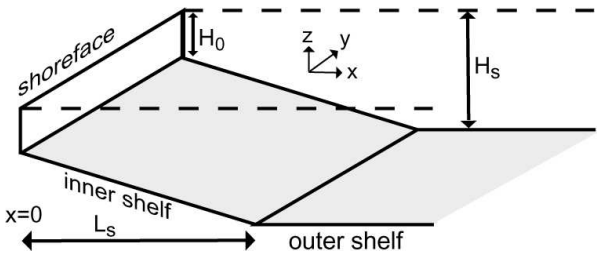

Figure 3.1: Sketch of the geometry of the model, representing the inner shelf (width L_s) and part of the outer shelf of a coastal sea. For further information, see the text.

in the vertical direction, $\vec{\tau}_s$ the wind shear stress vector, $\vec{\tau}_b$ the bottom shear stress vector, g the acceleration due to gravity, ρ the density of water, t the time and $\vec{\nabla}$ the horizontal nabla operator. The local water depth is given by $D = z_s - z_b$, where z_s is the free surface elevation and z_b is the bottom depth, both measured with respect to the undisturbed water level $z = 0$.

Both observations and model studies indicate that shoreface-connected ridges mainly develop during storms, tides do not play an important role (see Calvete et al., 2001a; Walgreen et al., 2002) and the timescales involved are about hundred years. This appears to justify the neglect of tidal forcing in the model (micro-tidal shelves are assumed) and the use of a probabilistic approach. Two realisations of the system are considered, corresponding to different weather conditions. During storms (which occur during a time fraction $\mu \sim 0.05$) large waves and strong currents cause significant sediment transport. In contrast, during fair weather conditions (time fraction $1 - \mu$) the waves and currents are not sufficiently strong to erode sediment from the bottom. Thus equations (3.1) and (3.2) are assumed to be representative for the situation during storms. The quasi-steady approximation is made in equations (3.1) and (3.2), such that terms involving time derivatives are excluded. This is because the hydrodynamic timescale is much smaller than the timescale on which the bed evolves. Also, the rigid-lid assumption is used, in which case the free surface effects in the local water depth are neglected, i.e. $D \simeq -z_b$. This is justified for small Froude numbers, typically $F^2 = U_0^2/(gH_0) \sim 0.001$ with $U_0 \sim 0.4$ ms^{-1} the characteristic current velosity.

The main forcing of the water motion is by wind and an alongshore pressure gradient. During storms the presence of large waves causes a wave-orbital velocity amplitude u_w, which is much larger than the wave-averaged velocity amplitude. This allows for a linearisation of the bed shear stress:

$$\vec{\tau}_b = \rho r \vec{v}$$

with r the bottom friction coefficient which is written in terms of a Chezy coefficient C_h (see Ribberink, 1987; Soulsby, 1997). For an overview of the most frequently used variables in this chapter, the reader is referred to appendix 3.D. This results in

$$r = \frac{g\langle|\hat{u}_w|\rangle}{C_h^2} \qquad C_h = \frac{\sqrt{g}}{\kappa} \ln\left(\frac{12D}{k_s}\right) \tag{3.3}$$

where $\hat{u}_w$ is the near-bed wave-orbital velocity and $\langle \, .. \, \rangle$ denotes a time average over many wave periods. Furthermore, κ is the von Karman's constant and k_s is the roughness length, which is proportional to a coarse grain size (see, for example, Ribberink, 1987; Lanzoni and Tubino, 1999). This formulation of the friction coefficient introduces a dependence on the grain size in the hydrodynamic equations. A characteristic value for the friction coefficient is $r \sim 0.7 \times 10^{-3}$ ms^{-1}.

Calvete et al. (2001b) found that it is essential for the growth of shoreface-connected ridges to parameterise the wave-orbital velocity increase in decreasing water depths. The description of the wave-orbital velocity as $\hat{u}_w = u_w \cos(\omega_w t)$ (symmetrical waves with frequency ω_w), with the amplitude given by

$$u_w = U_w \left(H_0/H\right)^{\frac{m}{2}}, \tag{3.4}$$

includes this effect. Here H is the undisturbed water depth, $U_w \sim 1$ ms^{-1} the amplitude at the shoreface boundary $x = 0$ and m a coefficient. Runs with a simple wave shoaling model indicate that $m \sim 1.6$.

3.2.2 Sediment characteristics

For a sediment mixture it is convenient to use a logarithmic scale (the phi scale) to describe the grain diameters. The definition is

$$d = 2^{-\phi} \qquad \text{or} \qquad \phi = -\log_2 d$$

where d is the grain diameter measured in units of mm (see Dyer, 1986). Accordingly, larger values of ϕ correspond to finer sizes. A sediment mixture is described by a probability distribution function $\mathcal{F}$ as a function of the grain size. This is the weight percentage of each grain size, hence $\mathcal{F}$ has the following property:

$$\int_{-\infty}^{\infty} \mathcal{F}(\phi)\, d\phi = 1$$

For many sand mixtures $\mathcal{F}(\phi)$ is approximately a Gaussian curve if plotted on this phi scale. In that case, two statistical properties describe the sediment distribution: the mean grain diameter ϕ_m and the standard deviation σ, defined as

$$\phi_m = \int_{-\infty}^{\infty} \phi \mathcal{F}(\phi) d\phi \qquad \sigma^2 = \int_{-\infty}^{\infty} (\phi - \phi_m)^2 \mathcal{F}(\phi) d\phi$$

The mean diameter is calculated as $d_m = 2^{-\phi_m}$. A measure of the sorting is given by the standard deviation of the distribution. Small values of σ corresponds to a sharply peaked curve, representing an almost uniform sample, and is classified as well sorted. A poorly sorted mixture of sediment has larger values of σ.

3.2.3 Sediment continuity

The hydrodynamic equations discussed above are supplemented with a sediment transport formulation, based on the concepts introduced by Bailard (1981) for the total load transport

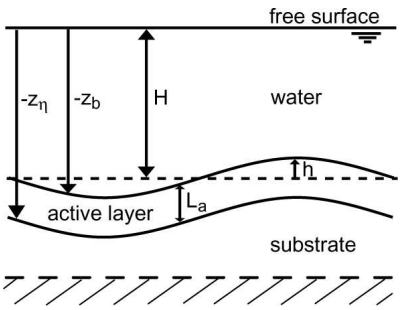

Figure 3.2: Definition of the sediment layer as used in the model. The thickness of the active layer is denoted by L_a and h is the elevation of the bottom with respect to a reference level.

on a sloping bed, and the bottom evolution equation. The evolution of the bottom is a result of divergence in the sediment flux and depends on the composition of the bottom sediment. The simplest models dealing with the effect of sediment sorting on bed level changes consider two separate layers in the bottom (Figure 3.2), see Ribberink (1987); Seminara (1995). The first is the active layer, which contains the material available for transport, and from now on $\mathcal{F}$ is defined as the corresponding probability density function for the grain sizes in this layer. Underneath this active layer a substrate is located with a probability density function of $\mathcal{F}_s$. The bottom location is denoted by $z_b = -H + h$, with H the undisturbed water depth and h the bed elevation with respect to this reference level. Furthermore, $z_\eta = z_b - L_a$ is the level of the interface between the active (surface) layer and the substrate. The active layer thickness, L_a, is in the order of $2-3$ times d_{90} (grain size for which 90% of the material is finer). The thickness of the total sediment column is considered to be so large that modifications of the sediment composition in the substrate, due to exchanges of sediment with the upper layer, can be omitted.

A well-mixed active layer ($\mathcal{F}$ is independent of the depth) and a time-independent grain size composition in the substrate ($\mathcal{F}_s$) are assumed. Consequently, a continuity equation exists for each fraction of grain size ϕ (Seminara, 1995; Armanini, 1995). It reads

$$(1-p)\left(\mathcal{F}_\eta \frac{\partial h}{\partial t} + L_a \frac{\partial \mathcal{F}}{\partial t} + (\mathcal{F}-\mathcal{F}_\eta)\frac{\partial L_a}{\partial t}\right) = -\vec{\nabla}\cdot\vec{q}_\phi \tag{3.5}$$

Sedimentation: $\frac{\partial z_\eta}{\partial t} = \frac{\partial}{\partial t}(h - L_a) > 0: \quad \mathcal{F}_\eta = \mathcal{F}$
Erosion: $\frac{\partial z_\eta}{\partial t} = \frac{\partial}{\partial t}(h - L_a) < 0: \quad \mathcal{F}_\eta = \mathcal{F}_s$

The terms on the left-hand side of equation (3.5) represent the bottom changes, changes in the sediment distribution in the active layer, and changes in the thickness of the active layer due to exchange of sediment with the substrate, respectively. Furthermore, $\vec{q}_\phi$ is the volumetric flux per unit width of grains of size ϕ and $p \sim 0.4$ is the porosity of the bed. In the initial growth stage of bedforms, sorting can be seen as the rearrangement of material in the active layer with negligible interaction between substrate and active layer (Ribberink, 1987; Seminara, 1995). This assumption, which implies that $\mathcal{F}_\eta = \mathcal{F}$, is adopted here.

We consider a discrete number (N) of grain sizes, such that $\mathcal{F}(\phi) = \sum_{i=1}^{N} \mathcal{F}_i\ \delta(\phi - \phi_i)$, with δ the Dirac delta function. Furthermore, we

use the fact that the morphodynamic timescale is much larger than the hydrodynamic timescale. This implies that the bed evolution for a discrete distribution of grain sizes and grains in class i (and diameter d_i) is given by

$$(1-p)\left(\mathcal{F}_i\frac{\partial h}{\partial t}+L_a\frac{\partial \mathcal{F}_i}{\partial t}\right)=-\vec{\nabla}\cdot\langle\vec{q}_i\rangle \tag{3.6}$$

Note that the sediment flux is averaged over the wave cycle. Together with the constraint $\sum_{i=1}^{N}\mathcal{F}_i = 1$ a closed system of equations is specified if $\vec{q}_i$ is known.

3.2.4 Sediment transport

Calvete et al. (2001b) demonstrated that both bed load and suspended load fluxes are needed to describe the growth and migration of the shoreface-connected ridges. The sediment flux, therefore, reads

$$\vec{q}_i=\vec{q}_{bi}+\vec{q}_{si}$$

where $\vec{q}_{bi}$ and $\vec{q}_{si}$ represent the bed load and suspended load contributions, respectively.

Bed load

The transport of sediment of class i depends on the shear stress exerted by the flow on the bed and on the grain properties. A general formulation for bed load transport of grains of size d_i over a flat bed is (Ribberink, 1987): $q_{bi} \propto \mathcal{F}_i\sqrt{g'd_i^3}\,\Theta_i^{\frac{b}{2}}$. Here $g' = g(\rho_s-\rho)/\rho$, $\rho_s = 2650$ kgm^{-3} is the density of the grains, $\rho = 1030$ kgm^{-3} is the water density and b is an exponent. In the case of uniform sediment the Shields parameter $\Theta_{i,u}$ is

$$\Theta_{i,u}=\frac{\tau}{\rho g' d_i}=\frac{u_*^2}{g'd_i} \qquad \text{and} \qquad \Theta_{i,u}=\frac{d_m}{d_i}\Theta_m$$

In this expression τ is the bed shear stress, u_* the friction velocity, d_m the mean grain size of a mixture, and Θ_m the Shields parameter corresponding to grains of size d_m. In a sediment mixture the effective Shields parameter Θ_i of sediment of size class i differs from $\Theta_{i,u}$. This is because the behaviour of a sediment mixture is influenced by the effect of dynamic hiding: finer grains feel fluid drag less intensely than larger grains. The effect is modelled by

$$\Theta_i=\frac{1}{\xi_i}\Theta_{i,u}=\frac{1}{\xi_i}\frac{d_m}{d_i}\Theta_m \tag{3.7}$$

with $\xi_i = \xi(d_i)$ a (dynamic) hiding function. According to field and laboratory data, ξ_i decreases with d_i/d_m. Thus, fine sand is less exposed to the shear stress than coarse sand. The effect of ξ_i is incorporated in a vectorial form of the bed load transport as follows:

$$\vec{q}_{bi}=\mathcal{F}_i\hat{q}\sqrt{g'd_m^3}\left(\frac{\Theta_m}{\xi_i}\right)^{\frac{3}{2}}\left[\frac{\vec{\tau}}{|\vec{\tau}|}-\lambda_b\vec{\nabla}h\right]$$

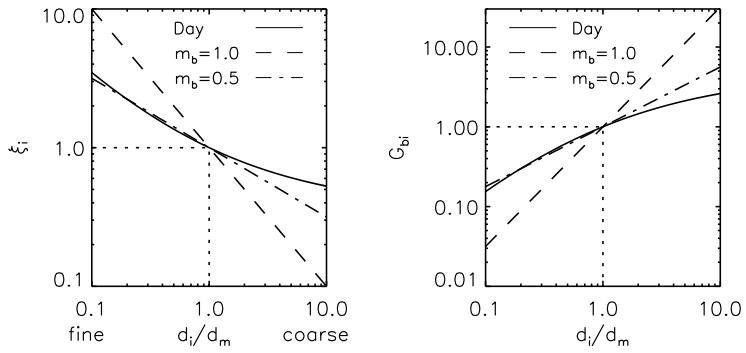

Figure 3.3: Different dynamic hiding functions ξ_i for the bed load sediment transport and the corresponding transport capacity functions G_{bi} as a function of d_i/d_m. Here d_i is the grain size class i, d_m the mean grain size and $m_b \equiv \frac{2}{3}c_b$. For further information see the text.

The exponent $b = 3$ is chosen consistent with the arguments presented by Bailard (1981) and $\hat{q} \sim 7.7$ is a constant. Note that static hiding effects related to the presence of a critical shear stress for erosion (see Ribberink, 1987; Seminara, 1995) are not modelled. Furthermore, it is assumed that all grains are transported in the same direction: $\vec{\tau}/|\vec{\tau}|$ is independent of the grain size and the effect of bottom slopes (see the discussion in Fredsøe and Deigaard, 1992, and references therein) are explicitly accounted for. The bottom perturbations are given by h and λ_b is a parameter which accounts for the gravitational effect of sediment movement on a sloping bottom. For simplicity we assume λ_b to be constant ($\sim$ 1).

The bottom shear stress vector used in the sediment transport is given by $\vec{\tau} = \rho\, c_f\, |\vec{v}_t|\, \vec{v}_t$. In this expression $\vec{v}_t$ is the total velocity, which consists of a wave-averaged velocity $\vec{v}$, as used in the hydrodynamic equations, and a wave contribution $\hat{u}_w$ ($\vec{v}_t = \vec{v} + \hat{u}_w$). The coefficient c_f is in some sense related to the drag used in the hydrodynamic equations, which was based on the Chezy coefficient. Here we assume that these are different and c_f is only related to the skin friction. A constant value of $c_f \sim 1 \times 10^{-3}$ is assumed. Application of these assumptions results in

$$\vec{q}_{bi} = \nu_b\, \mathcal{F}_i \mathcal{G}_{bi}\, |\vec{v}_t|^3 \left[\frac{\vec{v}_t}{|\vec{v}_t|} - \lambda_b \vec{\nabla} h \right] \qquad \mathcal{G}_{bi} = \left(\frac{1}{\xi_i} \right)^{\frac{3}{2}} \tag{3.8}$$

where $\nu_b = \hat{q}\, c_f \sqrt{c_f}/g' \sim 2 \times 10^{-5}$ s^{2}m^{-1} and $\mathcal{G}_{bi}$ is the bed load transport capacity function for sediment of size d_i. A simple hiding function is used: $\xi_i = (d_m/d_i)^{m_b}$. In Figure 3.3 the dynamic hiding function according to Day (see in Ribberink, 1987) and two simplified relations are shown ($m_b = 0.5$ and $m_b = 1$), together with the corresponding transport capacity functions. Note that grains of a diameter equal to d_m experience no hiding effects ($\xi_i = 1$).

As was discussed in section 3.2.3, the model for shoreface-connected ridges requires information about the wave-averaged bed load flux, $\langle \vec{q}_{bi} \rangle$, during storms. In that case the amplitude of wave-orbital motion is much larger than the mean current, thus $u_w \gg |\vec{v}|$.

Furthermore, the waves are supposed to be almost parallel to the wave-averaged current, which is mainly parallel to the coast. For the Long Island inner shelf (North America), with a coastline trending approximately southwest-northeast, the highest waves are related to the northeasterly storms and support this assumption. We will return to this in the discussion in chapter 6. This leads to

$$\langle \vec{q}_{bi} \rangle = \mathcal{F}_i \mathcal{G}_{bi} \vec{q}_b \qquad \vec{q}_b \simeq \frac{3}{2}\nu_b \left(u_w^2 \vec{v} - \frac{8}{9\pi}\lambda_b u_w^3 \vec{\nabla} h \right)$$
$$\mathcal{G}_{bi} = \left(\frac{d_i}{d_m} \right)^{c_b}, \quad c_b \equiv \frac{3}{2} m_b \tag{3.9}$$

We use $m_b = 0.5$, which yields $c_b = 0.75$ for the exponent in the transport capacity function. Thus, the bed load transport for grains with a diameter $d_i < d_m$ is reduced compared to the bed load transport of grains with diameter d_m due to dynamic hiding. On the other hand, the bed load transport for grains with a diameter $d_i > d_m$ is enhanced due to their higher exposure to the flow.

Suspended load

During storms it has been observed that the sediment on the inner shelf is mainly transported as suspended load (Green et al., 1995). The vectorial formulation of the suspended load flux reads

$$\vec{q}_{si} = C_i |\vec{v}_t| \left[\frac{\vec{v}_t}{|\vec{v}_t|} - \lambda_s |\vec{v}_t| \vec{\nabla} h \right] \tag{3.10}$$

In (3.10), C_i is the depth-integrated volume concentration of grains in class i, which includes all grain size dependence, and λ_s is the bed slope coefficient for suspended load transport. This coefficient is strictly also a function of the grain size: it is inversely proportional to the settling velocity of the grains. This effect is not included in this chapter, because the bedslope flux for suspended load is small compared to the advective flux (first term in (3.10)) for sand ridges of low heights and thereby would only intoduce a higher order effect. The bedslope fluxes are mainly responsible for surpressing the bedforms with very small wavelenghts. Since C_i is a monotonically increasing function of the bed shear stress τ, this formulation is consistent with that in Bailard (1981). However, it is modified for strong forcing conditions, whereas Bailard's expression was derived for relative moderate forcing conditions. This adjustment is also motivated by the analysis performed by Bayram et al. (2001), who demonstrated that Bailard's formulation underestimates the observed transport during storms. An expression for C_i is derived in appendix 3.A. In the case of fine sand, an approximate balance between sediment erosion and deposition near the bed exists, yielding

$$C_i = \mathcal{F}_i \delta_i E_i D \tag{3.11}$$

In this expression, E_i is the dimensionless entrainment of grains of diameter d_i and δ_i is the ratio of the thickness of the suspended load layer of these grains over the total water depth D. The thickness of the suspended load layer is given by k_z/w_{si}, with k_z the turbulent mixing coefficient for sediment particles, and w_{si} the settling velocity of grains in size class i. As

discussed in Calvete et al. (2001b), k_z is proportional to the water depth D (cf. Van Rijn, 1993), and therefore the parameter δ_i does not change in the offshore direction. Note that if the depth-integrated concentration changes linearly with the depth, the depth-averaged concentration is independent of the depth.

Two (out of many) formulations for the entrainment are considered, of which one is derived for sediment mixtures and one for uniform sediment. The formulation according to Van Rijn (1993) is $E_i \propto |\vec{v}_t|^3$ and is tested against laboratory experiments for uniform sediment. In previous work on shoreface-connected ridges this formulation was used (Calvete et al., 2001b; Walgreen et al., 2002, previous chapter). We use the Garcia and Parker (1991) formulation, which is based on results from laboratory experiments carried out with sediment mixtures, thereby accounting for possible hiding effects. The result is that $E_i \propto |\vec{v}_t|^5$ (for the complete expressions see appendix 3.A. Similar to the hiding expression for bed load, eq. (3.7), we write

$$\delta_i E_i = \zeta_i \, [\delta_i E_i]_u \equiv \mathcal{G}_{si} \, \delta_m E_{m,u} \tag{3.12}$$

with ζ_i the hiding function for the entrainment of sediment and δ_m is related to the thickness of the suspended load layer for grains of size d_m. The quantity $E_{m,u}$ is the entrainment of grains of diameter d_m only. The hiding function according to Garcia and Parker (1991) is

$$\zeta_i = \left[\lambda_{\mathrm{E}} \left(\frac{d_i}{d_m} \right)^{m_E} \right]^5 \tag{3.13}$$

The parameter m_E defines the importance of hiding for the entrainment of sediment, its default value is $m_E = 0.2$. A straining parameter, $\lambda_{\mathrm{E}} = 1 - 0.288\,\sigma$, is used with σ the standard deviation on the ϕ scale, as defined in section 3.2.2. It models the reduced mobility of the sediment mixture as its standard deviation increases and corrects for the otherwise overestimated entrainment rates. The entrainment of grains from all size classes decreases with increasing standard deviation of the sediment mixture in the active layer. This can be interpreted as the result of a more efficient packing of grains in the bottom sediment when grains of different sizes are present. Hence, a decrease in the porosity (=1-packing) found. Substituting expression (3.13) in (3.12), in combination with the results from appendix 3.A, yields for the transport capacity function of suspended load

$$\mathcal{G}_{si} = \lambda_{\mathrm{E}}^5 \left(\frac{d_i}{d_m} \right)^{c_s} \qquad\qquad c_s \equiv 5m_E + 4.5 - 6e_w \tag{3.14}$$

The first value in the definition of c_s incorporates hiding effects, whereas the second includes the dependence of the entrainment function on the particle Reynolds number. The coefficient e_w defines the dependence of the settling velocity on the grain size: $w_{si} \propto d_i^{e_w}$. The formulation of Hallermeier (see Soulsby, 1997) for fine to coarse sand yields $e_w = 1.1$, resulting in $c_s = -1.1$. Another formulation by Van Rijn (1993) for settling of grains in the sand range gives $e_w = 1.0$, resulting in $c_s = -0.5$. The negative value of the exponent physically means that the depth-integrated concentration for grains of sizes smaller than the mean is larger than for grains of sizes larger than the mean grain size. Combining eq. (3.11)-(3.14) yields for the concentration

$$C_i = \mathcal{F}_i \mathcal{G}_{si} C \qquad\qquad C = \delta_m E_{m,u} D = \delta_m \hat{E}_{m,u} |\vec{v}_t|^5 D$$

with $\hat{E}_{m,u} \sim 3 \times 10^{-4}$ m^{5}s^{-5} and $\delta_m \sim 0.19$. The averaged suspended load flux (3.10) during storms reads

$$\langle \vec{q}_{si} \rangle = \mathcal{F}_i \mathcal{G}_{si} \vec{q}_s \tag{3.15}$$

with $\mathcal{G}_{si}$ defined in (3.14) and

$$\vec{q}_s \simeq \frac{32}{5\pi} \delta_m \hat{E}_{m,u} D \left(u_w^5 \vec{v} - \frac{1}{7} \lambda_s u_w^7 \vec{\nabla} h \right) \tag{3.16}$$

Thus, for suspended load the flux of sediment decreases with an increasing diameter of the grain and the transport of all fractions is smaller than the transport in case of uniform sediment. The first effect is opposite to the hiding effect in bed load, while the second effect is not present in the model formulation for sorting in bed load.

3.3 Basic state, stability analysis and solution procedure

3.3.1 Basic state

We investigate the possible onset of bedforms as free morphodynamic instabilities on a planar morphology. The basic state is uniform in the alongshore direction, with a shore-parallel current $V(x)$. The corresponding bottom profile is sketched in Figure 3.1. The grain size distribution function F_i for the basic state can have an arbitrary structure in the cross-shore (x) direction without violating the equilibrium conditions. In this chapter we assume that F_i is independent of this coordinate. The basic state is characterised by

$$\begin{array}{llll} u = 0 & v = V(x) & z_b = -H(x) & z_s = s_0 y + z_{s0}(x) \\ r = r_0(x) & \mathcal{F}_i = F_i & \phi_m = \Phi_m & \sigma = \sigma_0 \end{array}$$

From the alongshore momentum balance (3.1) for the basic state it follows that

$$V(x) = \frac{\tau_{sy}/\rho - g s_0 H}{r_0}$$

The basic state velocity consists of a steady component, which is driven by a prescribed alongshore free surface pressure gradient $s_0 \sim 2 \times 10^{-7}$ and an alongshore wind stress $\tau_{sy} \sim -0.25$ Nm^{-2}, such that the characteristic basic state velocity is $U_0 = |V| \sim 0.4$ ms^{-1} at $x = 0$ in the negative y direction. This is a representative value of the storm-driven flow on the American Atlantic inner shelf (Niedoroda and Swift, 1981; Lentz et al., 1999). Note that the forcing by the density field is ignored, as its contribution has turned out to be negligible.

The characteristic magnitude of suspended load transport $Q_s = \frac{32}{5\pi} C_0 U_0$ is defined for uniform sediment of a grain size $d_m \sim 0.35 \times 10^{-3}$ m, with a representative value for the depth-integrated volume concentration of $C_0 = \delta_m \hat{E}_{mu} U_w^5 H_0 \sim 7.5 \times 10^{-4}$ m. For bed load transport the scale is $Q_b = \frac{3}{2} \nu_b U_w^2 U$ and the rate of bed over suspended load transport is $Q_b/Q_s \sim 0.016$.

3.3.2 Stability analysis

The stability of the basic state is considered by studying the evolution of small perturbations on this state. The linearised momentum and mass conservation equations are solved for a fixed bed level to find the perturbed velocity field as a function of the bottom topography. The flow variables are substituted in the bottom evolution equation to compute the changes in the bed.

Hydrodynamics

We consider solutions of the hydrodynamic equations (3.1) and (3.2) of the following form:

$$\begin{array}{rcrcl} \vec{v} & = & (0, V(x)) & + & (u'(x,y,t), v'(x,y,t)) \\ z_s & = & s_0 y + z_{s0}(x) & + & \eta'(x,y,t) \\ z_b & = & -H(x) & + & h(x,y,t) \\ r & = & r_0(x) & + & r'(x,y,t) \end{array}$$

The perturbations (indicated by primes) are assumed to be small with respect to their values in the basic state. The expressions for r_0 and r' are given in appendix 3.B. The linearised versions of the momentum equations (3.1) are

$$V\frac{\partial u'}{\partial y} - fv' = -g\frac{\partial \eta'}{\partial x} + \frac{\tau_{sx}}{\rho}\frac{h}{H^2} - r_0\frac{u'}{H} \tag{3.17}$$

$$u'\frac{\partial V}{\partial x} + V\frac{\partial v'}{\partial y} + fu' = -g\frac{\partial \eta'}{\partial y} + s_0\frac{h}{H} + r_0\frac{v'}{H} - r'\frac{V}{H} \tag{3.18}$$

and for mass conservation (3.2):

$$H\frac{\partial u'}{\partial x} + \frac{\partial H}{\partial x}u' + H\frac{\partial v'}{\partial y} - V\frac{\partial h}{\partial y} = 0 \tag{3.19}$$

Two-size mixture

As with perturbations in the hydrodynamics, small perturbations in the probability distribution function $\mathcal{F}_i$ are assumed, resulting in small perturbations in the mean grain size and standard deviation:

$$\mathcal{F}_i = F_i + f_i(x,y,t) \qquad \phi_m = \Phi_m + \phi'_m(x,y,t) \qquad \sigma = \sigma_0 + \sigma'(x,y,t)$$

In this chapter a two-size sand mixture is considered, with d_1 and d_2 the grain diameters of the fine and coarse size fraction, respectively ($\phi_1 \geq \phi_2$). A mean grain size of medium sand, characteristic of inner shelf sediment, is $d_m = 0.35$ mm or $\phi_m = 1.5$. The constraint on the distribution function yields:

$$F_1 + F_2 = 1 \qquad\qquad f_1 = -f_2 \tag{3.20}$$

The expressions for the mean grain size and the standard deviation (as defined in section 3.2.2) simplify to

$$\Phi_m = \phi_1 F_1 + \phi_2 F_2 \qquad\qquad \sigma_0^2 = F_1 F_2 (\phi_1 - \phi_2)^2$$

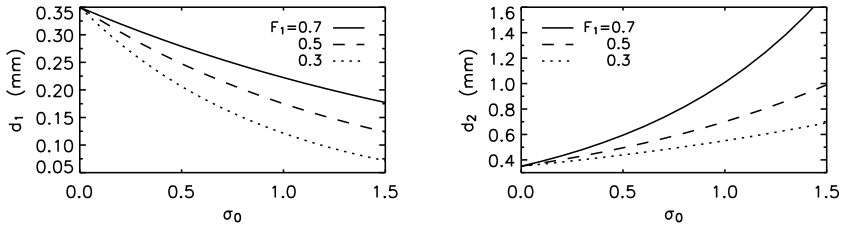

Figure 3.4: Dependence of the grain diameters d_1 (left) and d_2 (right) on the standard deviation of a two-size mixture with mean size $d_m = 0.35$ mm. The solid, dashed and dotted curves represent a larger weight percent of the grains in the finest grain size class ($F_1 = 0.7$), equal percentages of coarse and fine sand ($F_1 = 0.5$), and a larger weight percent of grains in the coarse size class ($F_1 = 0.3$).

From this we derive an expression for ϕ_1 and ϕ_2 in terms of the mean grain size and the standard deviation:

$$\phi_1 = \Phi_m + \sigma_0\sqrt{\frac{F_2}{F_1}} \qquad\qquad \phi_2 = \Phi_m - \sigma_0\sqrt{\frac{F_1}{F_2}} \tag{3.21}$$

For a fixed mean grain size, the values of the grain diameter of both size fractions as a function of the standard deviation are given in Figure 3.4, where $d_1 = 2^{-\phi_1}$ and $d_2 = 2^{-\phi_2}$. This is shown for different values of F_1.

Using the expressions given above, the perturbations in the mean grain size and standard deviation read

$$\phi'_m = \frac{\sigma_0}{\sqrt{F_2F_1}}f_1 \qquad\qquad \sigma' = \frac{\sigma_0(F_2 - F_1)}{2F_2F_1}f_1 \tag{3.22}$$

Sediment dynamics

The sediment flux consists of a bed load and a suspended load part: $\langle\vec{q}_{bi}\rangle = \mathcal{F}_i\mathcal{G}_{bi}\vec{q}_b$ and $\langle\vec{q}_{si}\rangle = \mathcal{F}_i\mathcal{G}_{si}\vec{q}_s$ (see expressions (3.9) and (3.15)). In particular,

$$\vec{q}_b = \vec{q}_{b0}(x) + \vec{q}'_b(x,y,t) \qquad \mathcal{G}_{bi} = G_{bi} + g_{bi}(x,y,t)$$
$$\vec{q}_s = \vec{q}_{s0}(x) + \vec{q}'_s(x,y,t) \qquad \mathcal{G}_{si} = G_{si} + g_{si}(x,y,t)$$

In the basic state only an alongshore transport component, which depends on the distance x to the shoreface, is present. Thus $\vec{\nabla}\cdot(F_iG_{bi}\vec{q}_{b0}) = \vec{\nabla}\cdot(F_iG_{si}\vec{q}_{s0}) = 0$. The transport capacity functions G_{bi}, G_{si} and the perturbations g_{bi}, g_{si} for bed load and suspended load are defined in appendix 3.C. Following the formulation for the roughness length k_s we use $L_a = d_m\,2^{\sigma}$ (see appendix 3.B); the thickness of the active layer in the basic state corresponds to $L_{a0} = 2^{\sigma_0 - \Phi_m}$. The linearised form of equation (3.6) is

$$(1-p)\left(F_i\frac{\partial h}{\partial t} + L_{a0}\frac{\partial f_i}{\partial t}\right) = -\vec{\nabla}\cdot\langle\vec{q}'_i\rangle \tag{3.23}$$

where

$$\langle \vec{q}_i' \rangle = F_i G_{bi} \vec{q}_b' + \vec{q}_{b0} \left(G_{bi} f_i + F_i g_{bi} \right) + F_i G_{si} \vec{q}_s' + \vec{q}_{s0} \left(G_{si} f_i + F_i g_{si} \right)$$

Summation of (3.23) over all size fractions, combined with the constraint on the distribution function, leads to an equation which relates the bed evolution to the sum of the sediment flux over all sizes. Back-substitution of this result into equation (3.23) yields the evolution of the probability function f_i. For two-size fractions $(i = 1, 2)$ the final equations read

$$(1-p)\frac{\partial h}{\partial t} = -[\vec{\nabla} \cdot \langle \vec{q}_1' \rangle + \vec{\nabla} \cdot \langle \vec{q}_2' \rangle] \tag{3.24}$$

$$(1-p) L_{a0} \frac{\partial f_1}{\partial t} = F_1 \vec{\nabla} \cdot \langle \vec{q}_2' \rangle - F_2 \vec{\nabla} \cdot \langle \vec{q}_1' \rangle \tag{3.25}$$

where

$$\begin{aligned}
\vec{\nabla} \cdot \langle \vec{q}_1' \rangle =& G_{b1} \left\{ F_1 \vec{\nabla} \cdot \vec{q}_b' + q_{b0} \left(F_1 T_{b5} + 1 \right) \frac{\partial f_1}{\partial y} \right\} \\
&+ G_{s1} \left\{ F_1 \vec{\nabla} \cdot \vec{q}_s' + q_{s0} \left(F_1 T_{s5} + 1 \right) \frac{\partial f_1}{\partial y} \right\} \\
\vec{\nabla} \cdot \langle \vec{q}_2' \rangle =& G_{b2} \left\{ F_2 \vec{\nabla} \cdot \vec{q}_b' + q_{b0} \left(F_2 T_{b5} - 1 \right) \frac{\partial f_1}{\partial y} \right\} \\
&+ G_{s2} \left\{ F_2 \vec{\nabla} \cdot \vec{q}_s' + q_{s0} \left(F_2 T_{s5} - 1 \right) \frac{\partial f_1}{\partial y} \right\}
\end{aligned}$$

The quantity f_2 is eliminated by using equation (3.20) and for a two-size mixture g_{b1}, g_{s1}, g_{b2} and g_{s2} are expressed in perturbations of the probability function f_1 (appendix 3.C). Also the expressions for q_{b0}, q_{s0}, $\vec{\nabla} \cdot \vec{q}_b'$ and $\vec{\nabla} \cdot \vec{q}_s'$ are given in this appendix. Equations (3.24), (3.25) and (3.20) give the set of equations to be solved for h and f_1. Together with (3.17), (3.18) and (3.19), they form a closed system.

Boundary conditions are that $u' = 0$ and $h = 0$ at the transition from the shoreface to the inner shelf ($x = 0$) and for $x \to \infty$. Furthermore, periodicity in the alongshore direction is assumed.

3.3.3 Solution procedure

The solutions for the bottom perturbations are topographic waves which propagate along the shelf and have a certain cross-shelf structure. They are of the form $h(x, y, t) = Re\left\{\hat{h}(x)\, \mathrm{e}^{iky + \Omega t}\right\}$: a similar expression holds for f_1. Here k is the alongshore wavenumber and Ω the complex frequency. The stability analysis yields, for each wavenumber k, solutions for Ω; its real part Ω_r being the growth rate, with Ω_r^{-1} the e-folding timescale. Furthermore, the imaginary part Ω_{Im} is the frequency. The migration velocity of the perturbation is obtained from $c = -\Omega_{Im}/k$. For a fixed value of the alongshore wavenumber k the different values of Ω correspond to different cross-shore modes.

Of specific interest are growing perturbations, which have $\Omega_r > 0$. The perturbation which has the maximum possible growth rate is called the preferred mode. The perturbed

velocity u' is expressed in the bottom perturbation h, by eliminating the free surface η' from the momentum equations and using mass conservation to express v' in u'. In this study the bottom friction is related to the grain size, thus a part of u' is related to f_1. Solving the equation for u' and substituting this in equations (3.24) and (3.25) results in an eigenvalue problem, which determines the cross-shore structure of h and f_1.

Equation (3.25) can be simplified, because the term on the left-hand side is a factor $L_{a0}/H_0 \ll 1$ smaller than the contributions on the right-hand side and can therefore be excluded. This factor was derived from equation (3.24), which defines the scale for the divergence of the sediment fluxes. The result is a decoupled set of equations for the bottom and the fraction of fine grains. Consequently, the eigenvalue problem for h and f_1 is reduced to a single eigenvalue problem for h and f_1 is an algebraic function of h. Therefore, the fraction of fine and coarse grains adapt instantaneously to changes in the bottom. Solutions of these equations were obtained by numerical (spectral) methods, for details see Falqués et al. (1996) and references therein.

3.4 Results

In this section the influence of the non-uniformity of the sediment on growth rates, migration velocities and wavelengths of the resulting bedforms is investigated. Furthermore, the resulting spatial variations in mean grain size and bottom topography are presented. Different experiments were performed, with particular emphasis on the sensitivity of the model results to the formulation of the hiding functions and the properties of the sediment. First, the influence of variation in sediment sizes was studied by varying the standard deviation of the distribution. Next, the sensitivity of the results to the hiding coefficients for bed and suspended load was investigated.

3.4.1 Parameter values

Values for the characteristic length and velocity scales were given in sections 3.2.1 and 3.3.1, respectively. An overview of the parameter values used for the different experiments is presented in Table 3.1; they are representative of conditions on Long Island inner shelf and are partly extracted from Figueiredo et al. (1982) and Schwab et al. (2000). For a list of frequently used variables see appendix 3.D. Note that the sediment has the same mean grain diameter in all experiments, while the diameters of the fine and coarse grains were allowed to vary. The results for $\sigma_0 = 0$ that are presented in the next section differ from the results for uniform sediment presented in chapter 2. This is due to different parameter values, or example for L_s and U_{tide}, that were used to represent the shelf of the Atlantic coast of America and the Belgian-Dutch shelf, respectively.

3.4.2 Standard deviation

The influence of the standard deviation of the mixture on the characteristics of the ridges was investigated. For a fixed mean grain size the standard deviation of the sediment was varied over a range, such that d_1 and d_2 are in the fine to coarse sand range. In this section the

	uniform Fig. 3.5	bimodal Fig. 3.5, 3.7(t)	bimodal Fig. 3.5, 3.7(b)	bimodal Fig. 3.6	bimodal Fig. 3.8
σ_0	0	0.2	1.0	0.5	0.5
F_1	1	0.5	0.5	0.5	0.7
F_2	0	0.5	0.5	0.5	0.3
Φ_m	1.5	1.5	1.5	1.5	1.5
ϕ_1	1.5	1.7	2.5	2.0	1.8
ϕ_2	1.5	1.3	0.5	1.0	0.7
d_1(mm)	0.35	0.31	0.18	0.25	0.28
d_2(mm)	0.35	0.41	0.71	0.50	0.60

Table 3.1: Parameter values for uniform and bimodal sediment.

default values of $c_b = 0.75$ and $c_s = -1.1$ are used. Figure 3.5 shows the changes in the growth rate and migration velocity of the dominant cross-shore mode (first cross-shore mode) for each wavenumber and for different values of the standard deviation. The change in the grain diameters of the fine and the coarse sediment fraction with σ_0 is shown in Figure 3.4 for $F_1 = 0.5$. Values are scaled by those of the preferred mode in the case of uniform sediment ($\sigma_0 = 0$). The maximum growth rate for uniform sediment is $\Omega_{ru} \sim 8.6 \times 10^{-3}$ yr^{-1}, attained for wavenumber $k_u \sim 1.9$ km^{-1} and the corresponding migration speed is $c_u \sim -0.9$ m yr^{-1}. The alongshore spacing between successive crests is $\lambda = 2\pi\, k_u^{-1} \sim 3.2$ km, and the timescale for the growth is $\Omega_{ru}^{-1} \sim 117$ yr. In the computations of the timescale it was assumed that storms prevail during a time fraction $\mu \sim 0.05$, whereas no growth of perturbations occurs during the remaining time fraction. Here we use the formulation for the entrainment of suspended sediment by Garcia and Parker (1991). In the case of $\sigma_0 = 0$, the growth rate and migration curves are similar to those obtained with the Van Rijn (1993) formulation, as was used by Calvete et al. (2001b).

A clear stabilising effect on growth rates of the bimodal mixture, as compared to uniform sediment, is found if the standard deviation is increased (Figure 3.5). This goes along with a (small) decrease of the wavenumber, i.e. increase in wavelength, of the bedforms. The migration velocities are enhanced. The maximum growth rate is reduced by $\sim 50\%$ for a bimodal sediment mixture with a standard deviation of $\sigma_0 = 0.5$. Migration velocities for this case increase to -1.2 m yr^{-1}. The preferred mode in this case has a wavelength $\lambda \sim 3.4$ km, and its spatial pattern is shown in Figure 3.6. The elevation of the bottom is indicated by the dark and light colours. The contour lines are those of the fraction of fine grains (with diameter d_1). More fine sediment ($f_1 > 0$) results in an increase in the mean grain size in phi-units ($\phi'_m \propto f_1$). The results indicate that f_1 is positive on the downcurrent (seaward) flank of the ridges, hence the mean grain size becomes finer in this area and coarser on the upcurrent (landward) flank. The spatial pattern of the perturbed bottom topography and of the perturbed mean grain size are approximately 90° out of phase. Note that the basic state velocity is directed from the top to the bottom of this figure ($V < 0$), so that the ridges are characterised by an upcurrent rotation.

The locations of the maxima and minima in the mean grain size depend on the value of the standard deviation σ_0 (or sorting index). Figure 3.7 shows a shore-normal cross-section

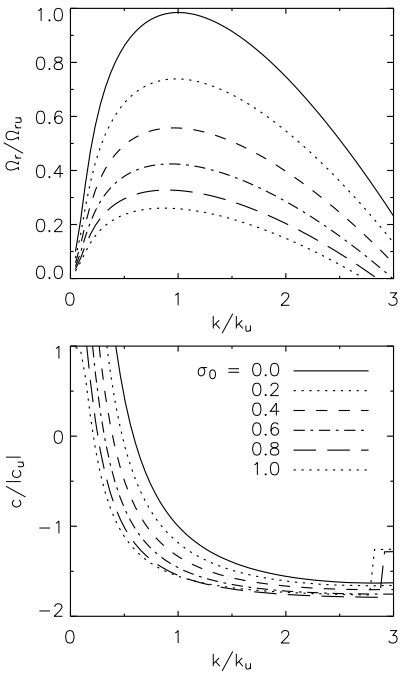

Figure 3.5: Growth rates (top) and migration velocities (bottom) of the dominant cross-shore mode as a function of the wavenumber k (scaled by the values for the preferred mode for uniform sediment) for different values of σ_0. The parameters used for the bimodal mixtures are: $F_1 = 0.5$, $c_b = 0.75$ and $c_s = -1.1$.

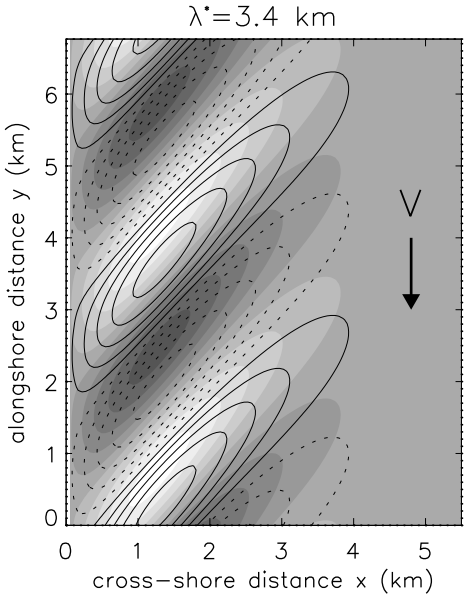

Figure 3.6: Bottom perturbations (greyscale; light: bars, dark: troughs) and perturbations in the fraction of fine grains (lines; solid: $f_1 > 0$, dotted: $f_1 < 0$) for $\sigma_0 = 0.5$, $F_1 = 0.5$, $c_b = 0.75$ and $c_s = -1.1$. The arrow indicates the direction of the basic state velocity.

of the bottom topography and fraction of fine grains for two different sorting indices. A decrease in the phase difference between the two patterns is found for larger values of the standard deviation. An interpretation of these results will be given in section 3.5.

Experiments were conducted to investigate the sensitivity of the model results to different values of the parameter F_1. It was found that, if the fraction of fine grains in the basic state $F_1 > 0.5$, the influence of the standard deviation on the bedform characteristics (wavelength, growth rate and migration speed) becomes stronger. On the contrary, if $F_1 < 0.5$ (more coarse grains than fine grains), these dependencies become weaker. Changing the value of F_1 does not affect the bottom pattern or the distribution of the mean grain size of Figure 3.6, but a different sorting pattern is obtained. In the case of $F_1 = 0.5$ it follows that $\sigma' = 0$ according to equation (3.22), hence no changes in the standard deviation occurred. In Figure 3.8 it is shown that for $F_1 = 0.7$ the sediment located on the seaward flank is finer ($\phi'_m > 0$) and better sorted ($\sigma' < 0$) than sediment on the landward flank, which is coarser and more poorly sorted ($\sigma' > 0$).

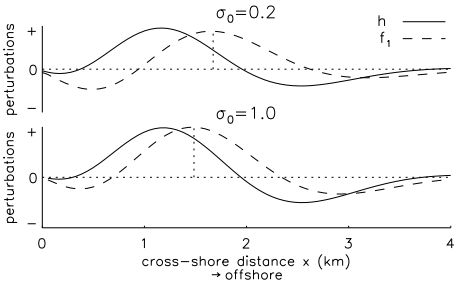

Figure 3.7: Cross-sections through a ridge, normal to the shore, of perturbations in bottom, h, and in the fraction of fine grains, f_1 (or similar in mean grain size, ϕ'_m). Quantities are scaled by their maximum values and shown for $F_1 = 0.5$ and a small standard deviation of the mixture (top: $\sigma_0 = 0.2$), as well as for a large value (bottom: $\sigma_0 = 1.0$). Furthermore, $c_b = 0.75$ and $c_s = -1.1$.

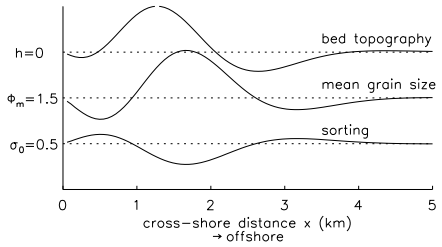

Figure 3.8: Cross-sections through a ridge, normal to the shore, of bed topography h, perturbations ϕ'_m in the mean grain size and perturbed sorting index (standard deviation) σ'. Results are shown for $F_1 = 0.7$, $\sigma_0 = 0.5$, $c_b = 0.75$ and $c_s = -1.1$.

3.4.3 Hiding functions: bed load

The characteristics of both the preferred bottom mode and the grain size distribution also depend on the coefficient c_b in the hiding function of the bed load transport, defined in eq. (3.9). Therefore, experiments were conducted in which c_b was varied. Physically this means that the hiding effects in the bed load transport were reduced or enhanced. The coefficient for the hiding in suspended load was kept constant at its default value $c_s = -1.1$.

In Figure 3.9 the characteristics of the preferred mode are shown as a function of the standard deviation for different values of c_b. The maximum growth rate $\Omega_{r\,\max}$, migration velocity $c_{\max}$ and preferred wavenumber $k_{\max}$ in the bimodal sediment case are scaled by their corresponding values for uniform sediment (being k_u, Ω_{ru} and $|c_u|$). The curves show, for all cases, a reduction in the wavenumber and growth rates, and an enhancement in migration rate if σ_0 is increased. A value of $c_b = 0$ implies that there is no hiding, $c_b = 1.5$ corresponds to a value of $m_b = 1$ in the hiding function (see Figure 3.3). The new information deducted from this figure is that the inclusion of a hiding function in the bed load transport formulation has little effect on the growth of the shoreface-connected ridges, but increasing hiding effects cause larger migration speeds. An interpretation of the results will be given in section 3.5.

In Figure 3.10 two cross-sections show the change in the distribution of the fraction of fine sediment for no hiding and strong hiding in the bed load flux. In the former case the selective suspended load transport results in an almost $90°$ out-of-phase relation between topography and mean grain size. An increase in the strength of the hiding in bed load ($c_b > 0$) reduces this phase shift, see Figure 3.10 (bottom).

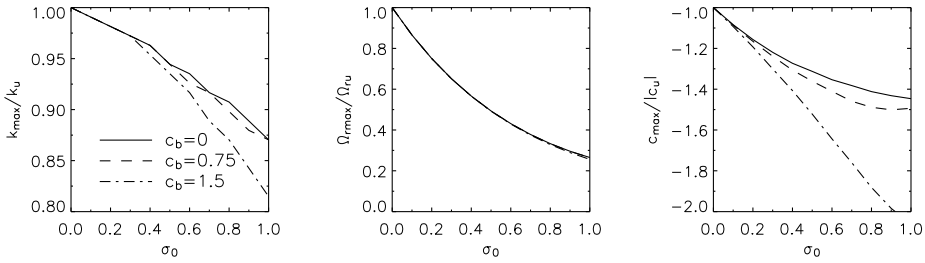

Figure 3.9: Wavenumber $k_{\max}$ of the preferred mode (scaled by its value k_u for uniform sediment), growth rates and corresponding migration velocities as a function of the standard deviation of the mixture σ_0. Results are shown for different formulations of the hiding function in the transport of bed load, with $c_s = -1.1$ and $F_1 = 0.5$.

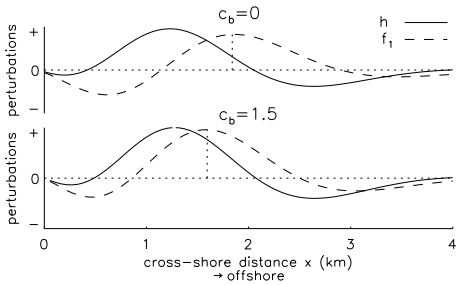

Figure 3.10: As in Figure 3.7, but for $\sigma_0 = 0.5$, $F_1 = 0.5$, $c_s = -1.1$ and $c_b = 0$ (top), $c_b = 1.5$ (bottom).

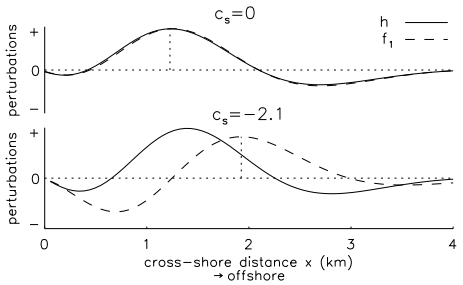

Figure 3.11: As in Figure 3.7, but for $\sigma_0 = 0.5$, $F_1 = 0.5$, $c_b = 0.75$ and $c_s = 0$ (top), $c_s = -2.1$ (bottom).

3.4.4 Hiding functions: suspended load

The same experiments were done to investigate the dependence of model results on the hiding coefficient c_s and the straining coefficient λ_{E} in the transport capacity function of suspended load transport (defined in eq. (3.14)). Only one of these parameters, c_s, can result in differences between the depth-integrated concentrations of the size classes in a sediment mixture, thereby introducing a mechanism for selective transport of suspended load.

The value of exponent c_s is mainly determined by two factors. The first is the dependence of the entrainment and the relative thickness of the suspended load layer on the grain size (including settling velocity and particle Reynolds number). The second factor is the strength of the hiding for the entrainment of sediment in suspension, indicated by the coefficient m_E in the hiding function ζ_i (equation (3.13)). We only investigated the influence of the second contribution and assumed $e_w = 1.1$ (section 3.2.4), i.e. $c_s = 5m_E - 2.1$. Without hiding effects in the entrainment ($m_E = 0$), the depth-integrated concentration of fine sediment is larger than that of coarse material. The inclusion of hiding effects (default: $m_E = 0.2$)

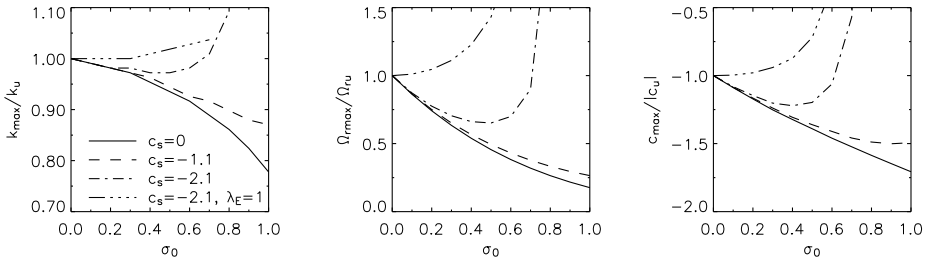

Figure 3.12: As in Figure 3.9, but now for different formulations for the hiding coefficient c_s in the suspended load transport and $c_b = 0.75$.

reduces the entrainment of fine sediment from the bed. Nevertheless, it still results in a depth-integrated concentration of fine material that is larger than that of coarse material. In the special case of $m_E = 0.42$ it follows that $c_s = 0$, hence, $\mathcal{G}_{si}$ is independent of the grain size. The higher concentration of fine sediment, as a consequence of their smaller settling velocities, is counterbalanced by a reduced entrainment flux of fine grains from the bed due to hiding effects. These three situations are shown in Figure 3.12 as $c_s = -2.1, -1.1$ and 0, including the straining factor and a constant value of $c_b = 0.75$. With higher standard deviations, a decrease in wavenumber and growth rates and an increase in migration rates is found. The growth rates are most strongly influenced.

The straining parameter λ_{E} in eq. (3.14) reduces the suspended load flux of both size classes in the sediment mixture, whereas the reduction becomes more important for larger values of σ_0. To demonstrate the importance of this parameter, results are also shown without straining ($\lambda_{\mathrm{E}} = 1$) and no hiding in the entrainment ($c_s = -2.1$). Figure 3.12 indeed reveals a change in the results: instead of a decrease in the maximum growth rate, an increase with σ_0 is found and the migration speed is decreased. This will be discussed in more detail in section 3.5.

The bedform and the mean grain size patterns are in phase if no grain size dependence is used in the suspended load transport ($c_s = 0$), with the finer sediment on the crests for $c_b > 0$ (see Figure 3.11, top). A phase shift between the mean grain size and the bed topography pattern is induced by the suspended load flux. In fact, the sediment is finer on the seaward (downcurrent) flank of the ridges for $c_s < 0$. These phase shifts do not change if the straining parameter is excluded.

Model tests indicated that the grain size patterns over shoreface-connected ridges are not affected by the grain size related bottom friction (see (3.3) and the expression for k_s in appendix 3.B) that was introduced in the hydrodynamic equations. Moreover, it turns out the related vorticity effects do not influence the instability mechanism, which is controlled by continuity effects.

3.5 Physical interpretation

The results presented in the previous section can be explained in physical terms. The concepts discussed here are based on mechanisms for the formation of shoreface-connected ridges under the assumption of uniform sediment, as presented earlier by Trowbridge (1995) and by Calvete et al. (2001b). They have demonstrated that the transverse slope of the bottom plays an essential role in the formation of the ridges. An offshore deflection of the current, i.e. $u' > 0$, results in a convergence of the sediment flux and the growth of upcurrent-oriented ridges. This behaviour is due to mass conservation of both water and sediment, as was demonstrated in Figure 1.7 in chapter 1. The presence of a ridge causes an enhanced convergence in both the water and sediment flux (with respect to that induced by the offshore movement of water and sand) on the downstream side of the ridge. Likewise, the divergence reduces on the upstream flank of the ridge. The result is that sediment is eroded (deposited) on the upstream (downstream) flank of the ridges. Therefore, downcurrent migration of the ridges takes place. It appears that the growth of the shoreface-connected ridges is mainly determined by the suspended sediment flux, while bed load transport determines the downcurrent migration of the bedforms.

In the case of a bimodal sediment mixture growth rates become smaller, migration rates speed up, the preferred length scale becomes longer, and sorting of sediment is observed. To understand these new features, we examined the effects of dynamic hiding in both bed load and suspended load in the bottom evolution equations (3.24) and (3.25).

3.5.1 Hiding in bed load

For the exponents in the transport capacity functions for bed load and suspended load we consider: $c_b > 0$ and $c_s = 0$, respectively. These assumptions allow for an interpretation of the results shown in Figure 3.12 and 3.11 ($c_s = 0$). The transport of suspended load is independent of the grain size, therefore only the effect of the straining parameter for suspended load and hiding in bed load are included. As a result, the equations for the evolution of the bottom and the fraction of fine sediment reduce to:

$$(1-p)\frac{\partial h}{\partial t} = -T_{b2}\vec{\nabla}\cdot\vec{q}_b' - \Lambda_{\mathrm{E}}^5\vec{\nabla}\cdot\vec{q}_s' - [T_{b1}+T_{b2}T_{b5}]\,q_{b0}\,\frac{\partial f_1}{\partial y} \tag{3.26}$$

$$0 = -T_{b3}\vec{\nabla}\cdot\vec{q}_b' - \Lambda_{\mathrm{E}}^5 q_{s0}\frac{\partial f_1}{\partial y} \tag{3.27}$$

where

$$T_{b1} = G_{b1} - G_{b2} \qquad T_{b2} = F_1G_{b1} + F_2G_{b2}$$
$$T_{b3} = F_1F_2(G_{b1} - G_{b2}) \qquad T_{b4} = F_2G_{b1} + F_1G_{b2}$$

The expressions for T_{b5} and Λ_{E} are given in appendix 3.C. The left-hand side of equation (3.27) has been set to zero, following the arguments presented in section 3.3.3. Furthermore, since $|q_{s0}| \gg |q_{b0}|$ (suspended load dominates over bed load transport), the terms proportional to q_{b0} are omitted in equation (3.27).

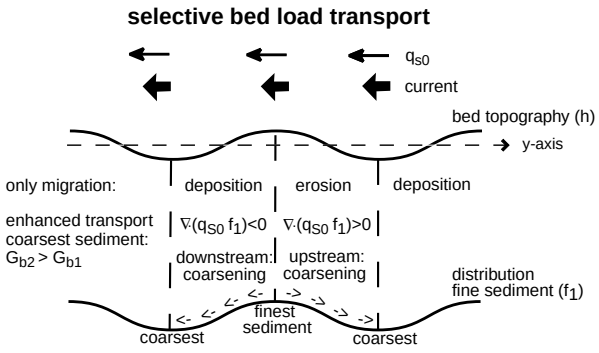

Figure 3.13: Schematic view of the selective bed load transport mechanism. The downcurrent migration induced by the bed load flux results in an erosion/deposition pattern, which is shifted with respect to the bed topography. Equation (3.27) requires the convergence rate of the bed load flux to be proportional to a change in the alongshore (i.e. downstream) fining of the sediment. In a deposition area ($\vec{\nabla}\cdot\vec{q}_b' < 0$), therefore $q_{s0}\,\partial f_1/\partial y < 0$ for the situation where transport of coarse material is favoured with respect to that of fine grains. The latter represents the selective bed load transport that results in $G_{b2} > G_{b1}$. When moving from the crest to the adjacent troughs a coarsening of the sediment is found.

To understand the alongshore variation in the mean grain size we consider the expression for $\vec{\nabla}\cdot\vec{q}_b'$, as given in appendix 3.C, and neglect bedslope effects. After substitution of expression (3.4) for the wave-orbital velocity it reads

$$\vec{\nabla}\cdot\vec{q}_b' \propto u_w^2\left[-(m+1)\frac{1}{H}\frac{\partial H}{\partial x}u' + \frac{V}{H}\frac{\partial h}{\partial y}\right]$$

This expression is simplified by applying scaling arguments, where the parameter values are $V \sim -0.4$ ms^{-1}, $H \sim 14$ m, $\partial H/\partial x \sim 1\times10^{-3}$ and $m \sim 1.6$. Assuming an irrotational flow an using the linearised mass-balance the first term is estimated to be a factor 100 smaller than the second term and is neglected. Since $q_{s0} \propto u_w^5 HV$ (appendix 3.C), this yields for equation (3.27):

$$\frac{\partial f_1}{\partial y} \propto -(G_{b1}-G_{b2})\frac{\partial h}{\partial y}$$

This result shows that the fraction of fine sand is either in phase or 180° out of phase with the topography. For bed load the transport capacity function is given by $G_{bi} = (d_i/d_m)^{c_b}$. If $c_b > 0$ it follows that $G_{b1} < 1 < G_{b2}$, leading to a reduced transport of fine sediment relative to the transport of coarse sediment. The relation between the bottom topography and the fraction of fine grains is therefore given by $f_1 \propto h$ for this situation. A schematic view of this selective transport mechanism is shown in Figure 3.13. The mean grain size is finest on the crests of the ridges, and explains the pattern shown in Figure 3.11 ($c_s = 0$).

The enhanced migration rates and reduced growth rates for a sediment bed composed of a bimodal mixture (Figure 3.12, $c_s = 0$) are understood from equation (3.26). The suspended

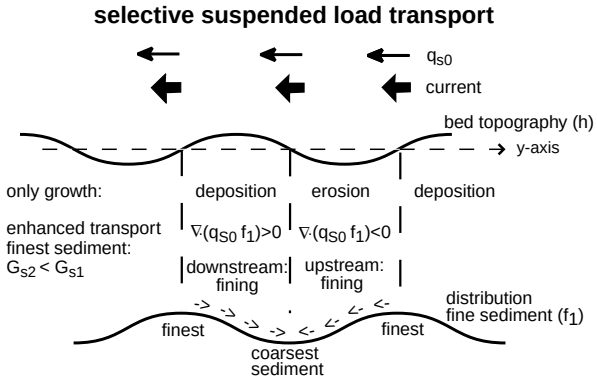

Figure 3.14: Schematic view of the selective suspended load transport mechanism. Suspended load mainly causes the growth of the ridges (erosion/deposition pattern almost in phase with the bottom topography). The deposition of suspended sediment is related to the gradient in the distribution of fine grains (eq. (3.29)). In a deposition area ($\vec{\nabla}\cdot\vec{q}_s' < 0$), therefore $q_{s0}\,\partial f_1/\partial y > 0$ for a situation where transport of fine material is favoured with respect to that of coarse sand. The latter represents the selective suspended load transport that results in $G_{s2} < G_{s1}$. The result is a downstream fining in the deposition area; the finest material is located approximately $\frac{1}{4}$ wavelength downstream of the crest.

load flux is only modified by the straining factor, when compared to uniform sediment. This factor is smaller than unity and determines the reduction of the growth rates by $\Lambda_{\mathrm{E}}^5 \sim 0.2$ for $\sigma_0 = 1$ (Figure 3.12, middle). The bed load flux is a factor T_{b2} different from the uniform sediment case. As $T_{b2} \geq 1$ for bed load transport, hiding effects cause a faster migration compared to uniform sediment, while it hardly changes the growth. The last term (redistribution of sediment) in eq. (3.26) could also change the migration, because f_1 is related to h. However, experiments indicated that this contribution is only of minor importance to the downcurrent migration.

3.5.2 Hiding in suspended load

For the investigation of hiding (and straining) in suspended load we set $c_b = 0$ and $c_s < 0$. This enables an interpretation of the results shown in Figures 3.9 and 3.10 ($c_b = 0$). The equations for the evolution of the bottom and the fraction of fine sediment reduce to

$$(1-p)\frac{\partial h}{\partial t} = -\vec{\nabla}\cdot\vec{q}_b' - T_{s2}\vec{\nabla}\cdot\vec{q}_s' - \left[T_{s1} + T_{s2}T_{s5}\right] q_{s0}\frac{\partial f_1}{\partial y} \tag{3.28}$$

$$0 = -T_{s3}\vec{\nabla}\cdot\vec{q}_s' - \left[T_{s4} + T_{s3}T_{s5}\right] q_{s0}\frac{\partial f_1}{\partial y} \tag{3.29}$$

where

$$T_{s1} = G_{s1} - G_{s2} \qquad T_{s2} = F_1 G_{s1} + F_2 G_{s2}$$
$$T_{s3} = F_1 F_2 (G_{s1} - G_{s2}) \qquad T_{s4} = F_2 G_{s1} + F_1 G_{s2}$$

Equation (3.29) relates alongshore changes in the fining of the bottom material to the convergence of the suspended load flux, and bed load contributions are neglected. In the second term on the right-hand side, $[T_{s4} + T_{s5}T_{s3}]$ is positive for realistic values of the parameters. In Figure 3.14 the mechanism for selective suspended load transport is sketched.

Substitution of the expression for $\vec{q}_s'$ (appendix 3.C) in equation (3.29) yields

$$-V\frac{\partial f_1}{\partial y} \propto (G_{s1} - G_{s2})\frac{\partial u_w}{\partial x}u'$$

In this expression $\partial u_w/\partial x < 0$ (waves induce less stirring of sediment in larger depth) and $V < 0$. The momentum equations are used to relate u' to h. Trowbridge (1995) already showed that the perturbations in the cross-shore velocity are in phase with the bottom perturbations ($u' > 0$ if $h > 0$). Hence, if the transport in suspension is more pronounced for the finer grains ($G_{s1} > G_{s2}$), this leads to $\partial f_1/\partial y \propto -u' \propto -h$. Consequently, the pattern of the mean grain size for suspended load is approximately 90° out of phase with the topography, such that the finer sediment is found on the downcurrent flank of the ridges. This effect is clearly seen in Figure 3.10 (top) for $c_b = 0$ and $c_s = -1.1$.

The reduced growth rates for graded sediment compared to uniform sediment can be understood from equation (3.28). Growth is mainly determined by the second term on the right-hand side, where the part related to the grain size is a factor T_{s2} different from that found in the case of uniform sediment. For selective suspended load transport, with hiding coefficient $c_s = -1.1$, the factor $T_{s2} < 1$. The presence of a straining parameter in the transport capacity function for suspended load (equation (3.14)) causes the total transport of the two grain sizes in a mixture to be less than the transport of sediment of a uniform grain size. A stabilising effect is found with an increasing standard deviation of the mixture (see Figure 3.9, $c_b = 0$), whereas the contribution of c_s to the transport capacity function has the opposite effect. Thus, a stronger hiding in suspended load (larger values of c_s) counteracts the stabilising effect of the straining. This explains why growth rates increase with increasing values of $|c_s|$ for a fixed value of σ_0 (see Figure 3.12).

The bed load contribution to the migration (downstream) is the same as for uniform sediment, but the contribution of suspended load (causing upstream migration) decreases with increasing values of σ_0, resulting in a net enhancement of the migration in the downstream direction. An additional contribution to the bottom evolution is given by the last term in eq. (3.28), which turns out to be very small.

If selective transport in both suspended and bed load is included, the pattern of the mean grain size resembles that found in the case of only hiding in suspended load. This is because the suspended load flux dominates over the bed load flux. The hiding function of the bed load flux slightly modifies the 90° phase difference (induced by suspended load) between the mean grain size and bed topography. This tendency is visible in Figure 3.10.

The standard deviation σ_0 of the mixture also influences the phase difference between the mean grain size and bottom topography. Because of the straining parameter λ_{E} in the selective suspended load flux, the latter decreases with increasing σ_0. The bed load flux is not changed by the straining parameter. This implies that the relative importance of the suspended load transport, with respect to bed load transport, decreases with increasing σ_0. Hence, the phase shift becomes smaller with increasing standard deviations, which explains the results shown in Figure 3.7.

3.6 Discussion

The model results are consistent with the field data, as discussed in section 3.1, see also chapter 1 of this thesis. The data reveal the mean grain size pattern is approximately 90° out of phase with topography, with the coarsest sand on the landward flank (upcurrent), and the finest sand on the seaward (downcurrent) flank. An exception to this very consistent pattern in the mean grain size, as observed on different shelves, concerns the shoreface-connected ridges along the Central Dutch coast (southern North Sea) (Van de Meene et al., 1996). No marked spatial variation in the mean grain size across the ridge topography is found, except for a weak tendency towards a better sorting (smaller standard deviations) at the crests of the ridges. A potentially important difference between the American Atlantic shelf and the Dutch shelf is the strength of the tidal current. Model experiments with both bimodal mixtures (this chapter) and uniform sediment (chapter 2) showed that adding tidal currents does not change the results. This suggests that tidal currents are not the cause of the difference in the observed patterns for the Dutch coast (strong tides) and North America (weak tides).

Besides the mean grain size, another aspect of the model results to be compared with the field data is the variation in the standard deviation over the ridges. For the American shelf the most pronounced differences in sorting characteristics are seen between sediment in the crest and trough. In general, the values of standard deviation of the sediment are higher in the troughs than on the crests of the ridges (Swift et al., 1972, 1978; Schwab et al., 2000). This is consistent with the sorting pattern found over the ridges along the central Dutch coast, in contrast to the lack of a variation in the mean grain size pattern. Data gathered from the German Bight (Antia, 1993) show that the surficial sediment found on the seaward flank are best sorted (small σ) and poorest in the troughs and on the landward flank. In the model the variation in the sorting index is determined by relation (3.22). Clearly, variations in sorting across the ridges in a two-size mixture are only present in the model if the fractions of fine and coarse grains in the basic state are not equal. Choosing $F_1 > F_2$ (weight percentage of fine sediment is larger than that of coarse sediment) yields that in areas where positive perturbations in the mean grain size are present the material is better sorted. Combined with the effect of hiding in suspended and bed load (finer seaward flank), this case provides a good representation of the data.

The results should be interpreted with care: the formulation for the selective transport of suspended and bed load are based on expressions which are found as a best fit with many different data sets (Zyserman and Fredsøe, 1994; Admiraal et al., 2000). These data are mostly based on measurements in shallow rivers and flume experiments and we assumed them to be also applicable to shallow coastal seas. However, in the sensitivity experiments it was shown that the trend for the changes in growth rate and the migration velocity is the same for a large range of values of the sediment parameters, such as for the exponents in the hiding functions and the composition of the sediment mixture.

3.7 Conclusions

In this chapter a model was developed and analysed to study the initial formation of shoreface-connected ridges and the corresponding grain size distribution on storm-dominated

shelves. The model consists of the depth-averaged shallow water equations, a sediment transport formulation and a mass balance of sediment. The sediment is represented by two grain size classes. Both bed load and suspended load sediment fluxes are considered, as are dynamic hiding effects. The basic state represents a storm-driven flow on an inner shelf with a transversely sloping bottom. The results of the model presented here indicate that, in the case of a sediment mixture, there is a positive feedback between storm-driven currents and the eroding bottom. This confirms and generalises earlier findings by Trowbridge (1995) and Calvete et al. (2001b) for a single grain size fraction.

The first objective of this research was to investigate the influence of sediment sorting on the temporal and spatial characteristics of shoreface-connected ridges. The stabilising effect of sediment sorting on the growth of bedforms, as found earlier in many laboratory experiments and other model studies, is also observed within the present model. Based on the experiments that were carried out, we conclude that the behaviour of growth rates is determined by the formulation for the hiding in suspended load. A reduced growth turns out to be mainly because of the presence of a straining parameter in the hiding function of suspended load. This accounts for the reduced mobility of grains in suspension with increasing standard deviations of the sediment mixture. If the straining parameter is excluded in the suspended load formulation the growth rate is increased with respect to that of uniform sediment. The migration of the shoreface-connected ridges is in the downcurrent direction and enhanced by the bimodal character of the sediment. Despite a suspended load flux which is much larger than the bed load flux, the migration is controlled by the bed load flux and its hiding coefficient c_b. Wavelengths of the bedforms are only slightly affected. A spatial phase shift of approximately 90° is found between the topography and mean grain size for shoreface-connected ridges: the coarsest material occurs on the landward (upcurrent) flank. Selective transport of sediment in suspension causes this phase shift.

The second objective of this study was to gain knowledge into the physical mechanism responsible for the observed grain size distribution over shoreface-connected ridges. Combining the observations with the model results and their subsequent analysis, leads to several conclusions with respect to the physical mechanisms which could be responsible for the observed sedimentary patterns. First of all, the persistent finer downcurrent flank of the ridges and the coarser sediment on the upcurrent flank appears to be in reasonable agreement with observed grain size distributions over shoreface-connected ridges. The model results support the assumption that the transport of sediment as suspended load cannot be neglected and that the corresponding flux of fine material is larger than of coarse material. The relative importance of the bed load flux can shift the pattern of the mean grain size more in-phase or out-of-phase with the topography. The model reproduces observed sorting patterns over the ridges (well/poorly sorted sediment on the seaward/landward side of the ridges) if the overall weight percentage of fine grains is larger than that of coarse grains. Another quantity that influences the phase shift is the standard deviation of the sediment: if it increases it causes a reduction in the importance of suspended load over bed load. Finally, the model results indicate that tidal currents and a grain size dependent formulation for the bottom friction coefficient do not change the sediment patterns for shoreface-connected ridges. In chapter 5 this study is extended into the nonlinear regime.

Appendix

3.A Suspended load concentration

The suspended load flux requires knowledge of the depth-integrated volumetric concentration of sediment. The latter is governed by

$$\frac{\partial C_i}{\partial t} + \vec{\nabla} \cdot (\vec{v}_t C_i) = w_{si}(\mathcal{F}_i E_i - c_{bi}) \tag{3.A-1}$$

The first term on the right-hand side is the flux of sediment into suspension, the second term is the deposition flux. Here w_{si} is the settling velocity of grains of size d_i, E_i is the dimensionless entrainment of these grains, and c_{bi} is the actual volume concentration near the bed. The entrainment of a size fraction is multiplied by the probability $\mathcal{F}_i$ that sediment of this grain size actually occurs.

For sand mixtures on inner shelves the settling period is much smaller than the hydrodynamic timescale. This implies that equation (3.A-1) reduces to an approximate balance between erosion and deposition flux near the bed:

$$\mathcal{F}_i E_i - \frac{C_i}{\delta_i D} = 0$$

The second term represents the deposition flux of these grains and is expressed in terms of the depth-integrated concentration C_i. Parameter δ_i is the ratio of the thickness of the suspended load layer of grains in class i over the total water depth D.

In Garcia and Parker (1991) an expression for the entrainment of a mixture of particles is obtained by analysing laboratory and field data. They find

$$E_i = A(\lambda_{\mathrm{E}} Z_i)^5 \qquad\qquad Z_i = \frac{u_*}{w_{si}} R_{pi}^{0.6} \left(\frac{d_i}{d_m}\right)^{0.2}$$

with $A = 1.3 \times 10^{-7}$ a constant. Hiding effects are covered by the last factor in the expression for Z_i. Furthermore, $\lambda_{\mathrm{E}} = 1 - 0.288\,\sigma$ is a straining parameter, $R_{pi} = \sqrt{g' d_i^3}/\nu$ is the particle Reynolds number of grains of size d_i and $\nu \sim 1.36 \times 10^{-6}$ m^{2}s^{-1} is the kinematic viscosity coefficient of water. The entrainment for uniform sediment (grain size d_m) reads

$$E_{m,u} = A Z_m^5 = \hat{E}_{m,u} |\vec{v}_t|^5 \qquad\qquad \hat{E}_{m,u} = A \left(\frac{\sqrt{c_f}}{w_{sm}} R_{pm}^{0.6}\right)^5$$

such that Z_m corresponds the value of Z_i for $d_i = d_m$. From this result it follows that the expression for $\mathcal{G}_{si}$ in eq. (3.12) is written as:

$$\mathcal{G}_{si} \equiv \zeta_i \left(\frac{\delta_i}{\delta_m}\frac{E_i}{E_m}\right)_u = \zeta_i \frac{w_{sm}}{w_{si}} \left(\frac{R_{pi}}{R_{pm}}\right)^3 \left(\frac{w_{sm}}{w_{si}}\right)^5$$

3.B Bottom friction coefficient

The expression for the grain roughness length used in the formulation for the bottom friction coefficient (see eq. (3.3)) reads $k_s = 3d_m\sigma_m$, with σ_m the geometric standard deviation, defined as $\sigma_m = 2^{\sigma}$. When expressed in terms of phi (section 3.2.2) it follows that $k_s = 3 \times 2^{\sigma - \phi_m}$ (defined in units of mm). Including small perturbations in the mean grain size and standard deviation in the friction parameter gives for the quantities that correspond to the basic state and the perturbation of the bottom friction parameter:

$$r_0 = \frac{2}{\pi}\frac{g\,u_w}{C_{h0}^2} \qquad r' \simeq \frac{2\,r_0}{C_{h0}}\left\{(\sigma' - \phi'_m)\ln 2 + \frac{h}{H}\right\} \tag{3.B-1}$$

The expression for the Chezy coefficient, as defined in section 3.2.1 with $D = H - h$, for the basic state is $C_{h0} = C_h(H, \Phi_m, \sigma_0)$. The perturbations in the bottom friction coefficient used in the momentum equations, with r' as defined in (3.B-1), is written in terms of the unknowns h and f_1 by using equation (3.22).

3.C Sediment flux

The transport capacity functions, defined in (3.8) and (3.14) for bed load and suspended load, was split into contributions which correspond to the basic state and the perturbed state, respectively. These results are used in section 3.3.2 and read

$$\begin{aligned}
&\mathcal{G}_{bi} = 2^{c_b(\phi_m - \phi_i)} \qquad G_{bi} = 2^{c_b(\Phi_m - \phi_i)} \qquad g_{bi} = c_b \ln 2\, G_{bi}\, \phi'_m = G_{bi} T_{b5} f_1 \\
&\mathcal{G}_{si} = \lambda_{\mathrm{E}}^5 2^{c_s(\phi_m - \phi_i)} \quad G_{si} = \Lambda_{\mathrm{E}}^5\, 2^{c_s(\Phi_m - \phi_i)} \quad g_{si} = G_{si}\left[c_s \ln 2\, \phi'_m + 5\frac{\lambda'_{\mathrm{E}}}{\Lambda_{\mathrm{E}}}\right] \\
&\qquad\qquad\qquad\qquad\qquad\qquad\qquad\quad = G_{si} T_{s5} f_1 \\
&\lambda_{\mathrm{E}} = 1 - 0.288\sigma \qquad \Lambda_{\mathrm{E}} = 1 - 0.288\sigma_0 \qquad \lambda'_{\mathrm{E}} = -0.288\sigma'
\end{aligned}$$

where

$$T_{b5} = c_b \ln 2 \frac{\sigma_0}{\sqrt{F_2 F_1}} \qquad T_{s5} = c_s \ln 2 \frac{\sigma_0}{\sqrt{F_2 F_1}} - 5\frac{0.288\sigma_0}{\Lambda_E}\frac{(F_2 - F_1)}{2F_1 F_2}$$

The total load sediment flux in the basic state only has an alongshore component and consists of contributions caused by bed load and suspended load, given by:

$$\vec{q}_{b0} = (0, q_{b0}) = (0, \frac{3}{2}\nu_b u_w^2 V) \qquad \vec{q}_{s0} = (0, q_{s0}) = (0, \frac{32}{5\pi}\delta_m \hat{E}_{m,u} u_w^5 HV)$$

The divergences of the perturbed sediment fluxes are

$$\vec{\nabla}\cdot\vec{q}_b' = \frac{3}{2}\nu_b\left\{u_w^2\left[\left(\frac{2}{u_w}\frac{\partial u_w}{\partial x}-\frac{1}{H}\frac{\partial H}{\partial x}\right)u'+\frac{V}{H}\frac{\partial h}{\partial y}\right]\right.$$
$$\left.-\frac{8}{9\pi}\lambda_b u_w^3\left(\frac{\partial^2 h}{\partial x^2}+\frac{3}{u_w}\frac{\partial u_w}{\partial x}\frac{\partial h}{\partial x}+\frac{\partial^2 h}{\partial y^2}\right)\right\}$$
$$\vec{\nabla}\cdot\vec{q}_s' = \frac{32}{5\pi}\delta_m\hat{E}_{m,u}\left\{5u_w^4 H\frac{\partial u_w}{\partial x}u'\right.$$
$$\left.-\frac{\lambda_s}{7}u_w^7 H\left[\frac{\partial^2 h}{\partial x^2}+\left(\frac{7}{u_w}\frac{\partial u_w}{\partial x}+\frac{1}{H}\frac{\partial H}{\partial x}\right)\frac{\partial h}{\partial x}+\frac{\partial^2 h}{\partial y^2}\right]\right\}$$

Here equation (3.19) has been used to eliminate v'.

3.D List of frequently used variables

c_b	exponent in bed load transport capacity function
c_s	exponent in susp. load transport capacity function
C_i	depth-integrated volume concentration of grain sizes in class d_i, m
d_1	grain diameter of finest sediment fraction, mm
d_2	grain diameter of coarsest sediment fraction, mm
d_m	mean grain size of a sediment mixture, mm
E_i	entrainment of sediment of diameter d_i in suspension
$E_{i,u}$	as E_i, but in the case of uniform sediment
$\mathcal{F}_i$	probability distribution function for size class i in the active layer
F_i	weight percent of the grains in the finest ($i = 1$) or coarsest ($i = 2$) grain size class in basic state
f_i	perturbation on F_i $(i = 1, 2)$
$\mathcal{F}_s$	probability density function in substrate
$\mathcal{G}_{bi}$	bed load transport capacity function for sediment of size d_i
G_{bi}	basic state bed load transport capacity function
g_{bi}	perturbation on G_{bi}
$\mathcal{G}_{si}$	suspended load transport capacity function for sediment of size d_i
G_{si}	basic state suspended load transport capacity function
g_{si}	perturbation on G_{si}

L_a	active layer thickness, m
L_{a0}	basic state active layer thickness, m
m	exponent in wave stirring function
m_b	exponent in hiding function bed load
m_E	exponent in entrainment of sediment in suspension
$\vec{q}_i$	total sediment flux of sediment of grain size d_i, $\mathrm{m^2 s^{-1}}$
$\vec{q}_{bi}$	bed load flux of grains d_i, $\mathrm{m^2 s^{-1}}$
q_{b0}	basic state alongshore bed load flux, $\mathrm{m^2 s^{-1}}$
$\vec{q}_b'$	perturbation in bed load flux, $\mathrm{m^2 s^{-1}}$
$\vec{q}_{si}$	suspended load flux of grains d_i, $\mathrm{m^2 s^{-1}}$
q_{s0}	basic state alongshore suspended load flux, $\mathrm{m^2 s^{-1}}$
$\vec{q}_s'$	perturbation in suspended load flux, $\mathrm{m^2 s^{-1}}$
u_w	wave-orbital velocity amplitude, $\mathrm{m s^{-1}}$
$\hat{u}_w$	near-bed wave-orbital velocity, $\mathrm{m s^{-1}}$
δ_i	ratio of the thickness of the suspended load layer of grains of diameter d_i over the total water depth
δ_m	ratio of the thickness of the suspended load layer of grains of diameter d_m over the total water depth
ζ_i	hiding function for entrainment of sediment in suspension
$\Theta_{i,u}$	Shields parameter for uniform sediment of size d_i
Θ_m	Shields parameter for sediment of size d_m
λ_E	straining parameter
Λ_E	basic state straining parameter
λ_E'	perturbation on Λ_E
ξ_i	dynamic hiding function for bed load
σ	standard deviation of the mixture on the phi scale
σ_0	standard deviation of the mixture in the basic state
σ'	perturbation on σ_0
τ	bed shear stress (skin friction), $\mathrm{N m^{-2}}$
$\vec{\tau}_b$	bed shear stress vector (form drag + skin friction), $\mathrm{N m^{-2}}$
ϕ_m	mean grain diameter on phi scale
Φ_m	basic state mean grain diameter
ϕ_m'	perturbation on Φ_m

Chapter 4

A model for grain size sorting over tidal sand ridges

Abstract

A model was developed and analysed to quantify the effect of graded sediment on the formation of tidal sand ridges. Field data reveal coarse (fine) sediment at the crests (in the troughs), but often phase shifts between the mean grain size distribution and the bottom topography occur. Following earlier work, this study is based on a linear stability analysis of a basic state with respect to small bottom perturbations. The basic state describes an alongshore tidal current on a coastal shelf. Sediment is transported as bed load and dynamic hiding effects are accounted for. A one-layer model for the bed evolution is used and two grain size classes (fine and coarse sand) are considered.

Results indicated an increase in growth and migration rates of tidal sand ridges for a bimodal mixture, whilst the wavelength of the ridges remains unchanged. A symmetrical tidal current results in a grain size distribution which is in phase with the ridges. Incorporation of an additional M_4 tidal constituent or a steady current results in a phase shift between the grain size distribution and ridge topography. These results are consistent with observations. The physical mechanism responsible for the observed grain size distribution over the ridges is also discussed. *

*This chapter is based on the paper entitled *A model for grain sorting over tidal sand ridges*, by M. Walgreen, H.E. De Swart and D. Calvete, submitted for publication in Ocean Dynamics.

4.1 Introduction

Tidal sand ridges are rhythmic bedforms that are observed on the outer part of meso-tidal shelves. A characteristic spacing between successive crests is 5-8 km and the ridges are rotated cyclonically with respect to the dominant tidal current. These characteristics have been explained in various studies dealing with tide-topography interaction (Zimmerman, 1981; Huthnance, 1982a). One aspect that has not been addressed so far is the role of graded sediment in the morphodynamics of tidal sand ridges. Analysis of field observations indicates the potential importance of graded sediment: a persistent spatial variation of the surficial sediments over these ridges is found, of which the cause is not well known. A well-documented example of a tidal sand ridge is the Middelkerke Bank along the Belgian coast (see, for example, Lanckneus et al., 1994; Houthuys et al., 1994; Vincent et al., 1998). The distribution of the mean grain size shows coarser sediment on the crests and a fining trend towards the troughs, see Figure 1.5 in chapter 1 of this thesis. Moreover, the location of the coarsest sediment is shifted seaward at the northern end of the Middelkerke Bank and landward at the southern end (Trentesaux et al., 1994). Data gathered from the more seaward located Kwinte Bank (Gao et al., 1994) indicate a similar grain size pattern, with the seaward flank typically consisting of coarser sediment than the landward flank.

The first objective of the present study was to gain understanding of the physical mechanisms responsible for the observed grain size distribution over the tidal sand ridges. In addition, the work was aimed at identifying possible causes for the shift between the crest and the maximum in the mean grain size. The second objective was to investigate the influence of sediment sorting on the temporal (i.e. growth and migration) and spatial characteristics of the ridges. Following earlier work, it is hypothesized that tidal sand ridges form as a free instability of a morphodynamic system. Calvete et al. (2001a) studied the initial formation of tidal sand ridges in the case of uniform sediment. In contrast to the open domain, as was used in earlier studies by Huthnance (1982a) and Hulscher et al. (1993), the shelf was bounded by a coast. In the present chapter the model is extended with a formulation for the transport of a sediment mixture. The approach is similar to that used by Walgreen et al. (2003), see also chapter 3 of this thesis, who investigated the effect of sediment sorting on the formation of other large-scale bedforms detected on coastal shelves, viz. shoreface-connected sand ridges. The model for tidal sand ridges differs from the one presented by Walgreen et al. (2003) in the sense that the dominant forcing is by tides, rather than by storms, and that suspended load transport is neglected.

In section 4.2 a brief description of the model is given, including the linear stability approach to solve the equations. Section 4.3 shows the influence of a bimodal sediment mixture, as compared to sediment with a single grain size, on the initial formation of tidal sand ridges. A physical interpretation of the model results is presented in section 4.4, followed by a comparison with field observations. In this last section the conclusions are given.

4.2 Model formulation and solution methods

A local model is used to investigate the flow-topography interaction on a tide-dominated coastal shelf. To this end, it is assumed that bedforms can develop as perturbations on an

alongshore-uniform basic state, as defined in section 4.2.3. The geometry of the model represents a semi-infinite domain, bounded on the landward side by the transition from the shoreface to the (sloping) inner shelf. Further seaward, a flat bottom is used to represent the outer shelf, see also Figure 2.2 in chapter 2.

4.2.1 Hydrodynamics

The water motion is described by the depth-averaged (2DH) shallow water equations.

$$\frac{\partial \vec{v}}{\partial t} + (\vec{v} \cdot \vec{\nabla})\vec{v} + f\vec{e_z} \times \vec{v} = -g\vec{\nabla} z_s - \frac{\vec{\tau_b}}{\rho D} \tag{4.1}$$

$$\frac{\partial D}{\partial t} + \vec{\nabla} \cdot (D\vec{v}) = 0 \tag{4.2}$$

Here $\vec{v}$ is the depth and wave-averaged velocity, f is the Coriolis parameter, $\vec{e_z}$ a unit vector in the vertical direction, g the acceleration due to gravity, ρ is the density, $\vec{\tau_b} = \rho r \vec{v}$ is a linearised bed shear stress, t is time and $\vec{\nabla}$ the horizontal nabla operator. The bottom friction coefficient is $r = c_d U \sim 10^{-3}$, where c_d is the drag coefficient and U a characteristic value for the depth-averaged velocity. In this chapter results will be presented for a grain size independent bottom friction. The local water depth is given by $D = z_s - z_b \simeq -z_b$, where z_s is the free-surface elevation and z_b is the bottom depth. A rigid lid is assumed, which also implies that the first term in equation (4.2) can be omitted. This is justified on the basis of a small Froude number. The main forcing in the momentum equations is due to a prescribed pressure gradient induced by a tidal wave propagating along the coast.

4.2.2 Sediment dynamics

A sediment mixture consisting of N different grain size classes d_i can be described using a logarithmic scale, the phi scale:

$$d_i = 2^{-\phi_i} \qquad \text{or} \qquad \phi_i = -\log_2 d_i$$

where d_i is measured in units of mm. The mean grain size and the standard deviation are defined as

$$\phi_m = \sum_{i=1}^{N} \phi_i \mathcal{F}_i \qquad\qquad \sigma^2 = \sum_{i=1}^{N} (\phi_i - \phi_m)^2 \mathcal{F}_i$$

Here $\mathcal{F}_i$ is the probability distribution function of the grain size class i and obeys the constraint $\sum_{i=1}^{N} \mathcal{F}_i = 1$. For an overview of the frequently used variables related to the sediment and transport characteristics, the reader is referred to appendix 3.D of chapter 3.

The hydrodynamic equations discussed in section 4.2.1 are supplemented with a sediment transport formulation, based on the concepts introduced by Bailard (1981) for bed load transport on a sloping bottom. In turn, the evolution of the bottom results from a convergence or divergence in the sediment flux. A one-layer model for the bed, based on the concept of an active transport layer overlaying an inactive substrate is used (see Ribberink, 1987; Seminara,

1995). The active layer is well mixed and has a thickness of L_a, in the order of $2-3$ mm. The exchange of sediment with the substrate is ignored. Consequently, the relation between the bottom evolution, the grain size evolution and the sediment flux of class d_i yields

$$(1-p)\left(\mathcal{F}_i\frac{\partial z_b}{\partial t}+L_a\frac{\partial \mathcal{F}_i}{\partial t}\right)=-\overline{\vec{\nabla}\cdot\vec{q}_{bi}} \tag{4.3}$$

In (4.3), $\vec{q}_{bi}$ is the volumetric flux per unit width of grains of diameter d_i and $p\sim 0.4$ is the porosity of the bed. The first term on the left-hand side of equation (4.3) represents the bottom changes, and the second describes changes in the sediment distribution in the active layer. Besides, the formation of tidal sand ridges takes place on a timescale which is much larger than the hydrodynamic timescale. For instance, Vincent et al. (1998) estimated the timescale for the growth of the Middelkerke Bank to be 10^2-10^3 years. Therefore, a tidally- and wave-averaged sediment flux is used, denoted by the overbar, and the flow adjusts instantaneously to the new bottom.

Tides are supposed to control the growth of tidal sand ridges. This is supported by the findings of Trentesaux et al. (1994), which show a near absence of wave-induced structures on the Middelkerke Bank. This implies that bed load is the dominant mode of transport and suspended load contributions can be neglected. A more elaborate discussion on this topic is given in section 4.4.3. In case of a single grain size the (wave-averaged) bed load transport reads (see also (2.6) in chapter 2)

$$\vec{q}_b=\nu_b\left|\vec{v}\right|^3\left[\frac{\vec{v}}{|\vec{v}|}-\lambda_b\vec{\nabla}h\right]$$

where ν_b is a coefficient, $\lambda_b\sim 1$ and h is the bottom level with respect to the alongshore-averaged bathymetry. Note that this flux relates to the velocity to the power three, and that it includes effects due to the local slope of the bottom. To calculate the sediment flux of a specific grain size within a sediment mixture, two additional corrections are made, such that

$$\vec{q}_{bi}=\mathcal{F}_i\mathcal{G}_{bi}\vec{q}_b$$

First, $\mathcal{F}_i$ corrects for the availability of grains of diameter d_i in the mixture. Second, dynamic hiding effects are included, represented by the function $\mathcal{G}_{bi}$. This is the bed load transport capacity function for sediment of grain size d_i, and accounts for the effect that finer grains feel the fluid drag less intensely than coarser grains. It is convenient to use the following expression

$$\mathcal{G}_{bi}=\left(\frac{d_i}{d_m}\right)^{c_b} \tag{4.4}$$

with the exponent c_b measuring the influence of the hiding on the transport of sediment. A default value of $c_b=0.75$ is used (see discussion in Walgreen et al., 2003, and chapter 3 of this thesis), which results in a reduced transport rate of the grain sizes finer than the mean grain size. At the landward and seaward boundaries of the model domain no cross-shore velocity component and no bottom changes are allowed.

4.2.3 Basic state

The possible onset of bedforms as free morphodynamic instabilities, which evolve on a basic state of the water-bottom system, is investigated. The model allows for a morphodynamic equilibrium, which is alongshore uniform:

$$\vec{v} = (0, V(x,t)) \qquad z_b = -H(x) \qquad z_s = s(t)y + z_{s0}(x,t)$$
$$\mathcal{F}_i = F_i \qquad \phi_m = \Phi_m \qquad \sigma = \sigma_0$$

It describes a shore-parallel current $V(x,t)$ over a fixed bottom $z_b = -H(x)$. The grain size distribution function F_i of the basic state can have an arbitrary structure in the x-direction. For simplicity, F_i is assumed to be independent of this coordinate. As a result, the mean grain size Φ_m and the standard deviation σ_0 are also uniform in the domain. The velocity of the basic state is a solution of the alongshore momentum equation (4.1):

$$\frac{\partial V}{\partial t} = -gs - \frac{rV}{H}$$

The alongshore gradient in the free surface, s, is defined by a steady component s_0 and two oscillating components:

$$s \equiv s_0 - s_1 \cos(\omega t) - s_2 \cos(2\omega t + \theta)$$

Here s_1 and s_2 are the amplitudes of the sea surface gradients with the frequency (indicated by ω) of the M_2 and of the M_4 tide, respectively. Furthermore, θ is a (constant) phase between the two tidal harmonics. The velocity of the basic state consists of a steady component, V_0, and an oscillatory component, due to the M_2 and M_4 tidal wave:

$$\begin{aligned} V(x,t) = V_0(x) &+ V_{M_2}(x)\sin(\omega t + \varphi_{M_2}(x)) \\ &+ V_{M_4}(x)\sin(2\omega t + \varphi_{M_4}(x) + \theta) \end{aligned} \tag{4.5}$$

where

$$V_0(x) = -\frac{gs_0H}{r} \tag{4.6}$$

The cross-shore profile of the tidal current amplitudes and phases are given by:

$$V_{M_2}(x) = \frac{gs_1H}{\sqrt{(\omega H)^2 + r^2}} \qquad \varphi_{M_2}(x) = \arctan\left(\frac{r}{H}\right)$$
$$V_{M_4}(x) = \frac{gs_2H}{\sqrt{(2\omega H)^2 + r^2}} \qquad \varphi_{M_4}(x) = \arctan\left(\frac{r}{2H}\right)$$

A similar tidal velocity field was also considered in chapter 2 of this thesis, for profiles see appendix 2.B. The values used for the basic state variables are given in section 4.3.1.

4.2.4 Stability analysis

The dynamics of small perturbations on this basic state are studied. In case of a positive feedback between the flow and the bottom perturbation, the basic state is unstable and rhythmic bottom features will develop. Solutions of the form

$$\begin{array}{lcrcl}
\vec{v} & = & (0, V(x,t)) & + & (u'(x,y,t), v'(x,y,t)) \\
z_s & = & s(t)y + z_{s0}(x,t) & + & \eta'(x,y,t) \\
z_b & = & -H(x) & + & h(x,y,t) \\
\vec{q_b} & = & \vec{q}_{b0}(x) & + & \vec{q}_b'(x,y,t) \\
\mathcal{G}_{bi} & = & G_{bi} & + & g_{bi}(x,y,t) \\
\mathcal{F}_i & = & F_i & + & f_i(x,y,t) \\
\phi_m & = & \Phi_m & + & \phi_m'(x,y,t) \\
\sigma & = & \sigma_0 & + & \sigma'(x,y,t) \\
L_a & = & L_{a0} & + & L_a'(x,y,t)
\end{array}$$

are substituted in the equations of motion and the results are linearised. In this chapter a two-size sediment mixture will be used, where d_1 (or ϕ_1) and d_2 (or ϕ_2) represent the sizes of the fine and coarse grains, respectively. The constraint on the grain size fraction becomes

$$F_1 + F_2 = 1 \qquad\qquad f_1 = -f_2 \tag{4.7}$$

The mean grain size and the standard deviation in the basic state simplify to

$$\Phi_m = \phi_1 F_1 + \phi_2 F_2 \qquad\qquad \sigma_0^2 = F_2 F_1 (\phi_1 - \phi_2)^2$$

From these expressions the values of of the grain diameters of the fine and coarse size class on the phi scale, i.e. ϕ_1 and ϕ_2, can be obtained as a function of Φ_m, σ_0 and F_1. Together with the relations given above, the perturbations in the mean grain size and standard deviation can be written as

$$\phi_m' = \frac{\sigma_0}{\sqrt{F_2 F_1}} f_1 \qquad\qquad \sigma' = \frac{\sigma_0 (F_2 - F_1)}{2 F_2 F_1} f_1$$

The linearised form of the bottom evolution equation (4.3) is

$$F_i \frac{\partial h}{\partial t} + L_{a0} \frac{\partial f_i}{\partial t} = -\vec{\nabla} \cdot \langle \vec{q}_{bi}' \rangle \tag{4.8}$$

where

$$\vec{q}_{bi}' = F_i G_{bi} \vec{q}_b' + \vec{q}_{b0} \left(G_{bi} f_i + F_i g_{bi} \right) \tag{4.9}$$

is the perturbed bed load flux and $\vec{q}_{b0}$, $\vec{q}_b'$ and $\vec{\nabla} \cdot \vec{q}_b'$ are given in appendix 4.A. The active layer thickness in the basic state is given by $L_{a0} = d_m 2^{\sigma_0}$ and from equation (4.4) it follows that

$$G_{bi} = 2^{c_b (\Phi_m - \phi_i)} \qquad\qquad g_{bi} = c_b \ln 2 \, G_{bi} \, \phi_m' \tag{4.10}$$

Summation of equation (4.8) over the two fractions and using the constraint (4.7) for the probability distribution, results in an equation relating the bottom evolution to the sum of the sediment flux over all sizes. Back-substitution of this result in equation (4.8) yields the evolution of the distribution function f_i. The final results are

$$(1-p)\frac{\partial h}{\partial t} = -[\overline{\vec{\nabla}\cdot\vec{q}'_{b1}} + \overline{\vec{\nabla}\cdot\vec{q}'_{b2}}] \tag{4.11}$$

$$(1-p)L_{a0}\frac{\partial f_1}{\partial t} = F_1\overline{\vec{\nabla}\cdot\vec{q}'_{b2}} - F_2\overline{\vec{\nabla}\cdot\vec{q}'_{b1}} \tag{4.12}$$

The solution of any perturbed variable is sinusoidal in the alongshore direction (with wavenumber k), and exponential in time (with complex frequency Ω). In particular, the bottom perturbations are topographic waves propagating along the shelf, of the form $h(x,y,t) = Re\{\hat{h}(x)\mathrm{e}^{iky+\Omega t}\}$. A similar expression holds for f_1. The stability analysis yields for each wavenumber k solutions for Ω and the corresponding cross-shore structures of the perturbed variables. The real part Ω_r of Ω is the growth rate, with Ω_r^{-1} being the e-folding timescale. Furthermore, its imaginary part Ω_{Im} is the frequency. The migration velocity of the perturbation is $c = -\Omega_{Im}/k$. Of specific interest are growing perturbations, which satisfy $\Omega_r > 0$. The preferred mode is defined as the mode with the largest growth rate. From the boundary conditions it follows that $u' = 0$ and $h = 0$ at the transition from the shoreface to the inner shelf ($x = 0$) and at $x \rightarrow \infty$. Solutions of the linear stability problem were obtained by numerical methods, for details see Calvete et al. (2001a) and references herein.

4.3 Results

The model was run for different parameter settings to meet the objectives of this study (see section 4.1). In particular, the sensitivity of the model results with respect to variations in the standard deviation of the mixture; the size distribution in the basic state; and the exponent c_b in the hiding function for bed load was investigated. First, a brief consideration of the most important characteristics of a typical tide-dominated coastal shelf is given. The results presented in this section are based on these values.

4.3.1 Shelf characteristics

On the Belgian coastal shelf, different types of sand ridges are present, classified according to the influence of tides and storms on the sea bed. The Flemish Banks, including the Middelkerke Bank, are tidal sand ridges located 10-20 km offshore, in a meso-tidal environment. To validate the model results, this shelf was used as a prototype. It is approximately 14 m deep at the transition from the shoreface to the inner shelf, 12 km wide, and 20 m deep on the outer shelf. The latitude is $52°$N, for which the Coriolis parameter $f \sim 1 \times 10^{-4}$ s^{-1}. Although the dominant hydrodynamical forcing is due to the M_2 tide, contributions of the M_4 constituent and residual currents can be present. The behaviour of the tidal current changes from almost symmetrical north of the Flemish Banks, to increasingly flood-dominated closer to the shore, with a residual flow directed towards the northeast (along a SW-NE trending coastline) (Lanckneus et al., 1994). This is in agreement with the residual sand transport to

	uniform Fig. 4.1	bimodal Fig. 4.1, 4.2, 4.3, 4.4	bimodal Fig. 4.1	bimodal Fig. 4.4
σ_0	0	0.5	1.0	0.4
F_1	1	0.5	0.5	0.8
F_2	0	0.5	0.5	0.2
Φ_m	1.5	1.5	1.5	1.5
ϕ_1	1.5	2.0	2.5	2.0
ϕ_2	1.5	1.0	0.5	1.0
d_1 (mm)	0.35	0.25	0.18	0.25
d_2 (mm)	0.35	0.50	0.71	0.50

Table 4.1: Parameter values for uniform and bimodal sediment used in the model experiments.

the northeast in a narrow coastal region and a southwest-directed transport in the offshore region. On the scale of the Belgian shelf, measurements indicate an almost zero long-term average of the steady current.

To illustrate the effect of the velocity profile on the formation of tidal sand ridges, three experiments were conducted. Firstly, a forcing by the M_2 tidal constituent was used, with a depth-averaged tidal current amplitude of 0.5 ms^{-1}. This means that the tidally-averaged alongshore sediment transport is zero. Secondly, asymmetry in the flow was introduced by adding an M_4 constituent to the forcing, where $V_{M_2} \sim 0.45$ ms^{-1}, $V_{M_4} \sim 0.05$ ms^{-1} (Williams et al., 2000). Lastly, an asymmetric current profile introduced by a steady component $V_0 \sim -0.05$ ms^{-1} (free surface forcing $s_0 \sim 4 \times 10^{-7}$), in addition to the V_{M_2} component, was investigated. The former two situations are characterised by a net alongshore (flood-dominated) current and a tidally-averaged sediment flux along the coast (in a north-easterly direction).

On the scale of the Belgian coastal shelf the sediment becomes coarser offshore, while locally the coarsest mean grain size is found on the crest of the ridges. For simplicity, in the basic state a uniform mean grain size of $d_m = 0.35$ mm ($\Phi_m = 1.5$), characteristic of surficial sediment on the Middelkerke Bank, was adopted throughout the domain. The sediment size distribution observed on the steep seaward flank of the sand ridge supports the use of a bimodal sediment mixture: two peaks were present, for the size classes of 0.25-0.30 mm and 0.42-0.50 mm (Vincent et al., 1998). The diameters of the two size classes in the sediment mixture were confined to non-cohesive sediment in the sand range ($3 > \phi_i > 0$). Table 4.1 presents the properties of the sediment mixtures used in the different experiments.

4.3.2 Sensitivity to standard deviation

The growth rates and migration velocities of the preferred mode for different compositions of the sediment bed are shown in Figure 4.1. The standard deviation σ_0 of the basic state increased from zero (i.e. uniform sediment) to a bimodal mixture in the case of forcing by a pure M_2 tide and a combined M_2, M_4 tide. A constant mean grain size and equal weight percentages of the two size classes in the basic state ($F_1 = F_2 = 0.5$) are assumed. As

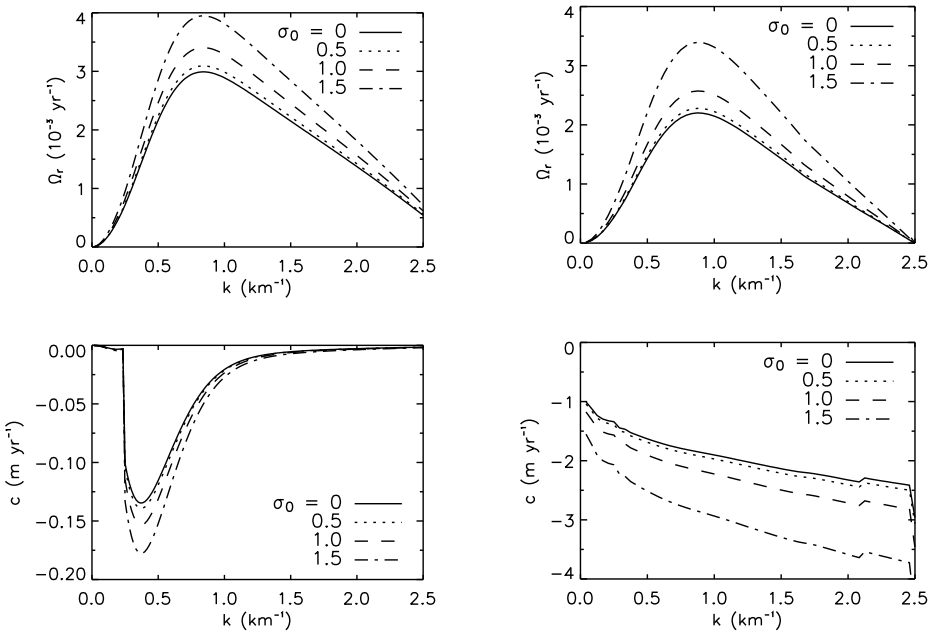

(a) M_2 (b) M_2 + M_4

Figure 4.1: Growth rate and migration velocity, c, of dominant cross-shore mode as a function of the alongshore wavenumber k for different values of the standard deviation and the same mean grain size in all experiments ($\Phi_m = 1.5$). Forcing by the M_2 tide (a), and M_2 + M_4 tides (b). The coeffi cient in the hiding function is $c_b = 0.75$.

a result, the grain sizes d_1 and d_2 change with σ_0, see Table 4.1 and Figure 3.4 of chapter 3. For a bimodal mixture growth rates and migration speeds increase with increasing σ_0. The wavelengths $(2\pi/k)$ of the ridges for which maximum growth rates are attained remain unchanged: 7.5 km and 7.2 km for M_2 and M_2+M_4 tidal conditions, respectively. The corresponding e-folding timescales for the initial growth are 320 yr (M_2) and 440 yr (M_2 + M_4) for a value of $\sigma_0 = 0.5$. The tidal sand ridges migrate with a speed of 0.04 myr^{-1} and 1.9 myr^{-1} in these two cases. The small nonzero migration velocity for a symmetrical (M_2) tidal forcing is due to the bedslope contribution in the sediment flux. In fact, the relative increase in growth and migration due to a changing standard deviation was larger for a combined M_2 and M_4 tide than for a symmetrical M_2 tide. Additional experiments were carried out with a velocity of the basic state consisting of a steady current V_0 and an M_2 tidal current. The results (not shown) indicate that growth rates and migration velocities again increase with σ_0. The bedforms migrate in the direction of the mean flow. This behaviour is similar to that obtained in the case of an asymmetrical flow driven by the M_2 and M_4 tidal constituents. In the situation where forcing includes both the M_4 tide and a steady sea surface gradient, it is possible to have a migration of the bedforms against the direction of the steady current. A

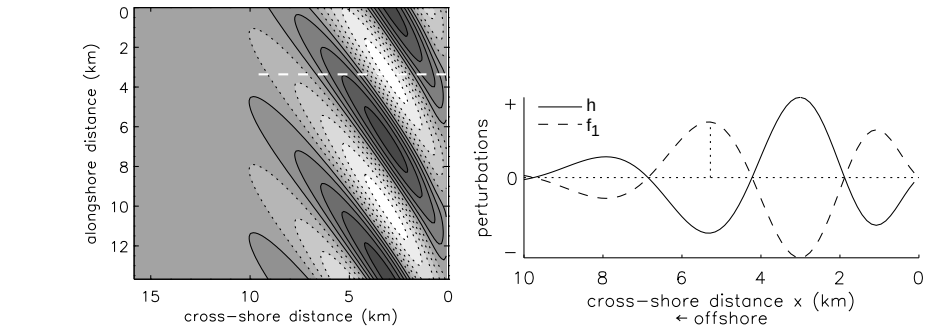

(a) M_2

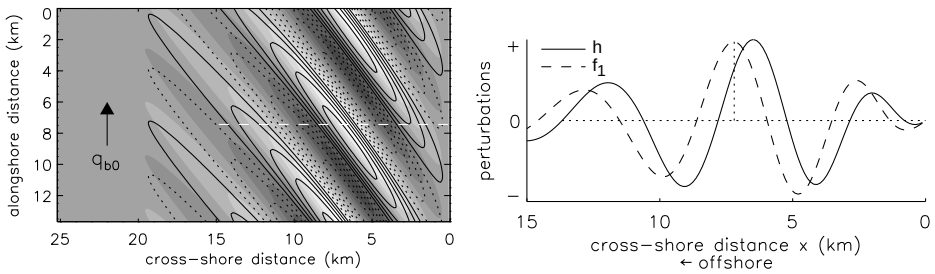

(b) M_2 + M_4

Figure 4.2: Bottom perturbations (greyscale; light: bars, dark: troughs) and perturbations in the distribution of mean grain size (solid lines: finer; dashed lines: coarser). Also shown is the variation of the bottom and mean grain size along a cross-section (location indicated by white dashed line in the contour plots), positive (negative) values of f_1 indicate a local fining (coarsening) of the bottom sediment. Ridges are shown for $\sigma_0 = 0.5,\ \Phi_m = 1.5,\ c_b = 0.75$ and forcing by M_2 tide (a), and M_2 + M_4 tides (b).

necessary condition is that the phase between the M_2 and M_4 tide is such that it introduces a residual sediment transport in the direction opposite to the residual sediment transport caused by the residual current. In addition, the amplitude of the M_4 tide should be at least $\sim\ 3-4$ times larger than the amplitude of the steady current. As such situations are not observed an the Belgian shelf, this is not further pursued.

The patterns of topographic perturbations (shaded) and variations in the mean grain size are shown in Figure 4.2, for parameter values of non-uniform sediment. The contour lines refer to the perturbation in the fraction of the finest grains, values along solid lines are positive and indicate a locally finer mean grain size. If a symmetrical tidal current is used, the grain size distribution is in phase with the ridge topography, with the finest sediments located in the troughs. Incorporation of an additional M_4 tide in the forcing results in a phase shift between

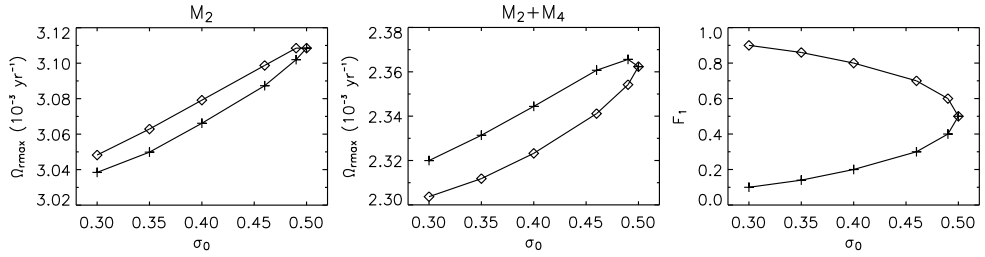

Figure 4.3: Growth rate Ω_r of the preferred mode as a function of the standard deviation of the mixture σ_0 of the basic state. Forcing due to M_2 tide (left), and M_2+M_4 tide (middle). The default value $c_b = 0.75$ is used. Results are shown for a bimodal mixture with fixed grain sizes $\phi_1 = 2.0$ and $\phi_1 = 1.0$, where changes in the basic state σ_0 result in variation of Φ_m and F_1 (right). Note that a larger weight percentage of ϕ_1 (i.e. $F_1 > 0.5$, indicated by diamonds), as well as a larger weight percentage of ϕ_2 ($F_1 < 0.5$, indicated by crosses) can result in the same value of σ_0.

the mean grain size and topography. In the present case of a flood-dominant tidal current (residual transport indicated by the arrow), the finest sediments are located on the upcurrent (seaward) flank and on the crests of the ridges. The underlying physics will be discussed in sections 4.4.1 and 4.4.2.

In order to test the robustness of these results, experiments were carried out in which the diameters of both fractions were fixed and the standard deviation was varied. This implies the changing of the composition of the sediment mixture, i.e., the mean Φ_m and the fractions F_1 and F_2 of the sediment in the basic state will change. A linear relation exists between Φ_m and F_1: higher values of F_1 correspond to higher values of Φ_m (i.e. finer mean grain sizes). The results in Figure 4.3 are only shown for the preferred mode (which has the largest growth rate). As before, the maximum growth rates and migration velocities (not shown) increase with the standard deviation. Wavelengths of the preferred mode do not change, and the perturbations in the bed and sediment distribution have the same characteristics as the ones shown in Figure 4.2. In the case of $\sigma_0 < 0.5$ two different compositions of the sediment mixture are possible for each value of the standard deviation. One with a larger percentage of fine grains (indicated by diamonds) and a mean grain size $\Phi_m > 1.5$, and a second with a larger percentage coarse grains (indicated by crosses) and $\Phi_m < 1.5$. Figure 4.3 demonstrates that, in case of forcing solely by an M_2 tidal current (left subplot), for a fixed value of σ_0 the instabilities grow fastest for a grain size distribution in the basic state which contains more fine than coarse sediment. The opposite occurs in case of a combined M_2, M_4 tidal current (middle subplot).

4.3.3 Sensitivity to hiding coefficient

Another series of experiments was conducted to investigate the influence of the intensity of the hiding in the bed load transport capacity function, as measured by the coefficient c_b. For all three velocity profiles (solely M_2, M_2 + M_4 and M_2 + M_0) the maximum growth rates and corresponding migration of the preferred mode are shown as a function of c_b (eq. (4.4) and Figure 4.4). The wavelength of the preferred mode does not depend on c_b. The experiments

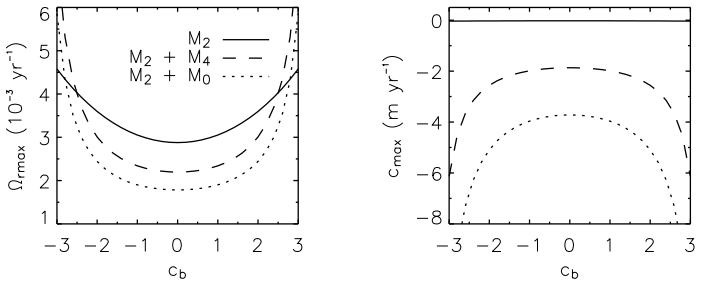

Figure 4.4: Growth rate and migration velocity of the preferred mode as a function of the coeffi cient c_b, indicating the strength of the dynamic hiding. Results are shown for a current forced by M_2 tide, M_2+M_4 tide, and M_2 tide + steady current. Other parameter values are: $F_1 = 0.5,\ \sigma_0 = 0.5,\ \Phi_m = 1.5$.

reveal enhanced growth rates and migration velocities for higher values of the exponent c_b, i.e. if dynamic hiding effects become stronger. Positive (negative) values of c_b correspond to a reduced (enhanced) bed load transport of fine grains with respect to coarse grains. The relative influence of hiding is larger for asymmetrical flows than for symmetrical flows. Apparently, an enhancement of both the growth and the migration of the ridges is present, irrespective of the sign of the hiding coefficient. The only change is in the distribution of fine sediment, as will be explained in the next section.

4.4 Discussion

In this section a physical interpretation of the grain size pattern, as found in the model is given. This is done for the two hydrodynamic conditions considered in the experiments of the previous section: symmetrical and asymmetrical tidal forcing. The mechanisms discussed here are based on the concepts of the formation of tidal sand ridges under the assumption of uniform sediment, as discussed in Huthnance (1982a); Hulscher et al. (1993); Calvete et al. (2001a) and section 1.7 of chapter 1. In addition, the model results are discussed in relation to field observations.

4.4.1 Symmetrical tidal forcing

The first situation concerns a pure symmetrical M_2 tidal forcing, for which the velocity V of the basic state obeys $\overline{V^3} = 0$. This implies that no alongshore sediment flux is present in the basic state and $\vec{q}_{b0} = 0$. A local change in the size distribution of the surficial sediment can be understood as a result of the interaction of the tidal current with the bottom. The difference in the sediment transport capacity of the two grain size classes, caused by hiding effects, reduces the erosion and deposition flux of the finest sediment fraction. Consequently, a fining of the sediment in the erosion areas, and a sediment coarsening in the deposition areas occurs. A symmetrical current causes only growth of the perturbations and (almost) no

migration, because the largest erosion takes place in the troughs and the largest deposition occurs on the crest of the ridges. This corresponds to a mean grain size pattern, which is 180° out of phase with the topography. A more quantitative way to understand the results, is to examine the equations for the evolution of the bottom. Using equation (4.9) and an M_2 tidal forcing, equations (4.11) and (4.12) reduce to

$$(1-p)\frac{\partial h}{\partial t} = -T_2 \vec{\nabla} \cdot \overline{\vec{q}_b'} \tag{4.13}$$

$$(1-p)L_{a0}\frac{\partial f_1}{\partial t} = -T_3 \vec{\nabla} \cdot \overline{\vec{q}_b'} \tag{4.14}$$

where

$$T_2 = F_1 G_{b1} + F_2 G_{b2} \qquad T_3 = F_1 F_2 (G_{b1} - G_{b2})$$

The form of the equations is identical, so that the relation between h and f_1 is given by

$$\frac{\partial h}{\partial t} = L_{a0}\left(\frac{T_2}{T_3}\right)\frac{\partial f_1}{\partial t}$$

Depending on the sign of coefficient T_3, a phase difference between the bottom topography and the spatial pattern of the fraction of fine grains of 0° or 180° is found. The latter case, with the finest sediment on top of the ridges, occurs for $T_3 < 0$, which means $G_{b1} < G_{b2}$, thus $c_b > 0$ (see Figure 4.2(a)).

The enhanced growth rates for bimodal mixtures compared to uniform sediment are derived from equation (4.13). In case of a sediment mixture the time evolution of the bottom topography only differs from the uniform sediment case by a factor T_2. For a hiding formulation as introduced in equation (4.10) the function $T_2 \geq 1$, leading to the enhanced growth of perturbations for a bimodal sediment mixture. This effect was illustrated in Figure 4.1(a).

4.4.2 Asymmetrical tidal forcing

The second case involves a forcing by an asymmetrical tidal current, which can be either due to a steady component or the combination of an M_2 and M_4 tide. The important difference with the previous case is the non-zero alongshore bed load flux in the basic state. This induces a migration of the ridges in the direction of the maximum tidal current. In turn, the sediment pattern is shifted alongshore with respect to the pattern found for the case of a symmetrical tidal current. In particular, a fining on the (erosive) upcurrent flank of the ridge is found (Figure 4.2(b)), instead of a fining in the trough. Equations (4.11) and (4.12) in case of an additional current contribution (V_{M_4} or V_0) read

$$(1-p)\frac{\partial h}{\partial t} = -T_2\overline{\vec{\nabla} \cdot \vec{q}_b'} - [T_1 + T_2 T_5]\,\overline{\vec{\nabla} \cdot (\vec{q}_{b0} f_1)} \tag{4.15}$$

$$0 = -T_3\overline{\vec{\nabla} \cdot \vec{q}_b'} - [T_4 + T_3 T_5]\,\overline{\vec{\nabla} \cdot (\vec{q}_{b0} f_1)} \tag{4.16}$$

where

$$T_1 = G_{b1} - G_{b2} \qquad T_4 = F_2 G_{b1} + F_1 G_{b2} \qquad T_5 = \frac{c_b \sigma_0 \ln 2}{\sqrt{F_2 F_1}}$$

The left-hand side of equation (4.12) is neglected. This because the dominant balance is between the terms in (4.16), representing the unequal erosion of fine and coarse sediment due to hiding effects and a redistribution of sediment due to advection by a non-zero background sediment flux. This is a crucial difference with the balance found in the symmetrical tide case. In the expression for the divergence of the perturbed sediment flux (see appendix 4.A) the term involving the cross-shore gradient in the cross-shore component of the current ($\partial u'/\partial x$) controls the growth of tidal sand ridges (Calvete et al., 2001a). The divergence of this flux can thus be approximated by

$$\overline{\vec{\nabla}\cdot\vec{q}_b'} \sim -2\overline{V^2}\frac{\partial\overline{u'}}{\partial x} + 3\frac{\overline{V^3}}{H}\frac{\partial h}{\partial y} \tag{4.17}$$

Here the second contribution on the right-hand side causes the migration of the bedforms. To find the relation between h and f_1 a flood-dominant current is considered, i.e. $\overline{V^3} < 0$. For a realistic ratio of the tidal current amplitudes V_{M_4}/V_{M_2} the first term in the above expression is dominant over the contribution of the migration, reducing equation (4.16) to

$$(T_4 + T_3T_5)\overline{V^3}\frac{\partial f_1}{\partial y} \propto T_3\overline{V^2}\frac{\partial\overline{u'}}{\partial x}$$

For realistic values of the standard deviation σ_0, it is found that $T_4+T_3T_5 > 0$. The perturbed residual velocity follows the bottom contours, with an offshore component on the seaward flank of the ridge and a landward component on the landward flank, resulting in a clockwise (anticyclonic) circulation around the bar, leading to $\partial\overline{u'}/\partial x \propto h$. If this is substituted in the expression above, it follows that

$$-\frac{\partial f_1}{\partial y} \propto (G_{b1} - G_{b2})h$$

and the size distribution is $\pm$ 90° out of phase with topography. If $c_b > 0$ then $G_{b1} < 1 < G_{b2}$ and a fining of the bottom sediment on the upcurrent (seaward) flank of the ridges occurs. In Figure 4.2(b) this case is shown, where the phase shift is less than 90° due to the additional contribution of the migration term in eq. (4.17).

The enhanced growth and migration rates for bimodal mixtures compared to uniform sediment for asymmetric tides are due to the same effects as those discussed in case of a symmetrical tidal forcing. The main difference between these two cases is the last term (redistribution of sediment) in equation (4.15), however, experiments indicate that this contribution is only of minor importance to the growth and migration of the tidal sand ridges.

4.4.3 Comparison with field observations

The model predicts tidal sand ridges with the crest rotated counter-clockwise at an angle of $30° - 35°$ with the tidal current axis, which is in good agreement with measurements (Vincent et al., 1998). Forcing the model with a symmetrical M_2 tide showed that the coarsest sediment is located on the crest of the ridges, consistent with the general trend that is detected in the field data of the Belgium shelf. Furthermore, if forcing by a flood-dominant tidal current is considered, hiding effects in the bed load transport result in a pattern of the mean grain

size that is comparable to that observed on the southern part of the Middelkerke Bank, i.e. with the coarsest sediment on the landward flank. According to the model results, the offshore decrease in the flood-dominance contributes to the shift in the location of the maximum mean grain size. It is found that, for a temporal phase between the M_2 and M_4 tidal constituents such that the residual sediment flux is in the ebb-direction, the coarsest sediment is located on the seaward flank. This is in accordance with the pattern found on northern end of the bank. Although it is not very clear from field data whether the ridges migrate or not, they mostly indicate erosion on the landward flank and deposition on the steep seaward flank (Berné et al., 1994). The model for the flood-dominated tidal current predictes the opposite pattern. An alongshore migration, leading to erosion on the seaward flank is found.

Other researchers have suggested that the shift in the pattern could be related to the steepness of the flanks of the ridges. In the direction perpendicular to their main axes, the profile of the ridges is asymmetrical, with a steep seaward flank (Lanckneus et al., 1994). Since in the present study a linear stability approach is used, only symmetrical (sinusoidal) perturbations were incorporated in the model, and this hypothesis cannot be verified. Further research with a nonlinear model could provide such information.

The influence of storms on tidal sand ridges and their sedimentary pattern is still a matter of debate. As banks may rise up to 4 m below low water level at spring tide, the small depths and the exposure to storm waves from the north renders them susceptible to waves. Vincent et al. (1998) pointed out that the combined effect of strong tidal flows and oscillatory wave-induced currents, acting approximately normal to the tide, mainly results in the (enhanced) re-suspension of the bottom sediment. However, no observable effect on the direction of transport was found. The bank volume was used by Lanckneus et al. (1994) to assess the impact of different weather conditions on the formation and maintenance of the Middelkerke Bank. They found that the bank volume decays in periods of winter storms, while the bank restores during long periods of fair weather. Despite large variations of the volume during the season, these data suggest that on the long-term the banks are in equilibrium with the hydrodynamic conditions. On the other hand, Vincent et al. (1998) presented data which show an upslope sediment transport during storms. This suggests that waves are important for the maintenance of the ridges, and not only act to prevent their unrestricted growth due to tidal currents alone. Besides the impact on the morphology, Houthuys et al. (1994) also focused on the effect of storms on the surficial sediment grain size. Quiet, pre-storm conditions (fair weather), which are supposed to represent the tidally forced equilibrium state, were compared with the sediment distribution after a normal autumn storm period. The main changes were a coarsening on the north-western flank, contrary to a fining of the landward flank. It was argued that waves coming from the north cause a winnowing of fines on the exposed seaward flank, and subsequent deposition an the landward flank. In short, there is no consensus in the literature regarding the influence of storms and waves on the formation of the tidal sand ridges on the Belgian shelf (Houthuys et al., 1994; Vincent et al., 1998). Also, the ratio of suspended load transport over bed load transport is poorly known. The influence of waves was not included in this study, and only bed load transport was accounted for. The largest influence of waves can be expected in the nonlinear regime, supported by work done by Huthnance (1982a), which indicates that the effect of wind-waves on the initial growth of tidal ridges is small, while the equilibrium height is reduced. This thesis only explores tidal sand ridges in the linear regime. Nevertheless, owing to these uncertainties, the application

of the results would be more appropriate for tidal sand ridges in deeper water in the southern North Sea. The main problem with this is that no extensive sediment data are available for the more offshore located ridges, so that no verification of the model results is possible.

Including a suspended load transport in a tidally dominated (i.e. fair weather) forcing corresponds to an additional sediment flux, related to a higher power in the flow velocity (see in Bailard, 1981). Such a flux would enhance the growth rate and migration speed of the bottom perturbations. It does not change the bottom patterns as presented in this chapter, but a grain size dependent suspended load flux (enhanced transport fines) could in principle reverse the mean grain size patterns as found for bed load only (reduced transport fines). It would require a suspended load flux of the same order of magnitude as the bed load flux during fair weather and a strong grain size dependence.

The present model, with the restriction to bed load transport and tidally dominated or fair weather conditions, is not directly applicable to other shelves. Sedimentological information on sand ridges and grain size distributions exists for the Bristol channel (Pattiaratchi and Collins, 1987) and for tidal sand ridges in the Florida inner shelf (Davis et al., 1993). Although interesting differences with the sorting pattern (e.g. the location finest and coarsest sediment on ridge topography) for ridges on the Belgium shelf are perceived, a comparison with these data is beyond the scope of this chapter.

4.5 Conclusions

In this chapter a model was developed and analysed to study the initial formation of tidal sand ridges and the corresponding grain size distribution on meso-tidal shelves. The sediment was transported as bed load and dynamic hiding effects resulted in the selective transport of the two grain size classes.

The objective of the present study was to gain insight into the physical mechanisms responsible for the observed grain size distribution over the tidal sand ridges. To this end, the temporal and spatial characteristics of tidal ridges in case of a bimodal sand mixture were compared with results obtained in case of a single grain size class. Growth rates and migration velocities increased with increasing standard deviation of the sediment mixture, yielding realistic timescales for the formation of the ridges. The wavelengths of the ridges remained unchanged if more than one size class was considered. Experiments also revealed the importance of different forcing conditions. A forcing by M_2 tidal currents, in combination with a reduced flux of fine grains, resulted in a grain size distribution which was in phase with the ridge topography. The coarsest mean grain size was located on the crests, representative of the general pattern of the data. A shift between the topographical pattern and the pattern of mean grain size was introduced by adding an M_4 tidal constituent or a steady current to the forcing. A flood-dominant tidal current, in combination with the hiding of the finest grains, resulted in a coarser landward flank. These results are in fair agreement with field observations on the Belgium shelf.

Appendix

4.A Sediment flux

$$
\begin{aligned}
\vec{q}_{b0} &= (0\ ,\ 3\nu_b V^3) \\
\vec{q}_b' &= \left(\nu_b \left[3V^2 u' - \lambda_b |V|^3 \frac{\partial h}{\partial x}\right], \nu_b \left[3V^2 v' - \lambda_b |V|^3 \frac{\partial h}{\partial y}\right]\right) \\
\vec{\nabla} \cdot \vec{q}_b' &= \nu_b \left[V^2 \left(\frac{2}{V}\frac{\partial V}{\partial x} - \frac{3}{H}\frac{\partial H}{\partial x}\right) u' - 2V^2 \frac{\partial u'}{\partial x}\right. \\
&\qquad \left. +3\frac{V^3}{H}\frac{\partial h}{\partial y} - \lambda_b |V|^3 \left(\frac{\partial^2 h}{\partial x^2} + \frac{\partial^2 h}{\partial y^2} + \frac{3}{V}\frac{\partial V}{\partial x}\frac{\partial h}{\partial x}\right)\right]
\end{aligned}
$$

Here the linearised mass conservation is used to eliminate v' in the expression for $\vec{\nabla} \cdot \vec{q}_b'$. It reads:

$$
v' \frac{\partial H}{\partial x} = V \frac{\partial h}{\partial y} - H \frac{\partial u'}{\partial x} - u' \frac{\partial H}{\partial x} \tag{4.A-1}
$$

Chapter 5

Nonlinear evolution of shoreface-connected ridges and grain sorting

Abstract

A nonlinear model for the long-term evolution of the topography of shoreface-connected ridges and the variations in the mean grain size over this topography is presented. The importance of nonlinear processes for their maintenance is suggested by field observations: the amplitude of shoreface-connected sand ridges can be quite large (several metres) with respect to the water depth and their shape is often asymmetrical (seaward flanks are steeper than landward flanks). The linear analysis of chapter 3 is extended into the nonlinear regime, using a spectral method. The focus is again on storm-dominated micro-tidal shelves. With this model it is shown that, starting from an initial state without bedforms, a pattern of shoreface-connected ridges with finite amplitudes develops, whilst the downcurrent migration velocity of these ridges remains constant in time. Also, the maximum variation in the mean grain size evolves towards a constant value. Furthermore, the results of the nonlinear model show the development of an asymmetrical ridge topography. At the same time, the spatial shift between the patterns in the mean grain size and bottom topography (as found from the linear analysis) decreases. The processes that cause these changes are identified and explained. Extrapolating the results for the final height of the ridges to realistic values of the slope of the inner shelf provides a good agreement with the height and timescale of formation obtained from field observations. However, the modelled maximum variation in the fraction of fine and coarse sediment over the ridges are much smaller than those measured in the field. The reasons for this discrepancy are also discussed.

5.1 Introduction

Shoreface-connected ridges and tidal sand ridges that are observed on many coastal shelves (Swift and Field, 1981; Antia, 1996; Dyer and Huntley, 1999; Van de Meene and Van Rijn, 2000a) usually concern bedforms with a considerable height (several metres). In the interpretation of the data it is often implicitly assumed that these bedforms are in equilibrium with the environmental conditions on the shelf. The main objective of the study presented in this chapter is to model this "final" state of the evolution of large-scale ridges, with particular emphasis on the mean grain size variations over these ridges. Sediment sorting is incorporated in a simple way, and this study should be regarded as a first step to improve the knowledge on the long-term evolution of large-scale sand ridges for nonuniform sediments.

In chapter 2-4 of this thesis idealised process-based models were used to model large-scale sand ridges. The results of these models indicate that shoreface-connected ridges and tidal sand ridges can initially form as inherent free instabilities of the coupled bottom-water system. The wavelength, migration velocity, characteristic e-folding growth time and the phase shift between the topography and the mean grain size, as calculated with these models, already showed a good agreement with the general characteristics of the observed ridges. Nevertheless, these results are based on a linear stability analysis of the model equations and are strictly speaking only valid for bedforms with small amplitudes (compared to the water depth) and for small variations in the fractions of the different grain size classes with respect to their undisturbed values. Field data suggest that the amplitude of both shoreface-connected sand ridges and tidal sand ridges can be a considerable fraction (sometimes over 50%) of the local water depth, thereby indicating the importance of nonlinear processes for their maintenance. Whether the results of the linear analysis still hold in the nonlinear regime must be investigated with a model that is based on a nonlinear stability analysis. In addition, more detailed field information on the spatial structure of the bedforms, such as the asymmetry in the shape, final height, maximum variation in mean grain size and timescale of formation, can be compared with the results obtained with a nonlinear model.

As demonstrated in the previous chapters, the physics of both types of large-scale bedforms is quite different. In order to keep the analysis transparent, the focus of this chapter is on the nonlinear dynamics of shoreface-connected ridges only. These are found on storm-dominated shelves, with a characteristic spacing between successive crests of 2-6 km. The ridges migrate in the direction of the storm-driven current, with a velocity of 1-10 myr^{-1}. The estimated timescale for formation from geological evidence is in the order of centuries. Field data often show a final 'equilibrium' amplitude in the topography of shoreface-connected ridges, ranging from 1 to 9 m. The crests can reach up to 1/3 of the water depth in the shallowest areas, and troughs are excavated by the same amount below the mean sea bed level (Dyer and Huntley, 1999). The mean grain size of the surficial sediment shows maximum variations over the ridge topography that normally range from 0.5-2.5 phi (0.7-0.2 mm), as can be seen in Figure 1.4 (chapter 1). The finest sediment is found between the crests and the seaward (downcurrent) troughs, the coarsest sediment is located between the landward trough and the ridge crest (Swift et al., 1978). The bottom profiles of the ridges are asymmetrical: they have steep slopes on the seaward side and more gentle slopes on the landward side. Thus, the flanks of the ridges are steeper in the direction of migration, i.e. downcurrent of the average alongshore storm driven flow.

Swift and Field (1981) studied the ridges on the Atlantic shelf of North America, and reported a decrease in the maximum side slopes with increasing distance offshore, while along with that, the ratio of seaward to landward slope and the cross-sectional area of ridges both increase. Typical values for the side slopes are between $0.75^\circ - 2.0^\circ$, which correspond to a typical ridge height of 6-9 m (Swift and Field, 1981). Extreme low and high values for the side slope are 0.2° and 7°, while the extremes for the height are 3 m and 12 m. The asymmetry ratio (seaward:landward slope) is at most 5:1 for the most offshore located shoreface-connected ridges, for the more onshore located ridges this ratio is 2:1. On the Virginia shelf of North America, Swift et al. (1972) observed ridges which have troughs that are much broader and less well defined than the narrow and rounded crests. Along the coast of Argentine, the ridges are locally double-crested (Parker et al., 1982). The most northern ridges have steeper seaward flanks, while further south they are more nearly symmetrical. The shoreface-connected ridges along Dutch coast (southern North Sea) show both symmetrically- and asymmetrically-shaped profiles, where the steep slope can be either on the landward or on the seaward side (Van de Meene et al., 1996). The height is between 1 and 6 m, and side slopes are gentle: they range from 0.1° (1:400) to 0.3° (1:200).

Besides the morphological asymmetry also textural asymmetries are reported. They usually concern abrupt transitions from fine to coarse sediment in the troughs, while the transition from coarse to fine sand is more gradual over the crest. The asymmetry in the mean grain size profile, as a deviation from a sinusoidal shape, is clearly seen in Figure 1.4. The North American ridges (Swift et al., 1978) show finer sediments on the steeper (and downcurrent) flanks, a pattern which is also found for the ridges far offshore. For the Scotian shelf, Canada, Hoogendoorn (1986) observed the finest mean grain size at the base of the downcurrent (steep) flank. A similar distribution of mean grain size is also observed with the ridges in the German Bight (Antia, 1993): the finest sediments are found on the seaward (and downcurrent) flank. Also the crests are clearly covered with sediment that is finer than the sediment found on the landward flanks and in the troughs. The profile of the ridges in the German Bight changes with the distance from the shore: from nearly symmetrically-shaped ridges into ridges with a steeper seaward side further offshore.

The long-term evolution and the final state of the shoreface-connected ridges was investigated by Calvete et al. (2002) and Calvete and De Swart (2003). The work reported in these papers is a nonlinear extension to the linear work presented in Trowbridge (1995) and Calvete et al. (2001b). Their method involves the expansion of physical variables in truncated series of known eigenmodes of the linear system (given in Calvete et al., 2002) with unknown amplitudes. Substitution in the equations of motion and application of a Galerkin projection method then yields a system of nonlinear ordinary differential and algebraic equations for the amplitudes of the modes. This system was subsequently solved with standard numerical methods. The results of these models show the development of ridges that, after a few thousands years, reach a constant amplitude. In this saturated stage the bottom profiles are asymmetrical. The sediment flux is represented by a combination of bed and suspended load, where a parameterisation of the wave-stirring is included. In addition, the model of Calvete and De Swart (2003) includes a concentration equation and allows solutions which have an alongshore uniform structure and solutions with a longer spacing than that obtained from the linear analysis (subharmonics). The control parameter is the slope of the inner shelf, which turns out to be the limiting factor in their work. The method used is restricted to a small

slope of inner shelf, otherwise numerical instabilities occur. Nevertheless, extrapolation of the results to realistic values of the slope indicates good agreements with field data. From a physical analysis of the model output it was found that saturation behaviour is induced by nonlinear terms and that the bedslope terms in the sediment flux are key factors to reach a finite-amplitude.

So far, the nonlinear models for shoreface-connected ridges listed above are based on a single grain size which is used to represent the sediment flux. This motivates the main goal of this chapter, which is to provide insight in the physical mechanisms that play a role in the long-term development and maintenance of the shoreface-connected ridges in case of a sediment mixture. This will be done by generalising the nonlinear model, such that it is able to deal with the bottom evolution and the transport of sediment in the case of a mixture in the most simple way, following the theory discussed in chapter 3. By distinguishing the transport of two size classes, information on the final sediment distribution and the final amplitude of the variations in mean grain size can be retrieved from the model. For simplicity (and to keep the number of unknown variables to a minimum), the one-layer concept will be applied: an active transport layer is overlying an inactive substrate, with negligible interaction between them. This simplification has the (rather severe) restriction that the vertical variations in the mean grain size cannot be modelled. The advantage is that no rather ad hoc parameters of vertical sorting processes (Ribberink, 1987; Parker et al., 2000; Van Ledden et al., 2002a) need to be included, whereas this approach also yields insight in the basic performance of the model. We will return to these assumptions in the discussions in section 5.4 and chapter 6. The focus is again on storm-dominated micro-tidal shelves, with the model domain and parameters representative for the Long Island inner shelf of North America, as was also the location considered in chapter 3.

The specific questions that will be addressed are: how does the mean grain-size difference between crest and trough evolve in time, and does the use of multiple grain sizes influence the results for the bottom topography, as were found in case of a single grain size model? To this end, the model for shoreface-connected ridges in Walgreen et al. (2003) (chapter 3), which incorporates two grain size classes in the transport of sediment, is extended into the nonlinear regime. The techniques as discussed by Calvete et al. (2002) are used to obtain solutions.

In section 5.2 a brief summary of the model equations is given, including the methods used to solve the final system of equations. The main results of the nonlinear model for a single grain size are summarised. As will become clear in this section, the method used for the nonlinear analysis strongly depends on the results from linear analysis. Therefore, in section 5.3 first the relevant model results from a linear analysis are summarised (section 5.3.2 and 5.3.3), followed in section 5.3.4 by the results of the nonlinear analysis. The processes which are relevant for the physical mechanisms of the formation and maintenance of shoreface-connected ridges are illustrated in section 5.3.5. The main conclusions and a discussion on the results are given in section 5.4.

5.2 Model formulation and methods

5.2.1 Morphodynamic model: equations of motion

The model formulation and the linearised equations are identical to those that were already described in chapter 3. The interaction between the storm-driven current and the erodible bottom is considered on the domain shown in Figure 3.1, which includes the inner and outer shelf. A Cartesian coordinate system is used with x-axis and y-axis pointing in the cross-shelf and alongshelf direction. The selected bottom profile of the basic state reads

$$H = H_0 + \beta x \quad \text{for} \quad 0 \leq x < L_s \quad \text{and} \quad H = H_s \quad \text{for} \quad L_s \leq x < \infty$$

Thus, the undisturbed water depth H increases linearly on the inner shelf (width $L_s \sim 5.5$ km) and is constant on the outer shelf. The slope of the inner shelf is defined as $\beta = (H_s - H_0)/L_s$, where H_0 is the depth at the transition shoreface-inner shelf. Observations indicate that a realistic value for the slope of the inner shelf is $\beta_{obs} \sim 1.1 \times 10^{-3}$.

The water motion is described by the 2DH shallow water equations and mass conservation. They read

$$\frac{\partial \vec{v}}{\partial t} + (\vec{v} \cdot \vec{\nabla})\vec{v} + f\vec{e_z} \times \vec{v} = -g\vec{\nabla} z_s + \frac{\vec{\tau}_s - \vec{\tau}_b}{\rho D} \tag{5.1}$$

$$\frac{\partial D}{\partial t} + \vec{\nabla} \cdot (D\vec{v}) = 0 \tag{5.2}$$

Here $\vec{v}$ is the depth- and wave-averaged velocity, f the Coriolis parameter, $\vec{e}_z$ is a unit vector in the vertical, $\vec{\tau}_s$ the wind shear stress vector, $\vec{\tau}_b = \rho r \vec{v}$ the linearised bed shear stress vector, g the acceleration due to gravity, ρ the density of water and r is the bottom friction coefficient. Furthermore, t is time and $\vec{\nabla}$ is the two-dimensional (horizontal) nabla vector. The local water depth is given by $D = z_s - z_b$, where z_s is the free surface elevation and z_b is the bottom depth, both measured with respect to the undisturbed water level $z = 0$. The steady forcing of the water motion is caused by a prescribed longshore pressure gradient and a longshore wind stress. This model only represents conditions during storms, in which the water motion is characterised by strong waves (amplitude of the local near-bottom wave orbital motion is u_w) and a storm-driven net current. It is assumed that during fair weather conditions no sediment is transported, because the flow velocities are supposed to be below the critical velocity of erosion. Other forcing mechanisms that are not considered are the cross-shore wind stress, density gradients and tides. In the linear analysis, based on the depth-averaged shallow water equations, these appeared to have a minor influence on the dynamics of shoreface-connected ridges (Walgreen et al., 2002, and chapter 2). The bottom friction coefficient $r = c_d \langle |\hat{u}_w| \rangle$, where $c_d \sim 0.001$ is the drag coefficient which is assumed constant in this chapter. This is because in chapter 3 it was found that a grain-size dependent drag coefficient does not influence the initial formation of the shoreface-connected ridges. The wave-orbital velocity is defined as $\hat{u}_w = u_w \cos(\omega_w t)$ (symmetrical waves with frequency ω_w), with a depth-dependent amplitude. In accordance with the previous chapters on shoreface-connected ridges, it is given by $u_w = U_w (H_0/H)^{m/2}$. Here $U_w \sim 1$ ms^{-1} and $m \sim 1.6$. This means that we assume that in the inner shelf environment, with water depths

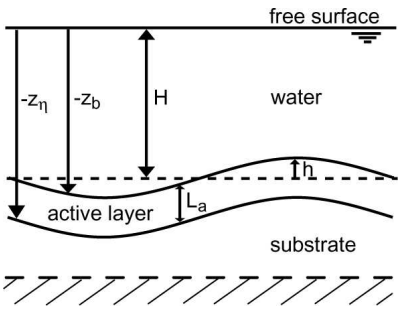

Figure 5.1: Definition of the sediment layer as used in the model. The thickness of the active layer is denoted by L_a and h is the elevation of the bottom with respect to a reference level.

of approximately 20 m, wave properties only depend on the reference depth and refraction and shoaling due to the presence of bedforms is not accounted for. This will be addressed in more detail in chapter 6. The expression is averaged over a wave period, indicated by $\langle..\rangle$.

For an extensive discussion on the equations used for the bottom evolution the reader is referred to section 3.2.3; here only the final equations are given. The bottom evolution and evolution of size distribution are based on a one-layer model for the bottom (see Figure 5.1). It involves a well-mixed active layer that overlies a substrate with a constant distribution in time. Furthermore, sand with two different grain sizes (d_1 and d_2 for fine and coarse material, respectively) is considered. Mass conservation for each size class yields

$$(1-p)\left(\mathcal{F}_i\frac{\partial z_b}{\partial t}+L_a\frac{\partial \mathcal{F}_i}{\partial t}\right)=-\vec{\nabla}\cdot\langle\vec{q_i}\rangle \qquad (i=1,2) \tag{5.3a}$$

where p is the bed porosity, $\mathcal{F}_i$ is the probability density function for grains of size d_i, $z_b = H-h$ the bed elevation with H the reference level and h the perturbation with respect to the undisturbed depth and $L_a \sim 0.02$ m is the thickness of the active layer. The instantaneous volumetric sediment flux per unit width during storms of grains with size d_i is indicated by $\vec{q_i}$; in (5.3a) it is averaged over a wave period. Using the constraint that $\sum_{i=1}^{N}\mathcal{F}_i=1$ with $N=2$ equation (5.3a) can be rewritten as:

$$(1-p)\frac{\partial z_b}{\partial t}=-[\vec{\nabla}\cdot\langle\vec{q_1}\rangle+\vec{\nabla}\cdot\langle\vec{q_2}\rangle] \tag{5.3b}$$

$$(1-p)L_a\frac{\partial \mathcal{F}_1}{\partial t}=-[(1-\mathcal{F}_1)\vec{\nabla}\cdot\langle\vec{q_1}\rangle-\mathcal{F}_1\vec{\nabla}\cdot\langle\vec{q_2}\rangle] \tag{5.3c}$$

The sediment flux for each grain size class (subscript $i=1$ indicates the class of fine sand, $i=2$ that of coarse sand) is composed of a bed load and a suspended load contribution, i.e. $\vec{q_i}=\vec{q}_{bi}+\vec{q}_{si}$. These are based on the formulations for a single grain size and corrected for availability of sediment in that size class and dynamic hiding effects. The latter refers to the fact that fine grains hide between the coarser grain, with the consequence that they do not experience the full stress of the water motion acting on the bed.

The formulations used for bed load sediment transport are

$$\langle \vec{q}_{bi} \rangle = \mathcal{F}_i \mathcal{G}_{bi} \vec{q}_b \qquad \vec{q}_b = \frac{3}{2} \nu_b u_w^2 \left(\vec{v} - \hat{\lambda}_b u_w \vec{\nabla} z_b \right) \qquad \mathcal{G}_{bi} = \left(\frac{d_i}{d_m} \right)^{c_b} \tag{5.4}$$

Here, $\mathcal{G}_{bi}$ is the transport capacity function for sediment with size d_i that is transported as bed load, coefficient c_b indicates the strength of the hiding (for a more extensive discussion see chapter 3) and d_m is the diameter of the local mean grain size. This formulation is based on the concept of dynamic hiding discussed by Day (see in Ribberink, 1987). The parameterisations for a single grain size are based on concepts discussed by Bailard (1981) for the transport during storms. The sediment flux parameterisation $\vec{q}_b$ is equal to the one in section 3.2.4 for bed load and averaged over the wave-period. The first contribution to $\vec{q}_b$ represents a stirring of the sediment by waves and the subsequent transport by the wave-averaged current. The second contribution to $\vec{q}_b$ (proportional to coefficient $\hat{\lambda}_b$) accounts for the preferred downslope movement of sediment. Here $\hat{\lambda}_b = \frac{8}{9\pi} \lambda_b$, with λ_b is the bedslope parameter of order 1 and $\nu_b \sim 2 \times 10^{-5}$ s^{2}m^{-1}.

For suspended load sediment transport the formulations are

$$\langle \vec{q}_{si} \rangle = \mathcal{F}_i \mathcal{G}_{si} \vec{q}_s \qquad \vec{q}_s = \nu_s u_w^5 D \left(\vec{v} - \hat{\lambda}_s u_w^2 \vec{\nabla} z_b \right) \qquad \mathcal{G}_{si} = \lambda_{\mathrm{E}}^5 \left(\frac{d_i}{d_m} \right)^{c_s} \tag{5.5}$$

where $\mathcal{G}_{si}$ is transport capacity function for sediment with size d_i for suspended load. Furthermore, $\lambda_{\mathrm{E}} = 1 - 0.288\sigma$ is a straining factor with σ the local standard deviation of the mixture. Besides the effect of hiding, the coefficient c_s also includes the effect of a grain size dependent settling velocity of the sediment, which is used in the derivation of the concentration. Note that $\vec{q}_s$ is a wave-averaged flux (the brackets are dropped). Its first (advective) contribution is obtained from $\langle C \vec{v}_t \rangle$, where $\vec{v}_t = \vec{v} + \vec{\hat{u}}_w$ is the total velocity. The depth-integrated volume concentration of sand C is, to a good approximation, determined by a local balance between entrainment and deposition. For the entrainment flux the formulation of Garcia and Parker (1991) is used, which has been validated against data for a sediment mixture. For deposition it is assumed that the near-bed volume concentration is proportional to the depth-mean concentration (see discussion in Van Rijn, 1993). The result is

$$C \simeq \delta_m \hat{E}_{m,u} |v_t|^5 D \tag{5.6}$$

where $\delta_m \sim 0.19$ is the ratio of the thickness of the suspended load layer of grains of size d_m over the water depth D, and $\hat{E}_{m,u} \sim 3 \times 10^{-4}$ s^{5}m^{-5} is related to the entrainment of these particles in uniform sediment. Comparing the expression for $\langle C \vec{v}_t \rangle$ with eq. (5.5), using the fact that the amplitude of the wave-orbital velocity u_w is much larger than the wave-averaged velocity amplitude $|\vec{v}|$, it follows that $\nu_s = \frac{32}{5\pi} \delta_m \hat{E}_{m,u} \sim 1 \times 10^{-4}$ s^{5}m^{-5}. Furthermore, a bedslope flux is included in the expression for the suspended load flux $\vec{q}_s$, with coefficient $\hat{\lambda}_s = \frac{1}{7} \lambda_s$. This is related to an 'efficiency' factor $\epsilon_s \sim 0.015$ and the settling velocity of sediment with size d_m: $w_{sm} \sim 0.04$ ms^{-1}, thus $\lambda_s = \epsilon_s / w_{sm} \sim 0.4$ sm^{-1}. This formulation uses the same ratio between the advective part and the bedslope part of the suspended load flux as used by Bailard (1981). In this paper an extensive discussion on the value of λ_s is included. A difference with the work of Calvete et al. (2002) is that both terms that contribute to $\vec{q}_s$ (proportional to $\vec{v}$ and $\hat{\lambda}_s$, respectively) are proportional to the volumetric concentration

C. This appeared to have little influence on the results and is consistent with the formulation used for the suspended load flux in chapter 3.

The boundary condition are such that the cross-shore flow velocity and the bottom perturbations are zero at the transition from the shoreface to the inner shelf ($x = 0$) and for $x \to \infty$. Also, no changes in the fraction of fine and coarse sediment are allowed at these boundaries.

The assumptions made to implement the equations in the final model are: a rigid lid approximation (small Froude number), thus $D = z_s - z_b \simeq -z_b$. A quasi-steady approximation allows the neglect of the time derivatives in hydrodynamic equations (5.1) and (5.2). This is because the bottom evolves on a timescale of centuries which is much longer than those of hydrodynamic processes (days-weeks). Also, a quasi-steady assumption is used in equation (5.3c), because the thickness of the active layer is relatively thin as compared to the water depth. This means that also the sediment distribution will adapt instantaneously to changes in the bottom. The expressions for the sediment fluxes $\vec{q}_b$ and $\vec{q}_s$ are derived for the case of symmetrical waves and do not allow for an onshore sediment transport to compensate for the slope effect of the reference bottom $\vec{\nabla} H$. Therefore, $\vec{\nabla} z_b$ is replaced by $\vec{\nabla} h$ in expressions (5.4) and (5.5), where h represents the bottom perturbations on the reference slope. Finally, in expression (5.6) for the concentration $D \simeq H - h$ is replaced by $H/(1 + h/H)$, and consequently also in (5.5). This means that for large-amplitude bottom perturbations more sediment is kept into suspension. The reason to adopt this depth dependence is one of numerical stability; the initial solutions are still consistent with the ones discussed in chapter 3.

5.2.2 Stability analysis

As was shown in the previous chapters and references therein, shoreface-connected ridges can form as a free morphodynamic instability of a basic state. The latter describes a steady storm-driven flow $V(x)$ over a shelf, characterised by a topography $H(x)$ and a distribution of fine and coarse sand $F_1(x)$ and $F_2(x)$, respectively, that only vary in the cross-shore (x) direction. Since the aim of this study is to analyse the dynamics of shoreface-connected ridges, it is convenient to split the model variables (velocity, free surface elevation, fraction of fine grains and bottom depth) in a basic state contribution and a perturbation on this basic state. Thus, $\Psi = \Psi_b + \psi$, where

$$\Psi = (u, v, z_s, \mathcal{F}_1, z_b) \qquad \Psi_b = (0, V, \zeta, F_1, -H) \qquad \psi = (u', v', \eta', f_1, h)$$

Note that Ψ_b and ψ are the vectors containing the information of the basic state and the perturbations, respectively. Details on how to calculate the basic state are discussed in section 3.3.1. It is assumed that the distribution function F_i is spatially uniform. These variables are used to compute the perturbations in the mean grain size, the standard deviation and the sediment flux (expressions (5.4) and (5.5)). The mean grain size is used in the formulations for the transport capacity functions, whereas the standard deviation only occurs in the suspended load function $\mathcal{G}_{si}$. For a complete formulation of these terms see Appendix 5.A.

Nonlinear analysis

The model variables that are split in a basic state contribution and a perturbation on the basic state, i.e. $\Psi = \Psi_b + \psi$, are substituted in the system of equations (momentum: (5.1), mass

balance: (5.2), fraction fine grains: (5.3c) and bottom evolution: (5.3b)). The properties of the basic state solutions are used to derive the equations for the perturbed variables, which can be written symbolically as

$$\mathcal{S}\frac{\partial \psi}{\partial t} = \mathcal{L}\psi + \mathcal{N}(\psi) \tag{5.7}$$

Here $\psi = (u', v', \eta', f_1, h)$ and $\mathcal{S}$ is a matrix which contains the temporal information of the perturbations. Furthermore, $\mathcal{L}$ is a matrix operator containing the linear contributions and $\mathcal{N}(\psi)$ is a vector operator containing the nonlinear contributions. The elements of $\mathcal{S}$, $\mathcal{L}$ and $\mathcal{N}(\psi)$ are given in Appendix 5.B. It shows that $\mathcal{S}$ only has one nonzero element, due to the term $\partial h/\partial t$ in equation (5.3c). This is consistent with the rigid lid and quasi-steady assumptions in the equations. The linear terms are the same as in chapter 3 and follow from the linearised system of equations.

In this study a spectral method is used to solve the system (5.7) of partial differential equations. The perturbations are expanded in known eigenmodes of the linear system, with amplitudes that are to be determined. This approach is used because the linear solutions already show a high resemblance with the observed ridges. Hence, at this point it is helpful to summarise the results of the linear stability analysis that will be used hereafter.

The linear perturbations are of the form $\psi(x, y, t) = \tilde{\psi}(x)e^{iky}e^{\Omega t} + c.c.$. Here $\tilde{\psi}(x)$ describes the known cross-shore structure of the perturbation, k is the longshore wavenumber and Ω is the complex growth rate. The real part Ω_r is the growth rate and the migration is obtained from the imaginary part: $c = -\Omega_{Im}/k$. For each possible longshore wavenumber k, growth rates (corresponding to different cross-shore mode numbers $n_k = (1, 2, 3, ...)$) can be computed by solving the eigenvalue problem. In previous chapters nearly always the dominant cross-shore mode, i.e. $n_k \equiv 1$, was shown. This is because the underlying assumption in a linear stability analysis is that the mode with the largest growth rate will dominate over all other modes since the model predicts exponential amplification for all modes. However, after some time the amplitudes will be quite large and nonlinear terms that are neglected in the linear stability analysis will become important. As a consequence, even modes that were damped in the linear case can be excited due to the nonlinear interaction between different modes.

For the expansion of the nonlinear solutions in the linear eigenmodes (as described in Calvete et al. (2002)), a truncated series of eigenmodes is selected. The mode with the largest initial growth rate ($k = K_M$) and its superharmonics will be used, i.e. $k = (2K_M, 3K_M, .., JK_M)$. Subharmonics, as considered by Calvete and De Swart (2003), are not included, i.e. perturbations with a wavelength longer than the wavelength of the linearly preferred mode cannot occur. The solutions are thus computed in a domain of alongshore length $L = 2\pi/K_M$, with periodic boundary conditions in the longshore (y) direction. Also the perturbation with an alongshelf-uniform structure, which describes the exchange between the inner and outer shelf and the inner shelf and the shoreface is not included. The reason to neglect them is that they hardly affect the solutions for h.

The structure of these different modes will be indicated by (j, n_j), where j is the alongshore mode number and n_j the cross-shore mode number. The number of eigenfunctions used in the time evolution is truncated at mode (J, N_J). The numerical values of the truncated numbers J and N_J should be chosen in such a way that the properties of the final

solution do not change if more modes are included. If this is the case then the main physics are represented correctly by the selected modes. The nonlinear solutions of the equations of motion are thus written as

$$\psi(x,y,t) = \sum_{j=1}^{J} \sum_{n_j=1}^{N_J} \begin{pmatrix} \hat{u}(t)\tilde{u}(x) \\ \hat{v}(t)\tilde{v}(x) \\ \hat{\eta}(t)\tilde{\eta}(x) \\ \hat{f}(t)\tilde{f}(x) \\ \hat{h}(t)\tilde{h}(x) \end{pmatrix}_{jn_j} e^{ijK_M\ y} + c.c.$$

Here, for example, $\hat{u}_{jn_j}(t)$ is the amplitude of the cross-shelf velocity component with mode-number (j, n_j) and $\tilde{u}_{jn_j}(x)$ is its known cross-shore structure. This expansion is inserted in the nonlinear system (5.7) and results in equations for the amplitudes $\hat{u}_{jn_j}, \hat{v}_{jn_j}, \hat{\eta}_{jn_j}, \hat{f}_{jn_j}$ and $\hat{h}_{jn_j}$. The equation for u' is projected on the adjoint linear eigenfunction of u', indicated as $\tilde{u}^+_{jn_j}$, the equation for v' on $\tilde{v}^+_{jn_j}$, etc. This means that the equations are multiplied by a specific adjoint and subsequently are integrated over the domain. These adjoint eigenfunctions are known solutions of a linear system. The reason for projecting onto the adjoint eigenfunctions is that this is a very effective way of solving the nonlinear system because they usually form a bi-orthogonal set with the eigenfunctions. For the case discussed in this chapter, where the only time-derivative is included in the equation for the bottom evolution h, it turns out that only the bottom modes and adjoint bottom modes form a bi-orthogonal set. This is due to the singularity of the $\mathcal{S}$ matrix which is a direct consequence of the quasi-steady approximation. This is a typical problem that arises in morphodynamic systems.

Finally, one ends up with a system of equations in terms of the amplitudes of mode (j, n_j). Of the five equations for each mode, four are algebraic equations, whereas one equation (for h) is a differential equations. The model discussed in this chapter is an extension of the nonlinear model for a single representative grain size class. This Galerkin projection method is solved numerically, using a third-order time integration scheme. A similar system of equations is given in Calvete (1999), where also more details about the computation of adjoint eigenfunctions and solving the final set of equations are given.

One final problem is left to discuss: the selection of modes and the truncation of spectral expansions. If the linear system is solved it turns out that, deep in the spectrum, there are modes which seem not physical. Their spatial structure is highly irregular and they also show strong variability on the outer shelf. If such modes are included in the spectral expansions as given above, they result in strong numerical instabilities. Therefore, these modes have to be a priori filtered. An effective way to do this is to assume that there is no spatial convergence of sediment transport on the outer shelf. This assumption has almost no effect on the correct modes, because they are trapped to the inner shelf, because they are trapped to the inner shelf, but it causes the growth rates of all spurious modes to vanish, thereby providing an efficient selection method.

5.2.3 Summary of previous model results

Previous modelling work (Calvete et al., 2002) already showed that the method discussed in section 5.2.2 of using linear eigenmodes is only successful in case that the transverse bot-

tom slope β of the inner shelf is small. The model which assumes uniform sediment shows the development of migrating ridges that ultimately reach a constant amplitude. Numerically stable solutions could only be obtained for a bottom slope (β) up to half of its realistic value. For large values of β solutions become unbounded at some time during the saturation process. Nevertheless, extrapolation of their findings (amplitude and pattern of saturated ridges, saturation timescale) to realistic values of the slope yields results that show good agreements with field data. Therefore, in experiments done with the nonlinear model for nonuniform sediment, that are presented in this chapter, a small value of the transverse bottom slope is taken. The advantage is that for this setting a relatively low number of modes is needed to obtain reliable solutions.

5.3 Results

The main motivation of the present study was to investigate whether it is possible to model the finite-amplitude behaviour of shoreface-connected sand ridges in combination with the long-term evolution of the local fractions of fine and coarse sediment. Therefore, numerical simulations were performed with the nonlinear spectral model that was derived in section 5.2. This is done for a storm-dominated shelf characterised by sediment composed of grains with two different sizes, for which the default model parameter values are given in section 5.3.1. The initial state represents a situation without ridges; only small random perturbations in the bottom (typical amplitudes of 10^{-4} m) are present. The linear solutions for the default case (section 5.3.2) are used as the expansion modes in the nonlinear spectral model. Their dependence on other values of the transverse bottom slope, the standard deviation and the bed load hiding coefficient is also presented (section 5.3.3). Section 5.3.4 shows the model results of the nonlinear analysis for the default parameter setting. The processes involved in the development of perturbations with a finite amplitude are illustrated in section 5.3.5. Finally, in section 5.3.6 results are presented of a sensitivity study to give an indication for the robustness of the model results at the final saturated state of the system.

5.3.1 Parameter values: default case

The default case is representative for the Long Island shelf ($\sim 40^\circ$ N) on the Atlantic coast of North America, thus the Coriolis parameter $f \sim 1 \times 10^{-4}$ s^{-1}. The bottom profile for the inner shelf (width $L_s = 5.5$ km) and outer shelf is indicated in section 5.2.1. Experiments are done with a mild bottom slope in the basic state: $\beta = 1.3 \times 10^{-4}$, which corresponds to an increase in depth over the width of the inner shelf from $H_0 = 14.0$ m to $H_s = 14.7$ m, as indicated in Figure 5.2. This slope is approximately 10% of its observed value in this area. Observations (Niedoroda and Swift, 1981; Lentz et al., 1999) show that typical values for the forcing during storms are

$$\tau_{sy} \sim -0.25 \text{ Nm}^{-2} \qquad s_0 \sim 2 \times 10^{-7} \text{m m}^{-1} \qquad U_w \sim 1 \text{ ms}^{-1}$$

where τ_{sy} is the alongshore component of the wind stress vector, s_0 is the alongshore component of the sea surface gradient and U_w the amplitude of the wave-orbital motion at $x = 0$. The resulting typical steady current amplitude is $U \sim 0.4$ ms^{-1}, of which the cross-shore

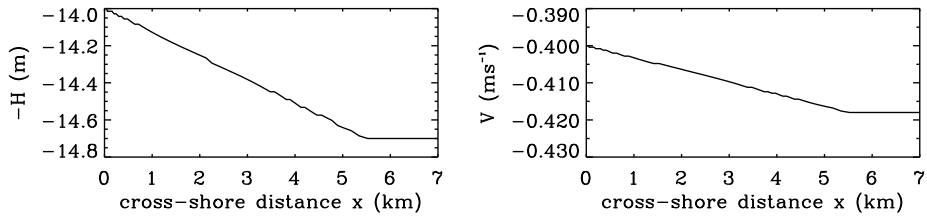

Figure 5.2: Basic state; cross-shore profi le of bottom (left) and velocity (right).

profile is shown in Figure 5.2 (right subplot). Furthermore, in the basic state equal amounts of fine and coarse sediment are present, which are uniform over the domain: $F_1 = F_2 = 0.5$. The mean grain size is $d_m = 0.35$ mm and for a standard deviation of $\sigma_0 = 0.50$ (default) these values correspond to a fine grain size class with a diameter of $d_1 = 0.25$ mm and a coarse fraction with $d_2 = 0.50$ mm. A typical value for the advective part of the bed load flux in the model is $Q_b = \frac{3}{2}\nu_b U_w^2 U \sim 1 \times 10^{-5}$ m^{2}s^{-1}. The advective suspended load flux is $Q_s = \nu_s U_w^5 H_0 U \sim 6 \times 10^{-4}$ m^{2}s^{-1}. Other parameter values are the typical magnitudes of the bedslope fluxes: $\frac{3}{2}\nu_b \hat{\lambda}_b U_w^3 H_0/L_s \sim 3 \times 10^{-8}$ m^{2}s^{-1} for bed load and $\frac{32}{5\pi}\hat{\lambda}_s \nu_s U_w^7 H_0^2/L_s \sim 2 \times 10^{-7}$ m^{2}s^{-1} for suspended load. The default case is defined by hiding in suspended and bed load, with values of $c_s = -1.1$ and $c_b = 0.75$, respectively. This means a reduced transport of the coarse grain size class for transport due to suspended load and a reduced sediment flux of the fine grain size class for bed load. For a more extensive motivation of these choices see Walgreen et al. (2003), also chapter 3.

The number of modes used in the nonlinear evolution was truncated at $J = 25$ (longshore) and $N_J = 16$ (cross-shore) for this value of β. The timestep involved in the time integration is 10 yr. This turned out to be sufficient: adding more modes or decreasing the timestep did not affect the behaviour of the solutions.

5.3.2 Linear analysis: default case

The growth rate curve of the linear perturbations evolving on the basic state of the model is shown in Figure 5.3. The default values for the model parameter are used. The largest possible growth rate $\Omega_{r,M}$ is found for a mode that has an alongshore wavenumber $k = K_M \sim 0.8$ km^{-1}. This is called the (initially) preferred mode. The corresponding wavelength is $\lambda = 2\pi k^{-1} \sim 7.6$ km, and its e-folding timescale for the growth is $\Omega_{r,M}^{-1} \sim 2.3 \times 10^3$ yr. As explained in section 5.2.2, the linear modes that are used as expansion modes in deriving the nonlinear spectral model equations are those with a longshore wavenumber of $k = (1, 2, .., J) \times K_M$. In this case only two of these modes have positive growth rates: the (1,1) mode with the wavenumber K_M and the (2,1) mode, with $k = 2K_M \sim 1.6$ km^{-1}. Both have a structure of one ridge in the cross-shore direction (cross-shore mode numbers $n_1 = 1$ and $n_2 = 1$). The spatial structures of the (1,1) bottom mode and of the mode with $n_1 = 2$, i.e. mode (1,2), are shown in Figure 5.4. The greyscale is used to indicate the height of the perturbations in the basic state topography (h), contour lines show the perturbation in the

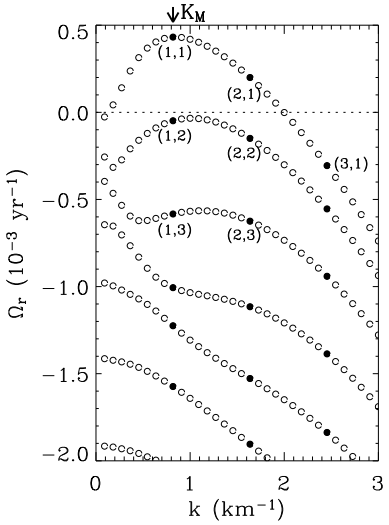

Figure 5.3: Linear growth rates as a function of the longshore wavenumber k. The largest growth rate is found for $k = K_M \sim 0.8$ km^{-1}. Parameters have their default values for nonuniform sediment. The filled dots indicate which modes from this plot are used in the nonlinear analysis.

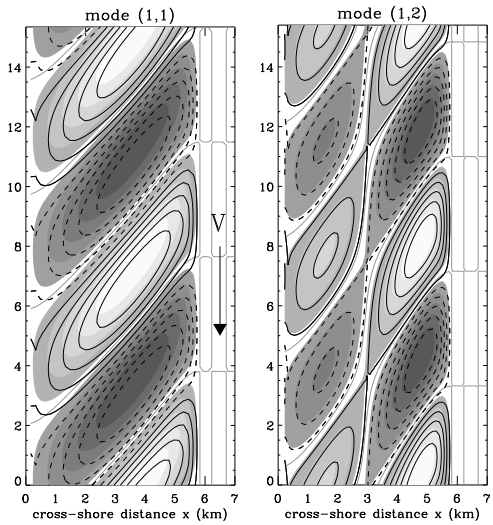

Figure 5.4: Structure of first two linear cross-shore modes for $k = K_M$ (mode (1,1) and (1,2)). Bottom perturbations are indicated by the greyscale (light: bars, dark: troughs); contour lines indicate the perturbation in the fraction of fine grains (solid: $f_1 > 0$, dashed: $f_1 < 0$). The arrow indicates direction of basic state longshore velocity V. Parameters have their default values for nonuniform sediment.

fraction of fine grains (f_1). The (1,1) mode clearly shows a phase shift between the pattern of h and f_1, whereas for mode (1,2) the shift is hardly present. This might be related to the fact that the growth rate of the preferred mode is dominated by suspended load. For the other modes, which grow slower, the bed load becomes relatively more important with respect to suspended load. In chapter 3 it was already discussed that the hiding in bed load favours a 0° phase shift between the fraction of fine sand and the topography, while suspended load favours a 90° phase shift. It should be kept in mind that a linear relation exists between the perturbations in the mean grain size (ϕ'_m) and the perturbations in the fraction of fine grains (f_1) (see in (5.A-2)).

5.3.3 Linear analysis: sensitivity to parameter values

The changes in the general characteristics of the linear modes if the slope of the inner shelf is increased towards more realistic values are plotted in Figure 5.5. It shows the variation in the wavenumber K_M of the preferred mode, its growth rate ($\Omega_{r,M}$) and migration velocity (c_M) versus β. The critical value for the slope of the inner shelf below which no instabilities grow is $\sim\ 0.03 \times 10^{-3}$. Larger values of β correspond to a smaller initial wavelength, a faster growth and a slower migration. The phase shift between the pattern of f_1 and h appears

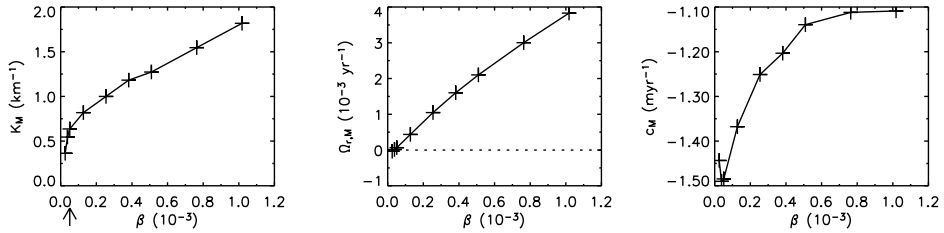

Figure 5.5: Wavenumber K_M of the preferred linear mode, growth rates and corresponding migration c_M velocities as a function of the slope of the inner shelf in the basic state. The default value for β is indicated by the arrow. Other parameters have their default values for nonuniform sediment.

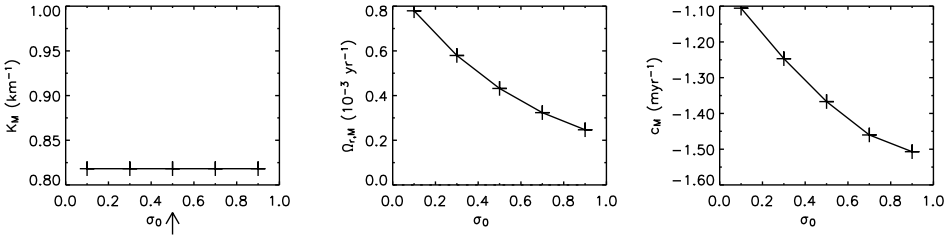

Figure 5.6: As in Figure 5.5, but for different values of the standard deviation σ_0 of the sediment mixture (arrow indicates the default value of σ_0). Other parameters, including β, have their default values for nonuniform sediment.

to increase slightly with higher values of β for the reason that was explained at the end of section 5.3.2.

The results for a nonuniform sediment mixture can be related to the results for uniform sediment by decreasing the standard deviation of the mixture. A default value of $\sigma_0 = 0.5$ in the basic state was used for the two-grain size mixture, whereas $\sigma_0 = 0$ by definition corresponds to a single grain size. As shown in Figure 5.6, within a realistic range of standard deviations, the wavenumber of the preferred mode does not change, its growth rate decreases with increasing values of σ_0 and its migration velocity increases. Thus, for identical slopes of the inner shelf, the number of linear modes that have positive growth rates is larger for sediment consisting of a single grain size than for a two-size mixture. These characteristics of the linear solutions do not strongly depend on the formulations of the hiding function in the transport of bed load (Figure 5.7). However, the relative strength of hiding in bed load sediment transport (represented by the coefficient c_b) with respect to the hiding in suspended load (represented by c_s) determines the phase shift between h and f_1. This will be investigated only by changing the value of c_b because the situation for $c_b = 0$ and $c_s \neq 0$ is the more interesting case. The reason for this will become clear in section 5.3.6. As mentioned above, this linear phase shift is $\sim 90^\circ$ for $c_b = 0$ and $c_s \neq 0$, and it decreases with larger values of c_b.

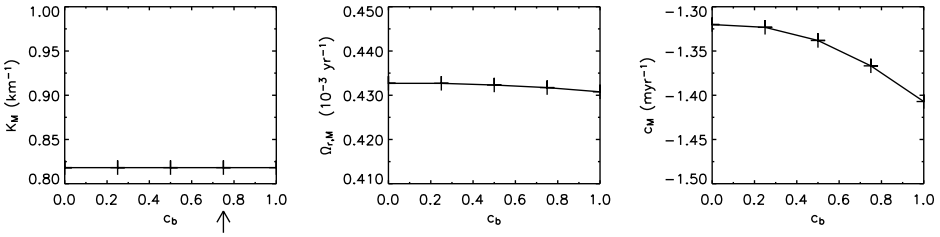

Figure 5.7: As in Figure 5.5, but for different formulations of the hiding function in the transport of bed load (arrow indicates the default value of c_b).

5.3.4 Nonlinear analysis: default case

Figure 5.8 (left subplot) shows for the default case the temporal evolution of the maximum and minimum heights (with respect to the level of the undisturbed bottom), as well as the evolution of the total height of the ridges. The subplot on the right shows the same characteristics, but for the fraction of fine sediment. In addition, Figure 5.9 shows the evolution of the amplitudes of the five modes that have the largest values at the final time of the simulation ($t \sim 25 \times 10^3$ yr). This is done for the amplitudes of h (defined as $|\hat{h}_{jn_j}|$) and f_1, where the structure of the bottom topography at a specific time is determined by the longshore (j) and cross-shore (n_j) mode numbers that have positive amplitudes.

The subplots of Figures 5.8 indicate that, in the initial stage of evolution, the height of the bedforms and the variation in the fraction of fine grains increase exponentially in time. After some time (in the present case after about 8×10^3 yr) amplitudes are large enough (although the height of the bedforms is only about 0.02 m) for nonlinear processes to start to grow, whereas their effect becomes important around $t \sim 15 \times 10^3$ yr. The consequence is that the full model results start to deviate from those predicted by the linear stability analysis (see the dashed lines in the two subplots of Figure 5.8). In Figure 5.9 it can be seen that nonlinear interactions between different modes are such that they cause excitation of modes which are linearly damped, such as the (2,2), (3,3) and (3.2) mode. This causes a reduction in growth of the height of both the bedforms and the size fractions and after about 20×10^3 yr they become even constant. The total height of the bottom perturbations in this saturated stage is approximately 0.72 m, which is slightly larger than the total change in depth over the inner shelf in the basic state. The total variation in the fraction of fine and coarse grains is rather small: less than 1% of their characteristic values $F_1 = F_2 = 0.5$ in the basic state. Figure 5.9 demonstrates that the saturated stage is still dominated by the (1,1) mode, which was also the initially preferred mode.

The spatial patterns of the perturbations in both the bottom and fraction of fine sediment at different times during the evolution are shown in Figure 5.10. The different greyvalues are indicative of the local elevation the bottom (light: crests, dark: troughs) that exist on an inner shelf with a transverse bottom slope, contour lines indicate the pattern in f_1. The bedforms which develop from the initially random pattern of modes with equal (small) amplitudes soon resemble shoreface-connected ridges. They migrate in the direction of the mean storm-driven flow (negative y-direction). Initially, a spatial phase shift between bottom perturbation and

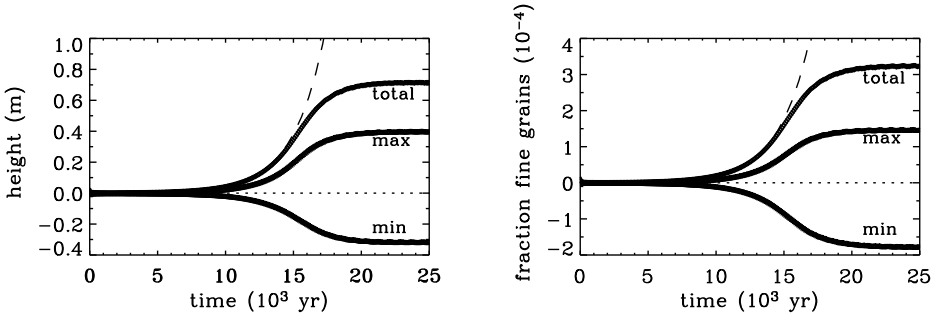

Figure 5.8: (Left) Time evolution of maximum, minimum and total height of the bedforms. (Right) Time evolution the total (=max-min) variations in the fraction of fine grains. The dashed line indicates the linear solution for the total. Default case.

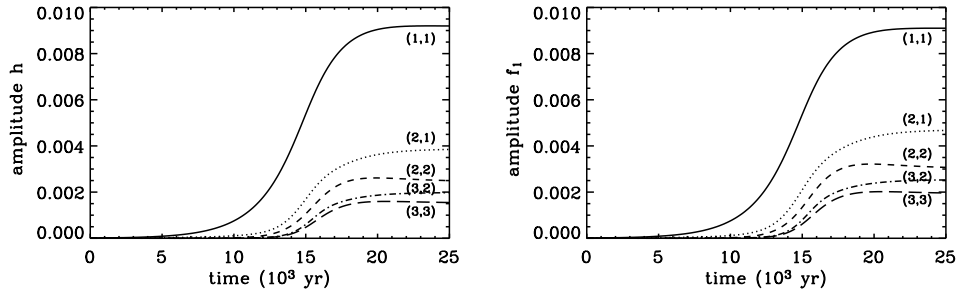

Figure 5.9: Time evolution of the amplitude of the five modes which have the largest values at the final time $t = 25 \times 10^3$ yr. (Left) Amplitudes of bottom modes $|\hat{h}_{jn_j}|$. (Right) Amplitudes of modes for fraction of fine grains $|\hat{f}_{jn_j}|$. Default case.

fraction of fine sediment is present. This is consistent with the results of a linear stability analysis, as presented in Figure 5.4. During the nonlinear stage of the evolution the spatial patterns of the bottom and fractions of fine and coarse sediment become asymmetrical. Most noticeable are the mild gradients on the landward (and upstream) sides and the steep gradients on the seaward (and downstream) sides. The ratio of the seaward slope and landward slope, once a constant amplitude of the ridges is reached, is 6:1. The steepening of the downstream flank ridges can also be seen in Figure 5.11 which shows the alongshore locations of one ridge crest and its downstream trough as a function of time. This figure also shows that in the saturated stage the ridges are still migrating with a speed that hardly deviates from that predicted by a linear stability analysis.

A new result is that the distance between location of ridge crest and the location where the finest sediment occurs decreases during the nonlinear evolution stage. In the final state this distance is so small that the finest sediment is almost located at the crests; likewise the coarsest sediment is found almost in the troughs. This tendency is rather difficult to relate to field data, as in general the finest sediments are observed at measurable distances downstream

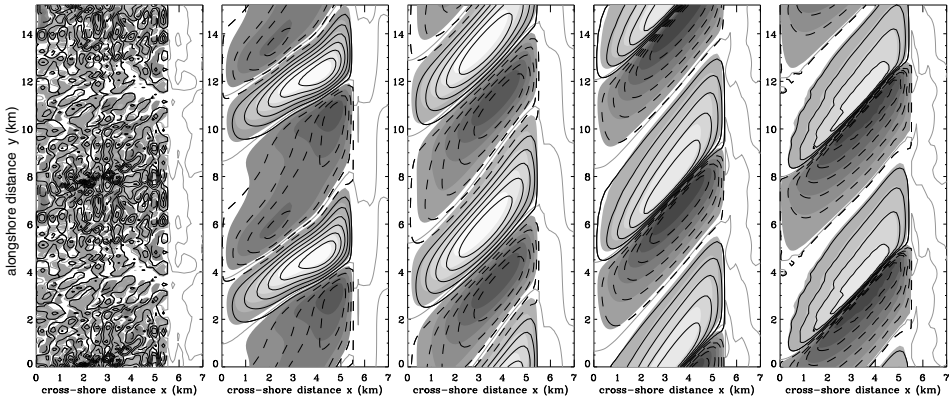

Figure 5.10: Contour plot of perturbations in bottom (greyscale) and fraction of fine grains (contour lines) at different times during the model simulation. Light areas indicate a crest, dark areas indicates a trough. Solid lines show increase in fraction of fine grains, dashed lines a decrease. For $t \sim 0, 2, 6, 16, 25 \times 10^3$ yr. Default case (initial state: ridges are absent). Note that the alongshore position of the crests and troughs changes between the plots; this is caused by a migration of the pattern in the negative y-direction.

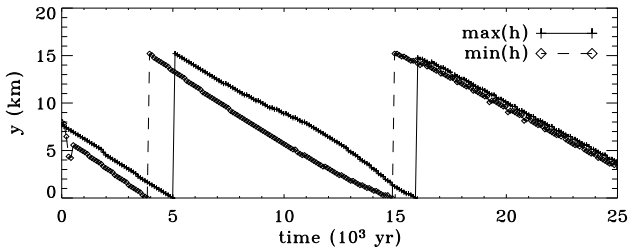

Figure 5.11: The y-coordinate of the location of the maximum and minimum bottom perturbations as a function of time. It shows the migration of the crest and its adjacent downcurrent (seaward) trough.

of the ridges. We will return to this aspect in the discussion and in chapter 6. At this point it is also important to remark that the time to reach the final saturated stage is quite long. However, it should be realised that in the simulations a rather small value of the transverse bottom slope β has been used. As will appear later on (section 5.3.6), the saturation timescale becomes considerably smaller if β is increased.

In short, during the evolution process the shape of the ridges evolves from symmetrical to highly asymmetrical, the height of the ridges ultimately becomes constant and the initial shift between the location of the maximum in f_1 and h decreases during the process of saturation. In order to gain further knowledge about these changes the model is analysed in more detail in the next subsection.

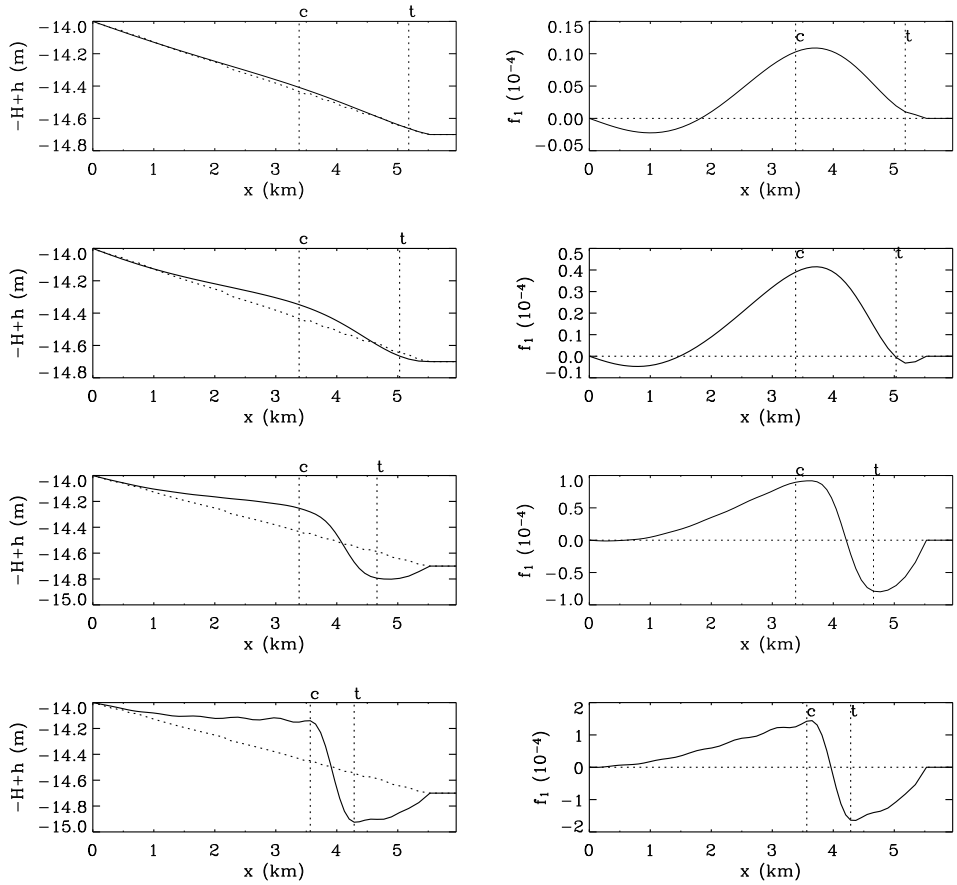

Figure 5.12: Shore-normal cross-sections of perturbations in depth $(-H+h)$ and fraction of fine grains (f_1) through the ridge top. The basic state distribution of the fraction of fine grains is $F_1 = 0.5$ and uniform in the domain. The dotted lines indicates the depth of the inner shelf in the basic state and the locations of the maximum of h (c: crest) and minimum of h (t: trough) for this shore-normal section. The sections are taken at $t \sim 10, 13, 16, 21 \times 10^3$ yr, with time increasing from top to bottom. The alongshore locations of these sections in time are indicated by $\max(h)$ in Figure 5.11.

5.3.5 Process analysis

The first step in understanding the model behaviour is to plot shore-normal cross-sections of the total depth $(-H + h)$ and the perturbations in the fraction of fine grains (f_1) at different times during the evolution through the highest point of the ridge crest. The results are shown in Figure 5.12; the corresponding alongshore y-coordinates at the different times can be found from Figure 5.11. The cross-shore bottom profiles clearly reveal that during the nonlinear evolution stage the depth at the landward side of the crest becomes almost constant. The seaward flank of the ridge has a slope of $\sim 0.05^\circ$ in the shore-normal direction. The ratio

of seaward and landward slope is most easily determined from a shore-parallel section: it increases from 1.2 (at $t \sim 10 \times 10^3$ yr), to 3 and 5 (at $t \sim 14$ and 17×10^3 yr). Note that in the nonlinear evolution stage (Figure 5.12 bottom) small-scale perturbations develop on top of the large-scale ridges.

Since morphodynamic changes are due to the divergence and convergence of the sediment flux it is useful to consider these as well. Moreover, to gain insight in the underlying processes, this convergence is split into parts related to suspended load and bed load. At first we focus on the temporal behaviour of the bedforms. As follows from eq. (5.3b), in this case it is not necessary to distinguish between fine and coarse sediment fractions because the different contributions are added. Rather, it is sufficient to make a further distinction into advective and bedslope (proportional to the terms $\hat{\lambda}_s$ and $\hat{\lambda}_b$) contributions. Cross-shore profiles of these contributions at different times during the development of the ridges (identical to those used in Figure 5.12) are shown in Figure 5.13. From this it follows that, during the linear stage, near the crest the convergence of the suspended load sediment flux is much larger than that of the bed load flux. In the area between the crest and the trough the convergence of the bed load flux is dominant. Thus, suspended load transport determines the growth, while bed load transport mainly determines the migration of the ridges in the initial phase of the development of the ridges.

First the growth and saturation process is investigated in more detail, i.e. the convergence of the suspended load flux. Advective processes cause growth, and the bedslope contribution causes decay, hence their the patterns are $\sim 180^\circ$ out-of-phase. During the initial stage the advective part dominates over the bedslope part, but the magnitude of the bedslope part rapidly increases with respect to that of advective part, until ultimately a balance is established with a negligible total convergence on the crest. This can also be seen in Figure 5.14, which shows the convergence of the advective and bedslope suspended load fluxes as a function of the total height of the ridges (left subplot) and the ratio of these two on the crest (right subplot). On the crest there is a net deposition of sediment due to convergence of the suspended load sediment flux. For a height of the ridges up to ~ 0.05 m (at $t \sim 12 \times 10^3$ yr) the magnitude of the convergence of the advective flux increases to a value which is $\sim 3.5\times$ larger than that of the bedslope flux. Beyond this point the divergence of the bedslope flux increases more rapidly than the convergence of the advective flux at the crest, until they ultimately balance. If a height of ~ 0.45 m (at $t \sim 16 \times 10^3$ yr) is reached another change in the behaviour is seen. Hence, the saturation of the height of the ridges occurs because the bedslope contribution in the suspended load sediment flux increases more rapidly than the advective contribution.

The increase in the bedslope flux can be related to the shape of the bottom profile. Note that the maximum convergence due to suspended load is not on the crest of the ridge, but shifted offshore and downcurrent with respect to the crest (see Figure 5.13, left panel). Thus the maximum deposition occurs on the high part of the seaward flank, whereas the maximum erosion due to suspended load shifts towards the deep part of this flank during the growth process, i.e. both extremes are on the seaward (steep) side of the ridge (at $t \sim 16 \times 10^3$ yr). As a result, suspended load is responsible for the asymmetrical bottom profile. The transition towards such a shape of the ridge is accompanied by a rapid increase in the second-order derivatives of the bottom perturbation (h_{xx} and h_{yy}) at the crest. This confirms the conclusion by Calvete and De Swart (2003) that, within the present model context, the bedslope term is important to reach the saturation. So, not only was a bedslope contribution to the sediment

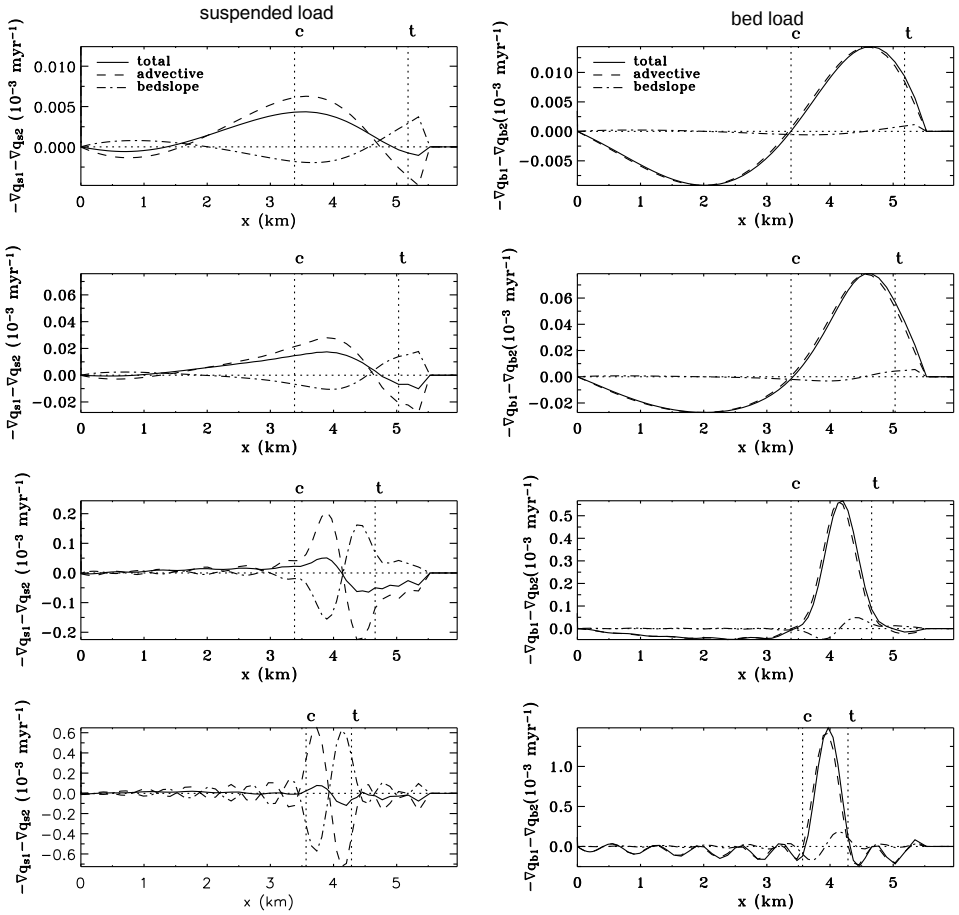

Figure 5.13: Shore-normal cross-sections of: (Left) the convergence of the total suspended load flux ($-\vec{\nabla}\cdot\vec{q}'_{s1} - \vec{\nabla}\cdot\vec{q}'_{s2}$). (Right) the convergence of the total bed load flux ($-\vec{\nabla}\cdot\vec{q}'_{b1} - \vec{\nabla}\cdot\vec{q}'_{b2}$). The total is split in an advective and a bedslope contribution, sections are taken through the ridge top. The vertical dotted lines indicated the locations of the maximum of h (c: crest) and minimum of h (t: trough) for this section. The sections are taken at $t \sim 10, 13, 16, 21 \times 10^3$ yr, with time increasing from top to bottom.

flux needed in the linear analysis to find a preferred wavelength of the perturbations, it also is essential in the mechanism which results in a reduction of the growth and a finite height of the ridges.

The convergence of the bed load sediment flux is also plotted in Figure 5.13 (right-hand panel). Cross-sections at different times show that this term causes downcurrent migration, specifically by its advective part. The bedslope contribution is negligible. Deposition occurs over almost the complete downstream (and seaward) flank, erosion over the upstream (and landward) flank, a pattern of erosion and deposition which does not change in time. This

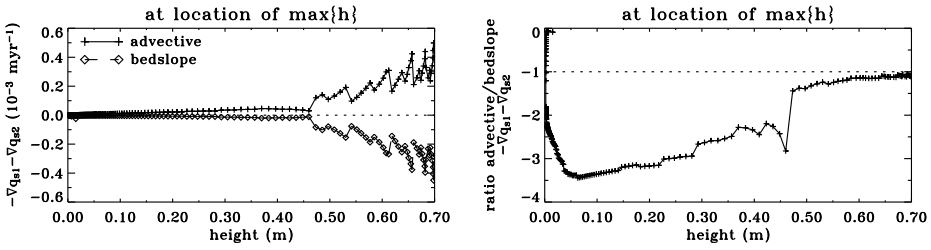

Figure 5.14: (Left) Convergence of the total suspended sediment flux ($-\vec{\nabla}\cdot\vec{q}'_{s1}-\vec{\nabla}\cdot\vec{q}'_{s2}$) as a function of the total height of the ridges. It is split into an advective and a bedslope contribution. The value is evaluated for each time of the computation at the location of the maximum bottom perturbation. (Right) Ratio of the advective over the bedslope contribution to the total convergence of the suspended sediment flux.

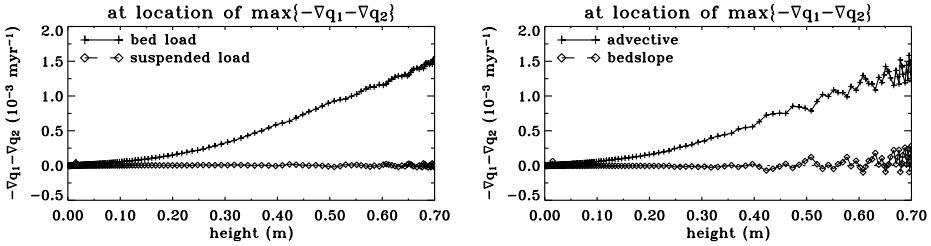

Figure 5.15: Convergence of the total sediment flux ($-\vec{\nabla}\cdot\vec{q}'_1-\vec{\nabla}\cdot\vec{q}'_2$) as a function of the total height of the ridges. It is split in a contribution due to bed load and suspended load (left), and into an advective and a bedslope contribution (right). The value is evaluated for each time of the computation at the location of the maximum convergence of the total flux.

migration behaviour is demonstrated in Figure 5.15 (left subplot), which shows that, at the location of the maximum convergence of sediment, the convergence of the bed load transport increases linearly with the height of the ridges. This location is on the downcurrent (seaward) flank of the ridges during the entire duration of the growth of the ridges and is a good representative of the sediment deposition halfway the flank of the ridge. For a constant wavelength (and therefore width) of the ridges the volume of sediment per unit width that has to be replaced to result in the migration is roughly proportional to the height of the ridge. This shows why the migration rates remain almost constant in time under a linear increase of the convergence of sediment with the height of the ridges. Furthermore, the divergence of the bedslope flux at this location remains small compared to the convergence of the advective part at all times, as demonstrated in Figure 5.15 (right subplot).

The analysis presented so far yields clues about the shape of the bedforms, their constant migration and the saturation of the growth of the bottom perturbations, but it does not explain the change in the spatial shift between the ridge topography and the pattern of the mean grain

size. The growth of the ridges was related to the superposition of the contribution of the fine and coarse sediment fraction to the convergence of the total sediment flux on the crest. In contrast, the evolution of the fraction of fine sediment is determined by the difference in erosion and deposition of fine and coarse grains, as can be traced back from equation (5.3c). The investigation of the nonlinear grain sorting process requires an analysis of the full spectral model. However, this is a difficult task, because of the many nonlinear terms involved. To facilitate the work, test experiments were performed to see which nonlinear terms are crucial for the evolution of the ridges and the grain sorting. It was found that the saturation still occurs if the nonlinear contributions in the equations for the bottom and the fraction of fine grains are excluded in the computations ($N_4 = N_5 = 0$, see appendix 5.B). Only minor differences with respect to the original results are found: the final height and saturation time are the same, and the (1,1) mode is dominant at all times. The main difference is that the amplitude of the higher modes for f_1 are more pronounced, e.g., the amplitude of mode (2,1) is now 64% of that of mode (1,1), rather than the 40% in the full nonlinear simulation. Therefore, it seems unlikely that the terms N_4 and N_5 are important for the mechanism underlying the saturation process.

Upon ignoring the nonlinear terms in the equations describing the dynamics of the fraction of fine sediment, equation (5.3c) becomes

$$-T_{b3}\vec{\nabla}\cdot\vec{q}_b' - T_{s3}\vec{\nabla}\cdot\vec{q}_s' \simeq \left[T_{s4} + T_{s3}T_{s5}\right] q_{s0}\frac{\partial f_1}{\partial y} \tag{5.8}$$

where $T_{b\cdot}$ and $T_{s\cdot}$ are known coefficients defined in appendix 5.B and it is used that in the basic state the suspended load sediment flux $\vec{q}_{s0} = (0, q_{s0})$ dominates over the bed load flux. For the present parameter setting a reduced transport of fine grains as bed load, i.e. $T_{b3} = F_1F_2(G_{b1} - G_{b2}) < 0$, is used and a reduced flux of coarse grains for suspended load yields $T_{s3} > 0$. The contribution between the brackets is positive. This is the same balance as for the linear system: the only parameters that can change in time are $\vec{q}_b'$ and $\vec{q}_s'$, which are the perturbed sediment flux for bed load and suspended load in case of uniform sediment, and f_1. Thus, the spatial pattern of f_1 is related to the patterns of the bed load and suspended load convergence. The temporal behaviour of the two contributions on the left-hand side of equation (5.8) is shown in Figure 5.16 for a shore-normal (left panel) and a shore-parallel (right panel) cross-section. The zero-crossings of the solid line indicate the position where $\partial f_1/\partial y = 0$, and thus an extremum in the fraction of fine grains, corresponding to the locations of the maximum and minimum value of the mean grain size ϕ_m (in phi-units). Initially, the maxima of the contributions related to bed load and suspended load transport are of similar magnitude, but shifted in location. During the evolution the spatial distribution of these terms change significantly, where at the final stage of saturation both show the largest contributions on the steep slope of the ridge. Furthermore, the term related to bed load transport has become dominant over the term related to suspended load transport along most of the cross-shore transect. The maxima in $\partial f_1/\partial y$ correspond to the locations where the largest gradients in f_1 occur, as shown in Figure 5.12 (right-hand panel) for the shore-normal cross-sections of f_1. The preferred sediment convergence over the seaward flank of the ridges causes the asymmetry in the pattern for the fraction of fine grains. The conclusion is that for these parameter settings the initial shift between the mean grain size pattern (or, similarly, that of the fraction of fine grains) and the topography can change in time

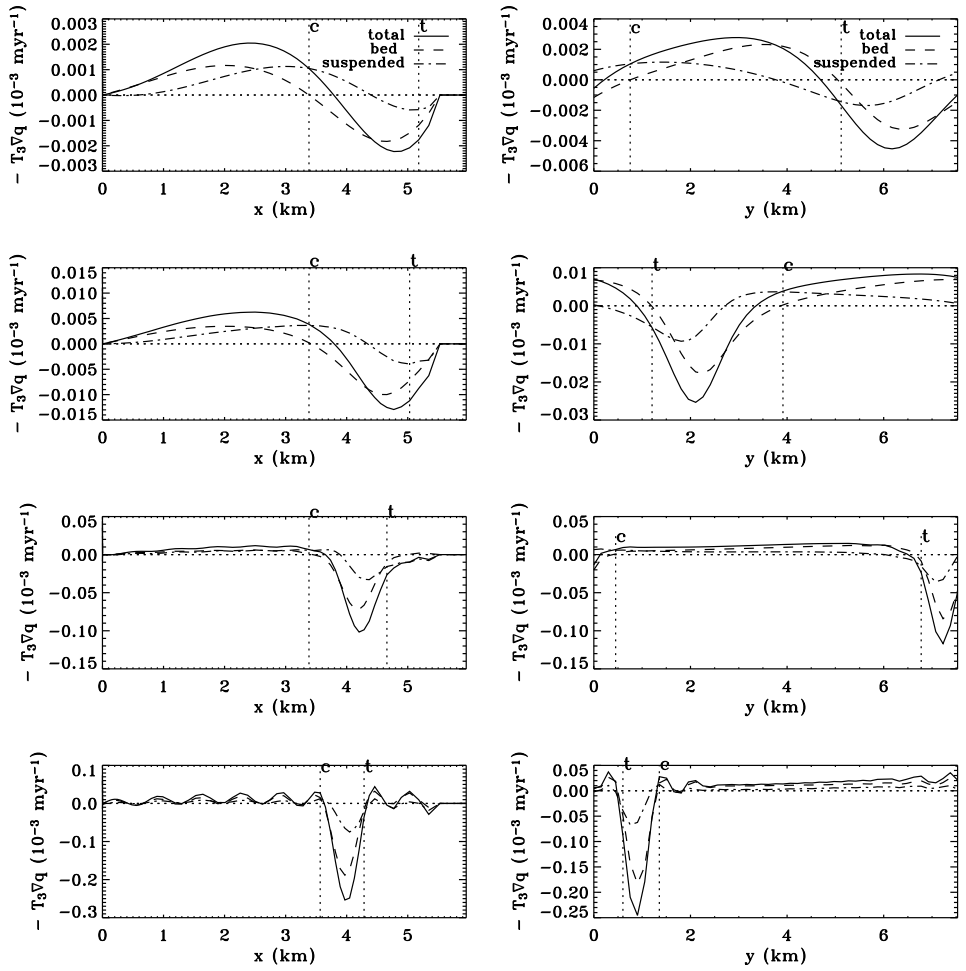

Figure 5.16: Shore-normal (left panel) and shore-parallel (right panel) cross-sections of $-T_{s3}\vec{\nabla}\cdot\vec{q}_s' - T_{b3}\vec{\nabla}\cdot\vec{q}_b'$, where $\vec{q}_s'$ and $\vec{q}_b'$ are the perturbed sediment flux for suspended and bed load, respectively and excluding grain size dependence. The total is split in a bed load and a suspended load part, sections are taken through the ridge top. The vertical dotted lines indicated the locations of the maximum of h (c: crest) and minimum of h (t: trough) for this section. The sections are taken at $t \sim$ 10, 13, 16, 21 $\times 10^3$ yr, with time increasing from top to bottom.

due to the changes in the pattern of suspended load and an increase in the relative importance of the bed load contribution.

Experiments with a change in the sign of the hiding coefficient for bed load ($c_b < 0$, thus $T_{b3} > 0$) show a reversed final pattern for the fraction of fine grains, whereas a change in sign for c_s does not change the final pattern. This leads to the conclusion that the pattern for

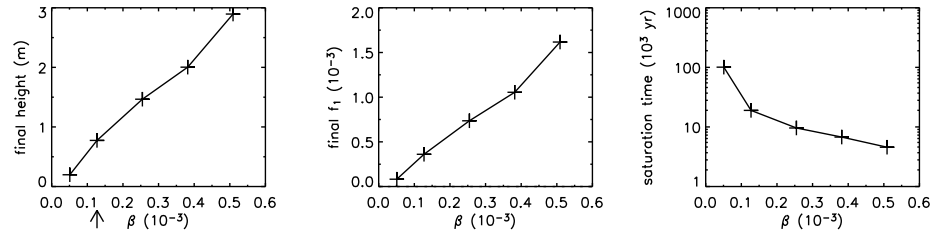

Figure 5.17: Total height of bedforms in the saturated state, total variation in the fraction of fine grains in the saturated stage (in the figure called: final f) and time needed for saturation as a function of the slope of the inner shelf in the basic state. The arrow indicates the default value of β, for which case the evolution in time towards the saturated stage is shown in Figure 5.8.

the mean grain size at the saturated state is determined mainly by the bed load flux and its hiding formulation. The interesting question is then what happens with the pattern in f_1 if the hiding in bed load is decreased, and only hiding in suspended load is included ($c_b = 0$). For this case, the linear analysis showed a phase shift of $\sim 90°$. These nonlinear results will be discussed in the next subsection, along with a sensitivity for the finite-amplitude results on the standard deviation and the slope of the inner shelf.

Equation (5.8) also gives an indication of the gradients in the fraction of fine grains that can be expected with this model. These gradients are determined by the selective transport of coarse and fine sediment that cause different amounts of erosion and deposition of the two fractions. This effect is represented by the terms (for bed load and suspended load, respectively) on the left-hand side of the equation. Here the case of $c_b = 0$ is used as an example. The differences in the fluxes correspond to a value of $T_{s3} \sim 0.09$. On the right-hand side contributions involve $[T_{s4} + T_{s3}T_{s5}] \sim 0.4$ and a longshore sediment transport in the basic state with magnitude Q_s. The relative ratio between the height of the bedforms and the maximum value of f_1 can be estimated if the expression for $\vec{\nabla} \cdot \vec{q}_s'$ (appendix 5.A.2) is written in terms of the bottom perturbations h. To do this, only the advective flux is considered and irrotational flow is assumed. Therefore, this estimate only applies to the linear stage of the evolution. With the linearised mass balance of water, a ratio of $|f_1/h| \sim 1 \times 10^{-4}$ m^{-1} is found. This is based on the characteristic scales for variations in the cross-shore (L_s) and longshore (K_M^{-1}) direction, the depth (H_0) and the slope of the inner shelf ($H_x \sim \beta$). The model results show that this ratio remains almost constant during the evolution in time. For the final stage the ratio f_1/h can be easily computed from Figure 5.8 and confirms the estimate obtained from equation (5.8). Although this figure was for $c_b \neq 0$, the results in the next section will show that this only enhances the ratio by a factor 4. Thus, the small values for f_1 seem inherent in the equation that is used for the grain size evolution. We will return to this in the discussion in section 5.4 and chapter 6. It should be kept in mind that in the model the transported sediment has the same composition as that of the bottom from which it is eroded.

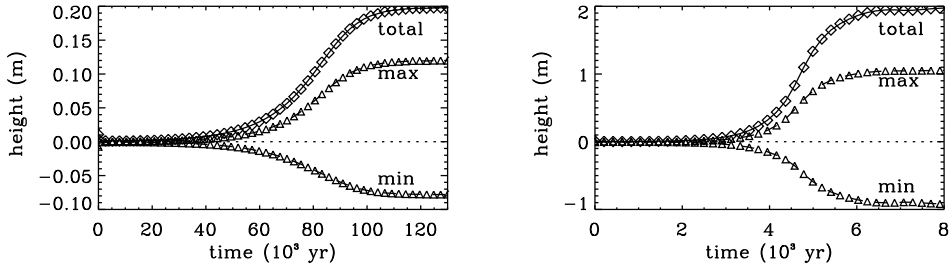

Figure 5.18: Time evolution of maximum, minimum and total height of the bedforms for $\beta = 0.05 \times 10^{-3}$ (left), and $\beta = 0.38 \times 10^{-3}$ (right).

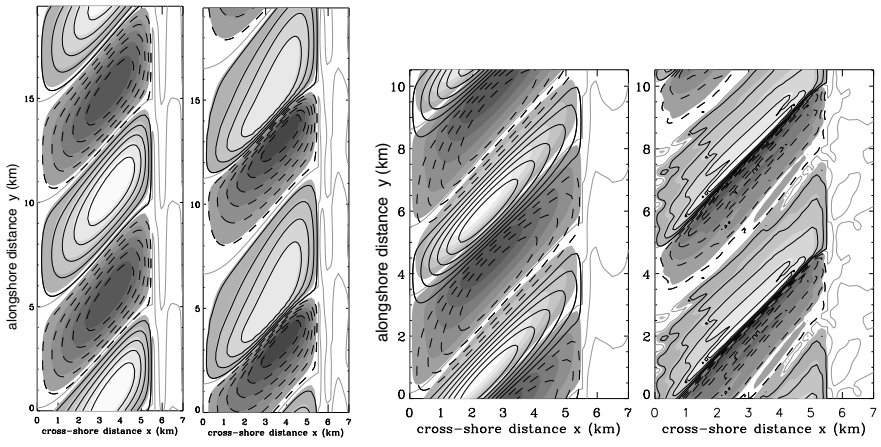

Figure 5.19: Contour plot of perturbations in bottom and fraction of fine grains for two different values of β and during the initial and final stage of development of the ridges. The two plots on the left are for values of the inner shelf slope smaller than the default setting: $\beta = 0.05 \times 10^{-3}$ and $t \sim 26 \times 10^3$ yr (left) and $t \sim 130 \times 10^3$ yr (right). The two plots on the right are for a higher value of the slope: $\beta = 0.38 \times 10^{-3}$ and $t \sim 3.1 \times 10^3$ yr (left) and $t \sim 6.2 \times 10^3$ yr (right). On the greyscale the light indicates a crest, dark indicates a trough. Solid (dashed) lines show increase (decrease) in fraction of fine grains.

5.3.6 Nonlinear analysis: sensitivity to parameter values

Additional experiments with this nonlinear model for shoreface-connected ridges were carried out for different values of the transverse bottom slope; all other parameters had their default values. The results shown in Figure 5.17 indicate that the final height of the ridges and the variation in the mean grain size increase for a higher transverse bottom slope of the inner shelf (Figure 5.17). The former trend is the same as was already found in the model for uniform sediment. Saturation occurs faster for higher values of β, related to the increase in linear growth rates (Figure 5.5). This is illustrated in Figure 5.18 for the evolution of the height of the ridges in time for two values of β. The qualitative behaviour remains the same.

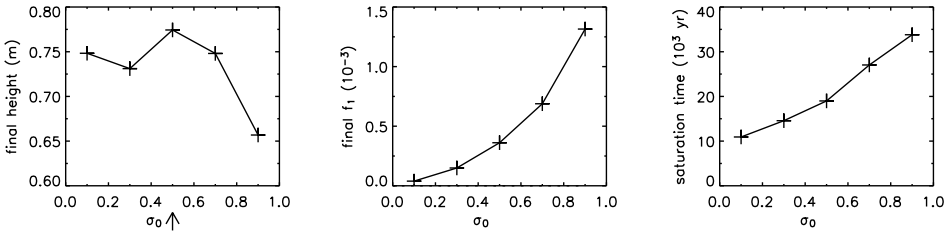

Figure 5.20: As in Figure 5.17, but dependence on the standard deviation of the sediment mixture in the basic state.

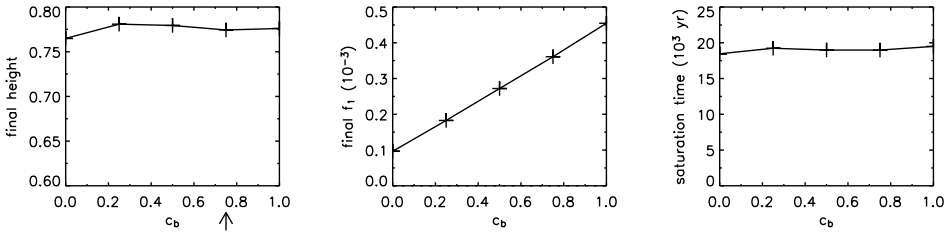

Figure 5.21: As in Figure 5.17, but dependence on the hiding coeffi cient in the bed load sediment transport function.

However, the bottom patterns clearly show an increase in asymmetry in the final state of the evolution of the ridges for larger slopes of the inner shelf, as demonstrated in Figure 5.19. The results are shown for a value of β near critical conditions and for a value resulting in highly nonlinear behaviour. The solutions become unbounded at some time during the saturation process for values of β larger than 0.55×10^{-3}, which is approximately 50% of the observed values.

Sensitivity experiments were also carried out by varying the standard deviation of the sediment mixture. Compared to the case pf uniform sediment the final height of the ridges is hardly changed, while increasing σ_0 causes an increase in the distribution range and amplitude of f_1 (Figure 5.20). The saturation time is enhanced for a larger difference between the two grain sizes.

Another series of experiments shows that the saturated state depends on the coefficient c_b in the hiding function for bed load. It enhances the variation in the mean grain size (Figure 5.21). However, if hiding is only included in suspended load, the behaviour of the amplitude for h and f_1 in time is significantly different. In Figure 5.22 this is shown: at $t \sim 15 \times 10^3$ yr mode (2,2) becomes the dominant mode for f_1, while for h mode (1,1) has the largest amplitude. For f_1 the amplitude of the mode (1,1) is only half of that of the (2,2) mode. This shows that superharmonic ($k > K_M$) modes are excited and they can become the dominant mode for f_1. For a single grain size, a change between the dominant (bottom) modes was only found when subharmonics ($k < K_M$) were included in the truncated series (Calvete and De Swart, 2003). In contrast to the change in time towards modes of f_1 with a

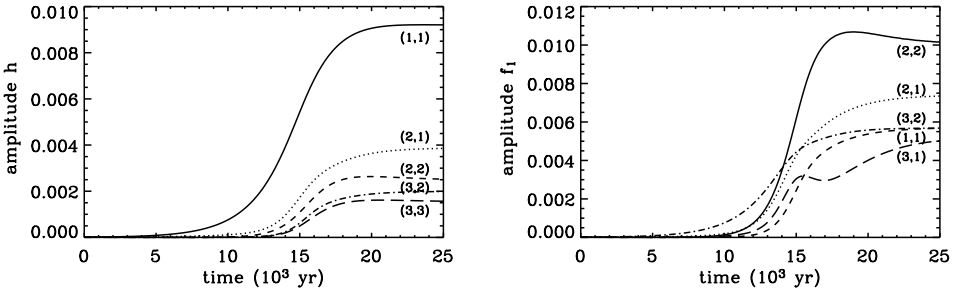

Figure 5.22: Time evolution of the five modes which have the largest amplitudes at the final time of computation at $t = 25 \times 10^3$ yr. (Left) Amplitudes of bottom modes $|\hat{h}_{jn_j}|$. (Right) Amplitudes of modes for fraction of fine grains $|\hat{f}_{jn_j}|$. No hiding in bed load ($c_b = 0$), other parameters have their default values.

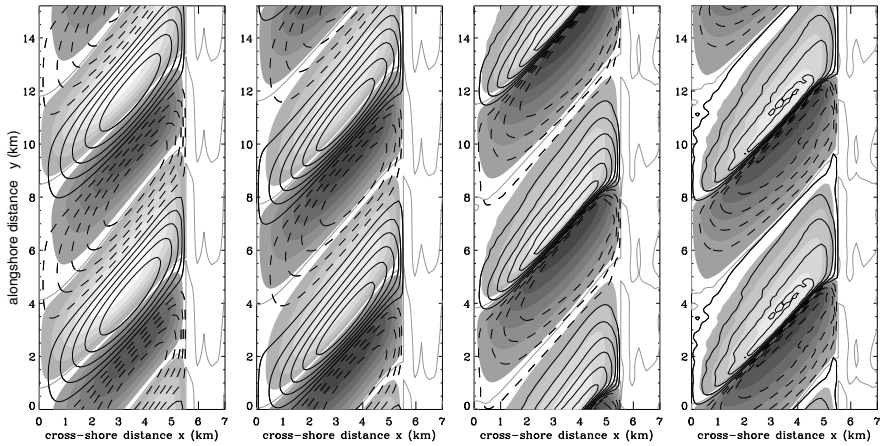

Figure 5.23: At $t \sim 6, 13, 16, 25 \times 10^3$ yr the plots show: perturbations in bottom (greyscale) and fraction of fine grains (contour lines). No hiding is used in the transport of sediment as bed load, i.e. $c_b = 0$, other parameters have their default values.

shorter wavelength than K_M, as found with the present model, the single grain size model showed a change towards modes of h with a longer wavelength. The bottom pattern in the saturated stage has the same characteristics as that obtained in the default case of hiding included in both the suspended and bed load flux. In Figure 5.23 the linear solution with an approximately 90° phase shift between h and f_1 is clearly recognised during the initial stage of development of the ridges. However, similar to the default case, the fraction of fine grains is largest on the crest of the ridge at the saturated state. In this case of only hiding in the suspended load flux the pattern of the fraction of fine grains is determined by the suspended

load flux, see equation (5.8) for $T_{b3} = 0$. If the hiding for suspended load flux is reversed ($c_s > 0$) the initial phase difference is $-90°$, which evolves into a final pattern in which h and f_1 are $180°$ out-of-phase. Thus, the final distribution due to hiding in suspended load flux also tends to adjust to the pattern to the shape of the ridge topography.

5.4 Discussion and conclusions

In this chapter a nonlinear model for the long-term evolution of the topography of shoreface-connected ridges and the variations in the mean grain size over this topography is presented. The model uses two grain size classes, includes dynamic hiding effects in both suspended and bed load sediment transport and is based on the one-layer concept for the bottom evolution. A linear stability analysis of the basic state of the model, characterised by a storm-driven flow over a longshore uniform shelf, showed the formation of ridges and of a mean grain size pattern as free instabilities of the morphodynamic system. The analysis is extended into the nonlinear regime, using a spectral method. This involves an expansion of the physical variables in a truncated series of modes of the linear system. Substitution of these expansions in the equations of motion and projection of the results on the adjoint eigenmodes yields a set of differential and algebraic equations for the unknown amplitudes of the different modes, which are solved numerically. With this method the finite-amplitude behaviour of shoreface-connected ridges under storm conditions is simulated, under the restriction of a small transverse bottom slope β of the inner shelf (up to $\sim 1/2$ of its realistic value). For large values of β solutions become unbounded at some time during the evolution.

With this model it was shown that, starting from an initial state without bedforms, a pattern of shoreface-connected ridges with finite amplitudes develop. Initially, the height of these ridges increases exponentially, but nonlinear effects cause a reduction of the growth, such that height tends to a constant value. At the same time, the maximum variation in the mean grain size evolves towards a constant value. The results clearly demonstrate that it is possible to simulate the finite-amplitude behaviour of shoreface-connected ridges in a model that is based on a mass balance for nonuniform sediment. The use of multiple grain sizes does not significantly change the final height and shape of the bottom topography that were obtained by Calvete et al. (2002) with a model based on a single grain size. For the default case a transverse bottom slope which is approximately 10% of its observed value was used. Stable solutions for the model could be obtained until a slope of approximately 50% of its observed vale. The shape of the ridges changes from symmetrical in the linear stage towards asymmetrical in the nonlinear stage. The asymmetry ratio of the seaward over the landward slope for the default case is $\sim 6 : 1$ after reaching the equilibrium amplitude, whereas the maximum side slope of the ridges is around $0.05°$.

The dependence of the final height and the maximum variation of f_1 on the transverse bottom slope β is also investigated. It appears that the saturation height and the asymmetry in the bottom profile and in the grain size profile increase with β, while the saturation time reduces. The results for the final height of the ridges can be extrapolated to realistic values of the slope of the inner shelf using the trend for increasing β as found in Figure 5.17. For a realistic slope this would give a final height of ~ 6 m after a period of $\sim 1 \times 10^3$ yr. These values agree rather well with those obtained from field observations. The asymmetry

ratio for the default slope is already larger than the highest values observed in the field. This may suggest that observed shoreface-connected ridges have not reached their final stage of development yet.

A serious shortcoming of the model is that the modelled maximum variation in the fraction of fine and coarse sediment over the ridges are much smaller than those measured in the field. Extrapolating towards realistic slopes still indicates variations in the fraction of fines of only 0.004 ($\sim 1\%$ change on the initial value of 50% fines in the basic state). For a diameter of the fine and coarse grains of 250μm and 500μm, respectively, this corresponds to a total variation in the mean grain size of approximately 2μm. Observations suggest that the variations in the mean grain size are in the range of 200-500μm. This indicates that not all physical processes are incorporated correctly in the model. It should be realised that the assumptions that lead to the equation describing the evolution of the grain size fraction might not be valid for ridges with a significant height. The validity of the one-layer concept, which assumes a thin transport layer that is uniformly mixed over its depth and negligible interaction with the underlying substrate, might not be valid for the long timescales that are related to the formation of large-scale bedforms. This could be in principle overcome by using, for example, a two-layer model (cf. Ribberink, 1987) or a continuous distribution in the vertical (cf. Van Ledden et al., 2002a) that account for vertical sorting. However, a major drawback of this approach is the large number of extra parameters which are poorly known. We will return to this point in the next chapter.

A constant height of the ridges is reached as a result of a balance between the deposition related to the advective part of the suspended sediment flux and erosion related to the bedslope part over the crest. The maximum deposition due to the advective part of the suspended sediment flux is not on the crest, but shifted towards the seaward flank of the ridge and results in asymmetry in the profile. At the same time, the contribution related to the bed slope flux starts to increase more rapidly compared to the advective part. Thus, the mechanism for saturation is strongly related to the bedslope flux for suspended load, which is proportional to the bedslope coefficient λ_s. Further model experiments with an improved formulation for λ_s could therefore be interesting, although little is known about this parameter. In this work it is assumed that this coefficient is constant, i.e. independent of the direction (x, y) and the grain size fraction. The result is that the grain size dependence in the advective and bedslope flux is the same. The maximum deposition as a result of bed load is located approximately halfway between the crest and trough, and shows a linear increase with the height, thereby a constant migration velocity is attained in time. A possible additional mechanism for saturation that is excluded in the present model is a stirring of sediment by waves that is larger at the crests than in the troughs. This remains a topic of future research.

A remarkable result is that the distance between location of ridge crest and the location where the finest sediment occurs decreases during the nonlinear evolution stage. The linear analysis showed a spatial shift between the variations in the mean grain size and the ridge topography, with the maximum fraction of fine grains located just seaward (downcurrent) of the crest. This phase shift is also observed in the field (cf. Figure 1.4). The spatial shift changes if the ridges develop an asymmetrical profile: in the final state this distance is so small that the finest sediment is located almost at the crests; likewise the coarsest sediment is found almost in the troughs. This tendency is rather difficult to relate to field data, as most fine sediments are observed at measurable distances downstream of the ridges.

Experiment have shown that the nonlinear terms in bottom evolution equation are only of minor importance for the development of perturbations with a finite amplitude: saturation still occurs if these are neglected. These terms tend to enhance the amplitude of the small-scale bedforms which develop at the final stage of development of the large-scale ridges. The most important nonlinear contribution in the system of equations that is essential for the saturation of the ridges is the one in the continuity equation for water. With this in mind, the change in the distance between the maximum in h and f_1 in the model can be linked to two effects. The first is an increase in the importance of bed load sediment transport (with respect to suspended load) in time. The mean grain size pattern for dominant bed load transport, including a hiding formulation to reduce the flux of fine grains, is in phase with topography. For suspended load transport a 90° phase shift is the initially preferred pattern. The second effect is a change in the pattern of the divergence of the suspended load flux ($\vec{\nabla} \cdot \vec{q}_s'$) in time. Initially, its pattern is such that it mainly results in the growth of perturbations, followed by a stage in which it enhances the asymmetry. At the final stage $\vec{\nabla} \cdot \vec{q}_s'$ is almost in phase with $\vec{\nabla} \cdot \vec{q}_b'$ and mainly influences the migration of the ridges. The first effect is dominant for our default case, where the second one is responsible for a shift in the phase when the hiding in bed load is neglected. Comparing these results with the $\sim 90^\circ$ out-of-phase relation between mean grain size and topography in field data, might lead to the hypothesis that most ridges are not yet in equilibrium with the present-day hydrodynamic conditions.

Appendix

In this appendix the subscripts x, y, xx and yy indicate the first and second derivatives with respect to x and y.

5.A Sediment flux

5.A.1 bed load

The bed load flux in the basic state, the perturbations in the bed load flux and its divergence for a single grain size are based on the expression for $\vec{q}_b$ in (5.4) and read

$$\begin{aligned}
\vec{q}_{b0} &= (0, q_{b0}) = (0, \frac{3}{2}\nu_b u_w^2 V) \\
\vec{q}_b' &= \frac{3}{2}\nu_b \left(u_w^2 u' - \hat{\lambda}_b u_w^3 h_x \, , \; u_w^2 v' - \hat{\lambda}_b u_w^3 h_y \right) \\
\vec{\nabla} \cdot \vec{q}_b' &= \frac{3}{2}\nu_b \left\{ u_w^2 \left[u_x' + v_y' - m\frac{H_x}{H} u' \right] - \hat{\lambda}_b u_w^3 \left[h_{xx} + h_{yy} - \frac{3}{2} m \frac{H_x}{H} h_x \right] \right\}
\end{aligned}$$

The perturbed bed load flux and its divergence for sediment with a grain size diameter d_i in a sediment mixture are

$$\begin{aligned}
\langle \vec{q}_{bi}' \rangle &= (F_i + f_i)(G_{bi} + g_{bi})(\vec{q}_b' + \vec{q}_{b0}) - F_i G_{bi} \vec{q}_{b0} \\
\vec{\nabla} \cdot \langle \vec{q}_{bi}' \rangle &= (G_{bi} + g_{b1})(\vec{q}_b' \cdot \vec{\nabla} f_i + f_{iy} q_{b0}) + (F_i + f_i)(\vec{q}_b' \cdot \vec{\nabla} g_{bi} + g_{biy} q_{b0}) \\
&\quad + (F_i + f_i)(G_{bi} + g_{bi}) \vec{\nabla} \cdot \vec{q}_b'
\end{aligned}$$

The bed load transport capacity function, and the corresponding basic state G_{bi} and perturbation g_{bi} (including higher order terms) are

$$\mathcal{G}_{bi} = 2^{c_b(\phi_m - \phi_i)} \qquad G_{bi} = 2^{c_b(\Phi_m - \phi_i)} \qquad g_{bi} = G_{bi}(2^{c_b \phi'_m} - 1) \tag{5.A-1}$$

where the mean grain size is written in terms of a basic state value (Φ_m) and a perturbation (ϕ'_m)

$$\phi_m = \Phi_m + \phi'_m \qquad \Phi_m = \phi_1 F_1 + \phi_2 F_2 \qquad \phi'_m = \frac{\sigma_0}{\sqrt{F_1 F_2}} f_1 \tag{5.A-2}$$

Thus the linearised part of the perturbed transport capacity function, indicated by $\mathcal{L}(..)$, is $\mathcal{L}(g_{bi}) = G_{bi} T_{b5} f_1$, with $T_{b5} = c_b \ln 2\sigma_0 / \sqrt{F_2 F_1}$. The linearised parts of the flux divergences due to the fine and coarse sediment class read

$$\mathcal{L}(\vec{\nabla} \cdot \langle \vec{q}'_{b1} \rangle) = G_{b1} \left[F_1 \vec{\nabla} \cdot \vec{q}'_b + q_{b0}[1 + F_1 T_{b5}] f_{1y} \right]$$
$$\mathcal{L}(\vec{\nabla} \cdot \langle \vec{q}'_{b2} \rangle) = G_{b2} \left[F_2 \vec{\nabla} \cdot \vec{q}'_b - q_{b0}[1 - F_2 T_{b5}] f_{1y} \right]$$

Here the constraint on the distribution $\mathcal{F}_i$ is used to eliminate f_2. It also fixes the relation between the basic state values of the fraction of fine and coarse grains, i.e.

$$F_1 + F_2 = 1 \qquad\qquad f_1 + f_2 = 0$$

5.A.2 Suspended load

The suspended load flux in the basic state, the perturbations in the suspended load flux and its divergence for a single grain size are based on the expression for $\vec{q}_s$ in (5.5) and read

$$\begin{aligned}
\vec{q}_{s0} &= (0\ ,\ q_{s0}) = (0\ ,\ \nu_s u_w^5 HV) \\
\vec{q}'_s &= \nu_s u_w^5 \frac{H}{1 + h/H} \left(u' - \hat{\lambda}_s u_w^2 h_x\ ,\ v' - \frac{h}{H} V - \hat{\lambda}_s u_w^2 h_y \right) \\
\vec{\nabla} \cdot \vec{q}'_s &= \nu_s u_w^5 \frac{H}{1 + h/H} \left\{ u'_x + v'_y - \frac{5}{2} m \frac{H_x}{H} u' - \hat{\lambda}_s u_w^2 \left[h_{xx} + h_{yy} + \frac{7 u_{wx}}{u_w} h_x \right] \right\} \\
&\quad + \nu_s u_w^5 \frac{1}{1 + h/H} \left[H_x - \frac{(h_x - h H_x / H)}{1 + h/H} \right] \left[u' - \hat{\lambda}_s u_w^2 h_x \right] \\
&\quad - \nu_s u_w^5 \frac{h_y}{(1 + h/H)^2} \left[V + v' - \hat{\lambda}_s u_w^2 h_y \right]
\end{aligned}$$

Here $\nu_s = \frac{32}{5\pi} \delta_m \hat{E}_{m,u}$. The expressions for $\vec{\nabla} \cdot \langle \vec{q}'_{s1} \rangle$ and $\vec{\nabla} \cdot \langle \vec{q}'_{s2} \rangle$ are the same as for bed load, but with the transport capacity functions and sediment flux terms replaced by the ones for suspended load. The suspended load transport capacity functions, and the corresponding basic state and perturbation (including higher order terms) are

$$\mathcal{G}_{si} = (1 - 0.288\sigma)^5 2^{c_s(\phi_m - \phi_i)}$$
$$G_{si} = (1 - 0.288\sigma_0)^5 2^{c_s(\Phi_m - \phi_i)} \qquad\qquad g_{si} \simeq G_{si}(2^{c_s \phi'_m} - 1)$$

where the standard deviation is spit in a basic state σ_0 and a perturbation σ',

$$\sigma = \sigma_0 + \sigma' \qquad \sigma_0^2 = F_2 F_1 (\phi_1 - \phi_2)^2 \qquad \sigma' = \frac{\sigma_0 (F_2 - F_1)}{2 F_1 F_2} f_1$$

The linear part of the perturbed transport capacity function is $\mathcal{L}(g_{si}) = G_{si} T_{s5} f_1$, where

$$T_{s5} = c_s \ln 2 \frac{\sigma_0}{\sqrt{F_2 F_1}} - 5 \frac{0.288 \sigma_0}{(1 - 0.288 \sigma_0)} \frac{(F_2 - F_1)}{2 F_1 F_2}$$

5.B Matrix elements

The partial differential equations describing the evolution of the flow, mass, fraction of fine grains and bottom can be symbolically written as

$$\mathcal{S} \frac{\partial \psi}{\partial t} = \mathcal{L} \psi + \mathcal{N}(\psi) \tag{5.B-1}$$

where

$$\mathcal{S} = \begin{pmatrix} 0 & 0 & 0 & 0 & 0 \\ 0 & 0 & 0 & 0 & 0 \\ 0 & 0 & 0 & 0 & 0 \\ 0 & 0 & 0 & 0 & 0 \\ 0 & 0 & 0 & 0 & S_{55} \end{pmatrix} \qquad \mathcal{L} = \begin{pmatrix} L_{11} & L_{12} & L_{13} & 0 & 0 \\ L_{21} & L_{22} & L_{23} & 0 & L_{25} \\ L_{31} & L_{32} & 0 & 0 & L_{35} \\ L_{41} & L_{42} & 0 & L_{44} & L_{45} \\ L_{51} & L_{52} & 0 & L_{54} & L_{55} \end{pmatrix} \qquad \psi = \begin{pmatrix} u' \\ v' \\ \eta' \\ f_1 \\ h \end{pmatrix}$$

Here $L_{11-15}, L_{21-25}, L_{31-35}$ are the same as for uniform sediment. Also the nonlinear contributions $\mathcal{N}(u', v', \eta')$ are same as in the uniform sediment case. The elements of the linear matrix $\mathcal{L}$ are

$$\begin{aligned} L_{11} &= V \frac{\partial}{\partial y} + \frac{r}{H}, & L_{12} &= -f, & L_{13} &= \frac{\partial}{\partial x} \\ L_{21} &= V_x + f, & L_{22} &= V \frac{\partial}{\partial y} + \frac{r}{H}, & L_{23} &= \frac{\partial}{\partial y}, & L_{25} &= -\frac{s_0}{H} \\ L_{31} &= H \frac{\partial}{\partial x} + H_x, & L_{32} &= H \frac{\partial}{\partial y}, & & & L_{35} &= -V \frac{\partial}{\partial y} \end{aligned}$$

$$
\begin{aligned}
L_{41} &= \delta_b T_{b3} u_w^2 \left[\frac{\partial}{\partial x} - m\frac{H_x}{H}\right] + T_{s3} u_w^5 H \left[\frac{\partial}{\partial x} + (1-\frac{5}{2}m)\frac{H_x}{H}\right], \\
L_{42} &= \delta_b T_{b3} u_w^2 \frac{\partial}{\partial y} + T_{s3} u_w^5 H \frac{\partial}{\partial y}, \\
L_{44} &= \delta_b (T_{b4} + T_{b3}T_{b5}) u_w^2 V \frac{\partial}{\partial y} + (T_{s4} + T_{s3}T_{s5}) u_w^5 H V \frac{\partial}{\partial y}, \\
L_{45} &= -\delta_b T_{b3} \hat{\lambda}_b u_w^3 \left[\frac{\partial^2}{\partial x^2} + \frac{\partial^2}{\partial y^2} - \frac{3}{2} m \frac{H_x}{H}\frac{\partial}{\partial x}\right] \\
&\quad -T_{s3} \hat{\lambda}_s u_w^7 \left[\frac{\partial^2}{\partial x^2} + \frac{\partial^2}{\partial y^2} + (1-\frac{7}{2}m)\frac{H_x}{H}\frac{\partial}{\partial x}\right] \\
L_{51} &= \delta_b T_{b2} u_w^2 \left[\frac{\partial}{\partial x} - m\frac{H_x}{H}\right] + T_{s2} u_w^5 H \left[\frac{\partial}{\partial x} + (1-\frac{5}{2}m)\frac{H_x}{H}\right], \\
L_{52} &= \delta_b T_{b2} u_w^2 \frac{\partial}{\partial y} + T_{s2} u_w^5 H \frac{\partial}{\partial y}, \\
L_{54} &= \delta_b (T_{b1} + T_{b2}T_{b5}) u_w^2 V \frac{\partial}{\partial y} + (T_{s1} + T_{s2}T_{s5}) u_w^5 H V \frac{\partial}{\partial y}, \\
L_{55} &= -\delta_b T_{b2} \hat{\lambda}_b u_w^3 \left[\frac{\partial^2}{\partial x^2} + \frac{\partial^2}{\partial y^2} - \frac{3}{2} m \frac{H_x}{H}\frac{\partial}{\partial x}\right] \\
&\quad -T_{s2} \hat{\lambda}_s u_w^7 \left[\frac{\partial^2}{\partial x^2} + \frac{\partial^2}{\partial y^2} + (1-\frac{7}{2}m)\frac{H_x}{H}\frac{\partial}{\partial x}\right]
\end{aligned}
$$

where $\delta_b = (\frac{3}{2}\nu_b)/\nu_s$ is the ratio of the wave stirring for bed load and suspended load. The nonzero element of the temporal matrix $\mathcal{S}$ is $S_{55} = 1/\nu_s$ Furthermore,

$$
\begin{aligned}
T_{b1} &= G_{b1} - G_{b2} & T_{s1} &= G_{s1} - G_{s2} \\
T_{b2} &= F_1 G_{b1} + F_2 G_{b2} & T_{s2} &= F_1 G_{s1} + F_2 G_{s2} \\
T_{b3} &= F_1 F_2 (G_{b1} - G_{b2}) & T_{s3} &= F_1 F_2 (G_{s1} - G_{s2}) \\
T_{b4} &= F_2 G_{b1} + F_1 G_{b2} & T_{s4} &= F_2 G_{s1} + F_1 G_{s2}
\end{aligned}
$$

The nonlinear contributions of the vector $\mathcal{N} = (N_1, N_2, N_3, N_4, N_5)$ are

$$
\begin{aligned}
N_1 &= u'u'_x + v'u'_y + \frac{ru'}{H-h} - \frac{ru'}{H} \\
N_2 &= u'v'_x + v'v'_y + \frac{r(V+v')}{H-h} - \frac{rV}{H-h} - \frac{rv'}{H} - \frac{s_0 h}{H-h} + \frac{s_0 h}{H} \\
N_3 &= -u'h_x - u'_x h - v'h_y - v'_y h \\
N_4 &= -(1-F_1)[\vec{\nabla}\cdot\langle\vec{q}'_1\rangle - \mathcal{L}(\vec{\nabla}\cdot\langle\vec{q}'_1\rangle)] - F_1[\vec{\nabla}\cdot\langle\vec{q}'_2\rangle - \mathcal{L}(\vec{\nabla}\cdot\langle\vec{q}'_2\rangle)] \\
&\quad f_1(\vec{\nabla}\cdot\langle\vec{q}'_1\rangle + \vec{\nabla}\cdot\langle\vec{q}'_2\rangle) \\
N_5 &= -[\vec{\nabla}\cdot\langle\vec{q}'_1\rangle - \mathcal{L}(\vec{\nabla}\cdot\langle\vec{q}'_1\rangle)] - [\vec{\nabla}\cdot\langle\vec{q}'_2\rangle - \mathcal{L}(\vec{\nabla}\cdot\langle\vec{q}'_2\rangle)]
\end{aligned}
$$

Here $\vec{q}'_i = \vec{q}'_{bi} + \vec{q}'_{si}$ and $\mathcal{L}(\vec{\nabla}\cdot\langle\vec{q}'_i\rangle)$ is the linearised part of $\vec{\nabla}\cdot\langle\vec{q}'_i\rangle$.

Chapter 6

Discussion and conclusions

The work presented in this thesis concerns the dynamics of shoreface-connected ridges and tidal sand ridges. These large-scale bedforms are found on the inner and outer shelf of coastal seas in water depths of 10-20 m. The motivation of this work is to improve the understanding of the mechanisms related to their formation and the processes that determine their main characteristics. Existing literature already showed that this insight could be achieved with the use of idealised morphodynamic models. The basic concept behind these models is that bedforms can develop as a result of the interaction between the water motion and the sandy sea bottom. The approach of this thesis is to extend existing models with new physical processes of which field data suggest the potential importance, in particular the role of grain size sorting. Mathematical methods based on a stability analysis are applied, whereas numerical methods are used to solve the equations.

In this chapter the aspects of the model that have improved our understanding of large-scale sand ridges are discussed, using the main results of chapters 2 to 5. The more specific research questions that were formulated in section 1.8 are addressed in more detail in these chapters. First, the basic assumption related to the formation of tidal sand ridges and shoreface-connected ridges is discussed and the results for the impact of storms and tides are summarised. Second, the main results obtained with the linear analysis for grain size sorting are given, followed by a presentation of the results of the nonlinear analysis. The crucial assumptions in the model for the evolution of the grain size distribution are discussed. In addition, we focus on the representation of the sediment transport and waves in the model. Finally, suggestions are given for further research.

Formation process: basic hypothesis

The basic assumption underlying this thesis is that large-scale sand ridges can solely form as free instabilities on a flat sea bottom. Nevertheless, there is no consensus on this point in the literature. Other theories relate their presence to old geological relicts, which might be subsequently reworked by the present-day hydrodynamics (Swift et al., 1985; McBride and Mosow, 1991; Dyer and Huntley, 1999). The interpretation of field observations often does not give the exclusive answer to all the mechanisms that play a role. In this thesis we have

not elaborated on theories that are based on solely geological aspects. The results of stability models can indicate whether the hydrodynamic processes incorporated are likely to play a role. An important part of this thesis concerns the unresolved question about the origin of the observed mean grain size pattern over the ridges. It explores the hydrodynamic processes that can lead to sediment sorting and the formation of large-scale sand ridges.

Storms and tides

The literature on large-scale sand ridges (cf. Van de Meene and Van Rijn, 2000a; Dyer and Huntley, 1999, and refernces herein) already indicated that shoreface-connected ridges and tidal sand ridges both have crests up to several metres in height. They also have an elongated shape with a length of the crest of a few kilometres. Tidal ridges dominantly prevail in a meso-tidal environment, whereas shoreface-connected ridges prevail when storms dominate the hydrodynamic forcing on the continental shelf. A characteristic difference between these two types of ridges is the orientation of the crest: cyclonic with respect to the tidal current axis (in case of tidal sand ridges) or upstream oriented, i.e. seaward ends are shifted upstream with respect to the steady alongshore current, in case of shoreface-connected ridges.

A question that was raised is: On which coastal shelves can we expect to find these shoreface-connected ridges and tidal sand ridges? A primary requirement is a sandy (inner) shelf. Trowbridge (1995) showed that an essential condition for the development of shoreface-connected ridges is that the inner shelf has a transverse bottom slope. Thus, these ridges are likely to be more prominent (i.e. grow faster) on that part of the coastal shelf where the slopes are largest. They form under storm conditions, during which waves cause a stirring of the sediment into the water column and the subsequent transport is due to steady currents (Calvete et al., 2001b). Tidal sand ridges, on the other hand, form merely under a significant tidal current amplitude and fair weather conditions (Huthnance, 1982a; Hulscher et al., 1993; Calvete et al., 2001a) and their formation is not restricted to a sloping seabed.

In chapter 2 a model was presented that combines two model realisations in a statistical way: one state representing the dominant forcing conditions for shoreface-connected ridges and one state representing forcing conditions for tidal ridges. This model yields insight in the conditions under which the simultaneous existence of both types of bedforms on different locations of the same coastal shelf (on the inner and outer shelf, respectively) can be found. An example shelf where both types of bedforms are found is the Dutch-Belgian shelf (southern North Sea), with the tidal ridges located further offshore. The results indicated that both shoreface-connected ridges and tidal sand ridges can only be present on meso-tidal shelves where storms occur frequently enough to induce a steady current (averaged over many storm periods) with an amplitude that compares with the tidal current amplitude. Already for realistic storm fractions, the growth of shoreface-connected ridges on the slopes of the inner shelf prevents the formation of tidal sand ridges on this part of the shelf. Consequently, they only occur further offshore, i.e. on the outer shelf. For parameter values representing southern North Sea conditions, the probability of storms (time average over many years) for which shoreface-connected ridges grow on the inner shelf and tidal sand ridges on the outer shelf of the model domain is in the range of $\sim 2 - 8\%$. This estimate agrees with statistical data for wind speed and direction related to southwestern storms on this shelf. The absence of tidal sand ridges on the Atlantic shelf of North America can be (at least partly) attributed to the

small tidal current amplitudes.

Grain sorting

In chapters 3 and 4 a first step was taken to understand the observed grain size pattern over shoreface-connected ridges and tidal sand ridges. The model for a single grain size was extended such that it accounts for the sediment flux of fine and a coarse grains and the evolution of the fractions of fine and coarse grains in the bottom sediment. Within an idealised model context, it was shown that dynamic hiding (reduced mobility of one fraction) leads to the development of a spatially non-uniform mean grain size and sorting pattern over the bedforms.

For shoreface-connected ridges (chapter 3) the model represents a micro-tidal inner shelf, where the water motion is forced by storms. Essential different results were found when grain sorting is included in the bed load or suspended load sediment flux. The pattern that was obtained from a linear model analysis and hiding in suspended load transport agrees well with the field observations for shoreface-connected ridges (cf. Swift et al., 1978; Parker et al., 1982; Antia, 1996). The latter show a persistent spatial phase shift of approximately 90° between the topography and mean grain size: the coarsest sediment occurs on the landward (and upcurrent) flank, the finest on the seaward (and downcurrent) flank. Model results only showed this phase shift when grain sorting was included in suspended load transport, while for hiding in bed load the patterns are in-phase. The spatial changes in the fractions of fine and coarse grains are fixed by the erosion and deposition patterns. In case of suspended load transport the maximum deposition occurred near the crest (resulting in growth of the ridges), while in case of bed load maximum deposition occurred on the downstream flank (resulting in migration of the ridges). These results stress the importance of a selective suspended load sediment transport during storms, for which the flux of fine material is larger than that of coarse material.

Adding hiding effects in the bed load flux shifted the pattern of the mean grain size more in-phase (by using a reduced transport of fine grains) with the topography. Model tests indicated that introducing a grain size dependent bed shear stress in the momentum equations, i.e. a feedback between changes in the sediment composition and the current, did not change the patterns of the mean grain size and sorting over shoreface-connected ridges. Also, the combination of a steady and a tidal current (as compared to only a steady current) did not significantly influence the results of the linear model. A stabilising effect of sediment sorting on the growth of shoreface-connected ridges was obtained by the model, while the wavelength of the ridges was slightly increased. In the context of the experiments that were carried out in this thesis, it can be concluded that growth rates are determined by the formulation of dynamic hiding in the suspended load flux. A reduced growth (compared to that of sediment with a single grain size) turns out to be mainly caused by the presence of a straining parameter in the hiding function of suspended load. This parameter accounts for the reduced mobility of grains in the sediment mixture due to more efficient packing. In this thesis, such an effect was not included in the bed load flux because it is not used in most empirical formulas that exist for bed load hiding. The main effect of hiding in bed load was that it enhances the migration velocity of the shoreface-connected ridges.

Marked variations in the mean grain size are also observed over tidal sand ridges. Field data for the Belgian shelf reveal coarse (fine) sediment at the crests (in the troughs), but

phase shifts between the mean grain size distribution and the bottom topography can also occur. The forcing of the model in case of tidal ridges (chapter 4) is dominated by tides and represents fair weather conditions only; the sediment is transported as bed load. The validity of this assumption was already discussed in chapter 4. Experiments revealed the importance of different tidal constituents for the spatial pattern in the grain size distribution. A symmetrical tidal forcing, in combination with a reduced bed load flux of fine grains, resulted in a grain size distribution that was in phase with the ridge topography. The coarsest mean grain size was located on the crests, in agreement with the data of the Belgian shelf. When a steady component was added to the external forcing (or an asymmetrical tidal current was used by adding an overtide) the coarsest sediment was found on the flank downstream of the net alongshore current. Thus, the offshore decrease in the flood-dominance in this region (Lanckneus et al., 1994) could contribute to the shift in the location of the maximum mean grain size. Growth and migration rates of tidal sand ridges increased for a two-grain size mixture, the wavelength is only slightly affected.

Linear versus nonlinear

A linear stability analysis is representative for the initial formation stage of the bottom perturbation: it only allows for symmetrical (sinusoidal) perturbations, which grow exponentially in time. The question is how the results of such an analysis are related to ridges of a finite amplitude. The evolution (saturation process) towards ridges with an equilibrium amplitude is accompanied by nonlinear interactions between different modes (each representing a solution with a specific longshore and cross-shore structure). Therefore, in chapter 5 the long-term dynamics of shoreface-connected ridges were studied, along with the evolution of the mean grain size patterns. The nonlinear analysis uses a truncated series of solutions (eigenmodes) of the linear analysis to compute this final state. A nonlinear analysis for tidal sand ridges was beyond the scope of this thesis.

Starting from random initial conditions, a field of shoreface-connected ridges develops. Initial amplitudes increase exponentially and then the nonlinear terms become important. After several thousands of years the amplitude of the ridges becomes constant. The initially preferred mode also dominates in the nonlinear regime and the spacing of the ridges and their migration velocity remain constant during the evolution. During the saturation process the shape of the ridges changes from symmetrical to asymmetrical, with a steeper seaward (and downstream) flank. This asymmetry is often observed in field data for shoreface-connected ridges. Besides, the spatial shift between the patterns in the mean grain size and bottom topography (as found from the linear analysis and in the field observations) decreased. In the final state the relative distance between the crest and the location of the finest mean grain size was very small. This was related to a change in the erosion and deposition pattern of suspended load and the relative importance of bed load with respect to suspended load.

A limitation of the method used for the nonlinear model is that it does not permit calculations for realistic slopes of the inner shelf. For values larger than 50% of observed values, numerical instabilities develop during the evolution process, causing unbounded behaviour. Extrapolation of the model results towards realistic bottom slopes yielded estimates of the bedform height, saturation time and migration velocity that agree well with field data. However, a large discrepancy exists between the observed and modelled maximum variation in

the mean grain size. The latter gives values that are approximately a factor 100 smaller than those obtained from field measurements. The reason for this discrepancy must be sought in the neglect of physical processes in the equation that describes the evolution of the fraction of fine and coarse grains. Here we will discuss the validity of the assumptions that underlie this equation and their possible implications.

One possibility that may explain the too small grain size variations in the model is that the one-layer model for the bottom evolution is not valid for bedforms that evolve on timescales of 100-1000 years. The basic idea was that sediment is only transported from a bottom layer of a few centimetres thick, in which no vertical sorting an negligible interaction with the layer below occurs. If the exchange of sediment between the transport (surface) layer and the underlying substrate occurs on a faster timescale than the bottom evolution, the sediment flux between the two layers can significantly influence the grain size distribution in the upper layer. This is likely to occur, because the presence and migration of small-scale bedforms on top of the large-scale ridges can cause a significant reworking of the sediment. Introducing such an exchange flux changes the balance in the evolution equation for the fractions of fine and coarse grains and introduces a possibility for additional growth of the mean grain size variations.

A second possibility is that the surficial sediment is a response to forcing conditions that are not accounted for in the model. For shoreface-connected ridges the forcing is only representative of storms. The suggestion has been raised by Swift et al. (1972) that the development of ridges occurs during storm periods, whereas the surficial sediment pattern mainly develops during the intermediate periods of fair weather. They relate the size-fractioning of the sediment at the crest and on the flanks to low-amplitude swell waves with associated strong asymmetrical bottom currents. Besides, during fair weather conditions wind-induced Ekman transport and horizontal density gradients caused by river discharges generate a net cross-shore circulation in the vertical plane, such that the near-bottom flow is directed landward (Van der Giessen et al., 1990; De Ruijter et al., 1997; Niedoroda and Swift, 1981). Measurements indeed reveal a landward transport of sediment during calm weather. This is opposite to the circulation in storm conditions: current measurements on the North American Atlantic shelf indicate that storms cause strong offshore directed bottom currents (downwelling conditions) (Swift et al., 1978; Swift and Field, 1981; Niedoroda et al., 1984). Furthermore, observations (Swift et al., 1978; Parker et al., 1982) show that while the shape of the ridges changes between symmetrical and asymmetrical, the surficial grain size pattern is more consistent with the finest sediments on the seaward flank. With the main deposits consisting of storm-related layers (Figueiredo et al., 1982), fair weather induced variations in the mean grain size can not be present below the surface. The vertical sediment cores that could provide such information are scarce and the often complex structure of the deposited layers under the migrating ridges makes it impossible (at this moment) to verify this hypothesis on the basis of field data only.

Including a fair weather transport in the model introduces a highly nonlinear relation between the sediment fluxes and the current. For a steady flow this could introduce other bottom and grain size patterns, which can have a different amplitude and shape with respect to the ones found in case of solely storm conditions. Furthermore, in the models presented in this thesis the vertical structure of the currents is neglected. Although the main characteristics (shape, height) of the ridge topography are represented quite well with depth-averaged cur-

rents, the sediment distribution in a thin surface layer can be more strongly determined by the near-bed currents.

One last aspect in the modelling of sediment mixtures is that in the present study the number of grain size classes used is only two, while in fact the distribution covers a wide range of grain diameters. In the context of idealised models, accounting for more grain fractions does not seem to lead to more insight in the physical processes because the mechanisms causing the sediment sorting do not change and therefore no major changes are expected.

Currents, waves and sediment flux

The morphodynamic models presented here consist of the depth-averaged (2DH) shallow water equations, a sediment transport formulation and a bottom evolution equation. The uncertainty in the latter is already discussed above. The formulation of the sediment transport also requires some further discussion. It should be noticed that there is still a lack of fundamental knowledge (and data) on the sediment transport processes in coastal seas, especially during storms. The parameterisations used in this study for the sediment transport and their extension towards sediment mixtures are based on several assumptions. These should be discussed in the context of idealised models, where the philosophy is to include only processes that are expected to play a key role in the dynamics of the phenomena under investigation. The transport formula that are used in stability models for the formation of bedforms have evolved from a simple bed load formulation that is given by a constant times the velocity (Trowbridge, 1995), towards formulations which include bedslope effects, suspended load fluxes and the effect of wave-stirring (cf. Falqués et al., 1996, 2000; Calvete et al., 2001a,b). With the good results obtained with these models, which consider a single grain size only, the next step was to generalise them to include multiple grain sizes in a simple manner. Dynamic hiding effects that are mostly based on empirical relations deduced from measurements in shallow rivers and flume experiments were applied to shallow coastal seas. The convergence of the sediment flux determines the pattern of erosion and deposition and thereby not only the characteristics of the bedforms, but also the pattern in the fraction of fine and coarse grains. Therefore, we again focus on the (single grain size) transport parameterisations that were used as a basis for the multiple grain size formulations in this thesis.

The derivation of the sediment flux during storms is based on assumptions regarding the wave amplitude, direction and asymmetry of the velocity field with time. The amplitude of the wave-orbital velocity is large compared to the wave-averaged velocity (due to the wind shear stress, pressure gradients and tides). A linear relation exists between the advective part of the sediment flux and the wave-averaged velocity ($\vec{v}$), thus $\vec{q} = K\vec{v}$. In the case that the waves are directed parallel to the velocity $\vec{v}$ (i.e. almost shore-parallel), K is a scalar that represents a wave-stirring factor. In a more elaborate expression which is valid for different angles between the direction of the wave incidence and the net current, K becomes a tensor, such that the net sediment flux and net current have different directions. This may lead to changes in the growth and migration rate of the bedforms.

Furthermore, the impact of waves is restricted to symmetrical waves. In this first-order approximation waves only result in the stirring of sediment and no net sediment transport (due to wave-asymmetry) is modelled. In the model it is assumed that the onshore flux of sediment due to wave-asymmetry is compensated by the offshore bedslope flux due to the transverse

bottom slope of the inner shelf. Therefore, the bedslope flux only acts in case of perturbations in the bottom. At present, boundary conditions are such that no sediment exchange is allowed between the inner shelf and shoreface and thus the model does not account for a dynamical interaction of the ridges with the coastline. In the context of the nonlinear analysis this can be studied by including solutions with an alongshore uniform structure, as was already done by Calvete and De Swart (2003) for shoreface-connected ridges.

The wave effect in the nonlinear model is incorporated in the same way as in the linear model: wave properties only depend on the undisturbed reference depth and refraction and shoaling due to the presence of bedforms is not accounted for. For ridges with a considerable height the impact of waves on the crest is stronger than in the troughs, an effect which is not included in the model due to this simplification. Such a mechanism would result in an increased stirring above the ridges and smaller stirring in the troughs (see also discussion in Calvete et al., 2001b), thereby contributing to the saturation process that leads to a finite-amplitude. The processes that caused a stabilisation in the growth of the shoreface-connected ridges in the present model were related to a change in the pattern for the suspended sediment flux with an increased height of the ridges (chapter 5). Including the local depth in the parameterisation of the wave effects in this flux could therefore influence the evolution of the ridges. Such a generalisation is in fact not allowed, because the parameterisation is strictly only valid for parallel depth contours. Also other effects that influence the wave-impact, such as refraction and partial breaking of waves, should then be accounted for in an appropriate manner.

Further research

In the context of the models that are presented in this thesis a few problems that have not been addressed can be studied relatively easily. In chapters 3 and 4 the initial formation of grain sorting patterns is investigated for either storm or fair weather conditions. A similar study for a combined forcing by both conditions, as was done in chapters 2 for uniform sediment, could give an indication of the influence of storms (fair weather) on the grain size distribution over tidal sand ridges (shoreface-connected ridges). Another interesting experiment is when the reference state is extended to include a cross-shelf gradient in the mean grain size. A seaward fining trend is reported for the areas of shoreface ridges on the American Atlantic shelf and the German Bight (Swift et al., 1978), while on the Belgian shelf, where also tidal ridges are present, the sediment becomes finer in the landward direction. This introduces new terms in the bottom evolution equations and they will influence the dynamics of grain sorting.

As mentioned above, the effect of bedforms on the wave stirring could be a valuable extension of the model. To account properly for the effect of bedforms on the wave stirring, a sophisticated wave transformation model, based on e.g. the eikonal equation, would be required. Application of such a method to the nearshore region of a straight barred coast already showed succesful results (Calvete et al., 2003).

In the subsection 'linear versus nonlinear', the suggestion was raised that a more realistic representation of the bottom layer is needed to represent the grain size pattern correctly, e.g. by introducing an exchange layer to the one-layer model. This could be done. Nevertheless, the present knowledge on vertical sorting processes is very limited (see, for example, Blom and Ribberink, 1999; Parker et al., 2000) and a verification of the model results would be

very difficult.

Bearing in mind the previous remarks with regard to the formulation for the sediment fluxes, it is important too realise that the most crucial nonlinear contributions for the finite-amplitude evolution of the shoreface-connected ridges originate from the mass balance equation. Similar results were found by Idier and Astruc (2003), who analysed the results of a nonlinear model for tidal sand ridges, and showed that saturation is mostly due to hydrodynamic processes, albeit for a different case (viz. it is based on a single grain size, tidal current forcing and different solution methods). It would be interesting to investigate whether the saturation for shoreface-connected ridges is influenced by the quasi-steady assumptions and the neglect of free-surface variation on the water depth in the hydrodynamic equations.

The analysis of a 3D flow over an uneven bed, which is a complicated problem, is considered to be one of the most important topics for further research, especially in the context of the origin of the mean grain size patterns. Finally, also tests should be performed with more complex process-oriented models, such as Delft3D, that attempt to describe all physical processes. For instance, they are better suited to investigate the optimal number of grains that is needed to describe the sorting processes correctly and experiments with larger slopes of the inner shelf and arbitrary geometries could be performed. Furthermore, complex process-oriented models are suitable to be used for studying practical problems in the coastal zone, such as the dynamical interaction of large-scale ridges with the coast.

Bibliography

Admiraal, D. M., Garcia, M. H., Rodriguez, J. F., 2000. Entrainment response of bed sediment to time-varying flow. Water Resour. Res. 36 (1), 335–348.

Amos, C. L., Nadeau, O. C., 1988. Surficial sediments of the outer banks, Scotian Shelf, Canada. Canadian journal of earth sciences 25, 1923–1944.

Antia, E. E., 1993. Surficial grain-size statistical parameters of a North Sea shoreface-connected ridge: patterns and process implication. Geo-Marine Lett. 13, 172–181.

Antia, E. E., 1996. Shoreface-connected ridges in German and US Mid-Atlantic bights: similarities and contrasts. J. Coastal Res. 12, 141–146.

Armanini, A., 1995. Non uniform sediment transport: dynamics of the active layer. J. Hydr. Res. 33 (5), 611–622.

Bailard, J., 1981. An energetics total load sediment transport model for a plane sloping beach. J. Geophys. Res. 86, 10938–10954.

Bayram, A., Larson, M., Miller, H. C., Kraus, N. C., 2001. Cross-shore distribution of longshore sediment transport: comparison between predictive formulas and field measurements. Coastal Eng. 44, 79–99.

Berné, S., Trentesaux, A., Stolk, A., Missiaen, T., de Batist, M., 1994. Architecture and long term evolution of a tidal sandbank: The Middelkerke Bank (southern North Sea). Mar. Geol. 121, 57–72.

Blom, A., Ribberink, J. S., 1999. Non-uniform sediment in rivers: vertical sediment exchange between bed layers. In: I.A.H.R. Symposium on River, Coastal and Estuarine morphodynamics, Genova. Vol. I.

Calvete, D., 1999. Morphological stability models: shoreface-connected sand ridges. Ph.D. thesis, Universitat Politécnica de Catalunya, Departament de Fisica Aplicada, Spain.

Calvete, D., De Swart, H. E., 2003. A nonlinear model study on the long-term behaviour of shoreface-connected sand ridges. J. Geophys. Res. 108 (C5), 3169, doi:10.1029/2001JC001091.

Calvete, D., De Swart, H. E., Falqués, A., 2002. Effect of depth-dependent wave stirring on the finite amplitude of shoreface-connected sand ridges. Cont. Shelf Res. 22, 2763–2776.

Calvete, D., Dodd, N., Falqués, A., 2003. Morphological development of nearshore bedforms. In: Smith, J. M. (Ed.), Coastal Engineering 2002. Vol. 3. World Scientific.

Calvete, D., Falqués, A., De Swart, H. E., Walgreen, M., 2001b. Modelling the formation of shoreface-connected sand ridges on storm dominated inner shelves. J. Fluid Mech. 441 (C5), 169–193.

Calvete, D., Walgreen, M., De Swart, H. E., Falqués, A., 2001a. A model for sand ridges on the shelf: effect of tidal and steady currents. J. Geophys. Res. 106 (C5), 9311–9326.

Davies, A. M., Kwong, S. C. M., Flather, R. A., 1997. Formulation of a variable-function three dimensional model, with applications to the M_2 and M_4 tide on the North-West European Continental Shelf. Cont. Shelf Res. 17 (2), 165–204.

Davis, R. A., Klay, J., Jewell, P., 1993. Sedimentology and stratigraphy of tidal sand ridges southwest Florida inner shelf. J. Sed. Petr. 63 (1), 91–104.

De Ruijter, W. P. M., Visser, A. W., Bos, W. G., 1997. The Rhine outflow: A prototypical pulsed discharge plume in a high energy shallow sea. J. Mar. Sys. 12, 263–276.

Dyer, K. R., 1986. Coastal and estuarine sediment dynamics. John Wiley & Sons, Chichester.

Dyer, K. R., Huntley, D. A., 1999. The origin, classification and modelling of sand banks and ridges. Cont. Shelf Res. 19, 1285–1330.

Falqués, A., Calvete, D., Montoto, A., 1998. Bed-flow instabilities of coastal currents. In: Dronkers, J., Scheffers, M. B. A. M. (Eds.), Physics of Estuaries and Coastal Seas. Balkema, Rotterdam.

Falqués, A., Coco, G., Huntley, D. A., 2000. A mechanism for the generation of wave-driven rhythmic patterns in the surf zone. J. Geophys. Res. 105 (C10), 24071–24087.

Falqués, A., Montoto, A., Iranzo, V., 1996. Bed-flow instability of the longshore current. Cont. Shelf Res. 16 (15), 1927–1964.

Figueiredo, J. A. G., Sanders, J. E., Swift, D. J. P., 1982. Storm-graded layers on inner continental shelves: examples from southern Brazil and the Atlantic coast of the central United States. Sed. Geol. 31, 171–190.

Foti, E., Blondeaux, P., 1995. Sea ripple formation: the heterogenous sediment case. Coastal Eng. 25, 237–253.

Fredsøe, J., Deigaard, R., 1992. Mechanics of coastal sediment transport. World Scientific, Singapore.

Gao, S., Collins, M. B., Lanckneus, J., De Moor, G., Van Lancker, V., 1994. Grain size trends associated with net sediment transport patterns: an example from the Belgian continental shelf. Mar. Geol. 121, 171–185.

Garcia, M., Parker, G., 1991. Entrainment of bed sediment into suspension. J. Hydr. Eng. 117 (4), 414–435.

Gerkema, T., 2000. A linear stability analysis of tidally generated sand waves. J. Fluid Mech. 417, 303–322.

Green, M. O., Vincent, C. E., McCave, I. N., Dickson, R. R., Rees, J. M., Pearson, N. D., 1995. Storm sediment transport: observations from the British North Sea shelf. Cont. Shelf Res. 15 (8), 889–912.

Hoogendoorn, E. L., 1986. Morphology, lateral migration, and internal structures of shoreface-connected ridges, Sable Island Bank, Nova Scotia, Canada. Geology 14, 400–403.

Houthuys, R., Trentesaux, A., De Wolf, P., 1994. Storm influences on a tidal sandbank's surface (Middelkerke Bank, southern North Sea). Mar. Geol. 121, 23–41.

Hulscher, S. J. M. H., 1996. Tide-induced large-scale regular bed form patterns in a three-dimensional shallow-water model. J. Geophys. Res. 101 (C9), 20727–20744 (96JC01662).

Hulscher, S. J. M. H., De Swart, H. E., De Vriend, H. J., 1993. The generation of offshore

tidal sand banks and sand waves. Cont. Shelf Res. 13 (11), 1183–1204.

Huthnance, J. M., 1982a. On one mechanism forming linear sand banks. Est., Coastal and Shelf Sci. 14, 79–99.

Huthnance, J. M., 1982b. On the formation of sand banks of finite extent. Est., Coastal and Shelf Sci. 15, 277–299.

Idier, D., Astruc, D., 2003. Analytical and numerical modeling of sandbanks dynamics. J. Geophys. Res. 108 (C3), 3060, doi:10.1029/2001JC001205.

Lanckneus, J., De Moor, G., Stolk, A., 1994. Environmental setting, morphology and volumetric evolution of the Middelkerke Bank (southern North Sea). Mar. Geol. 121, 1–21.

Lanzoni, S., Tubino, M., 1999. Grain sorting and bar instability. J. Fluid Mech. 393, 149–174.

Lentz, S., Guza, R. T., Elgar, S., Feddersen, F., Herbers, T. H. C., 1999. Momentum balances on the North Carolina inner shelf. J. Geophys. Res. 104 (C8), 18205–18226.

Liu, Z. X., Xia, D. X., Berne, S., Wang, K. Y., Marsset, T., Tang, Y. X., Bourillet, J. F., 1998. Tidal deposition systems of China's continental shelf, with special reference to the eastern Bohia Sea. Mar. Geol. 145 (3-4), 225–253.

Ludwick, J. C., 1989. Bed load transport of sand mixtures in estuaries: a review. J. Geophys. Res. 94 (C10), 14315–14326.

Maes, F., Cliquet, A., Seys, J., Meire, P., Offringa, H., 1997. Limited atlas of the Belgian part of the North Sea. Tech. rep., University of Ghent, Dept. of Public International Law (Maritime Institute), Belgium and Institute for Nature Conservation, Brussel, Belgium.

McBride, R. A., Mosow, T. F., 1991. Origin, evolution, and distribution of shoreface sand ridges, Atlantic inner shelf, U.S.A. Mar. Geol. 97, 57–85.

Neméth, A. A., Hulscher, S. J. M. H., de Vriend, H. J., 2002. Modelling sand wave migration in shallow shelf seas. Cont. Shelf Res. 22, 2795–2806.

Niedoroda, A. W., Swift, D. J. P., 1981. Maintenance of the shoreface by wave orbital currents and mean flow: observations from the Long Island coast. Geophys. Res. Lett. 8 (4), 337–340.

Niedoroda, A. W., Swift, D. J. P., Figueiredo Jr., A. G., Freeland, G. L., 1985. Barrier island evolution, Middle Atlantic shelf, U.S.A. part II: evidence from the shelf floor. Mar. Geol. 63, 363–396.

Niedoroda, A. W., Swift, D. J. P., Hopkins, T. S., Ma, C.-M., 1984. Shoreface morphodynamics on wave-dominated coasts. Mar. Geol. 60, 331–354.

Off, T., 1963. Rhythmic linear sand bodies caused by tidal currents. Bulletin of the American Association of Petroleum Geologists 47 (2), 324–341.

Parker, G., Lanfredi, N. W., Swift, D. J. P., 1982. Seafloor response to flow in a Southern Hemisphere sand-ridge field: Argentine inner shelf. Sed. Geol. 33, 195–216.

Parker, G., Paola, C., Leclair, S., 2000. Probabilistic exner sediment continuity equation for mixtures with no active layer. J. Hydr. Eng. 126 (11), 818–826.

Pattiaratchi, C., Collins, M., 1987. Mechanisms for linear sandbank formation and maintenance in relation to dynamical oceanographic observations. Prog. Oceanogr. 19, 117–176.

Prandle, D., 1980. Co-tidal charts for the southern North Sea. Dt. hydrogr. Z. 33, 68–81.

Restrepo, J. M., 2001. Wave-current interactions in shallow waters and shore-connected ridges. Cont. Shelf Res. 21, 1331–1360.

Ribas, F., Falqués, A., Montoto, A., 2003. Nearshore oblique sand bars. J. Geophys. Res.

108 (C4), 3119, doi:10.1029/2001JC000985.

Ribberink, J. S., 1987. Mathematical modelling of one-dimensional morphological changes in rivers with non-uniform sediment. Ph.D. thesis, Tech. Univ. Delft, The Netherlands.

Roos, P. C., 2003. Tech. rep., Dept. of Civil Engineering, University of Twente, The Netherlands, personal communication.

Schuttelaars, H. M., De Swart, H. E., 1999. Initial formation of channels and shoals in a short tidal embayment. J. Fluid Mech. 386, 15–42.

Schwab, W. C., Thieler, E. R., Allen, J. R., Foster, D. S., Swift, B. A., Denny, J. F., 2000. Influence of inner-continental shelf geologic framework on the evolution and behavior of the barrier-island system between Fire Island Inlet and Shinnecock Inlet, Long Island, New York. J. Coastal Res. 16 (2), 408–422.

Seminara, G., 1995. Effect of grain sorting on the formation of bedforms. Appl. Mech. Rev. 48 (9), 549–563.

Short, A. D., 1999. Handbook of beach and shoreface morphodynamics. Wiley, Chichester.

Soulsby, 1997. Dynamics of marine sands. Thomas Telford, London.

Swift, D. J. P., Field, M. E., 1981. Evolution of a classic sand ridge field: Maryland sector, North American inner shelf. Sedimentology 28, 461–482.

Swift, D. J. P., Holliday, B., Avignone, N., Shideler, G., 1972. Anatomy of a shoreface ridge system, False Cape, Virginia. Mar. Geol. 12, 59–84.

Swift, D. J. P., Niedoroda, A. W., Vincent, C. E., Hopkins, T. S., 1985. Barrier island evolution, Middle Atlantic shelf, U.S.A. part I: shoreface dynamics. Mar. Geol. 63, 331–361.

Swift, D. J. P., Parker, G., Lanfredi, N. W., Perillo, G., Figge, K., 1978. Shoreface-connected sand ridges on American and European shelves: a comparison. Est. and Coastal Mar. Sci. 7, 257–273.

Talmon, A. M., Van Mierlo, M. C. L. M., Struiksma, N., 1995. Laboratory measurements of the direction of sediment transport on transverse alluvial-bed slopes. J. Hydr. Res. 33 (4), 495–517.

Trentesaux, A., Stolk, A., Berné, S., 1999. Sedimentology and stratigraphy of a tidal sand bank in the southern North Sea. Mar. Geol. 159, 253–272.

Trentesaux, A., Stolk, A., Tessier, B., Chamley, H., 1994. Surficial sedimentology of the Middelkerke Bank (southern North Sea). Mar. Geol. 121, 43–55.

Trowbridge, J. H., 1995. A mechanism for the formation and maintenance of the shore-oblique sand ridges on storm-dominated shelves. J. Geophys. Res. 100 (C8), 16071–16086.

Van de Kreeke, J., Robaczewska, K., 1993. Tide-induced residual transport of coarse sediment; application to the Ems estuary. Neth. J. Sea Res. 31 (3), 209–220.

Van de Meene, J., 1994. The shoreface-connected ridges along the central Dutch coast. Ph.D. thesis, Univ. Utrecht, The Netherlands, Nederlandse geografische studies, KNAG, Utrecht.

Van de Meene, J. W. H., Boersma, J. R., Terwindt, J. H. J., 1996. Sedimentary structures of combined flow deposits from the shoreface-connected ridges along the central Dutch coast. Mar. Geol. 131, 151–175.

Van de Meene, J. W. H., Van Rijn, L. C., 2000a. The shoreface-connected ridges along the central Dutch coast - part 1: field observations. Cont. Shelf Res. 20, 2295–2323.

Van de Meene, J. W. H., Van Rijn, L. C., 2000b. The shoreface-connected ridges along the central Dutch coast - part 2: morphological modelling. Cont. Shelf Res. 20, 2325–2345.

Van der Giessen, A., De Ruijter, W. P. M., Borst, J. C., 1990. Three-dimensional current structure in the Dutch coastal zone. Neth. J. Sea Res. 25, 45–55.

Van der Molen, J., 2000. A 2DH numerical model of tidally induced sand transport in the Southern North Sea. In: Yanagi, T. (Ed.), Interactions between Estuaries, Coastal Seas and Shelf Seas. Terra Scientific Publishing company.

Van Ledden, M., Van Kesteren, W. G. M., Winterwerp, J. C., 2002a. A classification for erosion behaviour of sand-mud mixtures. Cont. Shelf Res. Submitted.

Van Ledden, M., Wang, Z., Winterwerp, J., De Vriend, H., 2002b. Sand-mud morphodynamics in a short tidal basin. In: Physics of estuaries and Coastal Seas (PECS2002), Hamburg, Germany 2002.

Van Rijn, L. C., 1993. Principles of sediment transport in rivers, estuaries and coastal seas. Aqua Publ., Amsterdam.

Vincent, C. E., Stolk, A., Porter, C. F. C., 1998. Sand suspension and transport on the Middelkerke Bank (southern North Sea) by storms and tidal currents. Mar. Geol. 150, 113–129.

Vittori, G., Blondeaux, P., 1992. Sand ripples under sea waves. part 3. brick-pattern ripple formation. J. Fluid Mech. 239, 23–45.

Walgreen, M., Calvete, D., De Swart, H. E., 2002. Growth of large-scale bed forms due to storm-driven and tidal currents: a model approach. Cont. Shelf Res. 22 (18-19), 2777–2793.

Walgreen, M., De Swart, H. E., Calvete, D., 2003. Effect of grain size sorting on the formation of shoreface-connected sand ridges. J. Geophys. Res. 108 (C3), 3063, doi:10.1029/2002JC001435.

Williams, J. J., MacDonald, N. J., O'Conner, B. A., Pan, S., 2000. Offshore sand bank dynamics. J. Mar. Sys. 24, 153–173.

Wright, L. D., 1995. Morphodynamics of inner continental shelves. CRC Press, Boca Raton (FL).

Zimmerman, J. T. F., 1981. Dynamics, diffusion and geomorphological significance of tidal residual eddies. Nature 290, 549–555.

Zyserman, J. A., Fredsøe, J., 1994. Data analysis of bed concentrations of suspended sediment. J. Hydr. Eng. 120 (9), 1021–1042.

Samenvatting

Dynamica van zandruggen in kustzeeën: de invloed van stormen, getij en korrelgrootte sortering

Voor de kust van Nederland, op de bodem van de Noordzee, bevinden zich zandruggen. Kennis hierover is relevant voor onder andere de aanleg van vaargeulen voor de scheepvaart, booreilanden voor olie- en gaswinning, een vliegveld in zee en de winning van zand. De motivatie van het onderzoek dat is samengevat in dit proefschrift is het verkrijgen van meer fundamentele kennis van het dynamische gedrag van zandruggen.

Kenmerken van zandruggen

Zandruggen zijn langgerekte zandbanken van enkele tientallen kilometers lang en een paar kilometers breed, die zich bevinden op de bodem van ondiepe kustzeeën. Deze kustzeeën vormen de overgang van het land naar de diepe oceaan. Een typisch voorbeeld hiervan is de Noordzee. In figuur 1.3 is het deel voor de Belgische kust weergegeven, waarbij de donkere vlakken de ondiepere delen markeren. In waterdiepten van ongeveer 5-30 m vormen de zandruggen een ritmisch patroon dat zorgt voor een glooiing in de zeebodem. De kammen (het hoogste gedeelte van de zandruggen) kunnen een hoogte bereiken van enkele meters. In dit figuur is te zien dat zandruggen voorkomen in groepen, op verschillende locaties en met verschillende oriëntaties van de kammen ten opzichte van de kustlijn. Voor dit proefschrift maken we onderscheid tussen twee soorten zandruggen: kustaangehechte banken en getijbanken, waarvan de belangrijkste kenmerken hieronder besproken worden.

Waarneming laten zien dat kustaangehechte banken (*'shoreface-connected ridges'*) voorkomen in kustzeeën die gedomineerd worden door een sterke windgedreven (storm-gedreven) stroming langs de kust. Zij bevinden zich in een waterdiepte tussen de 5 en 20 meter en worden gekenmerkt door een hoek van $20 - 50^\circ$ tussen de kammen en de kustlijn. Het zeewaarts uiteinde is hierbij stroomopwaarts verplaatst. In de Noordzee komen de kustaangehechte banken voor langs de kust van Nederland en België (zie figuur 2.1), en voor de Duitse Waddeneilanden. Ook langs grote delen van de Atlantische kust van Noord Amerika en voor de kust van Argentinië zijn ze aanwezig. In figuur 1.4 (linker afbeelding) zijn de kustaangehechte banken voor Long Island (Noord Amerika) duidelijk zichtbaar in de dieptecontouren die schuin weglopen van de kust. Deze banken verplaatsen zich in de

richting van de stormgedreven stroming, met een snelheid van ongeveer 1-10 meter per jaar. Naast de topografische variatie, ofwel de veranderingen in waterdiepte die de ruggen markeren, is in dezelfde gebieden ook een opvallende variatie in de korrelgrootte verdeling van het oppervlakte sediment aanwezig. Het sediment aan het oppervlak van de ruggen bestaat voornamelijk uit zand, met slechts kleine hoeveelheden modder, grof schelpen materiaal en grind. Voor kustaangehechte banken bevindt het gemiddeld fijnste sediment mengsel zich op de stroomafwaartse (en zeewaartse) zijde van de ruggen, terwijl het grofste sediment zich op de stroomopwaartse (en landwaartse) zijde bevindt. In de rechter afbeelding van figuur 1.4 is dit patroon geïllustreerd voor een sectie gemeten dwars op de kust van Long Island. Deze variaties over de ruggen domineren vaak over grootschaligere trends in de omgeving.

In gebieden waar het getij een belangrijke rol speelt in de waterbeweging, treft men veelal een ander type zandruggen aan: getijbanken (*'tidal sand ridges'*). De kammen van deze zandruggen zijn cyclonaal, d.w.z. anti-kloksgewijs op het Noordelijk Halfrond, geroteerd ten opzichte van de dominante getijstroomrichting. De getijbanken hebben afmetingen van dezelfde grootte orde als voor kustaangehechte banken. De hoogste kammen zijn echter waargenomen voor de, meestal in dieper water gelegen, getijbanken. Het is niet goed bekend of getijbanken zich verplaatsen. Ook over dit type zandruggen is een duidelijke variatie van de gemiddelde korreldiameter van het oppervlakte sediment waargenomen. Een voorbeeld hiervan is weergegeven in figuur 1.5 voor de Belgische kustzee. Het grofste sediment ligt nu juist rond de kammen van de banken. Het begrijpen van deze variaties in korreldiameter over zandruggen is één van de doelstellingen van dit onderzoek.

Beiden typen zandruggen ontstaan over een tijdsperiode van decennia tot eeuwen. Door deze langzame evolutie geven waarnemingen geen uitsluitsel over alle mechanismen die hierbij een rol spelen. Daarnaast ontbreken vaak gegevens die zowel informatie geven over de topografie, de waterbeweging en de hoeveelheid verplaatst sediment. Eén van de theorieën voor het ontstaan van zandruggen is gebaseerd op de hypothese dat ze een dynamisch geheel vormen met de waterbeweging, waarbij er sprake is van een actieve interactie tussen beiden. Dit is de grondslag van het werk in dit proefschrift.

Onderzoeksmethode

De aanpak van het onderzoek is om bestaande morfodynamische modellen uit te breiden. Een morfodynamisch model beschrijft de waterbeweging en de evolutie van de bodem aan de hand van de fysische vergelijkingen. Hierbij is een sterk versimpelde (geïdealiseerde) weergave van de werkelijkheid gebruikt. Zo is bijvoorbeeld de gebruikte geometrie van de kust geschetst in figuur 2.2. In de beschrijving van de waterbeweging worden slechts de belangrijkste processen meegenomen. Voor de gebieden waar zandruggen voorkomen zijn dit vooral de wind- en getijgedreven stromingen. Aangezien het interessegebied horizontale afmetingen heeft van een paar kilometers en de waterdiepte slechts enkele tientallen meters is, worden alleen de dieptegemiddelde (horizontale) snelheden beschouwd.

De basisgedachte achter de bodemevolutie is dat door hogere stroomsnelheden meer sediment getransporteerd kan worden. Veranderingen in de stroomsnelheid zorgen daarmee voor de erosie van sediment van de zeebodem op de ene plaats en depositie op een andere plaats. Deze verandering in de stroomsnelheid kunnen ontstaan door veranderingen in de

lokale waterdiepte, die veroorzaakt worden door de aanwezigheid van kleine oneffenheden op een vlakke bodem. Onder sommige omstandigheden zorgt dit voor een toename van de depositie van sediment, waardoor kleine verstoringen in de bodem kunnen uitgroeien tot bodemvormen.

Zandruggen ontstaan op tijdschalen (decennia-eeuwen) die veel langer zijn dan de dominante tijdschalen voor de waterbeweging (seconden - dagen). In het model worden om deze reden slechts de netto verplaatsingen van het sediment gedurende enkele golf- en getijperioden meegenomen. Op deze manier kunnen met behulp van wiskundige methoden oplossingen gezocht worden die de belangrijkste kenmerken (oriëntatie, golflengte, migratie en groeisnelheid) van de ruggen reproduceren. De analyse van dit soort modellen geeft inzicht in de fysische mechanismen die essentiëel zijn voor het bestaan van een bepaald type bodemvorm. De toepassing van deze onderzoeksmethode is in het verleden al succesvol gebleken voor verschillende soorten bodemvormen, waaronder ook zandruggen.

Resultaten

In hoofdstuk 2 zijn de processen onderzocht die het samen voorkomen van zowel kustaangehechte banken als getijbanken in eenzelfde kustzee kunnen verklaren. Deze situatie doet zich onder andere voor langs het centrale deel van de Nederlandse kust (figuur 2.1), waar de getijbanken zich verder uit de kust bevinden. Dit gebied wordt gekenmerkt door de aanwezigheid van een sterke getijstroom en het met enige regelmaat voorkomen van stormen.

Het gebruikte model beschrijft zowel de situatie tijdens stormen, als tijdens rustig weer condities. De eerste kenmerkt zich door een sterke windgedreven stroming, transport van sediment in suspensie in de waterkolom en een sterke opwerveling van het sediment door golven. Onder deze omstandigheden voorspelt het model de groei van kustaangehechte banken. De tweede situatie is representatief voor een waterbeweging aangedreven door het getij en transport van sediment aan de bodem. Hiermee kunnen getijbanken worden gesimuleerd. Essentiële condities voor het tegelijkertijd voorkomen van beide typen zandruggen zijn bepaald uit een combinatie van bovenstaande modeltoestanden. Dit zijn de aanwezigheid van zowel een sterke getijstroming, als een storm frequentie (gemiddeld tijdspercentage stormen over tientallen jaren) die hoog genoeg is om te zorgen voor een stroming van vergelijkbare grootte. De stroomsnelheden zijn hierbij ongeveer 0.5 m/s. Voor de zuidelijke Noordzee betekent dit een stormfrequentie van 2-8%, welke overeenkomt met schattingen uit winddata. In dit hoofdstuk is, net als in de bestaande modellen voor zandruggen, aangenomen dat het zand op de bodem gekenmerkt wordt door één enkele korreldiameter.

De nadruk in dit proefschrift (hoofdstuk 3-5) ligt op het modelleren van de waargenomen korrelgrootteverdelingen van het bodemsediment over de zandruggen. Om deze te kunnen modelleren is onderscheid gemaakt tussen transport van fijn en grof sediment. Verschillen hierin kunnen ontstaan door de invloed van *'hiding'*: de krachten die de korrels ondervinden door de stroming zijn kleiner voor de fijnere korrels, omdat deze afgeschermd ('verstopt') liggen tussen de grovere korrels. Voor bodemtransport zorgt dit voor een afname in de mobiliteit van de fijne sediment fractie. Voor sediment in suspensie neemt het transport van de fijne sediment fractie relatief toe ten opzicht van de grove fractie; dit komt doordat tevens is meegenomen dat grover sediment makkelijker uitzakt uit de waterkolom.

Hoofdstuk 3 en 4 laten zien dat *'hiding'* effecten binnen de context van een geïdealiseerd model voor zandruggen kunnen leiden tot de sortering van sediment, wat resulteert in een ruimtelijk niet-uniforme verdeling van de gemiddelde korrelgrootte in het gebied. Dit is gedaan voor kustaangehechte banken (hoofdstuk 3) langs de kust van Noord Amerika, een gebied waar getijbanken afwezig zijn. Storm condities komen hier frequent voor en getijstromen zijn verwaarloosbaar klein. De verdeling van sediment komt goed overeen met veldwaarnemingen: het fijnere sediment bevindt zich op de stroomafwaartse zijde. De verschuiving tussen de locatie van de maxima in de gemiddelde korrelgrootte verdeling en de locatie van de kammen van de ruggen is het gevolg van het dominante transport van sediment in suspensie. Daarnaast zorgt het meenemen van de interactie tussen de korreldiameters voor een verandering in de karakteristieken van de kustaangehechte banken: de groeisnelheid neemt af, en de migratiesnelheid en golflengte (afstand kam - kam) van de ruggen nemen toe.

In hoofdstuk 4 is de sortering onderzocht voor de getijbanken voor de Belgische kust. In tegenstelling tot de Atlantische kust van Noord Amerika is hier is de getijstroom dominant. De belangrijkste component hiervan is het M_2 getij, welke het resultaat is van de aantrekkingskracht tussen de zon en de maan en zorgt voor twee keer per dag hoog water. In het model wordt de invloed van stormen en golven verwaarloosd. Tijdens deze zogenaamde rustig weer condities is aangenomen dat het sediment transport alleen plaatsvindt aan de bodem. Onder de aandrijving van de waterbeweging door het M_2 getij ontstaat een patroon in de gemiddelde korreldiameter, waarbij het grofste sediment zich rond de kammen bevindt. Dit komt overeen met de waargenomen trend. De aanwezigheid van een windgedreven stroming naast het M_2 getij, kan het sorteringspatroon verschuiven ten opzichte van de topografie. Hetzelfde effect kan worden bereikt door het meenemen van een getijcomponent met een andere periode, zoals het M_4 getij, waardoor een asymmetrische getijstroom ontstaat (maximale vloed snelheid hoger dan maximale eb snelheid). Op sommige locaties zijn zulke verschuivingen waargenomen.

Bovenstaande resultaten zijn alleen representatief voor de eerste fase van het ontstaan van de ruggen, waarbij de hoogte van de kammen nog klein is ten opzicht van de waterdiepte. De toegepaste analyse methode (lineaire stabiliteitsanalyse) laat alleen exponentiëel groeiende oplossingen toe, en is daarom slechts een goede benadering voor de initiële groei. Deze beperking zorgt voor een relatief simpel stelsel van vergelijkingen, waardoor de interpretatie (oorzaak - gevolg) van de gevonden resultaten gemaakt kan worden. De vraag is echter hoe de resultaten kunnen worden gerelateerd aan de veldwaarnemingen van zandruggen met een eindige (maar niet kleine) hoogte.

In hoofdstuk 5 is de analyse van hoofdstuk 3 voor kustaangehechte banken hiertoe aangepast. De resultaten van de niet-lineaire analyse uit hoofdstuk 5 geven een indicatie van de uiteindelijke evenwichtstoestand van de banken. De schatting voor de evenwichtshoogte (enkele meters), tijd voor het bereiken van deze hoogte (enkele eeuwen) en migratie (enkele meters per jaar) komen goed overeen met de waarnemingen. Echter, de variaties in korreldiameter over de banken zijn onrealistisch klein, welke mogelijk een oorzaak heeft in de beschrijving van de bodemlaag van waaruit het sediment transport plaatsvindt. In hoofdstuk 6 worden de aannamen van de modellen die zijn gebruikt bediscussieerd. Tevens worden mogelijke punten van verbetering aangedragen.

Dankwoord

Uiteindelijk is het dan toch gelukt om het onderzoek af te ronden. Een moeilijke opgave, omdat onderzoek nooit helemaal af is. Gelukkig waren er meerdere personen die een bijdrage hebben geleverd aan de voltooiing dit werk. Op deze plek wil ik hen dan ook graag bedanken.

Tijdens mijn afstuderen werd ik door Huib de Swart gevraagd om het werk voort te zetten in een promotieonderzoek. Nog voor ik hieraan begon, kreeg ik van Huib en Theo Gerkema op het laatste moment de kans om deel te nemen aan de internationale zomerschool in Renesse. Deze zeer nuttige ervaring zorgde voor een vliegende start van mijn promotietraject, waarvoor ik erg dankbaar ben. De afgelopen jaren heb ik altijd erg plezierig kunnen samenwerken met Huib. De kwaliteiten van Huib als begeleider werden nog wel het meest duidelijk als ik het zelf even niet meer zag zitten. De besprekingen van het werk leidde zonder uitzondering tot volop nieuwe ideeën, welke tevens een zeer welkome bron van hernieuwde motivatie voor mij waren.

During my first years I also got a lot of support from Daniel Calvete. I could not have whished for a better expert at the IMAU in Utrecht. Even when he went back to Barcelona, and was very busy with his new occupations, he always made time to look at one of my problems. Daniel, thanks for helping with the code, the interpretation of new results and for providing comments on the papers. I would never have finished my Ph.D. in four years without your support! The opportunities I got to visit Albert Falqués and his group at the UPC in Barcelona were the trips abroad I enjoyed most. The discussions with Albert and his devotion to the work were always very inspiring.

Daarnaast wil ik natuurlijk ook de rest van de kustengroep bedanken voor de discussies over het werk en de goede sfeer die er de afgelopen jaren altijd was. De vrees dat ik het de laatste maanden zonder de gezelligheid van een kamergenoot zou moeten stellen is gelukkig niet uitgekomen. Uiteindelijk verlaten we de kamer bijna tegelijk en ik wens Sonja dan ook veel succes met de postdoc baan in Engeland.

De discussiepunten en nieuwe invalshoeken die mijn promotor Job Dronkers de laatste maanden aandroeg over het onderzoek hebben op de valreep nog veel toegevoegd aan dit proefschrift. De interesse van Will de Ruijter in het onderzoek en zijn bereidheid om klaar te staan als diplomatieke bemiddelaar heb ik zeer gewaardeerd. Ongetwijfeld zal ik de gezellige koffie en lunchpauzes met de collega's van het IMAU gaan missen.

Tijdens de afronding van het manuscript voor de leescommissie, leken de dagen opeens veel te kort. Niet in de laatste plaats omdat veel tijd ging zitten in het reizen met de trein tussen Delft en Utrecht. Gelukkig was er genoeg steun om dit wat te verlichten. Mijn voorstel om een dag in de week thuis aan de slag te gaan werd zonder enig tegenstribbelen goedgekeurd.

Het vertrouwen dat Huib daarmee in mij stelde was erg prettig. Gelukkig waren er nog genoeg verlofdagen over voor als er thuis dan toch teveel andere zaken waren die net even belangrijker leken.

Mijn paranimfen Mirjam en Floor maakten het daarnaast nog zeer aantrekkelijk om af en toe wat langer in Utrecht te verblijven. Elke maandagavond kon er worden aangeschoven voor het eten, gevolgd door een gezamelijke uurtje ontspanning/inspanning in het zwembad. Garrelt en ik hebben dankbaar gebruik gemaakt van deze gezellige service. Floor wil ik ook bedanken voor de vele suggesties om mijn Nederlandse samenvatting beter leesbaar te maken.

Als laatste, maar zeker niet als onbelangrijkste, wil ik ook Garrelt bedanken voor het mogelijk maken van het thuiswerken. Ons eigen computernetwerkje thuis werkte, na wat opstart problemen, prima. Als geen ander heb je mij gesteund bij het afronden van dit proefschrift.

Curriculum Vitae

Marianne Walgreen werd geboren op 21 augustus 1976 in Amstelveen. In september 1988 begon zij aan het VWO aan de openbare scholengemeenschap Snellius, later het Nieuwer Amstel genaamd, in Amstelveen. Na 6 jaar, in juni 1994, werd dit traject afgesloten met een diploma voor het atheneum. De interesse voor exacte vakken werd door een docent natuurkunde gestimuleerd: uit eigen ervaring kende hij een interessante opleiding in Utrecht. Zo kwam het dat zij in datzelfde jaar vertrok naar Utrecht om daar de opleiding meteorologie & fysische oceanografie (kortweg MFO) te volgen. Na een gemeenschappenlijke propadeuse met natuur- en sterrenkunde (april 1996) volgde het doctoraal diploma in de meteorologie & fysische oceanografie in juni 1999. Het afstudeeronderzoek over kustaangehechte banken gaf een mooie voorzet voor het promotieonderzoek dat hierna volgde. In september 1999 begon zij als assistent in opleiding aan het Instituut voor Marien en Atmosferisch onderzoek Utrecht (IMAU), in dienst van de Universiteit Utrecht. Dit werk heeft geleid tot dit proefschrift en zal in oktober 2003 worden verdedigd.